



**TRANSIENT TORSIONAL VIBRATION ANALYSIS
OF POLAR-CLASS PROPULSION SHAFTING SYSTEMS
UNDER ICE-PROPELLER INTERACTION LOADS**

by © Alessandro Zambon

*A Thesis submitted to the School of Graduate Studies
in partial fulfillment of the requirements for the degree of*

Doctor of Philosophy

Ocean and Naval Architectural Engineering

Faculty of Engineering and Applied Science

Memorial University of Newfoundland

June 1, 2022

St. John's, Newfoundland and Labrador, Canada

Abstract

The design of propulsion plants for Polar-Class vessels has to ensure the safety and preservation of ship operations in sea ice environments. In particular, the effects of ice-propeller interaction on shafting segments constitute a potential hazard for the integrity of the entire propulsion system. Collisions of ice blocks with propeller blades induce high torsional vibrations along shaftlines and cause the prime mover's output torque to fluctuate abruptly. These processes also undermine ships' propulsion efficiency and manoeuvring capability during icebreaking expeditions, as well as during ice navigation of commercial vessels and offshore operations. Consequently, the development of effective design methods dedicated to the dynamics of ship propulsion systems is fundamental to simulate the effects of ice-induced loads correctly. To this end, full-scale measurements have proven essential to support the evolution of robust design criteria and updated regulatory guidelines.

The research activity presented in this doctoral thesis aims to accomplish two objectives: firstly, delivering a modelling methodology to simulate the propulsion shaftlines of Polar-Class vessels, for the analysis of the torsional dynamic response caused by ice-propeller interaction processes; secondly, providing indications about the mathematical characterization of the ice-propeller torque pattern. The research project includes full-scale measurements conducted aboard the two Canadian Coast Guard icebreakers *Henry Larsen* and *Terry Fox*.

Torsional vibration data acquired from CCGS *Terry Fox*'s shaftlines validate an original mathematical model to simulate the dynamic torque delivered by Diesel engines. Besides,

an innovative integrated measurement system is installed aboard CCGS *Henry Larsen* ice-breaker to achieve concurrent monitoring of the shafts' dynamic response, sea ice conditions, and propulsive performance. The experimental measures obtained in open-water navigation are employed to validate the numerical models of both vessels' shaftlines. Conversely, the datasets of the ice-induced shaft responses are used to calculate the actual ice-propeller milling torques and correlate them to the ongoing ice conditions; this represents a unique outcome in this subject's state-of-the-art scenario. Alterations of the main properties of the rules' ice-propeller excitation—defined by the current design recommendations—are then tested to determine their influence on the shaftline dynamic response. Overall, the results suggest that the mathematical procedure defining the ice-propeller torque pattern, which is described in these guidelines, might need to be reviewed.

Acknowledgements

Thanks to my supervisors, who made it possible for me to expand my knowledge and grow professionally throughout my doctoral research experience.

Firstly, I must express my gratitude to my main supervisor, Dr. Lorenzo Moro, who had introduced me into the Engineering research sector during the development of my Master's thesis in 2017 and then gave me the opportunity to further evolve my scientific learning through this Ph.D., with professional guidance and dedication.

Secondly, I am greatly thankful to my ABS supervisor Dan Oldford P.Eng, whose wise mentoring made me remarkably improve my expertise in more technical contexts; he supported the work on this thesis and gave me precious advice for the continuation of my career.

Thanks to Drs. David Molyneux and Bruce Quinton for their availability and courtesy demonstrated throughout my academic work. Besides, thanks to my research group mates and the EN1035C lab folks for their fellowship during my four years at MUN.

Thanks to my family and all my friends for their incredible support, motivation, and closeness during my life back home in Italy and my whole academic career thereafter—especially through the unprecedented historical period we all experienced in 2020 and 2021.

Finally, I would like to include a curious personal note: thanks to James Cameron for his 1997 movie *Titanic*, which sparked and magnified my innate passion for the Ships' universe when I was a 7-year-old kid. I am not a spiritual person; nonetheless, the fact that I am concluding my Ph.D. in Newfoundland—the closest land to Titanic's wreckage—and almost exactly on the 110th anniversary of this liner's iconic voyage—April 1912—makes me wonder that perhaps, somehow, there could be a design behind this pattern.

The research project at the basis of this doctoral thesis was supported by the American Bureau of Shipping (ABS), the Canadian Coast Guard (CCG), the National Research Council of Canada (NRC), and the Department of Industry, Energy and Technology (IET) of the Government of Newfoundland and Labrador, Canada. Without their fundamental scientific and financial contributions, the achievements of this study would not have been possible.

Table of contents

Abstract	ii
Acknowledgements	iv
List of Tables	xiii
List of Figures	xvi
1 <i>Introduction and overview</i>	1
1.1 Problem statement	1
1.2 Modelling ship propulsion systems: background	3
1.2.1 Early developments	3
1.2.2 Recent studies	5
1.3 Navigation in Arctic environments: overview	9
1.4 Ice-propeller interaction and shaftline TVA: outline	11
1.4.1 Ice-induced loads on marine propellers	11
1.4.2 Ice-propeller interaction effects on ship propulsion systems	13
1.4.3 Ice environment monitoring	16
1.5 Scopes and contributions of the research	17
1.6 Synopses of the Chapters	20
1.7 Co-authorship statements	25
References	27

2	<i>A measurement system to monitor propulsion performance and ice-induced shaftline dynamic response of icebreakers</i>	37
	Abstract	37
	Keywords	38
2.1	Introduction	38
2.1.1	Environmental and economic framework	38
2.1.2	Role of the marine industry	40
2.1.3	Contribution of the present work	42
2.2	Materials and Methods	43
2.2.1	Overview of the instrumentation set and description of the case study vessel	43
2.2.2	Shaft thrust, torque, speed measurement at low frequency	45
2.2.3	Shaft speed measurement at high frequency	48
2.2.4	Ice condition monitoring	49
2.2.5	TT-Sense torque data validation via strain gauge measurements	51
2.2.6	Trials in ice-covered waters	53
2.3	Results	55
2.3.1	Validation of the TT-Sense torque measures	55
2.3.2	Analysis of the laser tachometer signal	59
2.3.3	Ice-induced perturbations on the shaft dynamic response	60
2.4	Discussion	68
2.5	Conclusions	70
	Acknowledgements	71

Abbreviations	72
References	72
3 Torsional vibration analysis of Diesel driven propulsion systems: the case of a	
<i>Polar-Class vessel</i>	77
Abstract	77
Keywords	78
3.1 Introduction	78
3.1.1 Diesel engine’s excitation modelling	80
3.1.2 Shaftline TVA and ice-propeller interaction	81
3.1.3 Contribution of the present work	82
3.2 Theoretical framework	84
3.2.1 Shaftline lumped-parameter model	84
3.2.2 Mathematical model of the Diesel engine driving torque	85
3.2.3 Propeller hydrodynamic torque characteristics	94
3.2.4 Mathematical model of the CPP control	95
3.2.5 Modeling procedure for the components of the lumped-element system	96
3.3 Application to a case study	99
3.3.1 The case study vessel	100
3.3.2 Full-scale measurements	102
3.3.3 Numerical model’s validation process	104
3.4 Validation of the numerical models	107
3.4.1 Shaft torque and power: experimental outcomes	107
3.4.2 Validation of the Diesel-engine torque mathematical model	109

3.4.3	Model updating	111
3.5	Ice-propeller interaction: TVA simulations	116
3.5.1	Ice-induced torque	116
3.5.2	Implementation to the case study vessel	117
3.5.3	Results	117
3.6	Discussion	122
3.6.1	Strengths and limitations	122
3.6.2	Future developments	124
3.7	Conclusions	125
	Acknowledgements	125
	Appendices to Chapter 3	126
3.A	Shaftline’s main specifications	126
3.B	Ice-propeller interaction torque	127
	References	129
4	<i>Torsional vibrations of Polar-Class shaftlines: correlating ice-propeller interaction torque to sea ice thickness</i>	135
	Abstract	135
	Keywords	136
4.1	Introduction	136
4.1.1	Ice-going vessel design: an overview	136
4.1.2	Experimental works on board ice-going ships	138
4.1.3	Ice-propeller interaction and shaftline modeling	139
4.1.4	Contribution of the present work	140

4.2	Methods	141
4.2.1	Case study	142
4.2.2	Shaftline model: development and validation	143
4.2.3	Full-scale measurements during icebreaking operations	149
4.2.4	Calculation of the ice-propeller interaction torque	153
4.2.5	Post-processing of the data	157
4.3	Results	158
4.3.1	Shaftline model validation	158
4.3.2	Full-scale measurements	162
4.3.3	Verification of the IM algorithm	165
4.3.4	Data analysis results: correlations between shaft data and ice thickness	168
4.4	Discussion	173
4.4.1	Comments on the results	173
4.4.2	Strengths and limitations of this work	177
4.4.3	Future work	179
4.5	Conclusions	180
	Acknowledgements	181
	Appendices to Chapter 4	181
4.A	Characteristics of the ice-propeller interaction torque in the IACS Polar Rules	181
4.B	Structural properties of the case study's shaftline numerical model	184
	References	186
5	<i>Impact of different characteristics of the ice-propeller interaction torque on the torsional vibration response of a Polar-Class shaftline</i>	191

Abstract	191
Keywords	192
5.1 Introduction	192
5.1.1 Background	192
5.1.2 Ice-propeller interaction loads: modelling and applications	193
5.1.3 Contribution of this work	196
5.2 Methods	197
5.2.1 Overview	197
5.2.2 Numerical model of the case study shaftline	198
5.2.3 Ice torque patterns	212
5.2.4 Simulation series and analysis of the results	219
5.3 Results and discussion	223
5.3.1 Equivalence between the condensed and expanded models	223
5.3.2 Scenario 1: ice-induced steady-state	229
5.3.3 Scenario 2: single-impact transient response	238
5.3.4 Scenario 3: transition between transient and steady-state conditions	243
5.4 Final remarks	247
5.4.1 Summary of the results	247
5.4.2 Strengths and limitations of this work	249
5.4.3 Future developments	250
5.4.4 Conclusions	250
Acknowledgements	252
Appendices to Chapter 5	252

5.A Numerical model of the case study’s shaftline: structural properties	252
References	255
6 <i>Summary and final remarks</i>	259
6.1 Summary	259
6.2 Conclusions and discussion on the outcomes	260
6.3 Future developments	263
References	264

List of Tables

1.1	Comprehensive outline of each Chapter’s contents and objectives.	24
2.1	Outline of the measurement system components.	44
2.2	Main specifications of the icebreaker CCGS <i>Henry Larsen</i>	45
2.3	Torque values from the different sources, for seven speed levels.	55
3.1	Main specifications of the CCG heavy icebreaker <i>Terry Fox</i>	100
3.2	Main specifications of CCGS <i>Terry Fox</i> ’s propulsion system components. .	101
3.3	Detailed specifications of the engine components.	101
3.4	Measurement-based shaft torque and power values at different CPP scenarios.	108
3.5	Values of $p_{0,spec}$ and $p_{peak,spec}$ from the Diesel engine specifications; the data points are provided for 7 $\ell_{P,spec}$ operating loads.	109
3.6	Parameters and results from the Diesel-engine model for all CPP scenarios (runs 1-6) and additional operation points (runs 7-10). φ_{peak} is expressed in degrees past TDC; $ \Delta P_{eng} $ is the absolute value of the relative deviation between $P_{eng}^*(\ell_P)$ and $P_{eng}(\ell_P)$	110
3.7	Torsional inertia and stiffness properties of the shaftline model.	113
3.8	Measured resonance frequencies vs. numerical model eigenfrequencies. . .	114
3.9	Ranges between maximum and minimum shaft response torque.	119

3.10	Shaftline components: specification, properties, dimensions.	126
4.1	Main specifications of the CCG icebreaker <i>Henry Larsen</i>	143
4.2	Summary of the measurement system components.	149
4.3	Resonance frequencies and eigenfrequencies for the torsional modes 1 to 3.	159
4.4	First three eigenfrequencies of the propeller blade and the shaftline model.	161
4.5	Shaftline material properties.	185
4.6	Mass moments of inertia of the model's nodes.	185
4.7	Torsional stiffness and damping.	185
5.1	Main specifications of the CCG heavy icebreaker <i>Terry Fox</i>	199
5.2	Main specifications of the CCGS <i>Terry Fox</i> 's propulsion system components.	200
5.3	Fixed parameters and initial conditions of the TVA simulation series.	220
5.4	Common eigenfrequencies of the condensed and expanded models, plus the resonance frequencies obtained through the full-scale measurements.	225
5.5	Main characteristics of the shaft response torque from the condensed and expanded models' TVAs.	227
5.6	Minimum speeds at the propeller and engine nodes from the condensed and expanded models.	227
5.7	Ratios between the $Q_{\text{peak},23}$ results obtained without and with ramps up-down.	234
5.8	Ratios between the $Q_{\text{range},23}$ results obtained without and with ramps up-down.	235
5.9	Ratios between the $Q_{\text{peak},23}$ results obtained with the <i>M</i> , <i>H</i> shape types to the <i>S</i> -shape homologous outcomes, for the Scenario 2.	240

5.10 Ratios between the $Q_{\text{range},23}$ results obtained with the M, H shape types to
the S -shape homologous outcomes, for the Scenario 2. 242

5.11 Shaftline material properties. 252

5.12 Detailed specifications of the engine components. 253

5.13 Mass moments of inertia of both models' nodes. 254

5.14 Torsional stiffness and damping coefficients. 254

List of Figures

2.1	Layout map of the measurement system installed on board CCGS <i>Henry Larsen</i>	46
2.2	Shaft instrumentation installed on the Starboard shaftline of CCGS <i>Henry Larsen</i>	46
2.3	TT-Sense® sensor: cross-section drawing (a); placement on the Starboard shaft (b).	47
2.4	Brüel & Kjær Type 2981 laser tachometer (a); placement on the Starboard shaft (b).	49
2.5	Railing support and positioning of the camera (a); view angle on the sea surface (b).	50
2.6	Floating frame for the calibration procedure: camera frame (a); zoomed view (b).	51
2.7	Arrangement of the shaft equipment (a); instrumentation attached to the shaft (b).	52
2.8	Route on October 17-18, 2019: larger view (a) and zoomed view (b) (via Google Earth®).	54

2.9	Route on March 15-18, 2020: larger view (a) and zoomed view (b) (via Google Earth®).	54
2.10	Shaft torque values ($Q_{\text{shaft,Gauge}}$ and $Q_{\text{shaft,Panel}}$) and fit curve of $Q_{\text{shaft,Gauge}}(n)$.	56
2.11	Open-water longitudinal speed of CCGS <i>Henry Larsen</i> ; 2 to 6 am, October 30, 2021.	58
2.12	Comparison of the experimental model-scale [41] and full-scale delivered power.	58
2.13	Shaft speed determined from the tachometer pulse signal. Under-sampling at 100 Hz.	59
2.14	Spectrum of $\omega(f)$ at $n = 169$ rpm, in steady-state conditions, at the Starboard-side shaftline.	60
2.15	Time series of Q , T , and n during forward-direction ice navigation, on October 17, 2019.	61
2.16	Ice thickness values: two frames corresponding to the events 2 (a) and 6 (b) in Fig. 2.15.	62
2.17	Pitch, roll and heave accelerations experienced by the ship during heavy-ice operations, October 2019.	63
2.18	Time series of Q , T , and n during forward-direction ice navigation, on March 16, 2020. The data series of both shafts' sensors are plotted.	65
2.19	Ice conditions characterizing the time interval of the dataset in Fig. 2.18.	66

2.20	Time series of Q , T , and n during baking-ramming icebreaking operations, on March 17, 2020. The data series of both shafts' sensors are plotted. . . .	67
2.21	Ice conditions characterizing the time interval of the dataset in Fig. 2.20. . .	68
3.1	Layout of the parts composing the present work.	84
3.2	Scheme of lumped-element system shaftline.	84
3.3	Simplified diagram of a piston, connecting rod, crank throw system. x is the piston's coordinate, L is the connecting rod's length, $s = 2r$ is the stroke length and r is the crank radius. φ is the crank angle, and β is the angle between the connecting rod and the vertical direction.	87
3.4	Pressure profile from [35] (a) and pressure curve $p_{\text{cyl}}(\varphi)$ as per Eq. 3.5 (b).	89
3.5	Torque delivered by a single cylinder ($Q_{\text{cyl}}(\varphi)$), acting on one crank arm. $Q_{\text{rec}}(\varphi)$ and $Q_{\text{p}}(\varphi)$ for a 4-stroke engine type. Specifically, $\alpha = 7.3$, $p_0 = 1.0$ bar, $p_{\text{peak}} = 123.2$ bar, $\varphi_{\text{peak}} = 16.3$ degrees past TDC.	90
3.6	Total torque on the engine crankshaft (in black), determined by superposing the cylinder contributions.	91
3.7	Procedure to calibrate the Diesel engine's mathematical model for a chosen ℓ_{p} .	93
3.8	Example of graphical representation of the propeller pitch angle variation versus time. The time-domain evolution that actually takes place is highlighted in yellow, while the instantaneous pitch variations calculated by the controller are dashed.	97
3.9	CCGS <i>Terry Fox</i> in ice-covered waters.	100

3.10	Route of the vessel during the free-running sea trials, on December 22-23, 2019.	102
3.11	Experimental apparatus scheme (a); strain gauge rosette and wireless data transmitter on the shaft (b).	103
3.12	Procedure to validate the Diesel engine’s mathematical model.	106
3.13	Outline of the shaftline model of the case study. The label “SG” indicates the location along the shaftline where the strain gauge was attached.	107
3.14	Torque absorbed by the propeller at n_{prop} , as a function of Φ (100% = Φ_{max}).	108
3.15	Measured microstrain spectra, for all Φ scenarios.	111
3.16	Measured microstrain spectra. Port-side, $\Phi = 0\%$ (a); Stbd-side, $\Phi = 45\%$ (b).	112
3.17	Modal shapes of the updated shaftline’s model, at $\Phi = 45\%$	115
3.18	Variation of $(f, \bar{f})_1$ and $(f, \bar{f})_2$ as Φ changes.	115
3.19	Comprehensive plot showing: CPP pitch angle evolution ($\Phi(t)$, (a)), ratio $q_{\Phi}(t)$ (b), propeller torques ($Q'_{ice}(t)$, (c) and $Q_h(t)$, (d)), engine node speed ($\omega_{eng}(t)$, (e)).	118
3.20	Time evolution of the torques acting on the propeller and engine nodes.	119
3.21	Shaft response torque in the segments 1 – 2, 2 – 3, 3 – 4 from both simulations.	120
3.22	Ice-induced torque on a 4-blade propeller. The ABS-DNV notations for the <i>IC</i> patterns are used [2, 12, 22].	129
4.1	Flowchart illustrating the paper outline.	142
4.2	CCGS <i>Henry Larsen</i> at sea.	143
4.3	Lumped-element system for CCGS <i>Henry Larsen</i> ’s shaftline.	144

4.4	Characteristic curve of the ED-delivered torque.	147
4.5	Layout of the equipment (a); instrumentation attached to the shaft (b). . . .	147
4.6	Starboard-side TT-Sense apparatus (a); Tachometer tape and support around the shaft (b); Camera mounting on the Upper Deck (c); Camera’s angle of view (d).	150
4.7	Configuration of the shaft sensors on board CCGS <i>Henry Larsen</i>	150
4.8	CCGS <i>Henry Larsen</i> ’s routes: October 17-18, 2019 (a); March 15-18, 2020 (b).	152
4.9	Microstrain ($\mu\epsilon$) vibration spectrum at 159 rpm.	159
4.10	Torsional modal shapes of the shaftline’s 9-DOF system.	160
4.11	Front view (a) and Top view (b) of the propeller’s hub-blade FE model. . . .	161
4.12	Data series clip from both TT-Sense meters, acquired on March 16, 2020. . .	163
4.13	Camera frames in icebreaking operations: Oct. 17, 2019 (a); Mar. 16, 2020 (b).	164
4.14	Flowchart outlining the IM verification process.	165
4.15	Plots of: nominal $Q_{ice,IACS}(PC = 4, IC = 1)$ (a); actual $Q_{ice}(t)$ (b).	166
4.16	Plots of: $Q_{hydro}(t)$, $Q_{ED}(t)$, $\dot{\theta}_1(t)$ (a); $\Delta\theta_{45}(t)$ (b).	166
4.17	Plots of: IM-output $Q_{ice}^*(t)$ (a); overlay of the two curves (b).	167
4.18	Forward direction C_F dataset: distribution and correlation curves between propeller torque and ice thickness (a); residuals plot of the regression that generates $\bar{Q}_{ice,F,all}$. The adjusted R^2 value of the fit equals 0.9803 (b). . . .	169
4.19	Forward direction C_F dataset: residuals plot of the regression that generates $\bar{Q}_{ice,F,int}$ (7 heavy-ice points excluded). The adjusted R^2 value of the fit equals 0.7087.	170

4.20	Forward direction C_F dataset: residuals plot of the regression that generates $\bar{Q}_{ice,F,max}$ (severe case points). The adjusted R^2 value of the fit equals 0.9469.	170
4.21	Forward direction C_F dataset: distribution and correlation curves between shaft power and ice thickness (a); residual plot of the regression that generates $\bar{P}_{s,F,int}$. The adjusted R^2 value of the fit equals 0.5056 (b).	172
4.22	Backward direction C_B dataset: data distributions of $\bar{Q}_{ice,B}$ (a) and $\bar{P}_{s,B}$ (b).	173
4.23	Comparison between the different $\bar{Q}_{ice,F}(\bar{h}_{ice})$ regression curves and the two series of $Q_{peak,Rules}(PC, IC, H_{ice})$ outcomes by considering the open propeller case with the <i>Henry Larsen's</i> properties. In detail, the “actual” points are derived from the outcomes of the Eq. 4.20, whereas the “max” points are obtained from calculating both values in the subequations of Eq. 4.20 first, and then taking the maximum among them.	176
4.24	Ice-induced torque on a 4-blade propeller. Three impact cases are shown, with the ABS nomenclature concerning IC [2, 30].	183
4.25	Ice-induced torque sequences for the three IC cases, with ramps applied [2].	184
5.1	Flowchart illustrating the paper structure.	197
5.2	CCGS <i>Terry Fox</i> in ice-covered waters.	199
5.3	Outline of the shaftline’s condensed model of the case study [51].	200
5.4	Outline of the shaftline’s expanded model of the case study.	203
5.5	Experimental apparatus scheme (a); shaft’s strain gauge and wireless data transmitter (b) [51].	205

5.6	Simplified diagram of a piston, connecting rod, crank arm assembly. x is the piston's coordinate, L is the connecting rod's length, $s = 2r$ is the stroke length and r is the crank radius. φ is the crank angle, and β is the angle between the connecting rod and the vertical direction. $\vec{F}_{\text{rec}}(\varphi)$ and $\vec{F}_{\text{p}}(\varphi)$ are the forces generated by the reciprocating parts and the combustion pressure, respectively [51].	206
5.7	(a) Cylinder torque as per Eq. 5.6; (b) DE overall torque as per Eq. 5.10 [51].	208
5.8	Characteristic curve of the EM-delivered torque.	210
5.9	Torque absorbed by the propeller at n_{prop} , as a function of Φ . The torque curve (black line) was determined through polynomial regression of the experimental points plus the overtorque operation point [51].	211
5.10	Ice-induced torque on a 4-blade propeller. Three <i>IC</i> s are shown: the images are taken as per the IACS Polar Rules [20], whereas the <i>IC</i> notations refer to the ABS-DNV nomenclature [2, 13].	214
5.11	Examples of ice-propeller torque patterns, with $Z = 4$. (a) Impacts with $IC = 1$ as per the ABS rules [2]; (b) impacts with $IC = 3$ as per the DNV rules [13].	214
5.12	Shaft torque profiles induced by ice-propeller milling processes, obtained in the studies by Veitch (a) and Wang et al. (b).	215
5.13	Three different curves to represent the torque of one ice-propeller impact. In this paper we use the <i>S</i> -shape curve plus the pulses obtained with $\epsilon = 4, 8$ in Eq. 5.17.	216

5.14	Three different curves to represent the torque of one ice-propeller impact. In this paper we use the <i>S</i> -shape curve plus the pulses obtained with $\epsilon = 4, 8$ in Eq. 5.17.	217
5.15	Examples of different ice-induced torque sequences, with several impacts. The application or not of the up-down ramps is indicated by “Ry” and “Rn”, respectively. The angular shift between the onset of one impact and the next one is set to be 90° , namely the shift obtained with a 4-blade propeller. . . .	218
5.16	Normalized modal shapes and natural frequencies: (a) condensed model; (b) Expanded model, where P, GB, D1, D2 indicate the nodes of the propeller, gearbox, TVD 1 and 2, respectively.	224
5.17	Spectrum of the measured microstrain ($\mu\epsilon$) at CPP $\Phi = 0\%$ and zero-thrust condition. The quantity ϵ is defined as the linear strain along the shaft’s circumferential dimension.	225
5.18	$Q_{\text{resp},12,23,34}(t)$ from the TVA applied to the two models.	226
5.19	$\omega_{\text{prop}}(t)$ and $\omega_{\text{eng}}(t)$ from the TVA applied to the two models.	228
5.20	Combined propeller torques and DE driving torque throughout a simulation, with the Q_{ice} combination identified by <i>M</i> -shape, $\alpha_{\text{ice}} = 60^\circ$, ramps applied.	229
5.21	(a) CPP Pitch angle evolution (Φ); (b) pitch corrective factor (q_Φ), (c) Ice- propeller torque (Q_{ice}); (d) propeller node speed (ω_{prop}); (e) hydrodynamic torque on the propeller (Q_h), for the combination identified by EM prime mover, <i>H</i> -shape, $\alpha_{\text{ice}} = 120^\circ$, no ramps.	230

5.22 Minimum rotational speeds reached by the prime mover node(s) in each model configuration of the Scenario 1. In particular, a polynomial fit curve is associated to each data series to show its trend as a function of α_{ice} . The outcomes from the simulations in which the shaftline’s speed is negative are disregarded in the fit curve calculations. 231

5.23 Contour plots of the $\omega_{PM,min}$ distribution for the configurations of the Scenario 1. The impact shape types are characterized by the exponent ϵ as per Eq. 5.19, and the *S*-type shape is considered to correspond to the case $\epsilon = 2$ (Fig. 5.13). 232

5.24 Peak torques ($Q_{peak,23}$) in the shaft segment between the nodes 2 and 3, in each model configuration of the Scenario 1. A polynomial fit curve is associated to each data series to show its trend as a function of α_{ice} . The outcomes from the simulations in which the shaftline’s speed is negative are disregarded in the calculation of the fit curves. 233

5.25 Contour plots of the $Q_{peak,23}$ distribution for the configurations of the Scenario 1. The impact shape types are characterized by the exponent ϵ as per Eq. 5.19, and the *S*-type shape is considered to correspond to the case $\epsilon = 2$ (Fig. 5.13). 234

5.26	Amplitude torques ($Q_{\text{range},23}$) in the shaft segment between the nodes 2 and 3, in each model configuration of the Scenario 1. A polynomial fit curve is associated to each data series to show its trend as a function of α_{ice} . The outcomes from the simulations in which the shaftline's speed goes below zero are disregarded in the fit curve calculations.	235
5.27	Contour plots of the $Q_{\text{range},23}$ distribution for the configurations of the Scenario 1. The impact shape types are characterized by the exponent ϵ as per Eq. 5.19, and the <i>S</i> -type shape is considered to correspond to the case $\epsilon = 2$ (Fig. 5.13).	236
5.28	Examples of $Q_{\text{resp},23}(t)$ torque curves, with DE prime mover, <i>M</i> -shape, $\alpha_{\text{ice}} = 90^\circ$. The same scale range is used in both vertical axes. (a) Simulation with ramps up-down applied; (b) Simulation with ramps up-down absent.	237
5.29	Combined propeller torques and EM driving torque throughout a simulation, with the Q_{ice} combination identified by <i>M</i> -shape, $\alpha_{\text{ice}} = 180^\circ$	238
5.30	Peak torques ($Q_{\text{peak},23}$) in the shaft segment between the nodes 2 and 3, in each model configuration of the Scenario 2. A polynomial fit curve is associated to each data series to show its trend as a function of α_{ice}	239
5.31	Contour plots of the $Q_{\text{peak},23}$ distribution for the configurations of the Scenario 2. The impact shape types are characterized by the exponent ϵ as per Eq. 5.19, and the <i>S</i> -type shape is considered to correspond to the case $\epsilon = 2$ (Fig. 5.13).	239

5.32	Range torques ($Q_{\text{range},23}$) in the shaft segment between the nodes 2 and 3, in each model configuration of the Scenario 2. A polynomial fit curve is associated to each data series to show its trend as a function of α_{ice}	241
5.33	Contour plots of the $Q_{\text{range},23}$ distribution for the configurations of the Scenario 2. The impact shape types are characterized by the exponent ϵ as per Eq. 5.19, and the <i>S</i> -type shape is considered to correspond to the case $\epsilon = 2$ (Fig. 5.13).	242
5.34	Examples of $Q_{\text{resp},23}(t)$ torque curves during a single ice-propeller impact, with DE prime mover, $\alpha_{\text{ice}} = 150^\circ$. The same scale range is used in both vertical axes. (a) Simulation with <i>S</i> -shape impact; (b) Simulation with <i>H</i> -shape impact.	243
5.35	Quantities $\omega_{\text{eng,min}}$, $Q_{\text{peak},23}$, and $Q_{\text{range},23}$ for four system configurations, as the number of the ice-propeller interaction impacts ranges from 1 to 30. A polynomial fit curve is associated to each data series to show its trend (solid thin lines).	244
5.36	Quantities $\omega_{\text{eng,min}}$, $Q_{\text{peak},23}$, and $Q_{\text{range},23}$ for the <i>H</i> -shape, $\alpha_{\text{ice}} = 120^\circ$ configuration, as the number of the ice-propeller interaction impacts ranges from 1 to 50. A polynomial fit curve is associated to each data series to show its trend (solid thin lines).	246

6.1 View from the CCG pier of CCGS *Henry Larsen* and St. John’s downtown at the dawn of August 10, 2019, before the vessel’s departure to undergo her open-water sea trials (a); The icebreaker CCGS *Terry Fox* moored at the CCG/Irving pier in the morning of December 22, 2019, getting ready before leaving for a two-day free-running test session (b). 265

Chapter 1

Introduction and overview

1.1. Problem statement

Navigation in sea ice environments poses several hazards to ship structures and, consequently, to the crew and passengers aboard ice-going vessels. Marine propulsion plants represent one of the most vital on-board systems to guarantee the autonomy and survivability of ships in ice-covered waters; at the same time, shafting segments and prime movers are also directly endangered by the effects of ice collisions with propellers. Therefore, appropriate models of the ice-propeller interaction process and the dynamics of shafting systems acquire foremost importance in the powering design of all Polar vessel types [19, 53, 87, 107]. Over the last decades, the Polar marine traffic has boosted due to increasing ice melting, global shipping trade, and natural resource exploitation, especially across the Arctic Ocean [6, 26, 102, 120]. As a consequence, to support the increasing demand for ice-going vessels of diverse types and their performance, shipbuilding industries and regulatory bodies need

updated guidelines to be used in ship-design processes [36, 52, 56].

The methodologies to model propulsion shafting systems of ships and their dynamics have undergone an evolution that started decades ago and continues nowadays. In particular, a relevant branch in this field is represented by Torsional Vibration Analysis (TVA) of shaftlines, as the most significant vibration sources connected to marine shaftlines consist of the propeller's hydrodynamic torsional load and the prime-mover driving torque [43, 44, 98]. The TVA research field encompasses both theoretical and experimental segments, as diverse external dynamic excitation, which results to be too complex to be simulated analytically, may pose severe hazards to the integrity of propulsion plant components [38, 76]. Achieving robust predictions of the torsional dynamic response of shafting systems, under diverse operational scenarios, constitutes a key point in the ship design process to ensure the target requirements concerning both propulsion performance and on-board safety [68].

The research project supporting this thesis seeks to deliver a versatile numerical methodology to perform TVAs of Polar-Class shaftlines, with either Diesel-driven or Electric prime movers, under the transient excitation caused by ice-propeller impacts. In parallel, this work produces novel experimental datasets that correlate sea ice scenarios to ice-induced torque, hence augmenting the state of the art concerning the ship-ice interaction topic. The results also provide additional remarks to consider updating the current rules' guidelines on the matter of ice-propeller design torque. Altogether, this thesis aims to contribute to improving the knowledge about modelling marine propulsion systems in relation to ice-propeller interaction processes.

1.2. Modelling ship propulsion systems: background

1.2.1. Early developments

TVA began to be investigated in the 70s, when the computational tools used in numerical analysis became widespread in all engineering branches [45, 92]. Initially, marine shaftlines were devised as linear, simplified systems, which generally included a limited number of numerical Degrees of Freedom (DOF) to represent the shaftline's structural properties [85, 91]. The research field was particularly focused on how to determine the first torsional vibration modes of marine shaftlines in efficient ways; Rao and Sanyal provided a comprehensive review on the state-of-the-art numerical techniques to calculate the torsional dynamics of Diesel-driven shafting systems [92]. A systematic computational procedure to model complex multi-branched systems, together with indications about both engine's and propeller's excitation, was outlined in [45]. Larsen studied the transient response of a marine transmission line with a specific focus on the shafting segments' alignment [59]. A particular importance was dedicated to the study of the coupling between the thrust and torque fluctuations on propellers, which induce torsional and axial vibration along the shafts, respectively [85]. In addition to that, in [47] the authors investigated also the effects of the coupled torsional-axial dynamics of shaftline-engine systems on the vibration response of primary structural elements. Selvaggi et al. conducted an experimental work to determine how the torsional damping contribution related to marine propellers is affected by blade geometry and operation points; the results were obtained through an innovative experi-

mental setup [96]. Initially, experimental models based on full-scale measurements were employed. In the studies [12] and [29], the authors focus on the transient behavior of marine shaftlines and its numerical modeling, and it is showed that concentrated-mass models yield satisfactory results in terms of torsional vibrations. In the former work, the authors used a simplified approach to model the Diesel engine components and excitation [12], whereas in the latter study it was shown that multi-element engine models are necessary when transient acceleration through the first resonance mode are concerned [29].

Besides the deterministic approach to carry out TVAs, probabilistic modelling methods were applied to evaluate, predict, and monitor the failure risk of shaft segments due to fatigue [80, 81, 82]. Specifically, the authors considered probabilistic formulations of both the external excitation components and the shaft dynamic stress response. In [80], statistic datasets about engine driving torque properties and shafts' structural failure were integrated to study how the exceedance of torsional stress thresholds deviated from the deterministic approach. With the same scope, in [82] more sophisticated mathematical methods in time domain were employed to estimate the occurrences of torsional stress maxima. In [81] instead, the authors simulated a marine propulsion system as a linear, lumped-element model, and then the torsional response of the system was analytically calculated as the linear superposition of the input torque spectra.

1.2.2. Recent studies

1.2.2.1 Shaftline modelling

Over the past couple of decades, Finite Element Analysis (FEA) has been gradually developed and applied to structural dynamics of mechanical systems. In [37], the authors examined the coupling between torsional and longitudinal dynamics over a marine shaftline entirely modeled via FE methods. The numerical results were benchmarked against model-scale measurements, yielding consistent agreement [37]. The torsional-axial coupled dynamics was also analyzed in [121], where the authors considered in detail the effects of the hydrodynamic thrust and torque acting on the propeller. Zhou et al. simulated the propeller blade excitation through 6-DOF analytical expressions, whereas the FE modeling part involved only the shafting segments. Differently, Murawski focused on the dynamic issues related to shaft alignment; a global FE analysis was applied in detail on the shaft segment bearings and foundations. Moreover, the surrounding ship structural elements and hull were modeled through FEA as well to take into account both the hydrodynamic wave loads and the ship structures' deformations applied to the hull and thus transmitted to the shaftline foundations [73].

The use of FEA provides a more precise structural representation of the system, but this method is computationally heavy. Also, several studies focused on the TVA modeling of marine Diesel engines, specifically on the interaction with the shafting systems they are coupled to. Next, as the available computational tools evolved, numerical methods integrating lumped-element models and FEA were progressively developed. Jenzer and

Keller exploited the advantages of FEA to determine with high detail the macroscopic properties of Diesel engine crankshafts, and then the propulsion line was simulated as a lumped-mass system; the results in terms of modal shapes and vibration transmissibility were checked against full-scale measurements [43]. Similarly, the modal superposition of multiple-DOF transmissibility functions was investigated in [105] to determine the extent by which the resulting torsional stress in the shaft segments is related to each modal shape.

Studies focused also on the complexity optimization of lumped-mass systems, namely how many DOFs are necessary to render reliable TVA predictions. Mendes et al. employed detailed FE modeling to determine the global characteristics of the rotating assembly components in a 4-stroke Diesel engine drive shaftline; a reduced-DOF model is hence established, and the results are compared to full-scale torsional vibration measures, with substantial agreement [71]. Senjanović et al. studied the differences in TVA outcomes that arise when considering a multi-DOF shaftline model or a corresponding model with 2 DOFs. The authors used Rayleigh-Ritz techniques to perform the simulations, and they demonstrate that the analytical procedure is convenient to be used especially for the first vibration mode of the system [97, 98]. Additionally, Murawski and Charchalis discuss about the advantages and drawbacks in undertaking two different methods to solve shaftline TVAs: one consists in a simplified, fully-analytical methodology, the other takes advantage of commercial numerical software [74].

In the present day, TVAs of ship propulsion systems take advantage of all modelling methodologies, since the available computational capability to perform simulations has remarkably advanced. Moreover, machine-learning techniques are also used to develop neural

network controllers of marine propulsion plants [57, 99]. FEA is especially employed to investigate particular and small-scale phenomena [37, 71, 75]. Conversely, FE-modeling could be inefficient throughout the early stage of the ship design process, due to its complexity. Hence, simplified lumped-element models are preferred to carry out TVA simulations when designers need flexibility and modularity to simulate multiple shaftline design solutions [38, 43, 74, 98]. Current research aims to improve the reliability and robustness of such simplified modelling methods: to this end, full-scale measurements are essential to support the development of versatile tools and at the same time providing in-field monitoring methods to prevent mechanical failures [25, 30, 76].

1.2.2.2 Prime mover modelling

Proper modelling procedures to simulate the mutual interaction between propeller loading, shaftline dynamics, and prime mover input is fundamental to monitor the torsional status of marine engine crankshafts. In fact, propellers and other machinery elements connected to the shaftline might cause transient loads that may lead to structural failure [25, 69, 76]. In particular, the design and simulation of Diesel-drive systems require a detailed modelling process due to the complexity of the engine output excitation.

Several factors compose the Diesel engine's output excitation; a global, detailed model is analyzed in [28], in which the author also considers the coupling relations between multiple DOFs in the cylinder-crank assembly. On the other hand, the oscillatory characteristics of the Diesel engine torque can be described through Fourier series, as adopted in [22, 25, 71, 98]. However, to employ this approach, specific technical data need to be provided

by the engine's manufacturer to construct the excitation curve; in detail, such datasets should include either experimental measures of the engine's output torque [25, 71, 98], or technical specifications related to the combustion process dynamics and fuel-gas flux controls [22]. Instead, Tsitsilonis and Theotokatos developed a tool to determine the in-cylinder combustion pressure curve by using measured torque signals as input, bypassing the practical obstacles in retrieving the Fourier series data for the engine's torque [106]. Polić et al. modeled the shaftline components and the Diesel engine cylinder-crank assemblies by using Bond-Graph (BG) elements [87, 89]. The BG-based model was then validated by employing FEA, which provided additional indications concerning the minimum number of DOFs to simulate the shaftline reliably [87].

Besides, Diesel-electric propulsion systems are frequently-employed solutions in modern ships, and electric motor drives have been increasingly adopted in marine applications because of their flexibility and efficiency [32, 84]. In numerical modelling, the torque output of diesel drives can be simulated through more straightforward mathematical models; nonetheless, the on-board power grid connecting the Diesel generators, the converters, and auxiliary components may demand more complex models, especially concerning power controls in variable-speed operations [1, 50, 101]. Studies focusing on the overall dynamics of both the electric prime movers and the shafts' torsional vibrations usually adopt lumped-element modelling options to simulate the propulsion line components [49, 114].

1.3. Navigation in Arctic environments: overview

The progress in ship-design and shipbuilding of Polar-Class vessels has acquired high importance as the Arctic Ocean marine traffic has expanded over the last decades [26, 70, 100, 119]. One of the driving forces behind the expansion of the marine traffic is the progressive melting of the Northern sea-ice cap, which facilitates the Arctic route viability for longer seasonal windows [21, 55, 120]. Moreover, the increasing exploitation of extensive LNG reservoirs and oilfields has boosted the offshore ship operations in the North [5, 6, 8]. Hence, controlling and defending the Arctic marine boundaries result in a strategic advantage for all Northern countries [67, 100]. The momentum of this global change in the environmental-economical scenario involves all vessels navigating across the Arctic; therefore, the International Maritime Organization (IMO) and the various Classification Societies have had to sustain a constant evolution of shipbuilding standards and regulations, with the scope of integrating concurrent goals concerning exhaust gas emissions, propulsion performance, and on-board safety [48, 51, 52, 56].

The significant intensification of the marine traffic across the Arctic Ocean caused an increase in the carbon emissions and the release of atmospheric pollutants [10, 13, 24, 72, 95]. An accurate study on the long-term influence on the air pollution due to the Canadian Arctic ship operations is presented in [23]: in it, the authors forecast a drastic increase of air pollutant concentration by 2030 if the marine traffic in the Arctic keeps growing as per the most recent estimations. Therefore, the shipbuilding industry shall deliver cleaner and more efficient Polar-Class vessels over the next decades, in compliance with up-to-date regulation

frameworks that impose standards and criteria on exhaust gas emissions [36, 86]. Designing upgraded propulsion systems and ship structures, in accordance with the evolving rules on fuel efficiency, represents an important challenge when the additional ice environment factor is considered in the design [35, 48, 51, 56]. As an example, Hanninen et al. and Irgens et al. present some state-of-the-art solutions applied to propulsion plants and power systems of Polar-Class vessels; the studies underline the advantages in adopting azimuthing propulsors to optimize manoeuvring performance and icebreaking capability, in relation to the most recent on-board noise and vibration criteria [31, 42].

On-board safety for crew members and high-reliability standards for the essential systems of ships represent primary issues to be considered when navigation in Polar environments is concerned [7, 56]. On this matter, research has been deeply focusing on risk assessment in relation to vessel survivability [20, 58]. The branch of risk-based analysis aims to support the design process by assessing a ship's operational reliability, which is related to the environmental scenario where the vessel is designed to operate. Therefore, evaluating the failure risk of the propulsion plants on board ice-going vessels assumes crucial importance to guarantee the continuity of operations and autonomy of ships in Polar waters [2, 15, 35]. New design methodologies, to be employed for the construction of modern Polar Class vessels, need to be developed and evolve, to adapt to new regulation tiers concerning both emissions and on-board safety [34, 35]. Overall, the evolution of on-board safety requirements, ship design methodologies, and pollutant emission criteria aim to the common goal of improving the economic sustainability of Arctic shipping [118].

1.4. Ice-propeller interaction and shaftline TVA: outline

Several research works have been conducted to study how the dynamic load induced by ice-milling phenomena on marine propellers can be represented numerically or analytically. Realistic models to simulate this excitation are fundamental to determine the propeller blade strength, to investigate the change in propulsion efficiency, and to study the ice-induced dynamic effects on the shafting system components through vibration analysis. Indeed, icebreaking operations and transit navigation along ice-covered routes enhance the vulnerability of propulsion systems of all types of Polar-Class vessels [20].

1.4.1. Ice-induced loads on marine propellers

Determining the characteristics of the ice-induced torque exerted on marine propellers constitutes a challenging task that jointly involves hydrodynamics, solid mechanics, and material science. The combined experimental-numerical results obtained by Veitch represented a groundbreaking work regarding the characterization of the ice-milling loads as a function of propellers' geometry [107]. Specifically, the overall ice-propeller interaction loading that propagates along the shaft can be represented as the combination of ice block impacts and ice-layer milling processes. However, the work of Veitch did not focus on the shaft's dynamic response following the ice-propeller impacts.

Advanced FEA modeling is employed in [65] and [27] to estimate the strength of Polar-Class propellers and thus optimize their geometrical design; in the work by [27] a neural network is established for the optimization process. In a similar way, Wang et al. used FEA

to investigate the time-domain, ice-milling process to obtain the corresponding dynamic loading and propeller blade response [109]. On the same subject, Ye et al. studied in more detail the dynamic pressure distribution induced by ice crushing on propeller blades [117]. In Norhamo et al.'s work, the authors investigated the strength assessment criteria for controllable-pitch propellers (CPP): the study highlights the significance of fatigue and dynamic analysis, on top of static loading scenarios, to determine the ice-induced stresses on CPP blades and spindle axis [83]. Lee utilized FE data from ice-propeller interaction simulations to develop a methodology that integrates a ship's design powering with propeller strength assessment [61, 62, 63].

Studying the ice-propeller interaction through numerical methods could require complex modeling procedures and high computational time. Hence, to better understand this phenomenon, model tests in a towing tank environment and full-scale measurements are fundamental. Khan et al. performed model-scale experiments to determine the linear superposition of different terms that compose the ice-induced load on the propeller blades [53]. Wang et al. studied through panel method modeling the propulsion coefficients of a podded propeller that undergoes ice crushing; the model was validated against towing tank data [110]. Scale-model test experiments in ice towing tanks were also carried out, aiming to validate numerical methods to characterize the ice-propeller interaction loading [9, 94]. In particular, Walker et al. used model-scale experiments to study how the hydrodynamic load on propellers develop during ice-milling processes [108]. The results yielded specific curves for the thrust and torque coefficients during diverse propulsive conditions [108].

1.4.2. Ice-propeller interaction effects on ship propulsion systems

Full-scale measurements on board ice-going vessels yield in-the-field data that play a key role in characterizing the diverse phenomena about ship-ice interaction. Three particular studies include a broad set of results about the effects of ice-propeller interaction on the propulsion efficiency during level ice navigation. Specifically, in [113] the case of the Canadian R-Class icebreaker *Henry Larsen* is investigated; the authors monitored the propulsion performance of the ship during different operational conditions. Dahler et al. considered an Arctic-going bulk carrier; the authors used their experimental results to calibrate a simulation tool for the shaftline's transient vibration prediction, and the dynamics of the vessel's two-stroke engine was analyzed in detail [14]. These represent pioneering works on the matter of ship-ice interaction effects, as in the past the design and construction of ice-going vessels was regarded as a secondary sector. Moreover, Jussila and Koskinen arranged a novel long-running, full-scale measurement system to study the ice-induced impact loads on the blades of a CPP [46].

Concurrently, model experiments simulating ice navigation are fundamental to test new design solutions and simulate diverse operational scenarios. Wang and Jones correlated the towing tank test results to full-scale measurements concerning the propulsion performance of the Canadian icebreaker *Terry Fox* [111]. Reimer et al. conducted a series of full-scale tests on board an icebreaker to establish a method that integrates model-scale tests on a prototype vessel with powering predictions under diverse icebreaking operations and ice types [93].

Recently, remarkable full-scale measurement campaigns were carried out to study the transient torsional vibration of shafting segments, to correlate the shaft dynamic response torque with the ice-induced load acting on the propeller blades. A joint Finnish and South-African research group conducted a vast experimental activity to study the global structural response and the ice-induced shaftline vibration on board the Polar Research Vessel S.A. *Agulhas II* [18, 104]. The ship operated both in the Baltic Sea [104] and in the Southern Atlantic Ocean between South Africa and Antarctica [17]. In the latter expedition, also the German icebreaker *Polarstern* was involved in the study; in detail, de Waal et al. focused on the thrust and torque fluctuation propagated along the vessel shafts, by employing torsional strain gauges [17]. In this study, the output, time-domain shaft torque signal was processed to obtain the input, ice-propeller interaction torque [19]. The transmission line was modelled as a lumped-element system, and the dynamic impedance matrix inversion was implemented through three different numerical methods [19, 40]. Also, Nickerson and Bekker discussed the effectiveness of additional mathematical methodologies to determine the input, ice-induced torque by using the output, measured shaft signals [77, 78]. The latter works consisted of deterministic algorithms to achieve the ice-induced excitation curve; in [16] the authors explore the utilization of probabilistic methods for the same scopes. Overall, this broad experimental-numerical research work did not study in detail how the prime mover's driving excitation dynamically evolve during ice-propeller interaction phenomena.

Besides, Polić et al. undertook a different approach to simulate Diesel engine drive propulsion systems [89]. Specifically, the authors modelled the shaftline's torsional DOFs by using Bond-Graph (BG) elements; the Diesel engine cylinders and corresponding crank

arms are simulated as a series of BG blocks each [88, 89]. The BG-based model was then validated with FEA, which provided additional indications concerning the minimum number of DOFs to be used to simulate the shaftline correctly, in particular during transient-state conditions [87]. Hence, the authors used the BG model and model-scale measurements to develop an inverse algorithm, which transforms the measured torsional displacement vibration signals into the ice-induced transient load [90]. To simulate the ice-propeller excitation, the authors used the guidelines delivered by the International Association of Classification Societies (IACS) [41], which provide an analytical description of the ice-milling torque pattern.

Conversely, several studies tackled the ice-related TVA problem with a fully-numerical approach; the IACS Rules' guidelines are then considered to define the ice-propeller loads to use in the simulations. Kinnunen et al. investigated the case of a Z-drive propeller system, driven by an Electric motor; a lumped-element model of the propulsion plant was developed with Simulink®, and the numerical outcomes were compared with the dynamic torque and speed readings acquired during full-scale measurements [54]. Batrak et al. employed a specific CAE software package to simulate the action of a marine Diesel engine and turbocharger directly coupled to a shaft [3]. The shaftline was modelled as a lumped-element system, and the author used the Kujawski-Gallager numerical technique as ODE solver [3, 4]. Yang et al. used instead the Newmark method algorithm to perform a time-domain TVA for the shaftline of an Ice-Class bulk carrier; the analyzed propulsion system featured a 2-stroke Diesel engine drive, which was simulated through a simplified model [116]. Furthermore, Burella et al. performed a sensitivity analysis through FEA on the

shaft structural properties of an Electric-drive propulsion system installed on board the Canadian Coast Guard (CCG) icebreaker *Henry Larsen*, to determine its response to ice-induced loads as a function of different shaftline characteristics [11]. Lecourt Jr analyzed the mathematical models for the complete powering system of a Diesel-Electric icebreaker; all components and control systems of the propulsion plant are integrated [60]. Similarly, Hill et al. provided a detailed mathematical description of the interdependent control systems applied to the propulsion plant of a Canadian R-Class icebreaker, characterized by twin shaftlines and three Diesel generators [33].

1.4.3. Ice environment monitoring

Besides, accurate full-scale measurements of the ice's main physical properties are essential to frame the environmental conditions during ice navigation. Monitoring the sea ice scenario in which ships operate provides data that characterize the ice loads on vessels' hull and propellers. High-precision equipment and software were often employed to achieve three-dimensional images of the ice floes [79, 112]; such measurements are useful to help tracking hazardous ice layers during low-visibility navigation. On the other hand, Lensu et al. focused more on the sole thickness parameter to characterize different ice scenarios [64]. Multiple ice properties as type, shape, age, concentration were concurrently measured and analyzed in [66] and [112]. Additionally, the outcomes were also employed to study Polar weather and climate evolution [112]. A broader experimental campaign, spanning four Austral summer seasons, was conducted by Suominen et al. on board the research vessel *S.A. Aghulas II*; in those voyages, the authors were able to collect a remarkable dataset that categorizes multiple

ice parameters also with respect to different season periods [103]. Hughes developed a monitoring system that integrates radar sensors and satellite imaging to provide real-time information to assist navigation in ice-covered waters [39]. The experimental data obtained through all these works are then useful to reproduce realistic scenarios in ice tank tests, as well as to benchmark numerical tools that simulate ships' navigation in ice, as in [115].

1.5. Scopes and contributions of the research

The objectives of this doctoral project are: (i) design and arrange a measurement system to monitor and produce integrated datasets of shaftline's dynamic response and sea ice conditions on board icebreakers; (ii) develop a numerical tool and procedure to perform ice-induced TVAs on shaftlines with different prime mover solutions; (iii) correlate the magnitude of ice-propeller interaction torque to the sea ice conditions, through full-scale measurements; and (iv) provide indications towards a potential review of the current regulatory guidelines concerning the definition of the ice-propeller torque pattern.

The diverse tasks of the research plan are outlined below:

- 1. Integrated measurement system.** The layout of the instrumentation installed on board CCGS *Henry Larsen* represents a novelty in this field: for the first time, optical thrust and torque meters are used to monitor ice-induced shaft dynamic response and propulsion performance (Chapters 2 and 4). As an element of innovation over previous studies [17, 104], laser tachometers are used to measure high-frequency speed variation signals, to characterize transient states during propeller load perturbations. Concurrently, the

sea ice conditions are monitored with a weatherproof camera, and additional data such as structural vibrations in the engine room and ship's course are acquired to produce an integrated dataset.

2. **Shaftline's TVA methodology.** Development of a comprehensive numerical procedure to simulate the transient torsional dynamics of propulsion systems. The lumped-element modelling concept introduced in [11] is considered and augmented to consider also the Diesel engine (DE) drive layout and CPP applications, whose mathematical models constitute novel features. Overall, the simulation tool is devised to have enhanced modularity and flexibility, in order to model an ample range of marine propulsion system configurations and external excitation patterns. I apply the methodology to the propulsion systems of two CCG icebreakers—*Henry Larsen* and *Terry Fox*—and both models are validated through full-scale vibration data.
3. **DE mathematical model.** The fully-analytical mathematical model (Chapter 3) to simulate the dynamic torque of a DE drive system constitutes a novel formulation of this complex quantity, which is usually modelled by using experimental data provide by marine engines' manufacturers [25, 71, 98]. Full-scale shaft vibration data were employed to validate the DE model's results in terms of output power. Advantages of this original DE torque model include its mathematical straightforwardness and independence from technical specifications that could be difficult to retrieve.
4. **CPP controller and its impact on the ice-propeller load.** Chapter 3 also presents an alternative and versatile algorithm to simulate the dynamic response of a CPP governor

during variable propeller's loading. Moreover, the effect of the CPP pitch's change is applied to the dynamic torque induced by ice impacts, through the IACS formulation [41]. The combination between ice-propeller interaction and CPP response is a novelty in this field.

5. **Correlation between sea ice thickness and propeller torque peaks.** Study of the relation between the ice-induced torque exerted on the propeller blades and the severity of the sea ice conditions. Sequences of torsional vibration data acquired by the shaft sensors on board *CCGS Henry Larsen* are processed to determine the ice-propeller interaction torque (Chapter 4). Correspondingly, images of the ice conditions in place are analyzed to determine the average ice layer thickness and thus characterize the ice's severity. Hence, the two datasets are coupled, to express the ice-propeller torque peak and the propulsive power as a function of the average ice thickness. These findings are absent in the published literature on the subject.
6. **Inversion algorithm.** Numerical method to obtain the unknown external excitation on the node of a lumped-element system by using the known measured signal of the relative motion between two nodes. This process has been devised to calculate the dynamic ice-induced torque applied to the *CCGS Henry Larsen's* propeller by using the torsional vibration data acquired by the shafts' torque sensors (Chapter 4). The main qualities of the algorithm regard its ease of implementation and the reduced computational time it requires.
7. **Indications to review and possibly amend the current IACS recommendations.** The

results presented in Chapters 3, 4, and 5 point out that the guidelines to determine the ice-induced torque excitation on propellers might need to be updated, with regard to a number of mathematical definitions in them. Precisely, discussed matters involve: the CPP dynamic variation effect applied to the ice-induced torque (Chapter 3); the relation between Polar Class notations and design ice thickness plus the definition of two parameters (Chapter 4); the application of the linear ascent and descent of ice-impact sequences (“ramps up-down”), together with the criteria to determine the characteristics of the design ice pulse (Chapter 5). In particular, Chapter 5 is dedicated to analyze the effects of different properties of the ice-propeller torque pattern on the TVA response resulting from a fixed shaftline model.

1.6. Synopses of the Chapters

This thesis is structured through the Manuscript Style. Chapters 2, 3, 4, and 5 correspond to four papers that either have been published as peer-reviewed journal articles (Chapters 2 and 3), or are undergoing a peer-review process (Chapters 4 and 5). The content of each paper is outlined over the following paragraphs.

- **Chapter 2** – *A measurement system to monitor propulsion performance and ice-induced shaftline dynamic response of icebreakers.* This paper presents a unique integrated measurement system that uses measuring equipment to monitor the propulsion performance of a Polar-Class vessel and ice-induced torsional vibrations along shaftlines. The system is installed on board the CCG icebreaker *Henry Larsen*, and it was devised in collaboration

with NRC. Two scopes are sought: firstly, the shafts' speed, torque, and thrust fluctuations during ice navigation are monitored to study the ship propulsion efficiency; secondly, visual recordings of the sea ice scenarios are employed to characterize the simultaneous torsional dynamic response of the shaftlines. Moreover, laser tachometers are installed to obtain high-frequency speed fluctuation signals. In the paper, I provide detailed descriptions of the measurement system arrangement and its components. I validate the torque sensors' data in steady-state conditions through measures acquired via shaft-attached strain gauges. Concerning the camera's visual data, the method to calibrate the sea-level distances to the video frame dimensions is also described. Excerpts of datasets obtained during icebreaking operations of the ship are also shown.

- **Chapter 3 – *Torsional vibration analysis of Diesel driven propulsion systems: the case of a Polar-Class vessel.*** This article outlines our methodology to model the torsional dynamics of fully-g geared, Diesel-drive propulsion systems. In it, the core part is represented by a novel analytical procedure to simulate the dynamic torque delivered by a Diesel engine. The CCG heavy icebreaker *Terry Fox* is considered as a case study: its propulsion plant includes two shaftlines driven by two 4-stroke Diesel engines each and equipped with CPPs. The system's numerical model includes also the CPP controller and its effects on the propeller's dynamic excitation. Full-scale measurements acquired during open-water sea trials are utilized to validate the Diesel-drive mathematical model, update the numerical eigenfrequencies of the system, and determine the curve of the propeller-absorbed hydrodynamic torque. The Chapter includes simulations of the dynamic response of the

shaftline's model by applying an ice-propeller transient excitation. The results indicate the effectiveness of the proposed methodology to simulate the Diesel engine torque, and the significance of considering the CPP pitch variation in transient-state conditions when ice-induced loads are concerned.

- **Chapter 4 – *Torsional vibrations of Polar-Class shaftlines: correlating ice-propeller interaction torque to sea ice thickness.*** This paper includes the integration of experimental data from the CCGS *Henry Larsen*'s icebreaking operations with numerical analysis, in order to establish a correlation between ice-propeller torque peak and sea ice thickness. Initially, the propulsion shaftline of the vessel is simulated as a lumped-element system, and the model is validated against full-scale data in open-water conditions. Then, I perform a series of numerical simulations to predict the ice-induced impact loads on the propeller by using measured dynamic torque data—through the shafts' optical sensors—as the analysis' input. These resulting values are correlated to the ice thickness data that are determined from the on-board camera apparatus to monitor the sea ice close to the hull. At the end, I compare this ice-propeller torque distribution with the homologous quantities calculated as per the Polar Class framework [41]. The results point out the necessity of reviewing the current regulatory guidelines regarding the determination of the design ice-induced torque on propellers.
- **Chapter 5 – *Impact of different characteristics of the ice-propeller interaction torque on the torsional vibration response of a Polar-Class shaftline.*** The last Chapter aims to determine the most significant properties of the ice-propeller torque affecting a shaftline's

torsional vibrations. I started from considering the ice torque pattern defined by the current Polar Rules [41]. Hence, I studied how the transient and steady-state conditions induced by the ice-propeller excitation change as the following four ice-impact properties are modified: pulse's shape, pulse's angular width, application of the linear rise and descent in the impacts' sequence, number of consecutive ice impacts. I performed a series of torsional vibration analyses, using a more detailed version of the numerical model to simulate CCGS *Terry Fox's* shaftline. In addition, I tested the system with Diesel engine and electric motor excitation models interchangeably. The results indicate that the ice impact span, the ramps up-down application, and the number of impacts are the most important factors to affect the shaftline's rotational speed drop and response torque. In particular, implementing or not the ice impact ramps is found to entail relevant changes in the TVA results; this outcome could suggest a review of the in-force regulatory guidelines.

Table 1.1 delineates the key concepts and innovation items of the four Chapters.

Table 1.1: Comprehensive outline of each Chapter’s contents and objectives.

Ch. Title	Concepts	Elements of novelty
2 <i>A measurement system to monitor propulsion performance and ice-induced shaftline dynamic response of icebreakers</i>	<ul style="list-style-type: none"> Integrated measurement system aboard the CCG icebreaker <i>Henry Larsen</i>; Presentation of some illustrative datasets obtained during operations in ice; Validation of the shaft torque measures via torsional vibrations. 	<ul style="list-style-type: none"> Unique arrangement of the measurement system’s components; Concurrent monitoring of ship’s propulsive performance and ice-induced dynamic response of the shafts; Full-scale data to correlate shaft vibrations to sea ice conditions.
3 <i>Torsional vibration analysis of Diesel driven propulsion systems: the case of a Polar-Class vessel</i>	<ul style="list-style-type: none"> Methodology to simulate the torsional dynamics of Diesel-drive shaftlines; CCGS <i>Terry Fox</i>’s propulsion system: model validation via full-scale data; TVA application to the case of ice-propeller torque excitation. 	<ul style="list-style-type: none"> Novel mathematical procedure that simulates the dynamic torque delivered by a Diesel engine’s analytically; Application of the CPP controller’s effects to the ice-induced propeller torque.
4 <i>Torsional vibrations of Polar-Class shaftlines: correlating ice-propeller interaction torque to sea ice thickness</i>	<ul style="list-style-type: none"> Full-scale datasets in icebreaking operations: shaft torque and sea ice videos; CCGS <i>Henry Larsen</i> shaftline’s numerical model: development and validation; Data processing to calculate the actual ice-propeller interaction torque. 	<ul style="list-style-type: none"> Correlation between sea ice thickness and ice-propeller torque peaks; Numerical method to invert linear mechanical systems, given measured data; Indications for a possible review of the IACS design recommendations.
5 <i>Impact of different characteristics of the ice-propeller interaction torque on the torsional vibration response of a Polar-Class shaftline</i>	<ul style="list-style-type: none"> Modifications of the IACS’ ice-propeller torque pattern to study the influence of diverse properties on the TVA results; Detailed Diesel-engine components in CCGS <i>Terry Fox</i>’s shaftline model; Alternative design solution for the prime mover excitation: geared Electric drive replacing Diesel engines. 	<ul style="list-style-type: none"> Angular span of each ice pulse and “ramps up-down” features: most significant properties affecting the shaftline’s speed drop and shaft stress in TVAs; Number of consecutive impacts: key parameter determining transient/steady-state loading and dynamic response.

1.7. Co-authorship statements

For each Chapter, the details on the articles' development and authorship are reported below.

- **Chapter 2.** This paper is a preprint version currently under review for publication in the peer-reviewed journal *Journal of Marine Science and Engineering*, and its authors are Alessandro Zambon, Lorenzo Moro, Jeffrey Brown (NRC), Allison Kennedy (NRC), and Dan Oldford (ABS). Alessandro Zambon designed the strain-gauge vibration measurement equipment and the ice-monitoring system, conducted the full-scale measurements in open-water conditions on board the case study vessel, analysed the results, interpreted the data, devised the paper's structure, and wrote most of its parts; Jeffrey Brown and Allison Kennedy contributed to the sections regarding the propulsion performance monitoring, and additional experimental data analyzed by NRC; Dan Oldford reviewed the paper and suggested refinements concerning the rules' subject, and gave his approval on behalf of ABS. Lorenzo Moro supervised the paper's development and contributed to edit the manuscript, refine its layout, and enhance concepts presented. All authors revised, edited, and made recommendations for improvements to earlier drafts of this paper.
- **Chapter 3.** This article has been published as a peer-reviewed journal paper in the issue 245 (February 2022) of the journal *Ocean Engineering*. The paper was authored by Alessandro Zambon and Lorenzo Moro. Alessandro Zambon led the development of the manuscript, conducted the full-scale measurements in open-water conditions on board the case study vessel, conceived and developed the novel mathematical model

of the Diesel engine torque, performed the numerical analyses, and wrote the entire article's sections; Lorenzo Moro provided significant indications to improve the paper's arrangement, format, and style. The two authors collaborated to edit and refine all parts of the paper, throughout the full process from development to final publication. CCG and ABS gave their approvals to publish the paper.

- **Chapter 4.** This paper is a pre-print version currently under review for publication in the peer-reviewed journal *Ocean Engineering*, and its authors are Alessandro Zambon, Lorenzo Moro, Allison Kennedy (NRC), and Dan Oldford (ABS). Alessandro Zambon arranged and conducted the strain-gauge vibration measurements on board the case study vessel in open-water conditions, devised the paper's structure, performed the numerical analyses—scripts' development, data handling and analysis, numerical results' processing—, and wrote all sections of the article. Lorenzo Moro supervised the paper's progress and contributed to edit the manuscript and thus refine the layout and the concepts therein presented. Allison Kennedy reviewed the text and gave her approval on behalf of NRC. Dan Oldford reviewed the text, gave indications concerning Rules' matters, and gave his approval on behalf of ABS. All authors revised and contributed to refine the earlier drafts of this paper.
- **Chapter 5.** This paper is a pre-print version to be submitted soon to the peer-reviewed journal *Ocean Engineering*; the paper was authored by Alessandro Zambon, Lorenzo Moro, and Dan Oldford (ABS). Alessandro Zambon devised the paper's scopes and structure, conducted the numerical analyses to produce the results discussed in the study—

scripts' development, data handling, and numerical processing—, and wrote all sections of the article. Lorenzo Moro contributed to revise the manuscript, improve its style, and enhance the concepts therein presented. Dan Oldford reviewed the paper, suggested improvements concerning the rules' terminology and details, and gave his approval on behalf of ABS. All authors collaborated to refine the article, which will be submitted to the journal's editor by March 2022.

References

- [1] Apsley, J. M., Gonzalez-Villasenor, A., Barnes, M., Smith, A. C., Williamson, S., Schuddebeurs, J. D., Norman, P. J., Booth, C. D., Burt, G. M., and McDonald, J. R. (2009). Propulsion drive models for full electric marine propulsion systems. *IEEE Transactions on Industry Applications*, 45(2):676–684. 8
- [2] Aziz, A., Ahmed, S., Khan, F., Stack, C., and Lind, A. (2019). Operational risk assessment model for marine vessels. *Reliability Engineering & System Safety*, 185:348–361. 10
- [3] Batrak, Y. A., Serdjuchenko, A. M., and Tarasenko, A. I. (2012). Calculation of propulsion shafting transient torsional vibration induced by ice impacts on the propeller blades. In *Proceedings of World Maritime Technology Conference (WMTC)*, Saint Petersburg, Russia. 15
- [4] Batrak, Y. A., Serdjuchenko, A. M., and Tarasenko, A. I. (2014). Calculation of torsional vibration responses in propulsion shafting system caused by ice impacts. In *Torsional Vibration Symposium*, Salzburg, Austria. 15
- [5] Blaauw, R. J. (2013). Oil and gas development and opportunities in the Arctic Ocean. In *Environmental Security in the Arctic Ocean*, pages 175–184. Springer. 9
- [6] Bogoyavlensky, V. et al. (2014). The Arctic and World Ocean: Current State, Prospects and Challenges of Hydrocarbon Resources Development. In *21st World Petroleum Congress*. World Petroleum Congress. 1, 9

- [7] Bond, J., Hindley, R. J., Kendrick, A., Kämäräinen, J., Kuuliala, L., et al. (2018). Evaluating Risk and Determining Operational Limitations for Ships in Ice. In *OTC Arctic Technology Conference*, Houston, TX, USA. Offshore Technology Conference. 10
- [8] Borch, O. J., Westvik, M. H., Ehlers, S., and Berg, T. E. (2012). Sustainable Arctic field and maritime operation. In *OTC 2012*, pages 1–10. Offshore Technology Conference. OTC23752. 9
- [9] Brouwer, J., Hagesteijn, G., and Bosman, R. (2013). Propeller-ice impacts measurements with a six-component blade load sensor. In *Third International Symposium on Marine Propulsors (SMP13)*, Tasmania, Australia. 12
- [10] Browse, J., Carslaw, K. S., Schmidt, A., and Corbett, J. J. (2013). Impact of future Arctic shipping on high-latitude black carbon deposition. *Geophysical research letters*, 40(16):4459–4463. 9
- [11] Burella, G., Moro, L., and Oldford, D. (2018). Analysis and validation of a procedure for a lumped model of Polar Class ship shafting systems for transient torsional vibrations. *Journal of Marine Science and Technology*, 23(3):633–646. 15, 16, 18
- [12] Carrera, G. and Rizzuto, E. (1997). Simulation of mechanical and thermodynamic performances of a ship propulsion plant in transient conditions. In *ASME 1997 Turbo Asia Conference*. American Society of Mechanical Engineers (ASME). 4
- [13] Chen, Q., Lau, Y.-y., Ge, Y.-E., Dulebenets, M. A., Kawasaki, T., and Ng, A. K. Y. (2021). Interactions between Arctic passenger ship activities and emissions. *Transportation Research Part D: Transport and Environment*, 97:102925. 9
- [14] Dahler, G., Stubbs, J. T., and Norhamo, L. (2010). Propulsion in ice – Big ships. In *International conference and exhibition on performance of ship and structure in ice - ICETECH*, Anchorage, AK, USA. 13
- [15] Daley, C. and Yu, H. (2009). Assessment of ice loads on stern regions of ice class ships. In *International Conference on ship and Offshore Technology*, pages 28–29, Busan, South Korea. 10
- [16] De Koker, N. and Bekker, A. (2021). Assessment of ice impact load threshold exceedance in the propulsion shaft of an ice-faring vessel via Bayesian inversion. *Structural Health Monitoring*, pages 1–13. 14
- [17] de Waal, R. J. O., Bekker, A., and Heyns, P. S. (2017). Bi-Polar Full Scale Measurements of Operational Loading on Polar Vessel Shaft-lines. In *Proceedings of the 24th International Conference on Port and Ocean Engineering under Arctic Conditions (POAC 2017)*, Busan, South Korea. 14, 17
- [18] de Waal, R. J. O., Bekker, A., and Heyns, P. S. (2018a). Data for indirect load case estimation of ice-induced moments from shaftline torque measurements. *Data in Brief*, 19:1222–1236. 14
- [19] de Waal, R. J. O., Bekker, A., and Heyns, P. S. (2018b). Indirect load case estimation for propeller-ice moments from shaft line torque measurements. *Cold Regions Science and Technology*, 151:237–248. 1, 14

- [20] Ehlers, S., Kujala, P., Veitch, B., Khan, F., and Vanhatalo, J. (2014). Scenario based risk management for arctic shipping and operations. In *ASME 2014 33rd International Conference on Ocean, Offshore and Arctic Engineering*. American Society of Mechanical Engineers (ASME). 10, 11
- [21] Gascard, J.-C., Riemann-Campe, K., Gerdes, R., Schyberg, H., Randriamampianina, R., Karcher, M., Zhang, J., and Rafizadeh, M. (2017). Future sea ice conditions and weather forecasts in the Arctic: Implications for Arctic shipping. *Ambio*, 46(3):355–367. 9
- [22] Gold, P. W., Philipp, T., Schelenz, R., and Buehren, M. (2003). Application of process calculation of the internal combustion engine for the analysis of torsional vibrations in marine drives. In *ASME 2003 Internal Combustion Engine Division Spring Technical Conference*, volume 36789, pages 329–337. American Society of Mechanical Engineers (ASME). 7, 8
- [23] Gong, W., Beagley, S. R., Cousineau, S., Sassi, M., Munoz-Alpizar, R., Ménard, S., Racine, J., Zhang, J., Chen, J., Morrison, H., et al. (2018). Assessing the impact of shipping emissions on air pollution in the Canadian Arctic and northern regions: current and future modelled scenarios. *Atmospheric Chemistry and Physics*, 18(22):16653–16687. 9
- [24] Granier, C., Niemeier, U., Jungclaus, J. H., Emmons, L., Hess, P., Lamarque, J.-F., Walters, S., and Brasseur, G. P. (2006). Ozone pollution from future ship traffic in the Arctic northern passages. *Geophysical Research Letters*, 33(13). 9
- [25] Guerrero, D. P. and Jiménez-Espadafor, F. J. (2019). Torsional system dynamics of low speed diesel engines based on instantaneous torque: Application to engine diagnosis. *Mechanical Systems and Signal Processing*, 116:858–878. 7, 8, 18
- [26] Gunnarsson, B. (2021). Recent ship traffic and developing shipping trends on the Northern Sea Route—Policy implications for future arctic shipping. *Marine Policy*, 124:104369. 1, 9
- [27] Guo, C., Han, K., Wang, C., Ye, L., and Wang, C. (2021). Evaluation and analysis of the static strength of ice-class propellers. *Ocean Engineering*, 235:109336. 11
- [28] Guzzomi, A. (2007). *Torsional vibration of powertrains: an investigation of some common assumptions*. PhD thesis, University of Western Australia. 7
- [29] Hafner, K. E. (1974). Torsional Stresses of Shafts Caused by Reciprocating Engines Running through Resonance Speeds. In *Mechanical Engineering*, volume 96, pages 58–58. American Society of Mechanical Engineers (ASME). 4
- [30] Han, H. S., Lee, K. H., and Park, S. H. (2016). Parametric study to identify the cause of high torsional vibration of the propulsion shaft in the ship. *Engineering Failure Analysis*, 59:334–346. 7
- [31] Hanninen, S., Viherialehto, S., Maattanen, P., and Heideman, T. (2020). Propulsion Solutions for Large Arctic Offshore Vessels. In *SNAME 25th Offshore Symposium*. Society of Naval Architects and Marine Engineers (SNAME). TOS-2020-001. 10

- [32] Hansen, J. F. and Wendt, F. (2015). History and state of the art in commercial electric ship propulsion, integrated power systems, and future trends. *Proceedings of the IEEE*, 103(12):2229–2242. 8
- [33] Hill, W. A., Creelman, G., and Mischke, L. (1992). Control strategy for an icebreaker propulsion system. *IEEE Transactions on industry applications*, 28(4):887–892. 16
- [34] Hindley, R. and Tustin, R. (2009a). Assessing Ice Strengthening Using Operational Scenarios. In *Proceedings of the International Conference on Port and Ocean Engineering Under Arctic Conditions*, number POAC09-52. 10
- [35] Hindley, R. J. and Tustin, R. D. (2009b). Guidance notes for the classification of stern first Ice Class ships. In *RINA International Conference on Ship and Offshore Technology: Ice Class Vessels*, pages 53–61, Busan, South Korea. Royal Institution of Naval Architects. 10
- [36] Hindley, R. J., Tustin, R. D., and Upcraft, D. S. (2007). Environmental protection regulations and requirements for ships for Arctic sea areas. In *RINA International Conference - Design and Construction of Vessels Operating in Low Temperature Environments*, pages 107–118, United Kingdom. Royal Institution of Naval Architects. 2, 10
- [37] Huang, Q., Yan, X., Wang, Y., Zhang, C., and Jin, Y. (2016). Numerical and experimental analysis of coupled transverse and longitudinal vibration of a marine propulsion shaft. *Journal of Mechanical Science and Technology*, 30(12):5405–5412. 5, 7
- [38] Huang, Q., Yan, X., Wang, Y., Zhang, C., and Wang, Z. (2017). Numerical modeling and experimental analysis on coupled torsional-longitudinal vibrations of a ship’s propeller shaft. *Ocean Engineering*, 136:272–282. 2, 7
- [39] Hughes, N. E. (2001). Ice Cam: For the Polar Seas, an environmental monitoring solution with implications for navigation and safety. *Sea Technology*, 42(11):36–40. 17
- [40] Ikonen, T., Peltokorpi, O., and Karhunen, J. (2015). Inverse ice-induced moment determination on the propeller of an ice-going vessel. *Cold Regions Science and Technology*, 112:1–13. 14
- [41] International Association of Classification Societies (IACS) (2006). Requirements concerning Polar Class - Polar Rules. Rev. 1 Jan 2007, Corr. 1 Oct 2007. 15, 19, 22, 23
- [42] Irgens, O.-J., Kokkila, K., Hänninen, S., et al. (2018). Propulsion Technology for Polar Expedition Ships. In *OTC Arctic Technology Conference*. Offshore Technology Conference. 10
- [43] Jenzer, J. and Keller, H. (2003). Torsional vibration and admissible limits in marine propulsion installations. In *ASME 2003 Internal Combustion Engine Division Spring Technical Conference*, pages 289–296. American Society of Mechanical Engineers (ASME). 2, 5, 6, 7
- [44] Jiang, X., Zhou, X., and Chen, K. (2015). Vibration characteristics of a marine propulsion shaft excited by the effect of propeller and diesel. In *2015 International Conference on Transportation Information and Safety (ICTIS)*, pages 893–897. IEEE. 2
- [45] Jonsson, K. (1996). Modelling of torsional vibrations in marine powertrains. Technical report, SAE Technical Paper. N. 960766. 3

- [46] Jussila, M. and Koskinen, P. (1989). Ice loads on CP-propeller and propeller shaft of small ferry and their statistical distributions during winter '87. In *Proceedings of the 8th International Conference on Offshore Mechanics and Arctic Engineering*, volume IV. 13
- [47] Kagawa, K., Fujita, K., Hirayama, T., Kokawa, H., and Nagamoto, R. (1986). Vibration of Long-stroke Type Marine Diesel Engine. *Naval Architecture and Ocean Engineering*, 24:211–222. 3
- [48] Kämäräinen, J. (2013). IMO regulations and Ice Class Rules. In *22nd International Conference on Port and Ocean Engineering under Arctic Conditions (POAC 2013)*. 9, 10
- [49] Kambrath, J. K., Changwoo, Y., Wang, Y., Yoon, Y.-J., Liu, X., Gajanayake, C. J., and Gupta, A. K. (2018). Direct Drive Propeller System Modelling and Active Protection. In *2018 IEEE Energy Conversion Congress and Exposition (ECCE)*, pages 3901–3908. IEEE. 8
- [50] Karakitsos, I. and Theotokatos, G. (2016). Modelling of diesel electric propulsion. *Proceedings of the Energy Efficient Ships, London, UK*, pages 23–24. 8
- [51] Kendrick, A. and Santos-Pedro, V. (2010). The future of polar shipping rules. In *International Conference and Exhibition on Performance of Ships and Structures in Ice - ICETECH 2010*, pages 31–35. 9, 10
- [52] Kendrick, A. M. (2014). Polar ship design standards - state of the art, and way forward. In *Transactions - Society of Naval Architects and Marine Engineers (SNAME)*, volume 122, pages 428–433, Houston, TX, USA. 2, 9
- [53] Khan, A. G., Hisette, Q., Streckwall, H., and Liu, P. (2020). Numerical investigation of propeller-ice interaction effects. *Ocean Engineering*, 216:107716. 1, 12
- [54] Kinnunen, A., Turunen, T., Koskinen, P., and Heinonen, J. (2017). Propulsion Shaft Line Ice-Induced Dynamic Torque Response. In *Proceedings of the 24th International Conference on Port and Ocean Engineering under Arctic Conditions (POAC 2017)*, Busan, South Korea. 15
- [55] Kitagawa, H. (2008). Arctic routing: Challenges and opportunities. *WMU Journal of Maritime Affairs*, 7(2):485–503. 9
- [56] Kitagawa, H. et al. (2011). Safety and Regulations of Arctic Shipping. In *The Twenty-first International Offshore and Polar Engineering Conference*. International Society of Offshore and Polar Engineers. 2, 9, 10
- [57] Kruszewski, J. (2014). Ship's Propulsion Neural Controller Main Engine-Pitch Propeller-Shaft Generator. *IFAC Proceedings Volumes*, 47(1):905–912. 7
- [58] Kujala, P., Goerlandt, F., Way, B., Smith, D., Yang, M., Khan, F., and Veitch, B. (2019). Review of risk-based design for ice-class ships. *Marine Structures*, 63:181–195. 10
- [59] Larsen, O. C. (1981). Some considerations of marine shafting design. *Industrial Lubrication and Tribology*. 3

- [60] Lecourt Jr, E. J. (1998). Using Simulation to Determine the Maneuvering Performance of the WAGB-20. *Naval Engineers journal*, 110(1):171–188. 16
- [61] Lee, S.-K. (2006). Rational approach to integrate the design of propulsion power and propeller strength for ice ships. *ABS Technical Papers*. Originally presented at the 2006 SNAME ICETECH conference; Banff, Canada, July 16-19, 2006. 12
- [62] Lee, S.-K. (2007). Engineering practice on ice propeller strength assessment based on IACS polar ice rule-URI3. In *10th International Symposium on Practical Design of Ships and Other Floating Structures*, *ABS Technical Papers*. Citeseer. 12
- [63] Lee, S.-K. (2008). Ice Controllable Pitch Propeller Strength Check Based on IACS Polar Class Rules. In *International conference and exhibition on performance of ship and structure in ice - ICETECH 2008*, pages 20–23, Banff, AB, Canada. *ABS Technical Papers*. 12
- [64] Lensu, M., Kujala, P., Kulovesi, J., Lehtiranta, J., and Suominen, M. (2015). Measurements of Antarctic sea ice thickness during the ice transit of SA Agulhas II. In *Proceedings of the International Conference on Port and Ocean Engineering Under Arctic Conditions (POAC 2015)*, Trondheim, Norway. 16
- [65] Liu, P., Bose, N., and Veitch, B. (2015). Evaluation, design and optimization for strength and integrity of polar class propellers. *Cold Regions Science and Technology*, 113:31–39. 11
- [66] Lu, W., Zhang, Q., Lubbad, R., Løset, S., Skjetne, R., et al. (2016). A shipborne measurement system to acquire sea ice thickness and concentration at engineering scale. In *Arctic Technology Conference*, St. John's, NL, Canada. OTC. 16
- [67] Łuszczuk, M. (2016). Military Cooperation and Enhanced Arctic Security in the Context of Climate Change and Growing Global Interest in the Arctic. In *Future Security of the Global Arctic: State Policy, Economic Security and Climate*, chapter 3, pages 35–54. Springer. 9
- [68] Magazinović, G. (2010). Regression-based assessment of shafting torsional vibration key responses. *Marine Technology*, 47(1):65–73. 2
- [69] Margaronis, I. E. (1992). The torsional vibrations of marine Diesel engines under fault operation of its cylinders. *Forschung im Ingenieurwesen*, 58(1-2):13–25. 7
- [70] Melia, N., Haines, K., Hawkins, E., and Day, J. J. (2017). Towards seasonal Arctic shipping route predictions. *Environmental Research Letters*, 12(8). 084005. 9
- [71] Mendes, A. S., Meirelles, P. S., and Zampieri, D. E. (2008). Analysis of torsional vibration in internal combustion: modelling and experimental validation. In *Proceedings of the Institution of Mechanical Engineers Part K Journal of Multi-body Dynamics*, volume 222, pages 155–178. 6, 7, 8, 18
- [72] Mjelde, A., Martinsen, K., Eide, M., and Endresen, Ø. (2014). Environmental accounting for Arctic shipping—A framework building on ship tracking data from satellites. *Marine pollution bulletin*, 87(1-2):22–28. 9

- [73] Murawski, L. (2005). Shaft line alignment analysis taking ship construction flexibility and deformations into consideration. *Marine Structures*, 18(1):62–84. 5
- [74] Murawski, L. and Charchalis, A. (2014). Simplified method of torsional vibration calculation of marine power transmission system. *Marine structures*, 39:335–349. 6, 7
- [75] Murawski, L. and Charchalis, A. (2015). An Estimation Method for the Torsional Vibration of the Marine Propulsion System. In *Solid State Phenomena*, volume 220, pages 71–80. Trans Tech Publications. 7
- [76] Murawski, L. and Dereszewski, M. (2020). Theoretical and practical backgrounds of monitoring system of ship power transmission systems' torsional vibration. *Journal of Marine Science and Technology*, 25(1):272–284. 2, 7
- [77] Nickerson, B. and Bekker, A. (2021). Recommendations for regularization in the inverse estimation of ice-induced propeller moments for ice-going vessels. *Cold Regions Science and Technology*, page 103378. 14
- [78] Nickerson, B. M. and Bekker, A. (2022). Inverse model for the estimation of ice-induced propeller moments using modal superposition. *Applied Mathematical Modelling*, 102:640–660. 14
- [79] Niioka, T. and Kohei, C. (2010). Sea ice thickness measurement from an ice breaker using a stereo imaging system consisted of a pairs of high definition video cameras. *International Archives of the Photogrammetry, Remote Sensing and Spatial Information Science, Kyoto Japan*, 38(8):1053–1056. 16
- [80] Nikolaidis, E., Perakis, A. N., and Parsons, M. G. (1985). Structural Reliability of Marine Diesel Engine Propulsion Shafting Systems. *Society of Naval Architects and Marine Engineers – Transactions*, 93:189–223. 4
- [81] Nikolaidis, E., Perakis, A. N., and Parsons, M. G. (1987). Probabilistic torsional vibration analysis of a motor ship propulsion shafting system: the input-output problem. *Journal of Ship Research*, 31(1). 4
- [82] Nikolaidis, E., Perakis, A. N., and Parsons, M. G. (1989). Probabilistic torsional vibration analysis of a marine diesel engine shafting system: the level crossing problem. *Journal of Applied Mechanics*, 56:953–959. 4
- [83] Norhamo, L., Bakken, G. M., Deinboll, O., and Iseskär, J. J. (2009). Challenges related to propulsor - ice interaction in arctic waters. In *First International Symposium on Marine Propulsors (SMP09)*, Norway. 12
- [84] Nuchturee, C., Li, T., and Xia, H. (2020). Energy efficiency of integrated electric propulsion for ships—A review. *Renewable and Sustainable Energy Reviews*, 134:110145. 8
- [85] Parsons, M. G., Srinivas, J., and Raju, V. (1983). Mode coupling in torsional and longitudinal shafting vibration. *Marine Technology*, 20(3):257–271. 3

- [86] Pietri, D., Soule I V, A. B., Kershner, J., Soles, P., and Sullivan, M. (2008). The Arctic shipping and environmental management agreement: a regime for marine pollution. *Coastal Management*, 36(5):508–523. 10
- [87] Polić, D., Æsøy, V., and Ehlers, S. (2016). Transient simulation of the propulsion machinery system operating in ice—modeling approach. *Ocean Engineering*, 124:437–449. 1, 8, 15
- [88] Polić, D., Æsøy, V., Ehlers, S., and Pedersen, E. (2014). Shaft response as a propulsion machinery design load. In *Proceedings of the ASME 2014 33rd International Conference on Ocean, Offshore and Arctic Engineering (OMAE2014)*, San Francisco, California, USA. 15
- [89] Polić, D., Ehlers, S., and Æsøy, V. (2017). Propeller Torque Load and Propeller Shaft Torque Response Correlation During Ice-propeller Interaction. *Journal of Marine Science Applications*, 16(1):1–9. 8, 14, 15
- [90] Polić, D., Ehlers, S., and Æsøy, V. (2019). Inverse modeling approach for transformation of propeller shaft angular deformation and velocity to propeller torque load. *Marine Structures*, 67. 15
- [91] Rao, D. K. (1984). Torsional vibration of crankshafts in reciprocating machines. *Shock and Vibration Digest*, 16(2):16–23. 3
- [92] Rao, D. K. and Sanyal, A. (1980). Torsional vibration of ship engine shafts. *Shock and Vibration Digest*, 12(12):3–8. 3
- [93] Reimer, N., Hisette, Q., and Schroeder, C. (2018). Full Scale Trials for the Validation of Ship Performance and Model Tests in Ice. In *OTC Arctic Technology Conference*. OnePetro. 13
- [94] Sampson, R., Atlar, M., and Sasaki, N. (2009). Propeller ice interaction-effect of blockage proximity. In *First International Symposium on Marine Propulsors*. 12
- [95] Schröder, C., Reimer, N., and Jochmann, P. (2017). Environmental impact of exhaust emissions by Arctic shipping. *Ambio*, 46(3):400–409. 9
- [96] Selvaggi, M., Bevilacqua, A., and Vignolo, G. (1973). Experimental research on propeller damping in torsional vibrations of marine propulsion plants. Technical report. Registro Italiano Navale (RINA). 3, 4
- [97] Senjanović, I., Ančić, I., Magazinović, G., Alujević, N., Vladimir, N., and Cho, D.-S. (2019a). Validation of analytical methods for the estimation of the torsional vibrations of ship power transmission systems. *Ocean Engineering*, 184:107–120. 6
- [98] Senjanović, I., Hadžić, N., Murawski, L., Vladimir, N., Alujević, N., and Cho, D.-S. (2019b). Analytical procedures for torsional vibration analysis of ship power transmission system. *Engineering Structures*, 178:227–244. 2, 6, 7, 8, 18
- [99] Shi, C., Guo, C., and Sun, C. (2009). Simulation and optimal control of diesel engine propulsion system. In *2009 WRI World Congress on Computer Science and Information Engineering*, volume 5, pages 87–91. IEEE. 7

- [100] Silber, G. K. and Adams, J. D. (2019). Vessel Operations in the Arctic, 2015-2017. *Frontiers in Marine Science*, 6:573–590. 9
- [101] Sørensen, A. J. and Smogeli, Ø. N. (2009). Torque and power control of electrically driven marine propellers. *Control Engineering Practice*, 17(9):1053–1064. 8
- [102] Stroeve, J. C., Markus, T., Boisvert, L., Miller, J., and Barrett, A. (2014). Changes in Arctic melt season and implications for sea ice loss. *Geophysical Research Letters*, 41(4):1216–1225. 1
- [103] Suominen, M., Bekker, A., Kujala, P., Soal, K., and Lensu, M. (2017). Visual Anctartic Sea Ice Condition Observations during Austral Summers 2012-2016. In *Proceedings of the 24th International Conference on Port and Ocean Engineering under Arctic Conditions (POAC 2017)*, Busan, South Korea. 16, 17
- [104] Suominen, M., Karhunen, J., Bekker, A., Kujala, P., Elo, M., Enlund, H., Saarinen, S., et al. (2013). Full-scale measurements on board PSRV SA Agulhas II in the Baltic Sea. In *Proceedings of the International Conference on Port and Ocean Engineering Under Arctic Conditions*, Espoo, Finland. 14, 17
- [105] Tang, B. and Brennan, M. J. (2013). On the influence of the mode-shapes of a marine propulsion shafting system on the prediction of torsional stresses. *Journal of Marine Science and Technology*, 21(2):209–214. 6
- [106] Tsitsilonis, K.-M. and Theotokatos, G. (2021). A novel method for in-cylinder pressure prediction using the engine instantaneous crankshaft torque. *Proceedings of the Institution of Mechanical Engineers, Part M: Journal of Engineering for the Maritime Environment*. 8
- [107] Veitch, B. (1995). *Predictions of Ice Contact Forces on a Marine Screw Propeller During the Propeller-Ice Cutting Process*. PhD thesis, Helsinki University of Technology, Finland. Acta Polytechnica Scandinavica, Mechanical Engineering Series. 1, 11
- [108] Walker, D., Bose, N., Yamaguchi, H., and Jones, S. J. (1997). Hydrodynamic loads on ice-class propellers during propeller-ice interaction. *Journal of marine science and technology*, 2(1):12–20. 12
- [109] Wang, C., Xiong, W. P., Chang, X., Ye, L. Y., and Li, X. (2018). Analysis of variable working conditions for propeller-ice interaction. *Ocean Engineering*, 156:277–293. 11, 12
- [110] Wang, J., Akinturk, A., and Bose, N. (2006). Numerical prediction of model podded propeller-ice interaction loads. In *25th International Conference on Offshore Mechanics and Arctic Engineering (OMAE2006)*, pages 667–674, Hamburg, Germany. American Society of Mechanical Engineers Digital Collection. 12
- [111] Wang, J. and Jones, S. J. (2008). Resistance and propulsion of CCGS Terry Fox in ice from model tests to full scale correlation. In *8th International Conference and Exhibition on Performance of Ships and Structures in Ice. Paper No. ICETECH08-125-RF*. 13
- [112] Weissling, B., Ackley, S., Wagner, P., and Xie, H. (2009). EISCAM—Digital image acquisition and processing for sea ice parameters from ships. *Cold Regions Science and Technology*, 57(1):49–60. 16

- [113] Williams, F. M., Spender, D., Mathews, S. T., and Bayly, I. (1992). Full Scale Trials in Level Ice with Canadian R-Class Icebreaker. In SNAME, editor, *SNAME Transactions*, volume 100, pages 293–313. 13
- [114] Xiao, N., Zhou, R., Xu, X., and Lin, X. (2016). Study on vibration of marine diesel-electric hybrid propulsion system. *Mathematical Problems in Engineering*, 2016. 8
- [115] Yang, B., Sun, Z., Zhang, G., Wang, Q., Zong, Z., and Li, Z. (2021). Numerical estimation of ship resistance in broken ice and investigation on the effect of floe geometry. *Marine Structures*, 75:102867. 17
- [116] Yang, H. J., Wu, Q. W., and Yang, J. (2020). Torsional Vibration Calculation for Propulsion Shaft of 1A Ice Class Ship. In *The 30th International Ocean and Polar Engineering Conference*. 15
- [117] Ye, L. Y., Guo, C. Y., Wang, C., and Wang, C. H. (2019). Prediction of the dynamic pressure distribution on a propeller blade under ice milling. *Ocean Engineering*, 188:106284. 12
- [118] Yumashev, D., van Hussen, K., Gille, J., and Whiteman, G. (2017). Towards a balanced view of Arctic shipping: estimating economic impacts of emissions from increased traffic on the Northern Sea Route. *Climatic Change*, 143(1-2):143–155. 10
- [119] Zhang, Y., Meng, Q., and Zhang, L. (2016). Is the Northern Sea Route attractive to shipping companies? Some insights from recent ship traffic data. *Marine Policy*, 73:53–60. 9
- [120] Zhang, Z., Huisingh, D., and Song, M. (2019). Exploitation of trans-Arctic maritime transportation. *Journal of cleaner production*, 212:960–973. 1, 9
- [121] Zhou, X., Qin, L., Chen, K., Niu, W., Jiang, X., Xiong, Y., Quan, J., and Wang, X. (2014). Vibrational Characteristics of a Marine Shaft Coupling System Excited by Propeller Force. In *The 21st International Congress on Sound and Vibration (ICSV21, Beijing, China)*. 5

Chapter 2

A measurement system to monitor propulsion performance and ice-induced shaftline dynamic response of icebreakers

Abstract

Polar navigation entails challenges that affect the continuation of ship operations in severe ice conditions. Due to ice-propeller interaction, propulsion shafting segments are often at a high risk of failure. Efficient methods for shaftline design are hence needed to ensure the safety of ice-going vessels and propulsion reliability. To this end, full-scale measurements have proven essential to support the development of ship-design tools and updated safety regulations for ice-going vessels. This paper presents a unique integrated measurement system that employs measuring equipment to monitor Polar-Class vessel performance and

shaftline dynamics during ice navigation. The system was installed on board the Canadian Coast Guard (CCG) icebreaker *Henry Larsen*. This experimental concept has two scopes: firstly, the shaft torque and thrust fluctuations during ice navigation are monitored to obtain information about the ship's propulsion efficiency; secondly, we seek to determine a correlation between sea ice conditions and shaft torsional dynamic response. In the paper, we describe the arrangement of the measurement system and the components it features. Finally, we present preliminary datasets acquired during two icebreaking expeditions.

Keywords

Ship propulsion systems; Marine shaftlines; Ice-propeller interaction; Polar Class; Vibration measurements; Icebreakers; Full-scale data.

2.1. Introduction

2.1.1. Environmental and economic framework

Over the last decades, the economic and strategic interests involving the exploitation of the Arctic Ocean region have become a pivotal factor in numerous industrial sectors of the world economy. Global warming is the most significant phenomenon that makes the anthropic activities possible in Polar waters, as the increasing ice melting process augments the viability of shipping routes [12, 32, 38, 49]. Two primary industrial sectors are mainly involved: energy resource supply chain and freight transportation. In the first case, the vast availability of oil and liquid natural gas in the Arctic region represents an attractive stimulus

for the energy sector to fulfill the global demand for energetic sources [1, 2]. In the second case, the recent expansion of the global trade system led to a significant increase of Polar route utilization [15, 33, 38].

On the other hand, the utilization of shipping routes in the northernmost seas has been expanding, and it is expected to increase over the next few decades [27, 48, 49]. Consequently, the increment in all-year-round marine traffic through the Arctic Ocean entails several issues concerning pollution and in particular greenhouse gas emissions. Overall, the general outcome resulting from extensive Arctic shipping depicts a worsening effect on the environment due to shipping-related pollutants, as shown in [5, 14, 28, 37]. Gong et al. provides a thorough analysis about the marine traffic effects on atmospheric pollution in the Canadian Arctic region, with a temporal span until 2030 [13].

The pollution generated by Arctic-going vessels significantly affects the economic sustainability of Polar shipping. Guaranteeing high proficiency levels for ships devised to operate in Polar environments is a challenging task, which requires accurate optimization plans to minimize the ship operations' costs and concurrently ensure the employment of updated technology [28, 46]. Therefore, updated regulation frameworks are necessary to make Arctic-going vessels comply with minimum requirements in terms of exhaust gas emissions, propulsion efficiency, and on-board safety [22, 34]. A detailed treatise on marine systems reliability criteria and environmental protection measures can be found in [16].

2.1.2. Role of the marine industry

The design and construction of ice-going vessels have recently acquired high importance due to the increase in demand for new Polar-Class vessels. Propulsion plants assume particular relevance in the design process of ice-going vessels: the structural properties of those systems and their components require particular consideration in order to be adequate to Arctic navigation [3, 23, 35, 45]. In particular, ice collisions with propeller blades represents a crucial phenomenon that endangers the integrity of shafting systems and may compromise the manoeuvring capability of ships.

Over the recent decades, the ice-propeller interaction process has been investigated through ice towing tank tests to determine its characteristics and how it relates to the hydrodynamic load [4, 21, 31]. In [21], the authors outlined an experimental methodology to identify the superimposed components of the combined ice and hydrodynamic load on propellers. A numerical model to estimate the ice loads on a podded propeller is presented in [42], where a model-scale pod is employed to validate the numerical results obtained through panel-method FEA. Model tests are often limited in providing results that can be reliably transferred to full-scale scenarios. Moreover, the utilization of model ice in towing tank experiments may lead to remarkable discrepancies with the actual ice effects.

Therefore, full-scale measurements are fundamental to sustain the advancement of ice-going vessels' shipbuilding and maintain safety regulations updated. Multi-objective, full-scale measurement campaigns aboard different types of Arctic vessels were carried out in the past to monitor the ship propulsion operation along with the ice-induced excitation on

the hull and propellers. In particular, Williams et al. monitored the CCG icebreaker *Henry Larsen* during level ice navigation [44], and Suominen et al. studied the ice-induced loads on the hull of the Polar Supply Research Vessel S.A. *Agulhas II* [40]. Regarding merchant ships, in [9] the authors considered the case of an Arctic-Class bulk carrier; the full-scale, ice-induced impacts on the CP propeller of a ferry ship are studied through a measurement chain with cutting-edge instrumentation in [20].

Accurate measures of the dimensions of ice floes are essential to categorize the surrounding ice conditions and the resulting ice-induced excitation on ship structures. Sophisticated equipment as stereoscopic cameras or laser detectors can be employed to get three-dimensional images of the sea ice [24, 30, 43]; in these cases, special post-processing software is necessary to elaborate the raw data. More specific ice block properties as type, shape, age, concentration are measured and analyzed in [25]. Structural measurements and ice condition visual data need to be integrated to define the operating scenarios of ships. On this matter, a joint Finnish and South-African research team conducted an extensive measurement campaign project on board an icebreaker and a research vessel, which navigated across the area comprised between Antarctica, South Africa, and Argentina [11, 39]. The authors employed strain gauges to measure the torsional response of the shafts, whereas the sea ice conditions were empirically assessed from the command bridge. The authors carried out a statistical analysis of the shaft load distributions and fatigue [10]. The acquired vibration data was then used to calculate the ice-propeller interaction torque [11, 18, 29].

2.1.3. Contribution of the present work

This paper outlines the features of a novel measurement system concept, which aims to monitor the propulsion performance and shaftline vibrations of Ice-Class vessels. The arrangement of the system was devised through a joint research project between Memorial University of Newfoundland (MUN, St. John's NL, Canada) and National Research Council of Canada – Ocean, Coastal and River Engineering Research Centre (NRC-OCRE, St. John's NL, Canada). Specifically, the scope of this experimental design is to provide an integrated dataset that includes shafts' dynamic response, sea ice conditions, and propulsion efficiency information during ice operations. In this work, we also present the application of the measurement system on board the CCG medium icebreaker *Henry Larsen*. The paper includes a series of example data acquired during two ice operation voyages of the vessel in two different Canadian Arctic regions. The work also provides a rare contribution to full-scale icebreaker performance data in Subarctic and high Arctic regions. The CCGS *Henry Larsen* has a unique multi-role service mission including open-water transits, nearshore icebreaking support, search and rescue, commercial escort, and northern resupply. The ship operates as far south as the St. Lawrence Seaway and in summer transits the northern latitudes of the Canadian Arctic Archipelago.

2.2. Materials and Methods

2.2.1. Overview of the instrumentation set and description of the case study vessel

In this section, we describe the components of the measurement system and their installation on board CCGS *Henry Larsen*. Optical meters are installed on both shafts to measure the thrust, torque, speed fluctuations. Using laser torque meters to measure both ice-induced dynamic response and monitor ship propulsion performance constitutes a novelty element in the field of full-scale measurements in ice navigation. Besides, the transient-state rotational shaft speed drop is measured with laser tachometers to obtain high-frequency speed fluctuation signals, which are synchronized with the optical sensors. Concurrently, the sea ice conditions are monitored through a high-resolution digital camera mounted on the port-side, bridge-deck railing. Its operation principle is to record the ice blocks turning over against the hull; thus, the video frames are then processed to estimate the average sea ice thickness. In addition, the data acquisition system records the NMEA¹ data broadcast over the ship's network; this dataset includes useful contextual information such as latitude and longitude, speed over ground and through water, weather conditions, and the status of the vessel's air bubbler system. Overall, the different datasets are synchronized by using the ship's network clock.

Table 2.1 describes the instrumentation set for a twin-propeller vessel; details on their role and operation are included.

¹Communication format defined by National Marine Electronics Association (NMEA) for marine utilization.

Table 2.1: Outline of the measurement system components.

Device	Manufacturer	Description	Operation	Items	Location
TT-Sense® sensor	VAF Instruments	Optical LED rotating sensor	Low-frequency measurement of the shaft torque, thrust, speed fluctuations	2	Propeller shafting segments (Port, Starboard)
Laser tachometer	Brüel & Kjær	CCLD laser probe	High-frequency measurement of the shaft rotational speed	2	Propeller shafting segments (Port, Starboard)
Outdoor HD Camera	HIK Vision	Weatherproof IP-POE camera	Video recordings of the sea surface close to the hull	1	Side railing of a higher deck, pointing vertically downwards
MTi-300 (IMU sensor)	XSens	Attitude Heading and Reference System (AHRS)	20-Hz filtered 6-DOF acceleration, heading, pitch, roll motions	1	Communication Room (upper superstructure)

The main specification of the CCG medium icebreaker *Henry Larsen* are reported in Table 2.2. The ship was built in 1989 and has been operating across the Eastern Canadian Arctic region. The propulsion system of the vessel is a Diesel-Electric plant, in which three 4-stroke Diesel AC generators power the two electric motors of the twin shaftlines. The propellers are fixed-pitch type (FPP).

Table 2.2: Main specifications of the icebreaker CCGS *Henry Larsen*.

Quantity		Value	Unit
Length overall	L_{OA}	99.8	[m]
Beam	B	19.6	[m]
Draught	d	7.3	[m]
Gross Tonnage	GT	6,166	[GT]
Total propulsive power	P_{TOT}	12.2	[MW]
Propeller diameter	D	4.120	[m]
Maximum propeller's rotational speed	n_{max}	180	[rpm]
Maximum transit speed	V_S	16	[kn]
Arctic Class certification	AC	4	[-]

Fig. 2.1 shows a schematic view of the arrangement, whereas Fig. 2.2 illustrates the positions along the shaftline where the devices were installed. We used a torsional strain-gauge rosette to validate the shaft torque data measured by the optical sensors; the rosette's location is indicated in Fig. 2.2 as well.

2.2.2. Shaft thrust, torque, speed measurement at low frequency

We installed one LED-optical sensor in each shaftline to measure the thrust and torque fluctuations as well as the instantaneous shaft speed with low-frequency output. In particular, we fixed the devices on the intermediate shaft segments, which are comprised between the

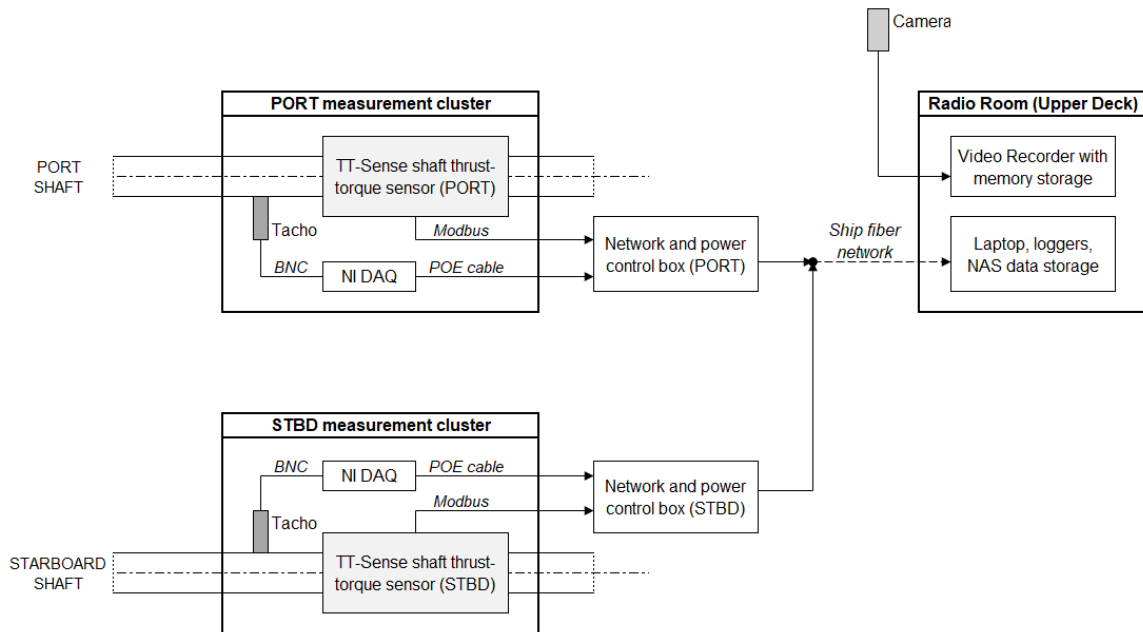


Figure 2.1: Layout map of the measurement system installed on board CCGS *Henry Larsen*.

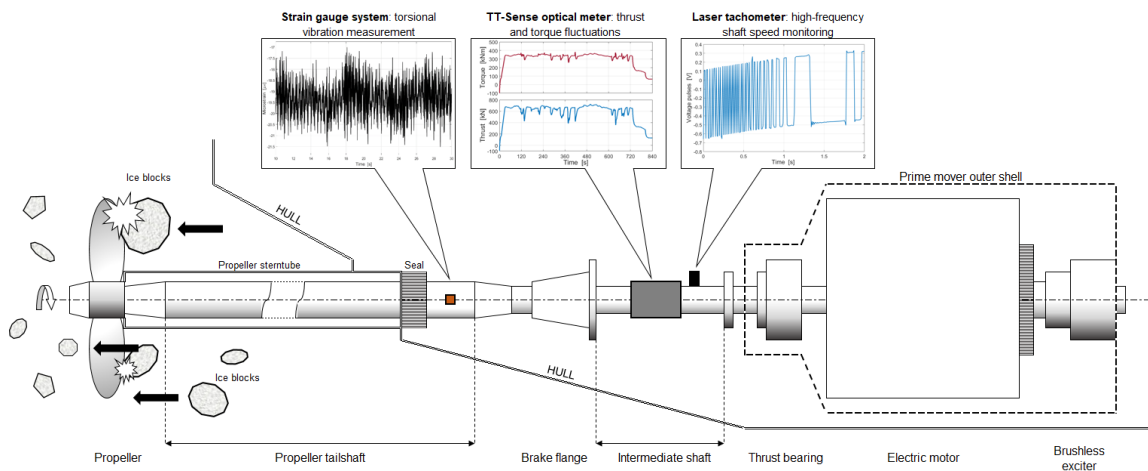


Figure 2.2: Shaft instrumentation installed on the Starboard shaftline of CCGS *Henry Larsen*.

brake wheel and the motor shaft flange; the shaft diameter is 477 mm. The principle of operation of the TT-Sense® sensor is based on detecting the relative axial, and angular motions between two rings fixed on the shaft. LED pointers are fixed on one ring, whereas optical detectors are mounted on the other ring and paired with the LED pointers. The axial and torsional vibrations of the two shaft sections where the rings are fastened produce

deviations of the LED beam positioning in the optical detectors, which are then converted into voltage signals. The rotating rings and LED sensors are powered through inductive coils that draw energy from a non-rotating, external circuit. The data signal is continuously transmitted from the rotor detectors to the stator control box via a wireless communication channel at 2.4 GHz. The output data is then processed to obtain the time series of shaft thrust, torque, and rotational speed, with a sampling frequency of 5 Hz, thus allowing to determine the shafts' dynamic response with low-frequency signals. Fig. 2.3 shows a cross-section of the sensor, where the shaft rings are represented², along with a photograph of the Starboard side sensor on board the vessel.

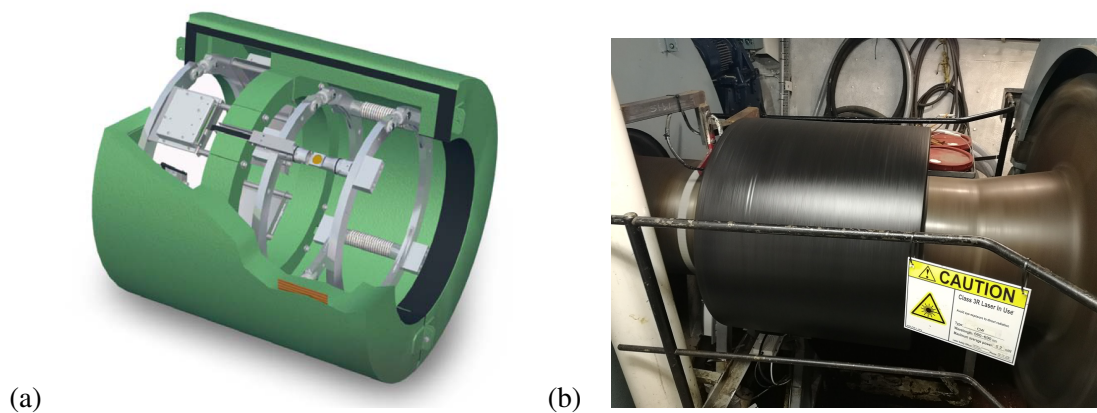


Figure 2.3: TT-Sense® sensor: cross-section drawing (a); placement on the Starboard shaft (b).

The TT-Sense® system is employed to record both the steady-state propulsion parameters and their transient perturbations induced by the ice-propeller interaction processes during ice operations. The low-frequency output data do not allow to perform a vibration analysis of the shaft, but they provide information about the peak amplitude of the torque shaft

²The sensor's graphical representation is retrieved from the manufacturer's website, at the address: www.vaf.nl/media/1434/tt-sense-optical-thrust-and-torque-measuring-systems-english-tib-664-gb-0215.pdf.

response caused by the ice-propeller interaction.

Furthermore, long-term, full-scale thrust and torque measurements constitute a means to evaluate the model test facilities at NRC, in a wide range of ice severity—full range of ice thickness and strength from first-year through to multi-year ice—as well as: (i) to evaluate the impact of hull and propulsion maintenance programs on performance; (ii) to support the improvement of operational fuel use; (iii) to support future icebreaker design and concept evaluation programs.

2.2.3. Shaft speed measurement at high frequency

Each shaft is equipped with a laser tachometer for the high-frequency measurement of the rotational speed. For the equipment on board CCGS *Henry Larsen*, we employed the “Type 2981” tachometer model produced by Brüel & Kjær. Fig. 2.4 shows the sensor and the installation setup. The tachometers are fixed on a vertical bracket, pointing toward a black-white striped reflective tape to produce a pulse signal (Fig. 2.4-b).

Overall, the reflective tape includes 100 white stripes and 100 black, all 7.5 mm wide, thereby providing 100 different pulses per shaft rotation. Each tachometer is connected to a National Instruments (NI) data acquisition NI-9230 module and NI-cDAQ-9181 chassis through a BNC-type cable. The data is then transmitted to the Control Box through an Ethernet cable, as indicated in the diagram of Fig. 2.1. The output signal has a frequency of 12.8 kHz, and we implemented the “Pulse Timing Method” to calculate the instantaneous shaft speed in rpm units [36]. Then, the resulting speed time history array is under-sampled at 100 Hz to reduce the necessary storage and the processing time to write the

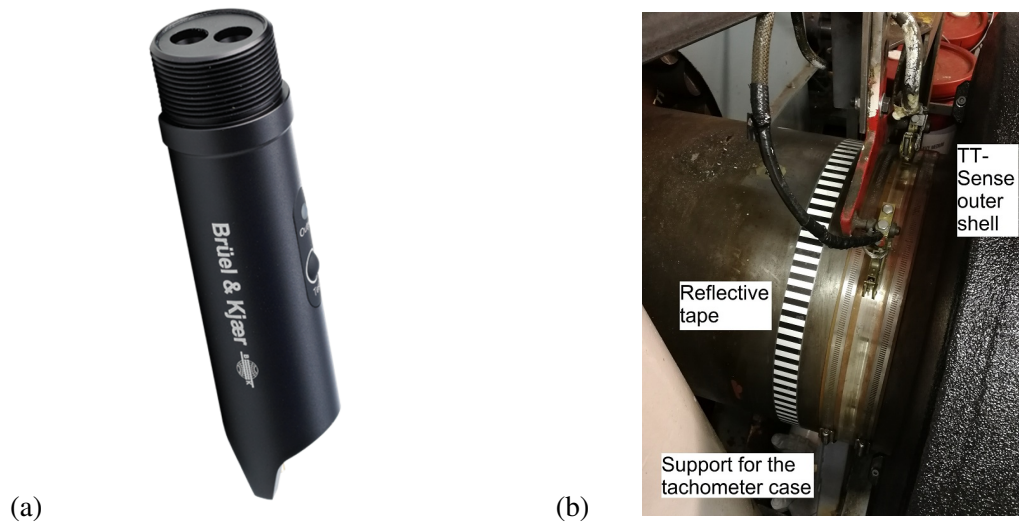


Figure 2.4: Brüel & Kjær Type 2981 laser tachometer (a); placement on the Starboard shaft (b).

data in the memory disks. A Nyquist frequency of 50 Hz is adequate to include the main torsional vibration modes of the shaftline [6, 7]. Therefore, from the time-domain rotational speed signals, we can determine the spectra of the angular velocity and of the torsional displacement of both shafts.

2.2.4. Ice condition monitoring

A high-definition, weatherproof IP camera is fixed to the Port-side railing of the Upper Deck, as shown in Fig. 2.5. The camera is positioned at a height of 13.6 m above sea level. The view is set to visualize the sea surroundings close to the ship hull by framing the water surface from a vertical line of view, as shown in Fig. 2.5. The camera is manufactured by HIK Vision, and it has a maximum resolution of 2 MP. The screen resolution is 1920×1080 pixel, and the camera is equipped with a digital zoom feature. A Power over Ethernet (PoE) cabling route provides the electrical power to the camera and carries the data directly to

the memory storage installed in the Network Video Recorder (NVR, Fig. 2.1). The NVR encases a 6-TB hard drive, in which approximately three months of continuous recording files can be stored. For our purpose, we scheduled the video recording program to operate for 12 hours a day.

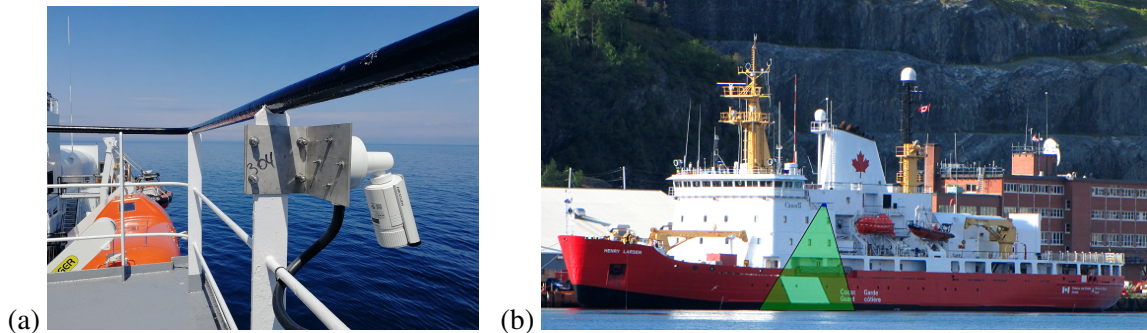


Figure 2.5: Railing support and positioning of the camera (a); view angle on the sea surface (b).

The task of the camera is to monitor the sea ice conditions during icebreaking operations; the thickness property of ice layers is the target quantity to characterize different ice scenarios. To determine that, we consider the occurrences when the ice floes flip over due to the ship icebreaking advancement. In those cases, the thickness dimension of the ice blocks can be directly visualized from the camera point of view. In order to obtain the scale length ratio correlating actual sea-level distances to the video frame dimensions, we employed a floating square-shaped frame, in which ticks are marked 10 cm apart along its 60-cm-long sides. Fig. 2.6 shows the frame as it appears in the recordings (Fig. 2.6-a) and a zoomed view of it, in which the minor marks are visible (Fig. 2.6-b). Once the scale ratio was set, we employed the software IC Measure® to process each video frame and determine the actual ice thickness values. Thereby, the ongoing ice conditions can be correlated to the shaftline dynamic response, which is monitored by the optical sensors.

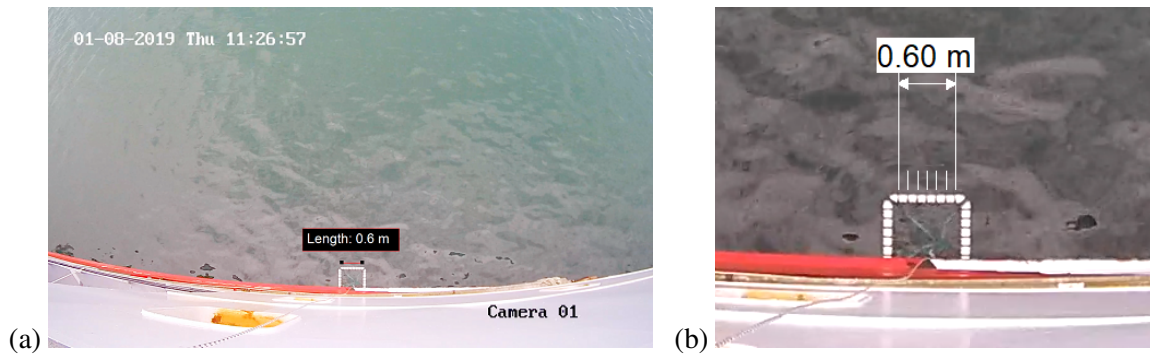


Figure 2.6: Floating frame for the calibration procedure: camera frame (a); zoomed view (b).

2.2.5. TT-Sense torque data validation via strain gauge measurements

To validate the shaft torque data measured by the TT-Sense, we installed a strain gauge system on the Starboard shaft to measure the dynamic torque at different propeller speeds during the vessel's open-water trials on August 10, 2019. An analogous measurement arrangement was employed on board CCGS *Terry Fox* to monitor shafts' vibrations at different loading conditions [47]. On CCGS *Henry Larsen*, the strain gauge outcomes were then compared with the concurrent measures of the TT-Sense. In the tests, the ship sailed around the northern end of the Avalon Peninsula in Newfoundland, Canada, with favourable weather, Sea State 2 conditions, and sea level deeper than 100 m. This ensured the shallow-water effects on the ship concerning low-frequency vibrations and wake field surrounding the propeller.

The strain gauge we employed was a full-bridge Wheatstone rosette (model CEA-06-250US-350) manufactured by VPG Sensors. In detail, we attached the gauge to the second tailshaft segment of the shaftline, which has a diameter of $d_o = 652$ mm and is located abaft the shaftline segment where the TT-Sense is installed (Fig. 2.2). We positioned the

grid pattern on the shaft surface according to [17]. The measurement output is the linear strain (ε) along the 45-degree direction with respect to the shaft sectional plane. The strain gauge terminals were wired to a differential analog channel input on a V-Link-200 Node® wireless data transmitter provided by LORD Sensing Systems Corp. A WSDA-200-USB® gateway interfaced the node to a laptop. We employed the software “SensorConnect”® to set up the node and perform the measurement runs, which were carried out with a sampling frequency of 256 Hz. Fig. 2.7 shows a schematic layout of the instrumentation (a) and its actual arrangement on board (b).

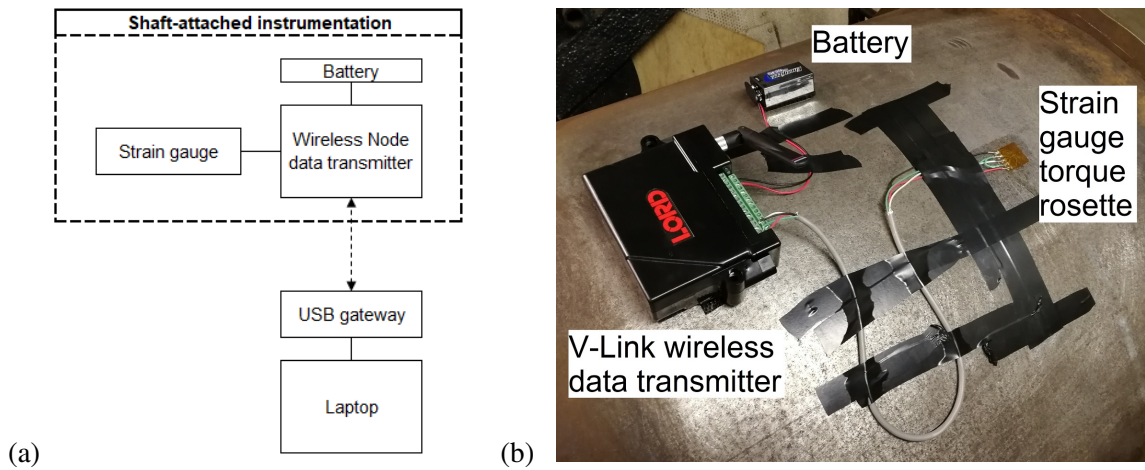


Figure 2.7: Arrangement of the shaft equipment (a); instrumentation attached to the shaft (b).

In the Wheatstone bridge strain gauge, the resistance of each coil is 350Ω ; the gauge factor was equal to $k_g = 2.10$. The output analog voltage scale was calibrated through the shunt calibration circuit incorporated in the node. The maximum measurable linear strain is $\varepsilon = 5 \%$. The node transmission power to the USB gateway was set to 10 dBm (decibel-mW). Overall, seven different steady-state speeds were considered during the sea trials, ranging from 66 rpm to 169 rpm. We acquired two 60-second long vibration data

recordings in correspondence with each propeller loading condition. The average strain value $\varepsilon_{\text{mean}}$ for each speed n was calculated as the mean value of the corresponding signals. Finally, the steady-state shaft torque $Q_{\text{shaft,Gauge}}(n)$ associated with a speed n is calculated as follows [17]:

$$Q_{\text{shaft,Gauge}}(n) = \frac{\pi E (d_o^4 - d_i^4)}{16 d_o (1 + \nu)} \varepsilon_{\text{mean}}(n) \quad (2.1)$$

where E and ν are the Young Modulus and the Poisson Ratio of the shaft steel, respectively; d_o and d_i are the outer and inner diameter, respectively. In this case, $d_i = 0$. The $Q_{\text{shaft,Gauge}}(n)$ obtained values are compared with the corresponding torque data measured by the Starboard TT-Sense ($Q_{\text{shaft,TT,Stbd}}$). Additionally, we consider the shaft torque values observed from the ABB® monitoring panel in the Engine Control Room as a further comparison term.

2.2.6. Trials in ice-covered waters

In fall 2019, CCGS *Henry Larsen* performed icebreaking trials in the Nunavut Arctic region. On October 17-18, the ship navigated from Franklin Strait to the Gulf of Boothia, passing through the Bellot Strait. Fig. 2.8 shows CCGS *Henry Larsen*'s route on those two days. The route's coordinates were obtained from the ship GPS logger, which tracks the vessel's position with a frequency of 1 Hz. In the expedition, the ship encountered heavy ice conditions. During icebreaking operations, the TT-sense meters measured the ice-induced perturbations of shaft thrust, torque, and speed, whereas the outdoor camera filmed the

ongoing sea ice conditions.

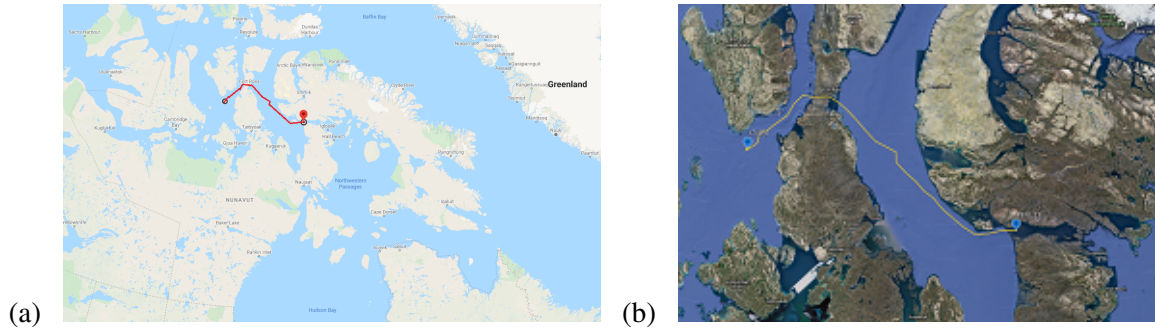


Figure 2.8: Route on October 17-18, 2019: larger view (a) and zoomed view (b) (via Google Earth®).

In winter 2020, the icebreaker carried out icebreaking operations in northern Newfoundland, Canada, across the strait region connecting Saint Barbe (NL) and Blanc Sablon (QC). The ship encountered ice also in the Twillingate and Fogo Island areas (central Newfoundland). The voyage took place on March 15-18; its route is shown in Fig. 2.9.

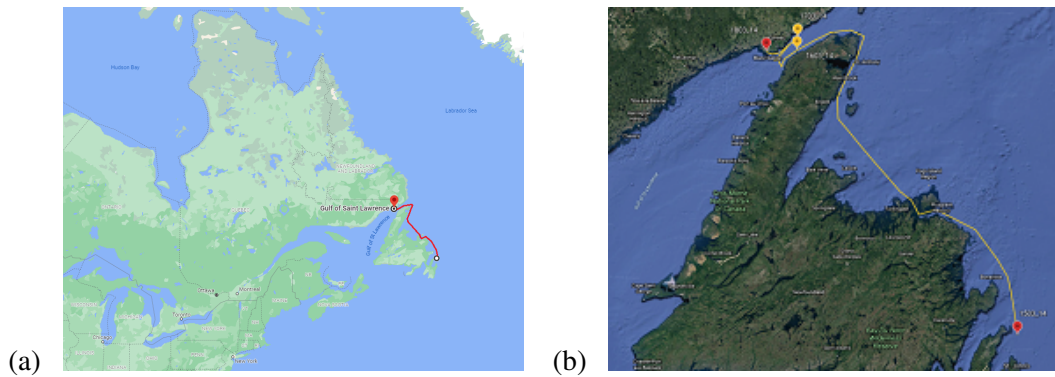


Figure 2.9: Route on March 15-18, 2020: larger view (a) and zoomed view (b) (via Google Earth®).

2.3. Results

2.3.1. Validation of the TT-Sense torque measures

Table 2.3 reports the results of the torque values read from the engine room control panel ($Q_{\text{shaft,Panel}}$) along with the measurements performed with the strain gauge system ($Q_{\text{shaft,Gauge}}$), and the mean steady state torque data acquired by the TT-Sense sensors for both shafts ($Q_{\text{shaft,TT,Stbd}}$ and $Q_{\text{shaft,TT,Port}}$). In the last column the percentage discrepancy between $Q_{\text{shaft,Gauge}}$ and $Q_{\text{shaft,TT,Stbd}}$ ($\Delta Q/Q_{\text{shaft,Gauge}}$) is shown.

Table 2.3: Torque values from the different sources, for seven speed levels.

Speed, n [rpm]	$Q_{\text{shaft,Panel}}$ [kNm]	$Q_{\text{shaft,Gauge}}$ [kNm]	$Q_{\text{shaft,TT,Stbd}}$ [kNm]	$Q_{\text{shaft,TT,Port}}$ [kNm]	$\Delta Q/Q_{\text{shaft,Gauge}}$ [%]
66	43.4	37.3	23.8	27.5	36.2
84	56.8	55.7	41.0	37.8	26.4
106	81.1	83.5	66.4	63.2	20.5
126	113.7	114.2	100.8	96.2	11.7
148	142.0	151.4	132.2	127.0	12.7
159	156.2	174.2	152.8	164.6	12.3
169	192.1	201.1	179.3	182.8	10.8

The higher deviations in $\Delta Q/Q_{\text{shaft,Gauge}}$ for the lower speed levels are due to the effects related to: (i) the manoeuvring operations ongoing at those speeds, which caused different incoming flux conditions to the propellers; (ii) the superposition of bending and axial vibration modes of the shaftline, which are excited by different propeller's harmonics in the low-frequency range; (iii) the different locations and shaft segment geometries where the TT-Sense sensors and strain gauge are positioned; (iv) the possible shift of torsional

vibration nodes due to the different added inertia of the water around the propeller at lower speeds. Fig. 2.10 shows the shaft torque outcomes from the strain gauge and the control panel as n varies, plus a regression curve for the $Q_{\text{shaft,Gauge}}$ series.

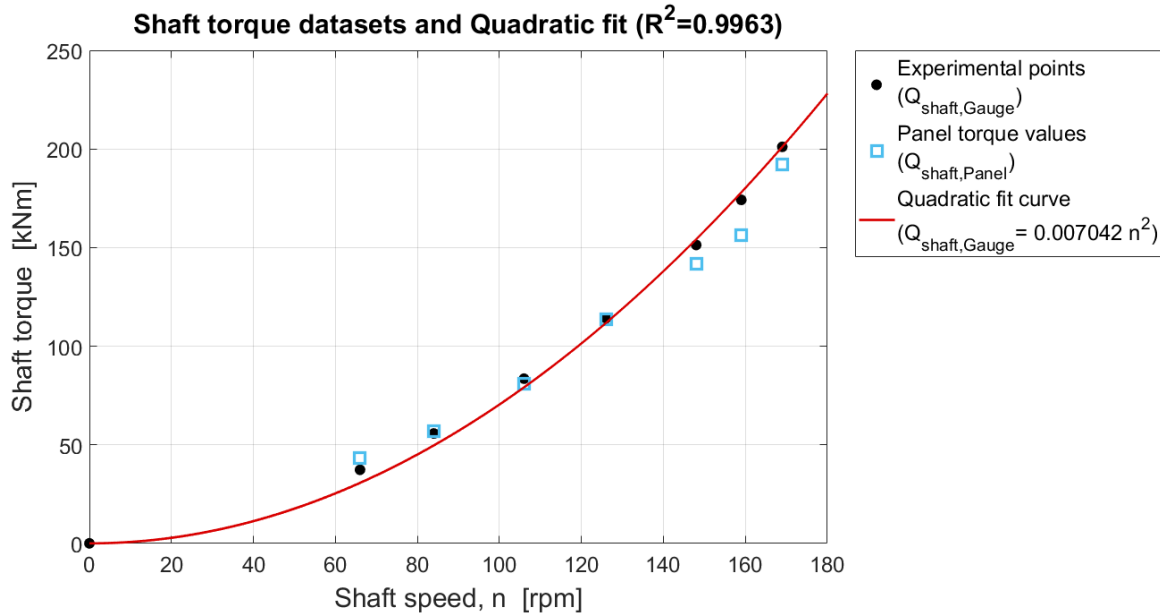


Figure 2.10: Shaft torque values ($Q_{\text{shaft,Gauge}}$ and $Q_{\text{shaft,Panel}}$) and fit curve of $Q_{\text{shaft,Gauge}}(n)$.

Two distinct patterns can be observed in Fig. 2.10. Firstly, it shows the correspondence between the $Q_{\text{shaft,Gauge}}$ values (black dots) and the $Q_{\text{shaft,Panel}}$ ones (blue marks): this fact confirms the reliability of the torsional vibration measurement obtained from the strain gauge, for every shaft speed. Secondly, the $Q_{\text{shaft,Gauge}}$ values demonstrate to fit a pure-quadratic curve as a function of n : this fact validates the propeller law assumption [26].

Specifically, in steady-state and open-water conditions the equivalence between $Q_{\text{shaft,Gauge}}$ and the propeller-absorbed torque (Q_{prop}) holds; the expression of Q_{prop} in this scenario can be expressed as follows [8]:

$$Q_{\text{prop}}(n) = K_Q(n) \rho n^2 D^5 \quad (2.2)$$

where K_Q is the propeller torque coefficient, ρ is the water mass density, n is the propeller's rotational speed in revolutions per second, D is the propeller diameter. The result of the regression analysis of $Q_{\text{shaft,Gauge}}(n)$ (red curve in Fig. 2.10) in terms of R^2 value shows that the quadratic trend of $Q_{\text{shaft,Gauge}}(n)$ is confirmed. Therefore, $K_Q(n)$ can be assumed as a constant parameter in Equation 2.2 in the case of FPP applications.

As an additional validation term of the TT-Sense output data, we compare the shaft effective power measured during short open-water time windows, at a constant speed, to model-scale results (ITTC 1957) that were measured in a 200-metre towing tank in St. John's (Newfoundland and Labrador, Canada) [41]. The time history of the vessel's longitudinal speed through water—obtained in a series of full-scale tests conducted on October 30, 2021—is shown in Fig. 2.11; the analyzed data clips are indicated through shaded segments. In addition to the shown segments, we also use a longer data sequence measured on the following day, at a cruising speed of ≈ 17 -18 kn. The model-scale experimental results [41] (black curve) are plotted along with the full-scale mean net power measured by the TT-Sense sensors (red dots) in Fig. 2.12. The speed used for the comparison is the measured longitudinal speed in open-water conditions; however, no adjustments were made for wind, waves, or transverse water current. The full-scale results are proved to correspond to the model-scale estimated values.

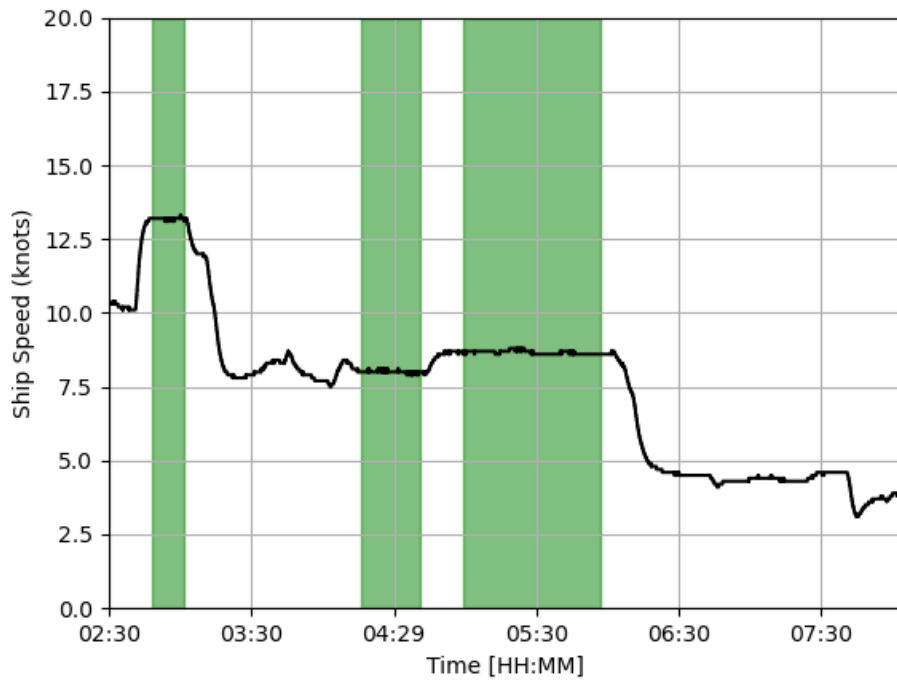


Figure 2.11: Open-water longitudinal speed of CCGS *Henry Larsen*; 2 to 6 am, October 30, 2021.

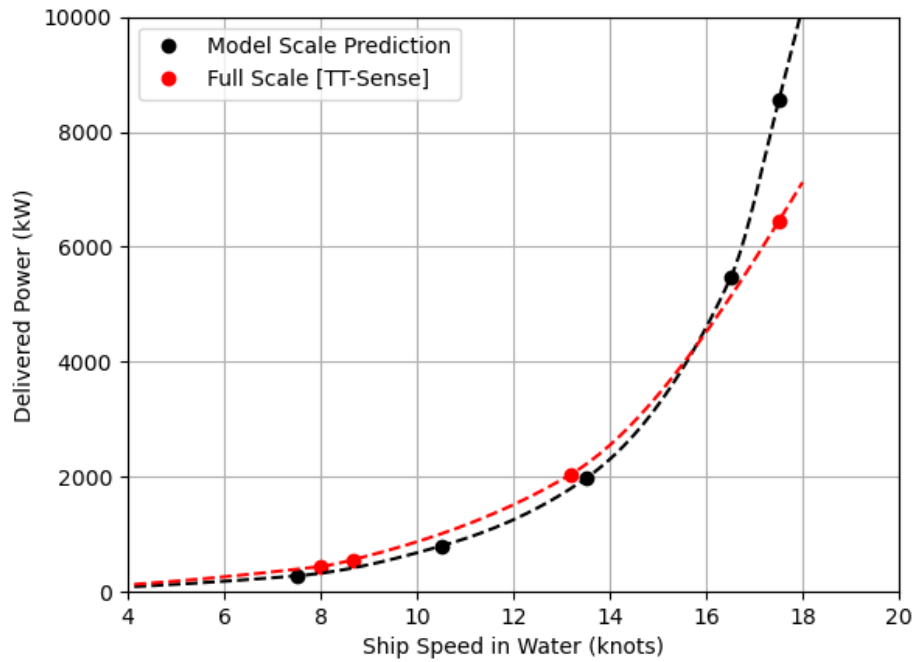


Figure 2.12: Comparison of the experimental model-scale [41] and full-scale delivered power.

2.3.2. Analysis of the laser tachometer signal

During the open-water sea trials, the shaft speed levels reported in Table 2.3 were reached progressively through successive steps. Fig. 2.13 shows the Starboard shaft rotational speed across a time window 2000-second long. The plot shows the speed steps corresponding to 106, 126, 148, and 169 rpm, with fluctuations of n around the mean value in each level. Larger-amplitude oscillations occur at 148 rpm, which is reached after the transition from the 126 rpm step ($t \approx 900$ s).

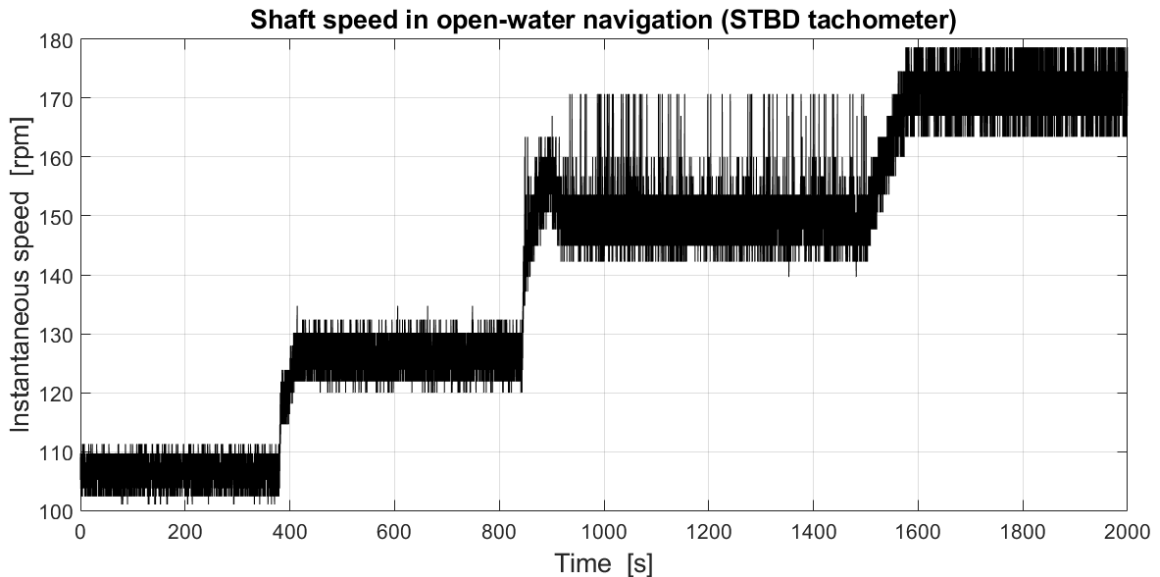


Figure 2.13: Shaft speed determined from the tachometer pulse signal. Under-sampling at 100 Hz.

Fig. 2.14 shows the spectrum of the angular speed signal ($\omega(f)$) at the 169 rpm speed level, which corresponds to the data of the last 400-second portion plotted in Fig. 2.13, over the frequency range f up to the Nyquist frequency—50 Hz. The fundamental frequency, which corresponds to the shaft rotation rate (2.82 Hz), is clearly visible together with its harmonics up to the 10th order (28.2 Hz). Subsequently, the spectrum of the angular

displacement ($\theta(f)$) can be derived numerically.

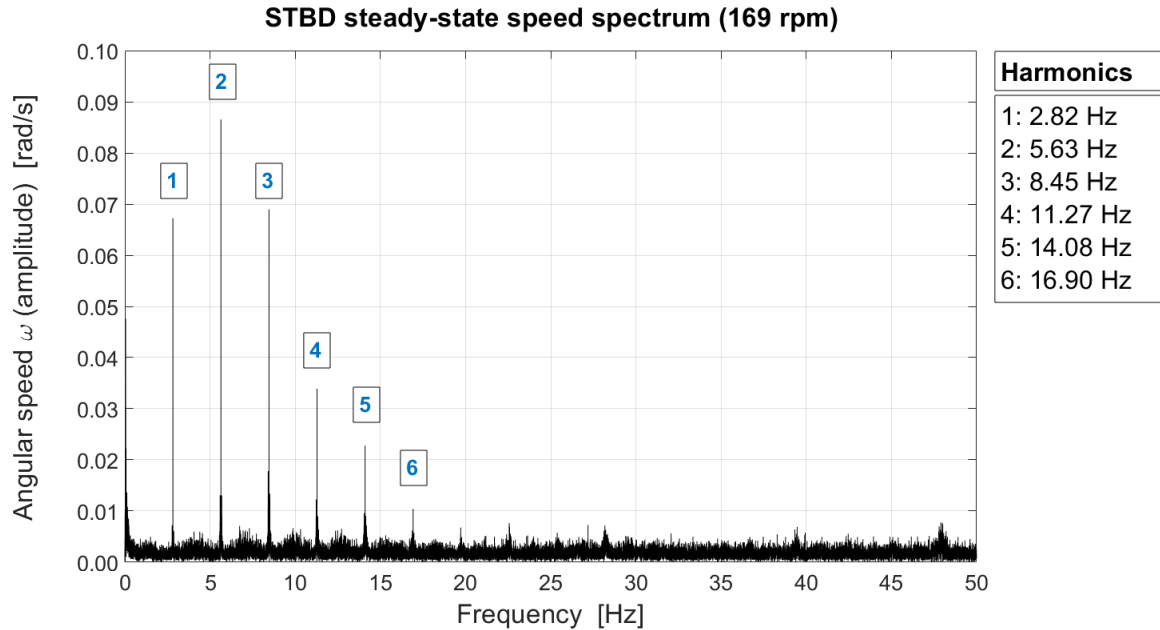


Figure 2.14: Spectrum of $\omega(f)$ at $n = 169$ rpm, in steady-state conditions, at the Starboard-side shaftline.

2.3.3. Ice-induced perturbations on the shaft dynamic response

Fig. 2.15 shows a 14-minute excerpt of the Starboard TT-Sense data output, acquired during the October 2019 voyage. The physical quantities that constitute the output dataset from each sensor include the shaft's torque Q (kNm), thrust T (kN), and speed n (rpm); in the plot, eight major perturbations are indicated and matched to the corresponding fluctuations of Q , T , and n .

In the 14-minute time window, the vessel moves forward starting from zero speed; in the end, it stabilizes at 45 rpm. The vertical lines in Fig. 2.15 match across time the onset of torque pulses with the corresponding fluctuations of thrust and shaft speed. In the plots, speed drop events that correspond to torque increases are more clearly visible in the events 3

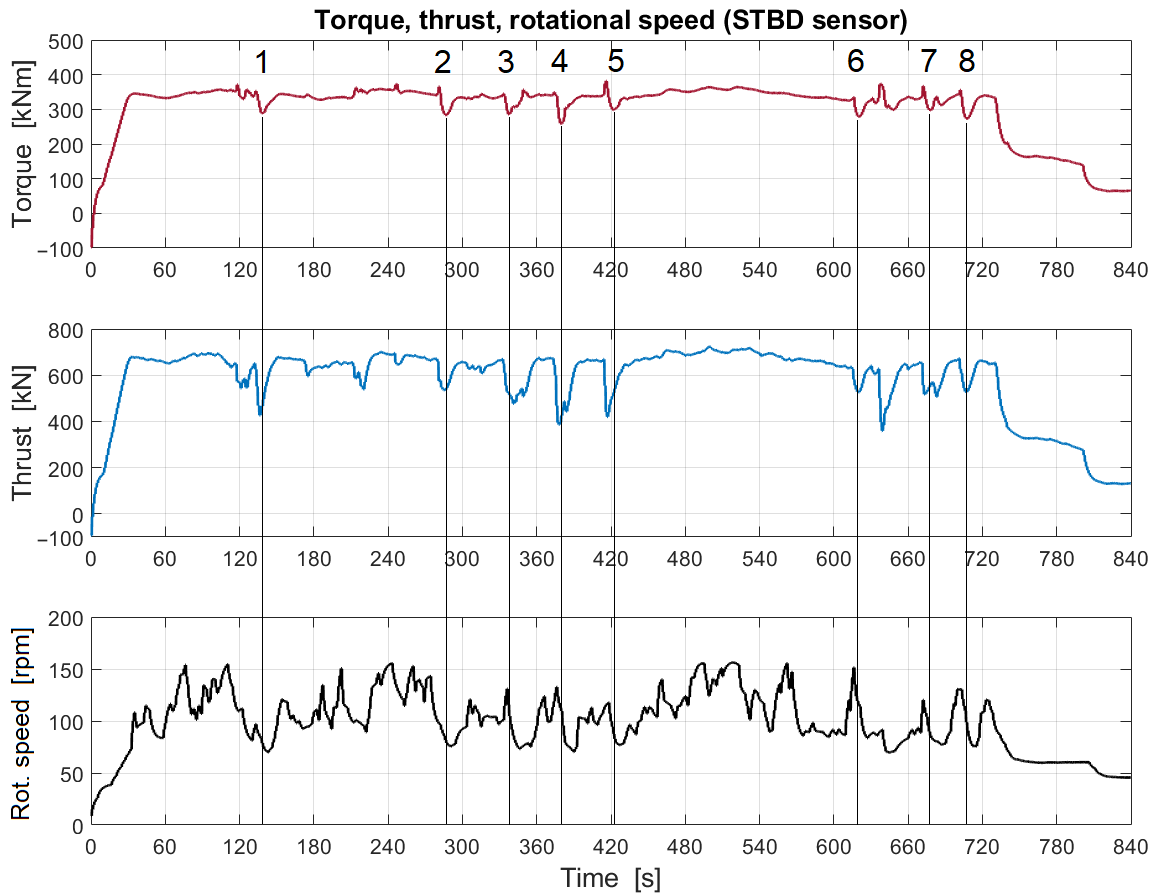


Figure 2.15: Time series of Q , T , and n during forward-direction ice navigation, on October 17, 2019.

to 8; concerning the 1 and 2 marks, the torque pulses appear to lag behind the corresponding speed drop. The signals of Q and T are acquired with their respective signs, depending on the load direction, whereas n is recorded with positive signs disregarding the shaft's rotation direction. The shaft's rotational speed fluctuates with larger excursions than the Q and T ones because the electric motor drive has a higher capability to sustain ample speed drops while the shaft's thrust and torque oscillate around their steady-state levels in short-term perturbations.

Fig. 2.16 shows two frames of the video recordings during the time window considered

above; the two frames (a) and (b) correspond to the instants around the events 2 and 6 shown in Fig. 2.15. The procedure presented in Section 2.2.4 was used to calculate the thickness values of the ice floes.

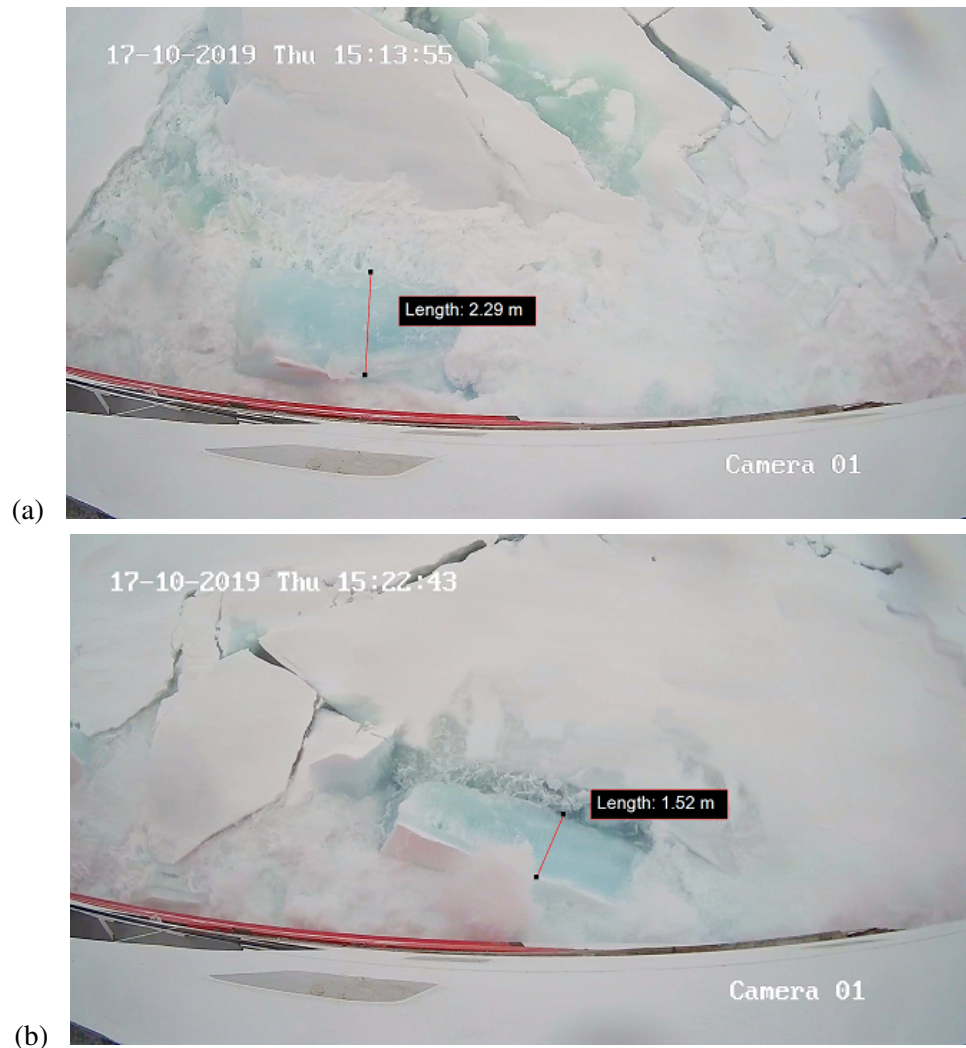


Figure 2.16: Ice thickness values: two frames corresponding to the events 2 (a) and 6 (b) in Fig. 2.15.

Fig. 2.17 shows the Inertial Measurement Unit (IMU) data acquired by the XSens device during the October 2019 voyage; the time window of the data clip corresponds to the one considered in Fig. 2.15. The vessel's trim angle in steady-state conditions corresponded to

2.5 degrees, whereas the heel angle was zero. Large vertical accelerations were experienced by the ship. The pitch angle changed dynamically during icebreaking operations, showing gradual bow's angle rises up to ≈ 1.5 degrees before rapid drops. This behavior was likely due to the hull's vertical motion during icebreaking processes. The roll angle fluctuations were limited to 2-3 degrees around the zero-degree position.

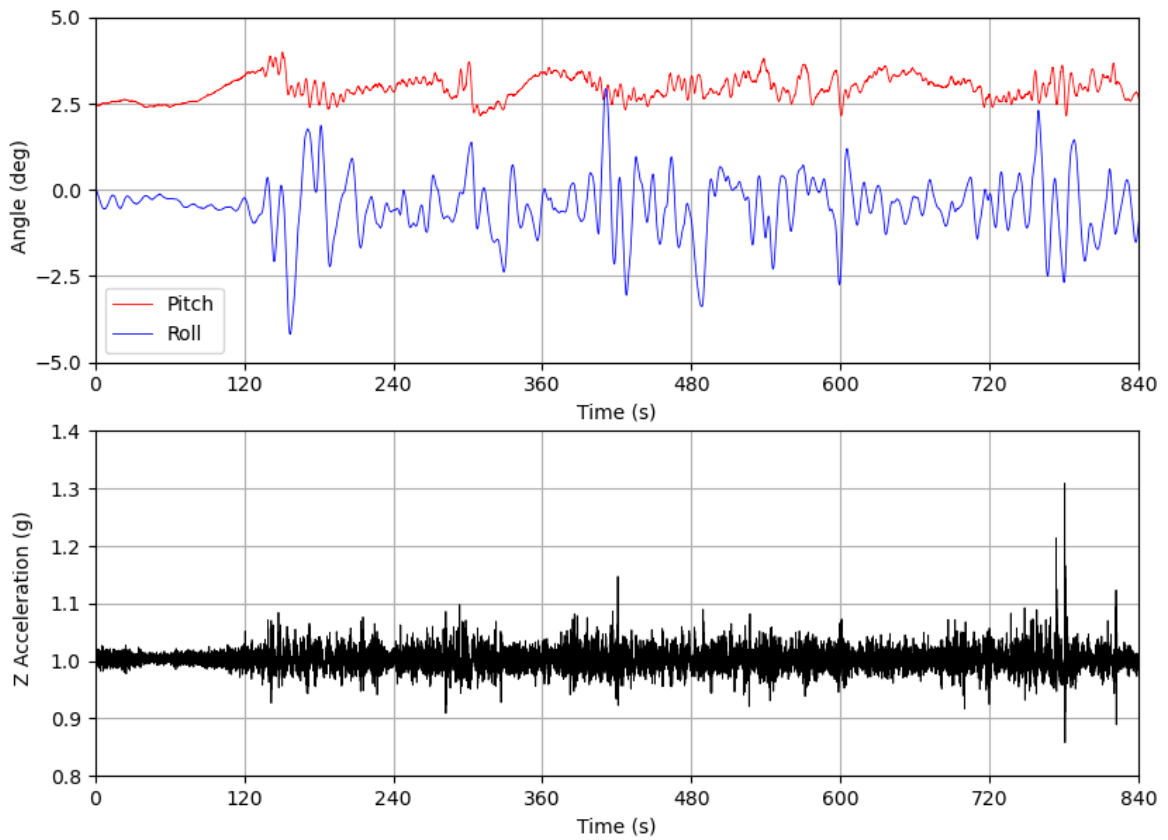


Figure 2.17: Pitch, roll and heave accelerations experienced by the ship during heavy-ice operations, October 2019.

Besides, the data acquired by the torque sensor can be used to determine the fluctuations in shaft power (P), which is calculated as the absolute value of the product between shaft torque (Q) and rotational speed (n , in rpm) as follows:

$$P = |Q| \left(2\pi \frac{n}{60} \right) \quad (2.3)$$

The variability in shaft power during icebreaking operations is useful to indicate how the energy rate required by the electric motors fluctuates, and thus monitor the status of the overall Diesel-electric power system through transient conditions. Fig. 2.18 includes a 6-minute dataset corresponding to forward-direction navigation in light ice, obtained during the March 2020 voyage. We calculated P through Equation 2.3 and the outcomes are plotted in parallel with the Q , T , n signals. From the shafts' rotational speed curves, it can be noticed that the vessel was advancing at a semi-steady pace as the fluctuations of n have a limited excursion. Hence, the pattern of P is driven by the Q variability. Fig. 2.19 shows the ice condition corresponding to this time interval.

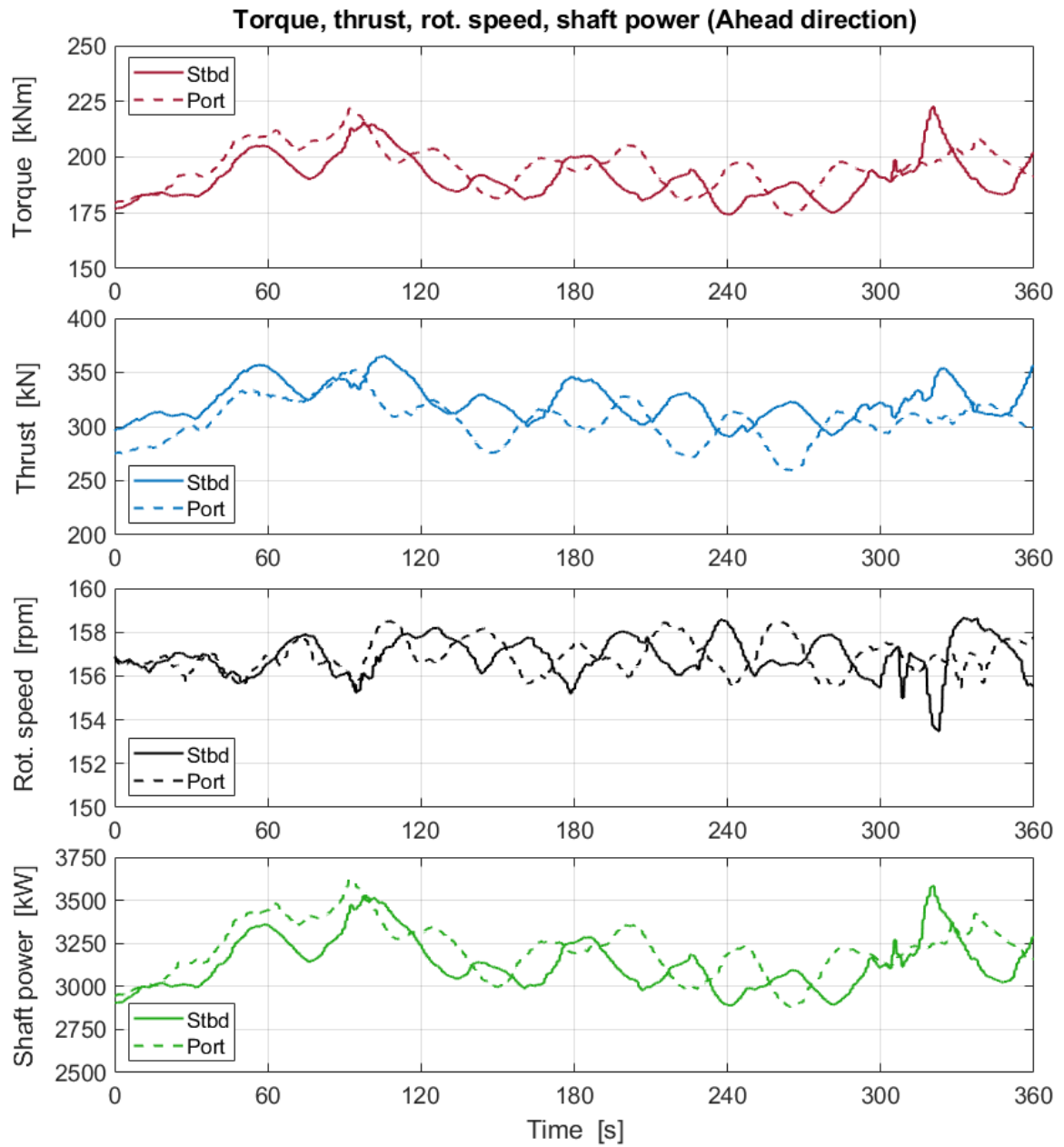


Figure 2.18: Time series of Q , T , and n during forward-direction ice navigation, on March 16, 2020. The data series of both shafts' sensors are plotted.



Figure 2.19: Ice conditions characterizing the time interval of the dataset in Fig. 2.18.

In addition, the experimental data measured during icebreaking operations and manoeuvring is important to evaluate the effects of abrupt changes in shaft structural response and power output efficiency over short time intervals. Fig. 2.20 shows an 8-minute dataset obtained during backing and ramming manoeuvres in heavy ice conditions, and the corresponding sea scenario is depicted in Fig. 2.21. In particular, the power value of 6 MW represents the upper limit that the three Diesel generators can deliver; it is reached at the two extremities of the time window and twice during the backing-ramming sequence. Also, the shaft speed is reported as a positive value disregarding the rotation direction. In the example of Fig. 2.20, we can observe that the Starboard shaft reverses direction at about $t \approx 90$ and 320 s. The curves indicate that the two shaftlines followed significantly different courses as the ship changed heading direction: while the Port-side shaftline maintained a more balanced power output, the Starboard-side propulsion line underwent three full excursions from zero to maximum power. Furthermore, the time series of the shafts' thrust provide

information concerning the ship's resistance during navigation across ice-covered sea.

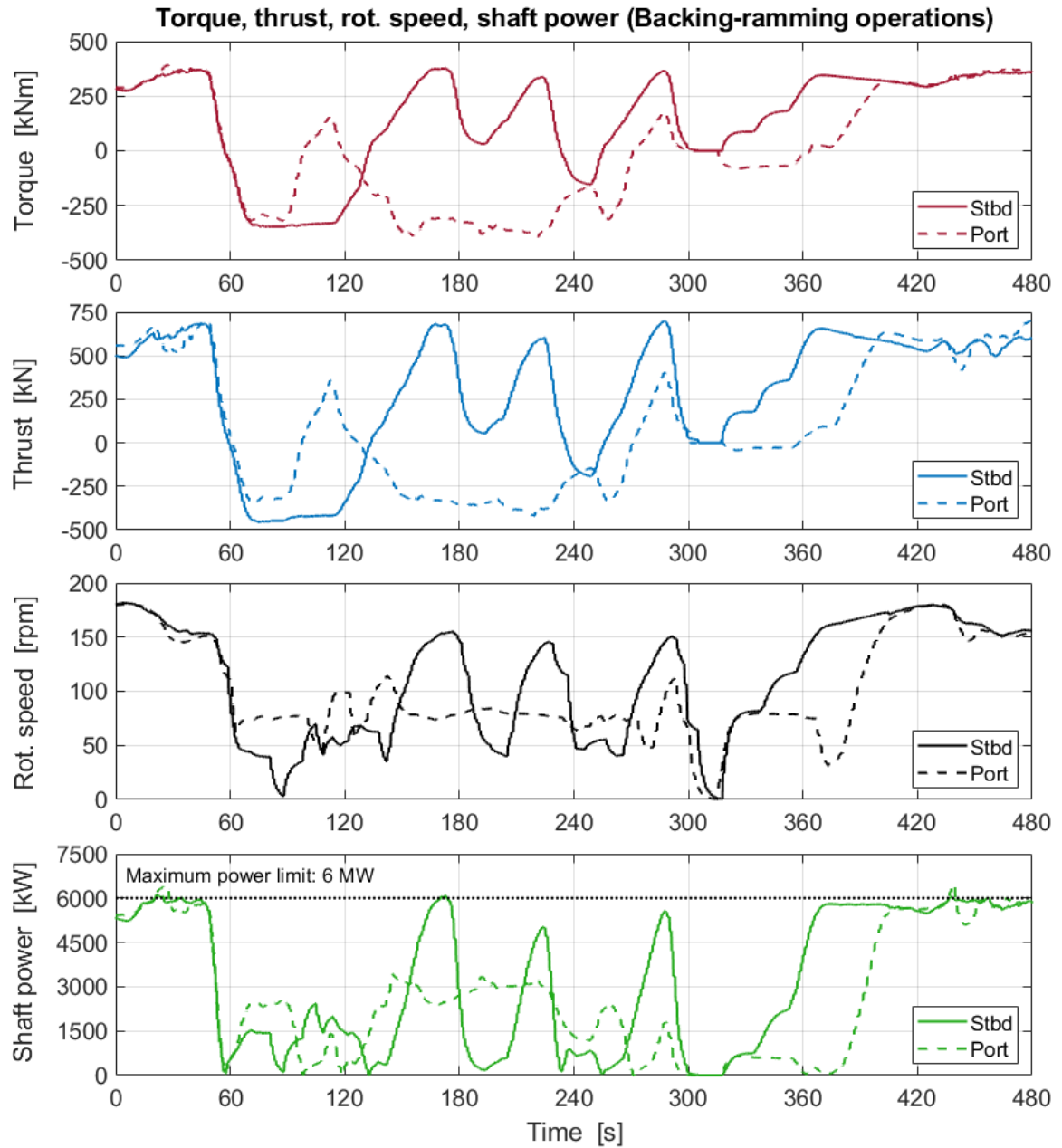


Figure 2.20: Time series of Q , T , and n during backing-ramming icebreaking operations, on March 17, 2020. The data series of both shafts' sensors are plotted.



Figure 2.21: Ice conditions characterizing the time interval of the dataset in Fig. 2.20.

2.4. Discussion

In this Section, the results shown in the previous parts are discussed sequentially.

- *TT-Sense validation through strain gauges.* As Fig. 2.10 and Table 2.3 show, the $Q_{\text{shaft,Gauge}}$ data correspond to the $Q_{\text{shaft,Panel}}$ values, thus confirming the reliability of the strain gauge apparatus. The results in Table 2.3 indicate that the relative discrepancy ($\Delta Q/Q_{\text{shaft,Gauge}}$) between the values measured by the TT-Sense and by the strain gauge decreases as the shaft speed increases. Since the TT-Sense and the strain gauge were installed on two different segments of the shaftline, the coupling of the axial, bending vibration modes at lower frequencies induces significant effects on the torsional responses in the two positions. In particular, the $Q_{\text{shaft,TT,Stbd}}$ and $Q_{\text{shaft,Gauge}}$ values differ significantly for $n < 100$ rpm: this fact remarks the higher uncertainty on the shaft torsional dynamics at lower speeds.
- *TT-Sense validation through open water performance data.* Fig. 2.12 clearly shows that

the TT-Sense device deployed on both shafts provides a sufficiently sensitive estimate of torque and power, which closely match detailed performance estimates via model-scale tests, in uncorrected open-water transits. Also, we showed that the dataset produced by the shaft optical sensors can be used to validate ship performance predictions during sea ice operations.

- *Tachometer measurements.* The dynamic rotational speed measured by the laser sensors allows us to study the torsional vibration response until 50 Hz, which is adequate to represent the major vibration modes of the shaftline and the external excitation spectra. Therefore, resonance events can be detected through these measurements. However, calculating the $\theta(f)$ spectrum (from $\omega(f)$) for a single shaft section is insufficient to determine the corresponding shaft torque, which can be obtained through two separate measurements at different sections.
- *TT-Sense data in sea ice navigation.* The TT-Sense sensors deliver continuous low-frequency data of the shafts' thrust and torque perturbations, along with their speed fluctuations. As we can see in Figs. 2.15, 2.18, and 2.20, the ice-induced torque amplitude can be evaluated in relation to the corresponding ice conditions. The sampling frequency of 5 Hz represents a limitation of the sensor, as it does not allow us to perform vibration analysis of the shaft response. On the other hand, the time tracking of T and Q over long time lapses provides comprehensive monitoring of the propulsion performance and efficiency. The dynamic shafts' responses—as it can be noticed in Figs. 2.15, 2.18, and 2.20—give clear indications on the operation type that the vessel undergoes.

- *Sea ice surface video recordings.* The ultimate goal of the camera imaging data is to characterize the sea ice conditions in terms of ice pieces' thickness. Specifically, the visual measurements aim to obtain information concerning the ice conditions as they are assessed by the bridge crew and through the Canada Weather Services' maps. In this way, the shaft response is correlated to the average sea ice scenarios evaluated during the navigation rather than the actual dimensions of the ice blocks that collide with the propeller. The sea ice imaging is not used to study the ice loads on the ship's hull. In the time window data considered in Fig. 2.15, the average thickness of the ice floes exceeds 1.5 m, which characterizes that specific ice type as thick first-year ice³ (Fig. 2.16). Regarding the ice conditions in the March 2020 session (Figs. 2.19 and 2.21), milder sea ice was encountered. The thickness values of the ice layers determined from the video recordings have been calculated by means of a graphic manipulation software frame by frame (Section 2.2.4); this procedure may be significantly time-consuming when hundreds of pictures are concerned; therefore, an IA software could be employed to automatically recognize the ice blocks and contour their physical boundaries in the frames.

2.5. Conclusions

In this paper, we presented a combined measurement system devised to monitor the ship propulsion performance and study the transient torsional behaviour of the shaftlines during icebreaking operations. The system was installed on board the CCG icebreaker *Henry*

³“Interpreting ice charts”, documentation provided by the Government of Canada weather services: <https://www.canada.ca/en/environment-climate-change/services/ice-forecasts-observations/publications/interpreting-charts/chapter-1.html>

Larsen. We showed a preliminary set of results from two expeditions of the vessel: first, open-water torque measurements to validate the optical torque sensor data were introduced; second, we presented a series of experimental data acquired during some icebreaking sessions. The results showed that datasets concerning: (i) shaft thrust, (ii) shaft torque, (iii) shaft speed, (iv) delivered power, (v) torsional vibration measures, and (vi) sea ice visual recordings could be integrated to provide a concurrent overview of the propulsion system status and the ongoing ice conditions. The instrumentation is going to be continuously employed during the future transit voyages and icebreaking operations of the ship. Large data clusters related to various operating scenarios will be obtained and later analyzed.

The Polar Rules issued by the International Association of Classification Societies (IACS) classify ice-going vessels in levels—to assess ships’ operational capability in ice environments—which constitute the Polar Class (PC) framework. One of the sea-ice properties that is key in characterizing each PC level is the ice layer’s thickness [19]. Hence, the full-scale experimental data obtained through our measurement system is fundamental for two primary purposes: first, to provide ship designers with experimental datasets to be used in future Polar-Class vessel design; second, to validate and possibly update the ice thickness criteria defined in the PC notation system.

Acknowledgements

This work was supported by the National Research Council of Canada (NRC), the American Bureau of Shipping (ABS), and the Department of Industry, Energy and Technology (IET)

of the Government of Newfoundland and Labrador, Canada.

The authors thank Mr. Mike Chaisson (CCG) and the crew members of CCGS *Henry Larsen* for their precious collaboration in accommodating the on-board fieldwork. We also acknowledge the technicians Tim Ennis and Keith Mews (NRC) for their essential contribution throughout the installation and set-up of the measurement devices aboard the CCGS *Henry Larsen*.

Abbreviations

The following abbreviations are used in this manuscript:

CCG	Canadian Coast Guard
CCGS	Canadian Coast Guard Ship
IMU	Inertial Measurement Unit
MUN	Memorial University of Newfoundland
NMEA	National Marine Electronics Association
NRC	National Research Council of Canada

References

- [1] Blaauw, R. J. (2013). Oil and gas development and opportunities in the Arctic Ocean. In *Environmental Security in the Arctic Ocean*, pages 175–184. Springer. 39

- [2] Bogoyavlensky, V. et al. (2014). The Arctic and World Ocean: Current State, Prospects and Challenges of Hydrocarbon Resources Development. In *21st World Petroleum Congress*. World Petroleum Congress. 39
- [3] Bose, N., Veitch, B., and Doucet, J. M. (1998). A design approach for ice class propellers. *SNAME Transactions*, 106:185–211. 40
- [4] Brouwer, J., Hagesteijn, G., and Bosman, R. (2013). Propeller-ice impacts measurements with a six-component blade load sensor. In *Third International Symposium on Marine Propulsors (SMP13)*, Tasmania, Australia. 40
- [5] Browse, J., Carslaw, K. S., Schmidt, A., and Corbett, J. J. (2013). Impact of future Arctic shipping on high-latitude black carbon deposition. *Geophysical research letters*, 40(16):4459–4463. 39
- [6] Burella, G. and Moro, L. (2017). Transient torsional analysis of polar class vessel shafting systems using a lumped model and finite element analysis. In *The 27th International Ocean and Polar Engineering Conference*, San Francisco, USA. 49
- [7] Burella, G., Moro, L., and Oldford, D. (2018). Analysis and validation of a procedure for a lumped model of Polar Class ship shafting systems for transient torsional vibrations. *Journal of Marine Science and Technology*, 23(3):633–646. 49
- [8] Carlton, J. S. (2007). *Marine Propellers and Propulsion*. Butterworth-Heinemann, Elsevier, 2nd edition. 56
- [9] Dahler, G., Stubbs, J. T., and Norhamo, L. (2010). Propulsion in ice – Big ships. In *International conference and exhibition on performance of ship and structure in ice - ICETECH*, Anchorage, AK, USA. 41
- [10] de Waal, R. J. O., Bekker, A., and Heyns, P. S. (2017). Bi-Polar Full Scale Measurements of Operational Loading on Polar Vessel Shaft-lines. In *Proceedings of the 24th International Conference on Port and Ocean Engineering under Arctic Conditions (POAC 2017)*, Busan, South Korea. 41
- [11] de Waal, R. J. O., Bekker, A., and Heyns, P. S. (2018). Indirect load case estimation for propeller-ice moments from shaft line torque measurements. *Cold Regions Science and Technology*, 151:237–248. 41
- [12] Gascard, J.-C., Riemann-Campe, K., Gerdes, R., Schyberg, H., Randriamampianina, R., Karcher, M., Zhang, J., and Rafizadeh, M. (2017). Future sea ice conditions and weather forecasts in the Arctic: Implications for Arctic shipping. *Ambio*, 46(3):355–367. 38
- [13] Gong, W., Beagley, S. R., Cousineau, S., Sassi, M., Munoz-Alpizar, R., Ménard, S., Racine, J., Zhang, J., Chen, J., Morrison, H., et al. (2018). Assessing the impact of shipping emissions on air pollution in the Canadian Arctic and northern regions: current and future modelled scenarios. *Atmospheric Chemistry and Physics*, 18(22):16653–16687. 39
- [14] Granier, C., Niemeier, U., Jungclaus, J. H., Emmons, L., Hess, P., Lamarque, J.-F., Walters, S., and Brasseur, G. P. (2006). Ozone pollution from future ship traffic in the Arctic northern passages. *Geophysical Research Letters*, 33(13). 39

- [15] Gunnarsson, B. (2021). Recent ship traffic and developing shipping trends on the Northern Sea Route—Policy implications for future arctic shipping. *Marine Policy*, 124:104369. 39
- [16] Hindley, R. J., Tustin, R. D., and Upcraft, D. S. (2007). Environmental protection regulations and requirements for ships for Arctic sea areas. In *RINA International Conference - Design and Construction of Vessels Operating in Low Temperature Environments*, pages 107–118, United Kingdom. Royal Institution of Naval Architects. 39
- [17] Hoffmann, K. (2001). Applying the Wheatstone Bridge Circuit. Technical report, Hottinger Baldwin Messtechnik (HBM) GmbH. Version W1569en-1.0. 52, 53
- [18] Ikonen, T., Peltokorpi, O., and Karhunen, J. (2015). Inverse ice-induced moment determination on the propeller of an ice-going vessel. *Cold Regions Science and Technology*, 112:1–13. 41
- [19] International Association of Classification Societies (IACS) (2006). Requirements concerning Polar Class - Polar Rules. Rev. 1 Jan 2007, Corr. 1 Oct 2007. 71
- [20] Jussila, M. and Koskinen, P. (1989). Ice loads on CP-propeller and propeller shaft of small ferry and their statistical distributions during winter '87. In *Proceedings of the 8th International Conference on Offshore Mechanics and Arctic Engineering*, volume IV. 41
- [21] Khan, A. G., Hissette, Q., Streckwall, H., and Liu, P. (2020). Numerical investigation of propeller-ice interaction effects. *Ocean Engineering*, 216:107716. 40
- [22] Kitagawa, H. et al. (2011). Safety and Regulations of Arctic Shipping. In *The Twenty-first International Offshore and Polar Engineering Conference*. International Society of Offshore and Polar Engineers. 39
- [23] Lee, S.-K. (2006). Rational approach to integrate the design of propulsion power and propeller strength for ice ships. *ABS Technical Papers*. Originally presented at the 2006 SNAME ICETECH conference; Banff, Canada, July 16-19, 2006. 40
- [24] Lensu, M., Kujala, P., Kulovesi, J., Lehtiranta, J., and Suominen, M. (2015). Measurements of Antarctic sea ice thickness during the ice transit of SA Agulhas II. In *Proceedings of the International Conference on Port and Ocean Engineering Under Arctic Conditions (POAC 2015)*, Trondheim, Norway. 41
- [25] Lu, W., Zhang, Q., Lubbad, R., Løset, S., Skjetne, R., et al. (2016). A shipborne measurement system to acquire sea ice thickness and concentration at engineering scale. In *Arctic Technology Conference*, St. John's, NL, Canada. OTC. 41
- [26] MAN (2011). Basic Principles of Ship Propulsion. Frederikshavn, Denmark. MAN Diesel & Turbo. 56
- [27] Melia, N., Haines, K., Hawkins, E., and Day, J. J. (2017). Towards seasonal Arctic shipping route predictions. *Environmental Research Letters*, 12(8). 084005. 39
- [28] Mjelde, A., Martinsen, K., Eide, M., and Endresen, Ø. (2014). Environmental accounting for Arctic shipping—A framework building on ship tracking data from satellites. *Marine pollution bulletin*, 87(1-2):22–28. 39

- [29] Nickerson, B. M. and Bekker, A. (2022). Inverse model for the estimation of ice-induced propeller moments using modal superposition. *Applied Mathematical Modelling*, 102:640–660. 41
- [30] Niioka, T. and Kohei, C. (2010). Sea ice thickness measurement from an ice breaker using a stereo imaging system consisted of a pairs of high definition video cameras. *International Archives of the Photogrammetry, Remote Sensing and Spatial Information Science, Kyoto Japan*, 38(8):1053–1056. 41
- [31] Norhamo, L., Bakken, G. M., Deinboll, O., and Iseskär, J. J. (2009). Challenges related to propulsor - ice interaction in arctic waters. In *First International Symposium on Marine Propulsors (SMP09)*, Norway. 40
- [32] Perovich, D. K. and Richter-Menge, J. A. (2015). Regional variability in sea ice melt in a changing Arctic. *Philosophical Transactions of the Royal Society A: Mathematical, Physical and Engineering Sciences*, 373(2045):20140165. 38
- [33] Pierre, C. and Olivier, F. (2015). Relevance of the Northern Sea Route (NSR) for bulk shipping. *Transportation Research Part A: Policy and Practice*, 78:337–346. 39
- [34] Pietri, D., Soule I V, A. B., Kershner, J., Soles, P., and Sullivan, M. (2008). The Arctic shipping and environmental management agreement: a regime for marine pollution. *Coastal Management*, 36(5):508–523. 39
- [35] Polić, D., Ehlers, S., Æsøy, V., and Pedersen, E. (2013). Propulsion Machinery Operating In Ice-A Modelling And Simulation Approach. In *Proceedings - 27th European Conference on Modelling and Simulation (ECMS 2013)*, pages 191–197. 40
- [36] Remond, D. (1998). Practical performances of high-speed measurement of gear transmission error or torsional vibrations with optical encoders. *Measurement Science and Technology*, 9(3):347. 48
- [37] Schröder, C., Reimer, N., and Jochmann, P. (2017). Environmental impact of exhaust emissions by Arctic shipping. *Ambio*, 46(3):400–409. 39
- [38] Silber, G. K. and Adams, J. D. (2019). Vessel Operations in the Arctic, 2015-2017. *Frontiers in Marine Science*, 6:573–590. 38, 39
- [39] Suominen, M., Bekker, A., Kujala, P., Soal, K., and Lensu, M. (2017). Visual Anctartic Sea Ice Condition Observations during Austral Summers 2012-2016. In *Proceedings of the 24th International Conference on Port and Ocean Engineering under Arctic Conditions (POAC 2017)*, Busan, South Korea. 41
- [40] Suominen, M., Karhunen, J., Bekker, A., Kujala, P., Elo, M., Enlund, H., Saarinen, S., et al. (2013). Full-scale measurements on board PSRV SA Agulhas II in the Baltic Sea. In *Proceedings of the International Conference on Port and Ocean Engineering Under Arctic Conditions*, Espoo, Finland. 41

- [41] Wang, J. (2021). CCG's Baseline Model Tests using Henry Larsen Icebreaker [NRC-OCRE-2021-TR-004]. Technical report, National Research Council of Canada - Ocean, Coastal and River Engineering (NRC-OCRE), St. John's, Canada. xvii, 57, 58
- [42] Wang, J., Akinturk, A., and Bose, N. (2006). Numerical prediction of model podded propeller-ice interaction loads. In *25th International Conference on Offshore Mechanics and Arctic Engineering (OMAE2006)*, pages 667–674, Hamburg, Germany. American Society of Mechanical Engineers Digital Collection. 40
- [43] Weissling, B., Ackley, S., Wagner, P., and Xie, H. (2009). EISCAM—Digital image acquisition and processing for sea ice parameters from ships. *Cold Regions Science and Technology*, 57(1):49–60. 41
- [44] Williams, F. M., Spender, D., Mathews, S. T., and Bayly, I. (1992). Full Scale Trials in Level Ice with Canadian R-Class Icebreaker. In SNAME, editor, *SNAME Transactions*, volume 100, pages 293–313. 41
- [45] Yang, B., Sun, Z., Zhang, G., Wang, Q., Zong, Z., and Li, Z. (2021). Numerical estimation of ship resistance in broken ice and investigation on the effect of floe geometry. *Marine Structures*, 75:102867. 40
- [46] Yumashev, D., van Hussen, K., Gille, J., and Whiteman, G. (2017). Towards a balanced view of Arctic shipping: estimating economic impacts of emissions from increased traffic on the Northern Sea Route. *Climatic Change*, 143(1-2):143–155. 39
- [47] Zambon, A. and Moro, L. (2022). Torsional vibration analysis of diesel driven propulsion systems: The case of a polar-class vessel. *Ocean Engineering*, 245:110330. 51
- [48] Zhang, Y., Meng, Q., and Zhang, L. (2016). Is the Northern Sea Route attractive to shipping companies? Some insights from recent ship traffic data. *Marine Policy*, 73:53–60. 39
- [49] Zhang, Z., Huisingh, D., and Song, M. (2019). Exploitation of trans-Arctic maritime transportation. *Journal of cleaner production*, 212:960–973. 38, 39

Chapter 3

Torsional vibration analysis of Diesel driven propulsion systems: the case of a Polar-Class vessel

Abstract

The reliability of marine propulsion plants of ice-going vessels is essential in preserving ship safety during ice navigation. Therefore, the development of reliable design tools of the transmission shafting systems is fundamental to simulate ice-propeller interaction processes correctly. This paper outlines a methodology to model the torsional dynamics of fully-g geared, Diesel-drive propulsion systems; specifically, a novel analytical model to simulate the dynamic Diesel engine torque is described. We consider the Canadian Coast Guard heavy icebreaker *Terry Fox* as a case study, whose propulsion plant includes two shaftlines driven

by two 4-stroke Diesel engines each and equipped with controllable pitch propellers (CPP). On this vessel, we performed full-scale measurements during open-water sea trials to: (i) validate the Diesel-drive mathematical model; (ii) update the numerical eigenfrequencies of the system; (iii) determine the curve of the propeller-absorbed hydrodynamic torque. Finally, we simulate the dynamic response of the shaftline's model by applying an ice-propeller transient excitation. The results indicate the effectiveness of the proposed methodology to simulate the Diesel engine torque, and the significance of considering the CPP pitch variation in transient-state conditions when ice-induced loads are concerned.

Keywords

Torsional vibration analysis; Ice-propeller interaction; Diesel engine simulations; Controllable Pitch Propellers; Icebreakers; Full-scale measurements.

3.1. Introduction

Torsional Vibration Analysis (TVA) is a relevant branch in the field concerning ship propulsion system simulations, as propellers and prime-movers represent major sources of torsional vibrations that can lead to structural failures [50, 58].

TVA began to be investigated in the 70s, when the computational tools became widespread in all engineering fields [28, 46]. Initially, marine shaftlines were conceived as simplified systems to simulate their primary structural properties [40]. In addition to the TVA deterministic approach, probabilistic methods have been applied to evaluate the failure

risk of shaft segments due to fatigue [39, 53]. More recently, Finite Element Analysis (FEA) started to be applied to TVA shaftline modelling [19, 48, 58]. The use of FEA provides a more precise structural representation of the system, but this technique is computationally heavy. In the studies [8, 17], the authors focused on the transient behavior of marine shaftlines and its numerical modelling; it was shown that concentrated-mass models yield satisfactory results in terms of torsional vibrations. Next, numerical methods integrating lumped-element models and FEA were progressively developed [35, 50]. Senjanović et al. studied the differences in TVA outcomes that arise when considering a multiple Degree-of-Freedom (DOF) shaftline model or a corresponding model with 2 DOFs. The authors used Rayleigh-Ritz techniques to perform the simulations; they demonstrated that the analytical procedures are effective to obtain the first vibration mode of the system, whereas the further modes are disregarded [49, 50]. Mendes et al. employed detailed FE modelling to determine the macroscopic properties of the components in a 4-stroke, Diesel engine drive shaftline; a reduced-DOF model was then established, and the results were benchmarked against full-scale torsional vibration measures, with substantial agreement [35]. Additionally, Murawski and Charchalis investigated the advantages and drawbacks in undertaking two different methods to solve shaftline TVAs: one consists in a simplified, fully-analytical methodology, the other uses commercial numerical software [37]. Proper modelling procedures to simulate the propeller-shaftline-engine mutual interaction are fundamental to study the effects of transient excitation, which could lead to structural failure of shafting segments or engine components [24, 38].

Currently, TVA of ship propulsion systems employs all the presented modelling method-

ologies. FEA is especially employed to investigate particular and small-scale phenomena [20, 35]. Conversely, FE-modelling could be unfit to be utilized in the early stage of ship design processes due to its complexity. Hence, simplified lumped-element models are preferred to carry out TVA simulations when designers need flexibility to simulate multiple shaftline design solutions [37, 50]. Contemporary research aims to improve the robustness of such simplified modelling methods, also with the support of experimental data [20].

3.1.1. Diesel engine's excitation modelling

An accurate simulation tool of propulsion systems' TVA has to include the excitation delivered by prime movers, which require particularly complex numerical models [36]. Several factors compose the Diesel engine's output excitation; a global, detailed model is analyzed in [16], in which the author also considers the coupling relations between multiple DOFs in the cylinder-crank assembly. On the other hand, the oscillatory characteristics of the Diesel engine torque can be described through Fourier series, as adopted in [14, 15, 35, 50]; however, to employ this approach, specific technical data need to be provided by the engine's manufacturer to construct the excitation curve. Tsitsilonis and Theotokatos developed a tool to determine the in-cylinder combustion pressure curve by using measured torque signals as input, bypassing the practical obstacles in retrieving the Fourier series data for the engine's torque [55]. Polić et al. modelled the shaftline components and the Diesel engine cylinder-crank assemblies by using Bond-Graph (BG) elements [42, 43]. The BG-based model was then validated by employing FEA, which provided additional indications concerning the minimum number of DOFs to simulate the shaftline reliably [42].

3.1.2. Shaftline TVA and ice-propeller interaction

Recently, the study of transient loads induced by ice-propeller interaction has constituted a crucial topic in the propulsion design and safety regulations for Polar-Class vessels [27, 29]. Icebreaking operations and transit navigation along ice-covered routes increase the vulnerability of propulsion systems of Polar-Class vessels [5, 26]. In particular, the overall ice-propeller interaction phenomenon can be represented as the combination of ice block impacts and ice-layer milling processes [56]. Determining the characteristics of the ice-induced excitation on marine propellers constitutes a challenging task that could require complex numerical modelling techniques. Hence, to better understand this phenomenon, model tests in a towing tank environment and full-scale measurements are fundamental. Khan et al. performed model-scale experiments to determine the linear superposition of different terms that compose the ice-induced load on the propeller blades [25]. Wang et al. studied through panel method modelling the propulsion coefficients of a podded propeller that undergoes ice crushing; the model was validated against towing tank data [57].

On the other hand, full-scale measurements are conducted on board ice-going vessels to obtain in-the-field data and then determine the characteristics of ice-induced propeller loads. A joint Finnish and South-African research group conducted a vast experimental activity to study the global structural response and the ice-induced shaftline vibrations on board the Polar Research Vessel S.A. *Agulhas II* [9, 52]. The ship operated both in the Baltic Sea and in the Southern Atlantic Ocean. In the latter expedition, also the German icebreaker *Polarstern* was involved in the study; de Waal et al. focused on the thrust and

torque fluctuation propagated along the vessel shafts by employing torsional strain gauges [9]. In this study, the output, time-domain shaft torque signal was processed to obtain the input, ice-propeller interaction torque [10]. The transmission line was modelled as a lumped-element system, and the dynamic impedance matrix inversion was implemented through three different numerical methods [10, 21].

Conversely, several studies tackled the ice-related TVA problem with a fully-numerical approach by using the International Association of Classification Societies (IACS) rules to characterize the ice-propeller loads. Batrak et al. employed a specific software tool to model a Diesel-drive shaftline and simulate its ice-induced, transient dynamics through the Kujawski-Gallager solver [4]. Furthermore, Burella et al. performed a sensitivity analysis through FEA on the shaft structural properties of an Electric-drive shaftline, to determine its response to ice-induced loads as a function of different shaft characteristics [6]. Polić et al. used the BG model and model-scale measurements to develop an inverse algorithm that transforms the measured torsional vibration signals into ice-induced transient loads exerted on the propeller blades [43, 44].

3.1.3. Contribution of the present work

This paper aims to outline a methodology to model ship propulsion shafting systems driven by a Diesel engine prime mover, to be used in the early design phases of a ship. We developed analytical models to simulate the Diesel engine driving torque and the Controllable Pitch Propeller (CPP) control. The shaftline is simulated through a linear, lumped-inertia, torsional-DOF system. Hence, we applied the modelling methodology to the Canadian

heavy icebreaker *Terry Fox*, and we validated the generated models against full-scale vibration data.

Thereafter, we perform a TVA simulation by applying an ice-induced torque to the propeller, to show how the Diesel engine output and the CPP's blade angle controller reacts to a transient perturbation. We also demonstrate that the ice-induced propeller torque is significantly affected by the instantaneous CPP configuration, which consequently proves a key variable to consider when CPPs are concerned in Polar-Class vessel shaftlines.

Fig. 3.1 shows the flowchart of the research activity presented in this paper.

First, we outline the steps to generate a propulsion line model (Fig. 3.1, Block 1, Subsection 3.2) which involves: (i) the generation of a lumped-parameter model of a propeller-shaft (Subsection 3.2.1); (ii) the development of a procedure to simulate a diesel engine's dynamic torque (Subsection 3.2.2); (iii) a procedure to calculate the hydrodynamic torque on a CP propeller (Subsection 3.2.3); (iv) an algorithm that implements the CPP blade angle controller (Subsection 3.2.4); (v) a method to model a lumped-element system of a shaftline (Subsection 3.2.5).

Then, we present the icebreaker used as a case-study vessel (Fig. 3.1, Block 2, Subsection 3.3.1), and the full-scale experimental measurements used to validate the numerical models (Block 3, Subsections 3.3.2, 3.3.3, Section 3.4).

Finally, the validated model is used to simulate the ice-induced transient response of the propulsion system (Fig. 3.1, Block 4, Section 3.5).

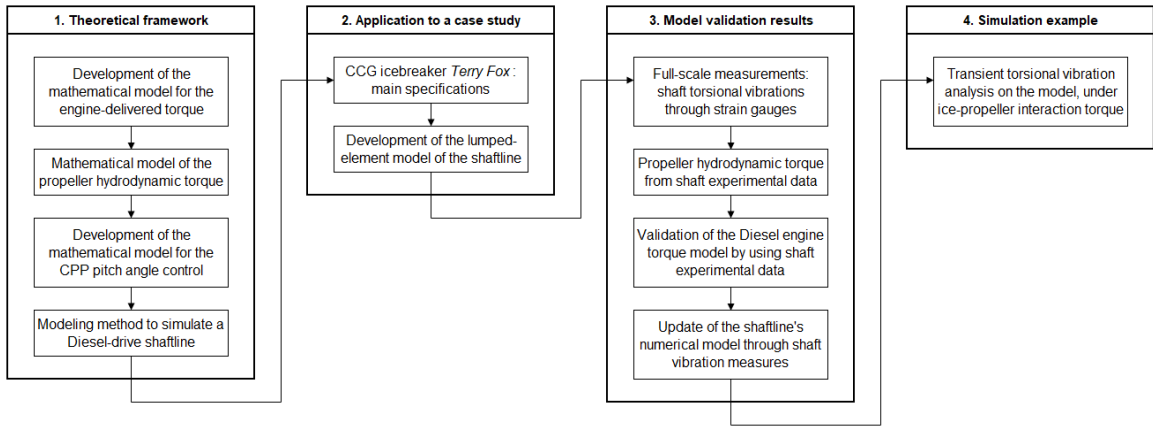


Figure 3.1: Layout of the parts composing the present work.

3.2. Theoretical framework

3.2.1. Shaftline lumped-parameter model

We used the classic approach of lumped-parameter elements to model the propeller-shaft, where the structural elements are modelled through a limited number of nodes (moments of inertia) connected to each other through shaft elements. The latter are characterized by linear torsional stiffness and damping properties [6, 37, 40, 50]. Fig. 3.2 shows the general layout of a shaftline model.

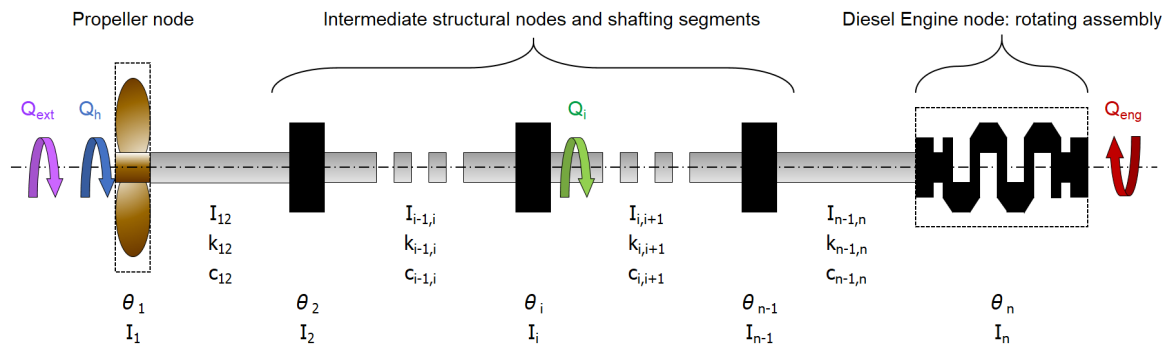


Figure 3.2: Scheme of lumped-element system shaftline.

The equation of motion of the lumped-parameter system can be written as follows:

$$[\mathbf{I}]\ddot{\vec{\theta}} + [\mathbf{C}]\dot{\vec{\theta}} + [\mathbf{K}]\vec{\theta} = \vec{Q} \quad (3.1)$$

where $[\mathbf{I}]$, $[\mathbf{C}]$, $[\mathbf{K}]$ are the torsional inertia, damping, stiffness matrices respectively; $\vec{\theta} = [\theta_1, \dots, \theta_n]^T$ is the vector of the systems' DOFs, and $\vec{Q} = [Q_1, \dots, Q_n]^T$ is the vector of the external torsional excitation terms. From Fig. 3.2, we notice that \vec{Q} consists of (i) the propeller's hydrodynamic torque Q_h ; (ii) generic transient torques Q_{ext} applied to the propeller node; (iii) the Diesel engine's driving torque Q_{eng} ; iv) generic torques Q_i applied to the intermediate nodes that draw power from the propulsion line.

In the following parts, we will present the mathematical models to describe the system's excitation entries in \vec{Q} and the CPP blade angle control; then, the procedure to model the nodes and shafting connections is outlined.

3.2.2. Mathematical model of the Diesel engine driving torque

In the system of Fig. 3.2, the Diesel engine is represented by a single node that includes the inertia contributions associated to all rotating parts, such as the crankshaft, engine flywheels, torsional damper. The overall engine-delivered torque (Q_{eng}) is determined by the superposition of the crank torque ($Q_{\text{cyl}}(\varphi)$) generated by each single cylinder, which includes two components as per Eq. 3.2:

$$Q_{\text{cyl}}(\varphi) = Q_{\text{rec}}(\varphi) + Q_{\text{p}}(\varphi) \quad (3.2)$$

where $Q_{\text{rec}}(\varphi)$ is the crank torque generated by the reciprocating motion of the piston-rod mass, $Q_{\text{p}}(\varphi)$ is the crank torque generated by the fueling, combustion gas pressure, and φ is the crank angle. In this study, we neglect the friction torque generated by the motion along the cylinder liner [31, 59].

3.2.2.1 Reciprocating mass torque

The crank torque generated by the reciprocating motion of the piston-rod $Q_{\text{rec}}(\varphi)$ is obtained from the kinematic and dynamic analysis of a piston-rod system [16, 36, 45]. Fig. 3.3 shows the geometrical configuration in a crank-rod-piston system. By assuming that the reciprocating mass (m_{rec}) includes the piston's mass and half the connecting rod's mass, while the other half of the latter is lumped at the crank pin, we can write Eq. 3.3:

$$Q_{\text{rec}}(\varphi) = \left(\vec{F}_{\text{rec}}(\varphi) \wedge \vec{r} \right) \cdot \hat{z} = -m_{\text{rec}} a_{\text{rec}}(\varphi) r \frac{\sin(\varphi + \beta)}{\cos \beta} \quad (3.3)$$

where $F_{\text{rec}}(\varphi)$ is the inertial force due to the reciprocating motion, \vec{r} is a vector of origin O and magnitude r , \hat{z} is a unitary vector which lays on the crankshaft rotational axis, according to a right-handed coordinate system, φ is the crank angle, and β is the angle between the connecting rod and the vertical direction. The piston's acceleration $a_{\text{rec}}(\varphi)$ is obtained via Eq. 3.4:

$$\begin{aligned}
a_{\text{rec}}(\varphi(t)) &= \ddot{x}(t) \\
&= \frac{d^2}{dt^2} [r(1 - \cos \varphi) + L(1 - \xi)] \\
&= \omega_{\text{eng}}^2 r \left[\cos \varphi \left(1 + \frac{\lambda \cos \varphi}{\xi} \right) + \lambda \sin^2 \varphi \left(\frac{\lambda^2 \cos^2 \varphi}{\xi^3} - \frac{1}{\xi} \right) \right]
\end{aligned} \tag{3.4}$$

where λ is r/L , ξ is defined as $\sqrt{1 - \lambda^2 \sin^2 \varphi}$, and ω_{eng} is the angular rotation rate of the crankshaft, namely $\omega_{\text{eng}} = \dot{\varphi}$.

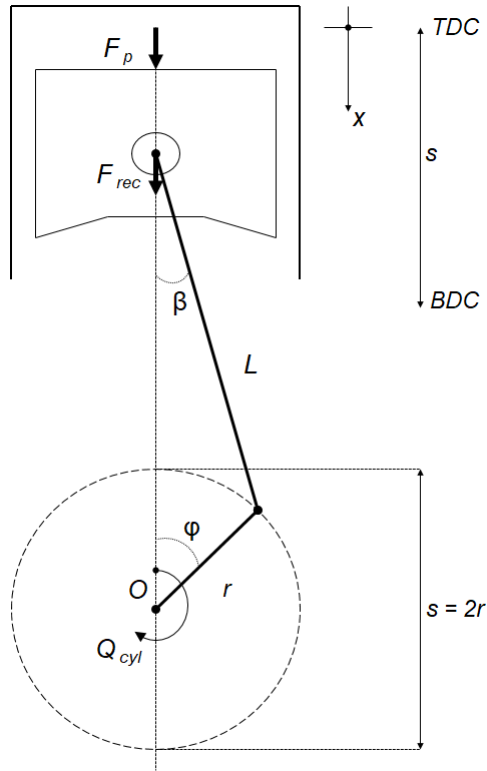


Figure 3.3: Simplified diagram of a piston, connecting rod, crank throw system. x is the piston's coordinate, L is the connecting rod's length, $s = 2r$ is the stroke length and r is the crank radius. φ is the crank angle, and β is the angle between the connecting rod and the vertical direction.

3.2.2.2 Combustion pressure torque

Expressions of $Q_p(\varphi)$ over a 2 or 4-stroke cycle are not generally available to ship designers, so we implemented a procedure to estimate it from the pressure curve $p_{\text{cyl}}(\varphi)$. This method is based on the fitting of two parameters of a piecewise power function. We developed the formulation of $p_{\text{cyl}}(\varphi)$ by considering the characteristics of typical combustion pressure curves retrieved from various engines' technical data, as the one shown in Fig. 3.4. The resulting formulation is presented below:

$$p_{\text{cyl}}(\varphi) = \begin{cases} p_0 + \frac{p_{\text{peak}} - p_0}{\varphi_{\text{peak}}^\alpha} \varphi^\alpha & \text{for } \varphi \in [0, \varphi_{\text{peak}}] \\ p_0 + \frac{p_{\text{peak}} - p_0}{(c\pi - \varphi_{\text{peak}})^\alpha} (c\pi - \varphi)^\alpha & \text{for } \varphi \in]\varphi_{\text{peak}}, c\pi] \end{cases} \quad (3.5)$$

where c is a parameter that equals 2 or 4 if the engine is 2 or 4 stroke type, respectively. The intake pressure value (p_0) is assumed to be constant over the pressure cycle. The combustion peak pressure (p_{peak}) occurs at the crank angle φ_{peak} , slightly after the angular position of the top-dead-center (TDC) [36]. p_0 , p_{peak} , φ_{peak} , and the exponent α depend on the engine relative load (ℓ_P), which is the ratio of the delivered power at a specific power output (P_{eng}) to the engine nominal power ($P_{\text{eng,max}}$) (Eq. 3.6).

$$\ell_P = \frac{P_{\text{eng}}}{P_{\text{eng,max}}} \quad (3.6)$$

Consequently, the parameter set $S_{\text{eng}}(\ell_P) = \{p_0, p_{\text{peak}}, \alpha, \varphi_{\text{peak}}\}$ identifies the curve $p_{\text{cyl}}(\varphi)$ at the engine load condition ℓ_P . As an example, Fig. 3.4(a) shows the combustion

pressure profile for a 4-stroke Diesel engine [35]; besides, Fig. 3.4(b) shows $p_{\text{cyl}}(\varphi)$ for three different ℓ_p cases.

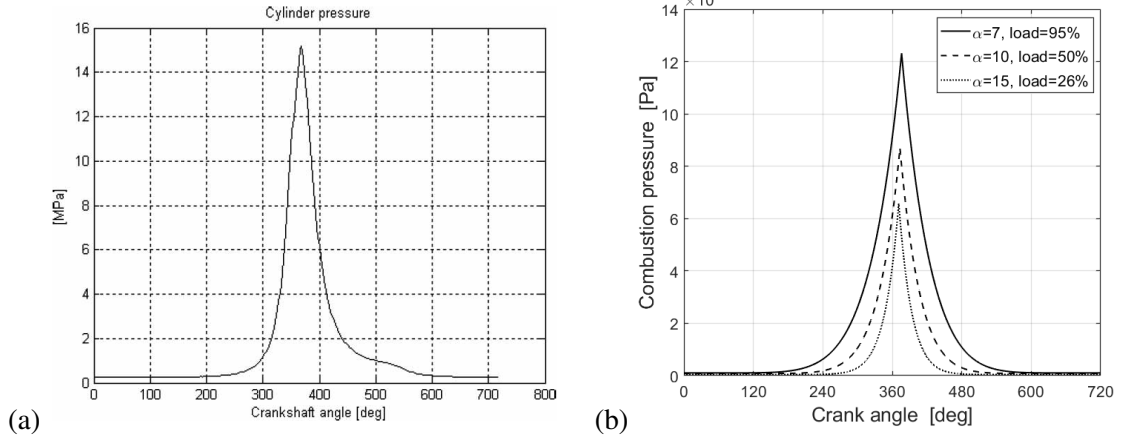


Figure 3.4: Pressure profile from [35] (a) and pressure curve $p_{\text{cyl}}(\varphi)$ as per Eq. 3.5 (b).

Once $p_{\text{cyl}}(\varphi)$ has been determined, we can calculate $Q_p(\varphi)$ as follows:

$$Q_p(\varphi) = \left(\vec{F}_p(\varphi) \wedge \vec{r} \right) \cdot \hat{z} = p_{\text{cyl}}(\varphi) A_{\text{cyl}} r \frac{\sin(\varphi + \beta)}{\cos \beta} \quad (3.7)$$

where $\vec{F}_p(\varphi)$ is the vertical force generated by the combustion pressure and exerted on the sectional area of the cylinder (A_{cyl}).

3.2.2.3 Superposition of the torque components

By combining $Q_{\text{rec}}(\varphi)$ and $Q_p(\varphi)$ we obtain $Q_{\text{cyl}}(\varphi)$ (Eq. 3.2). Fig. 3.5 shows an example of $Q_{\text{cyl}}(\varphi)$ as a function of the crankshaft angle.

The total torque delivered by the engine is calculated as shown in Eq. 3.8:

$$Q_{\text{eng}}(\varphi) = \sum_{i=1}^{n_{\text{cyl}}} Q_{\text{cyl}}(\varphi + \delta_i), \quad \delta_i = \left\{ 0, \frac{c\pi}{n_{\text{cyl}}}, \dots, \frac{c\pi}{n_{\text{cyl}}}(n_{\text{cyl}} - 1) \right\} \text{ [rad]} \quad (3.8)$$

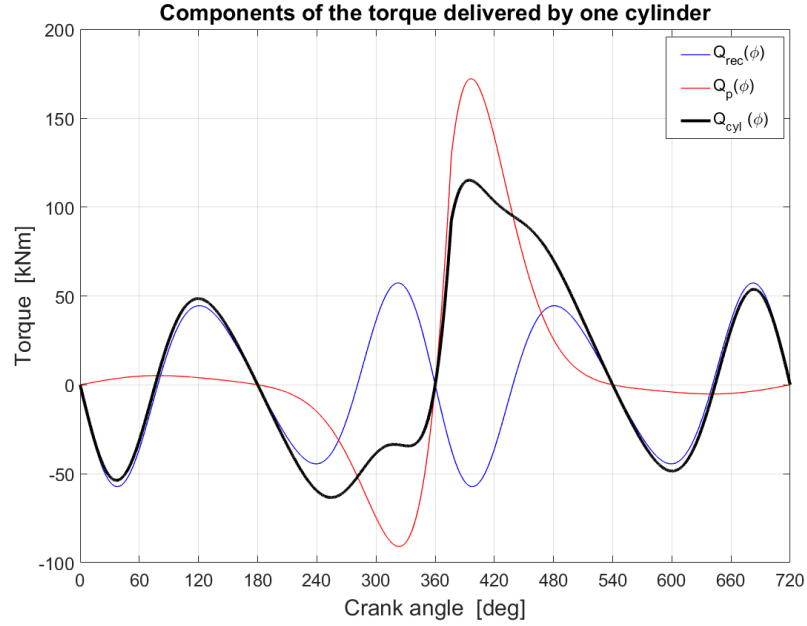


Figure 3.5: Torque delivered by a single cylinder ($Q_{cyl}(\varphi)$), acting on one crank arm. $Q_{rec}(\varphi)$ and $Q_p(\varphi)$ for a 4-stroke engine type. Specifically, $\alpha = 7.3$, $p_0 = 1.0$ bar, $p_{peak} = 123.2$ bar, $\varphi_{peak} = 16.3$ degrees past TDC.

where δ_i is the phase offset, determined by the engine firing sequence. We assume that all cylinders apply an identical torque (Q_{cyl}) to the crankshaft. Fig. 3.6 shows the resulting overall engine torque $Q_{eng}(\varphi)$ (black line). The positive area of the torque is filled in red.

3.2.2.4 Calibration of the Diesel engine's mathematical model

We developed a procedure to evaluate the parameter set $S_{eng}(\ell_P)$ for each given ℓ_P (Fig. 3.7).

The cylinder's intake pressure values (p_0) and combustion peak pressure data (p_{peak}) are usually provided by the Diesel engine manufacturers for multiple ℓ_P , while α and φ_{peak} need to be determined.

To calculate $\alpha(\ell_P)$, we first determine the output power ($P_{eng}(\ell_P)$) through Eq. 3.6. Hence, we calculate the Brake Mean Effective Pressure ($p_{BMEP}(\ell_P)$) [36] as shown in Equation 3.9:

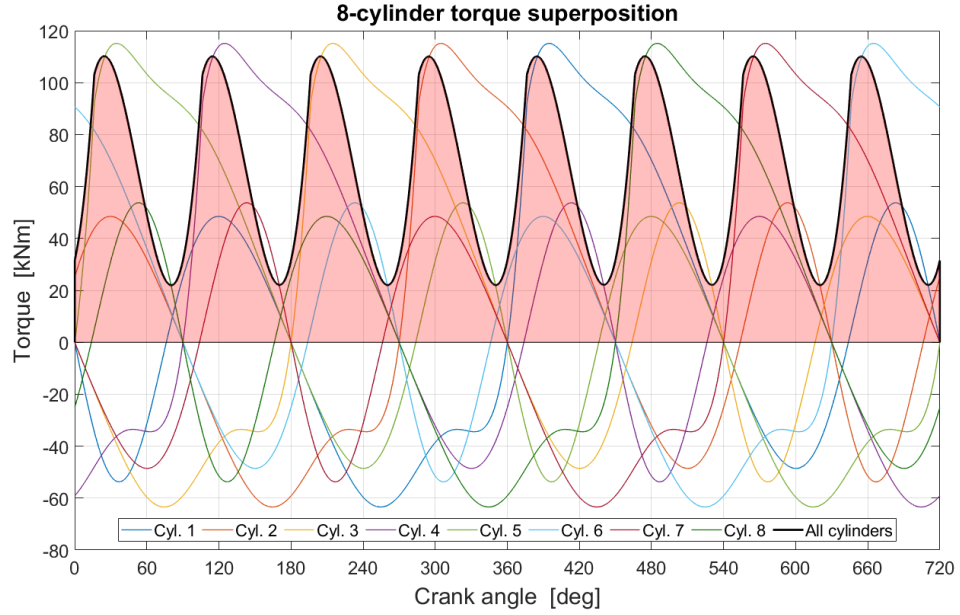


Figure 3.6: Total torque on the engine crankshaft (in black), determined by superposing the cylinder contributions.

$$p_{\text{BMEP}}(\ell_P) = \frac{c}{2} \frac{P_{\text{eng}}(\ell_P)}{n_{\text{cyl}} A_{\text{cyl}} s} \frac{2\pi}{\omega_{\text{eng}}} \quad (3.9)$$

where n_{cyl} is the number of cylinders in the engine.

Since p_{BMEP} is the mean pressure value in the cylinder during one engine cycle, we can write (Eq. 3.10):

$$p_{\text{BMEP}}(\ell_P) = \frac{1}{c\pi} \int_0^{c\pi} p_{\text{cyl}}(\varphi, \ell_P) d\varphi \quad (3.10)$$

which leads to:

$$p_{\text{BMEP}}(\ell_P) = p_0(\ell_P) + \frac{p_{\text{peak}}(\ell_P) - p_0(\ell_P)}{\alpha(\ell_P) + 1} \quad (3.11)$$

$p_{\text{BMEP}}(\ell_P)$ is known from Eq. 3.9; therefore, $\alpha(\ell_P)$ is determined by solving Eq. 3.12

using the value of $p_{\text{BMEP}}(\ell_P)$ just determined:

$$\alpha(\ell_P) = \frac{p_{\text{peak}}(\ell_P) - p_0(\ell_P)}{p_{\text{BMEP}}(\ell_P) - p_0(\ell_P)} - 1 \quad (3.12)$$

Finally, we determine $\varphi_{\text{peak}}(\ell_P)$ through the expression of $P_{\text{eng}}(\ell_P)$, as shown in Eq. 3.13:

$$P_{\text{eng}}(\ell_P) = \omega_{\text{eng}} n_{\text{cyl}} \bar{Q}_p(\ell_P) \quad (3.13)$$

where:

$$\bar{Q}_p(\ell_P) = \frac{1}{c\pi} \int_0^{c\pi} Q_p(\ell_P, \varphi_{\text{peak}}) d\varphi = \frac{A_{\text{cyl}} r}{c\pi} \int_0^{c\pi} p_{\text{cyl}}(\varphi, \ell_P, \varphi_{\text{peak}}) \frac{\sin(\varphi + \beta)}{\cos \beta} d\varphi \quad (3.14)$$

In Eq. 3.13, $\bar{Q}_p(\ell_P)$ is equal to the average overall torque delivered by a cylinder ($\bar{Q}_{\text{cyl}}(\ell_P)$) during a full c -stroke cycle, since the average value of $Q_{\text{rec}}(\varphi, \ell_P)$ is exactly zero across the interval $\varphi \in [0, c\pi]$.

Since $\varphi_{\text{peak}}(\ell_P)$ does not appear explicitly in Eq. 3.14, it was calculated via the Newton-Raphson method.

In addition to the parameter set $S_{\text{eng}}(\ell_P)$, by means of this procedure we obtain curves of each parameter as functions of ℓ_P .

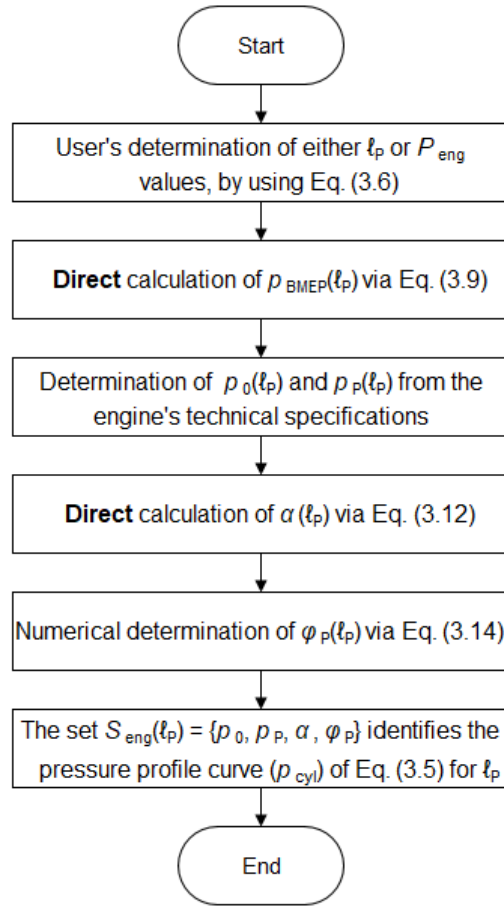


Figure 3.7: Procedure to calibrate the Diesel engine's mathematical model for a chosen ℓ_p .

3.2.2.5 Combustion pressure control

When the steady-state operation of the engine is perturbed, the governor adjusts the fuel injection rate to restore the original balance [36]. In the present work, we simulated the governor through a pure-proportional control that acts on the steady-state combustion peak pressure (\bar{p}_{peak}) [45, 51]. In this controller, the setpoint is the engine nominal speed, ω_{eng} . Hence, we can calculate the instantaneous, updated peak pressure value ($p'_{\text{peak}}(t)$) as a function of the difference between the instantaneous engine angular velocity ($\omega(t)$) and ω_{eng} ($\Delta\omega(t) = \omega(t) - \omega_{\text{eng}}$) (Eq. 3.15):

$$p'_{\text{peak}}(t) = \bar{p}_{\text{peak}} [1 + k_p \Delta\omega(t)] \quad (3.15)$$

where k_p is the instantaneous pressure corrective factor ((rad/s)⁻¹), which is determined by the engine governor specifications.

3.2.3. Propeller hydrodynamic torque characteristics

We simulate the external, torsional hydrodynamic excitation applied to the propeller node in the shaftline model (Fig. 3.2) through the torque Q_h . In detail, we consider Q_h to be a function of the propeller blades' pitch angle (Φ) and the rotational speed (n); in turn, n is a function of time (t).

In steady-state operation at the nominal propeller speed (n_{prop} , rps), the propeller torque $Q_h(\Phi, n_{\text{prop}})$ (Fig. 3.2) can be expressed as follows (Eq. 3.16) [7, 33]:

$$Q_h(\Phi, n_{\text{prop}}) = K_Q(\Phi) \rho n_{\text{prop}}^2 D_{\text{prop}}^5 \quad (3.16)$$

where ρ is the water's mass density, D_{prop} is the propeller diameter, and $K_Q(\Phi)$ is defined as the torque coefficient of the propeller in open water conditions [7, 33]. In our simulation scenario, we consider open-water conditions to define the dynamic Q_h both before and throughout the ice-propeller perturbation [30, 43]. Precisely, we assume that the vessel is initially navigating in uniform, undisturbed wake field; during the ice-milling process, Q_h is considered as a separable load, as described in [25].

Transient perturbations on the propulsion system affect $Q_h(\Phi, n_{\text{prop}})$, which deviates

from its steady-state conditions. Perturbations of the dynamic equilibrium can include changes in the engines' output load, ship manoeuvres, additional external loads applied to the propeller; the hydrodynamic torque exerted on the propeller then fluctuates. To account for this effect, we correct $Q_h(\Phi, n_{\text{prop}})$ by considering the instantaneous rotational speed ($n(t)$). We can write (Eq. 3.17):

$$Q_h(\Phi, t) = Q_h(\Phi, n(t)) = Q_h(\Phi, n_{\text{prop}}) \left(\frac{n(t)}{n_{\text{prop}}} \right)^2 \quad (3.17)$$

3.2.4. Mathematical model of the CPP control

The pitch angle of CPP blades changes accordingly to the absorbed hydrodynamic load, since the dynamic balance with the engine-driving torque and the propeller rotational speed needs to be maintained [7]. In this paper, we used a proportional controller to govern the pitch angle variation during transient propeller speed drops [13]. The correlation between speed change and pitch angle is provided by the propeller manufacturer.

The algorithm we implemented provides an iterative approximation of the value of the pitch angle of the CPP blades. Two quantities need to be considered: the sampling interval of the propeller's discrete control system (Δt_s), and the delay time that is required by the CPP mechanism to effectuate the pitch angle variation from the current state to the future, target state (Δt_m). It is assumed that $\Delta t_s < \Delta t_m$. The following steps and Fig. 3.8 outline the algorithm.

1. At $t = t_0$, the pitch angle equals $\Phi(t_0)$ and the propeller's rotational speed equals $\omega(t_0)$;

2. We calculate the pitch angle for the target state $t_0 + \Delta t_m$: $\Phi(t_0 + \Delta t_m)$, to account for the time lapse of the CPP control;
3. In the time span from $t = t_0$ to $t = t_0 + \Delta t_m$, $\Phi(t)$ changes linearly under the effect of the control system (red path in Fig. 3.8);
4. At $t = t_0 + \Delta t_s$, which occurs before $t = t_0 + \Delta t_m$, a new speed measurement is performed. Thus, the target pitch angle is recalculated, based on the instantaneous speed at $t = t_0 + \Delta t_s$;
5. The target pitch angle is thereby updated: at $t = t_0 + \Delta t_s$ the new target becomes $\Phi(t_0 + \Delta t_s + \Delta t_m)$. Hence, the CPP mechanism undertakes a new path with a new slope, which starts at $t = t_0 + \Delta t_s$ and ends at $t = t_0 + \Delta t_s + \Delta t_m$ (blue path in Fig. 3.8);
6. At $t = t_0 + 2 \Delta t_s$ the controller measures again the speed, determines a new pitch angle target, and so a new variation is superimposed (green path in Fig. 3.8, and then black path likewise);
7. This iterative procedure is repeated throughout the entire simulation.

3.2.5. Modeling procedure for the components of the lumped-element system

To model the displacements of the nodes of the shafting system under the excitation of the engine and propeller torques we just calculated, we follow the procedure employed in [6] and [50], which we briefly summarize hereinafter.

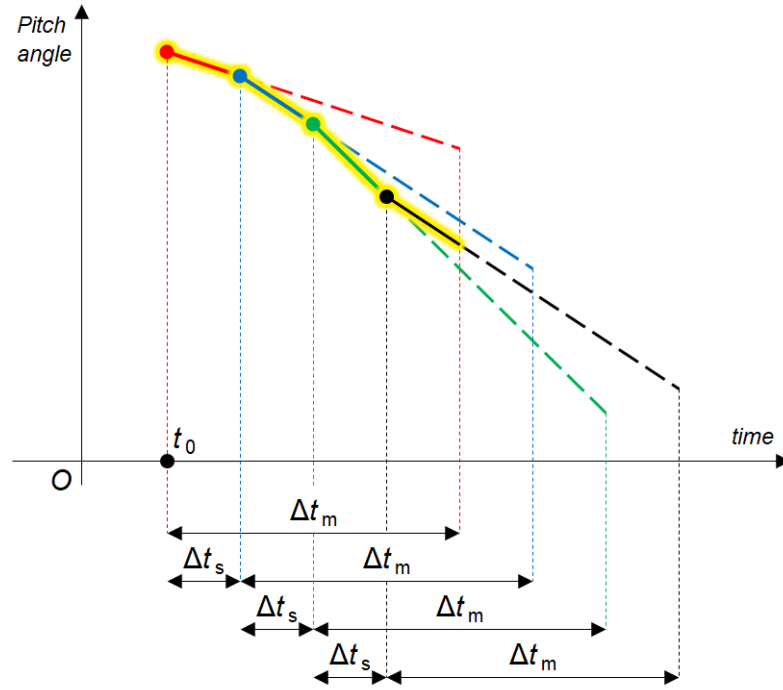


Figure 3.8: Example of graphical representation of the propeller pitch angle variation versus time. The time-domain evolution that actually takes place is highlighted in yellow, while the instantaneous pitch variations calculated by the controller are dashed.

3.2.5.0.1 Node modelling: propeller

The mass moment of inertia of the propeller node (θ_1) is the sum of the mass moment of inertia of the propeller (dry condition), and the contribution of the water's added mass. The added torsional inertia is calculated with the empirical formula of Eq. 3.18 [11, 41]:

$$I_{\text{prop,add}} = 0.0703 g \frac{\rho D_{\text{prop}}^5}{\pi Z} \left(\frac{P_{0.70R}}{D_{\text{prop}}} \right)^2 \left(\frac{A_E}{A_0} \right)^2 \quad [\text{kg.m}^2] \quad (3.18)$$

where g is the gravity acceleration, Z is the number of blades, A_E/A_0 is the expanded area ratio, and $P_{0.70R}$ is the pitch length at the propeller blade section at 70% of the radius.

3.2.5.0.2 Node modelling: engine and gearbox

The inertial properties of the Diesel engine's rotating parts are lumped into a single element. Likewise, the rotating gears of the gearbox are simulated with a single node.

In a branched propulsion system, the gearbox connects two sides of the transmission line that rotate at different speeds. We consider the entire system to rotate according to the propeller-branch, slow speed. Consequently, the inertia, stiffness, damping properties of the engine-branch (subscript F) are converted to their propeller-branch (subscript S) equivalents according to Eq. 3.19 [3, 36, 54]:

$$I_S = \gamma^2 I_F \quad k_S = \gamma^2 k_F \quad c_S = \gamma^2 c_F \quad Q_S = \gamma Q_F \quad (3.19)$$

where γ is the speed reduction ratio between the fast-speed and the slow-speed gears. These quantities are then inserted in the matrices $[\mathbf{I}]$, $[\mathbf{K}]$, $[\mathbf{C}]$, respectively (Eq. 3.1).

The gearbox is composed of multiple gears that rotate at different speeds, therefore the same approach is followed.

3.2.5.0.3 Node modelling: tailshaft flange and flywheel

With regard to the transmission line components such as coupling flanges and flywheels, we calculate their mass moments of inertia by subdividing them into uniform structural components, characterized by their corresponding material properties.

3.2.5.0.4 Shafting segment properties

The inertia of each shafting segment is split in two halves and lumped into the inertia values of two adjacent nodes. The equivalent viscous damping coefficient of the shaft connections is based on the material's hysteresis formulation. Therefore, the torsional stiffness ($k_{i,i+1}$) and damping ($c_{i,i+1}$) coefficients of the i -th shaft, which is comprised between the nodes i and $i + 1$, are calculated according to Eq. 3.20:

$$k_{i,i+1} = G \frac{J_{p,i,i+1}}{l_{i,i+1}} \quad c_{i,i+1} = S_1 \frac{k_{i,i+1}}{\omega_{\text{prop}}} \quad (3.20)$$

where G is the shear modulus of the material, $J_{p,i,i+1}$ is the polar moment of inertia of the shaft sectional area, $l_{i,i+1}$ is the shaft length, ω_{prop} is the shaft nominal angular speed. S_1 is the uni-dimensional damping factor, whose dimensionless value can be assumed as 0.005 for all shafts [1].

3.3. Application to a case study

The presented methodology was implemented on the *Terry Fox*, a heavy icebreaker operated by the Canadian Coast Guard (CCG). We measured the torsional vibrations of its propeller shafts, and used this data to: (i) calculate $Q_h(\Phi, n_{\text{prop}})$ and validate the Diesel engine's torque mathematical model (Subsection 3.3.3.1); and, (ii) update the structural properties of the shaftline model (Subsection 3.3.3.2).

3.3.1. The case study vessel

Table 3.1 reports the main properties of the CCG ship (CCGS) *Terry Fox*, which is depicted in Fig. 3.9. The propulsion plant of the ship consists of two shafting systems that drive two CPPs. Each shaftline is powered by two 4-stroke, 8-cylinder Diesel engines connected to the shaft through a reduction gearbox. A power take-off (PTO) electric generator is connected to the slow gear of each gearbox. Tables 3.2 and 3.3 show the main specifications of the engines and propulsion system elements.



Figure 3.9: CCGS *Terry Fox* in ice-covered waters.

Table 3.1: Main specifications of the CCG heavy icebreaker *Terry Fox*.

Quantity		Value	Unit
Length OA	L_{OA}	88.0	[m]
Beam	B	17.8	[m]
Service draft	d	8.3	[m]
Gross Tonnage	GT	4,234	[GT]
Maximum speed	$V_{S,max}$	16.0	[kn]
Nominal propulsion power	$P_{eng,tot}$	17.3	[MW]
Arctic Class	AC	4	[-]

Table 3.2: Main specifications of CCGS *Terry Fox*'s propulsion system components.

Quantity		Value	Unit
<i>Machinery</i>			
Diesel engine type		8TM410, Stork-Werkspoor	
Engine nominal power, at 100% load	$P_{\text{eng,max}}$	4,265	[kW]
Number of cylinders	n_{cyl}	8	[-]
Engine nominal speed	N_{eng}	600	[rpm]
Gearbox reduction ratio	γ	4.625	[-]
Maximum PTO drawn power	P_{PTO}	1,000	[kW]
PTO rotational speed	$N_{\text{PTO,max}}$	1,200	[rpm]
<i>Controllable Pitch Propeller</i>			
Diameter	D_{prop}	4.800	[m]
Nominal rotational speed	N_{prop}	129.73	[rpm]
Zero-thrust pitch angle at 70% <i>R</i>	Φ_{min}	-0.86	[deg]
Maximum pitch angle at 70% <i>R</i>	Φ_{max}	25.92	[deg]
Expanded blade area ratio	A_{E}/A_0	0.550	[-]
Number of blades	Z	4	[-]

Table 3.3: Detailed specifications of the engine components.

Parameter		Value	Unit
Cylinder bore	b	410	[mm]
Stroke (in-line)	s	470	[mm]
Crank throw radius	r	235	[mm]
Connecting rod length	L	1,140	[mm]
Connecting rod mass	m_{connrod}	427	[kg]
Piston mass	m_{pist}	223	[kg]
Crankshaft mass	m_{crank}	7,700	[kg]

3.3.2. Full-scale measurements

The torsional vibration measurements were performed on December 22-23, 2019, during open-water sea-trials. Fig. 3.10 shows the route undertaken by the vessel. During the tests, the sea state was characterized by an average wind speed of 11 knots and significant wave heights between 2.5 and 3.0 metres, corresponding to a Sea State 4 or 5. The overall wind and wave directions were oriented towards south-west¹.



Figure 3.10: Route of the vessel during the free-running sea trials, on December 22-23, 2019.

3.3.2.1 Instrumentation

To measure the shaft torsional vibrations, we installed two full-bridge torque rosettes on both “Intermediate Shaft 1” segments, precisely in the midpoint between the propeller tailshaft flange and the flywheel (Fig. 3.13). These were two gauges Wheatstone-bridge,

¹Information obtained from the St. John’s buoy datalog, which can be retrieved via the website: https://www.smartatlantic.ca/erddap/tabledap/SMA_st_johns.html

4-resistance, shear-strain rosettes manufactured by VPG Sensors, and they were attached to the shaft surface with the grid pattern at an angle of 45° with the shaft axis, according to [18]. The gauge single coils presented a $350\ \Omega$ resistance, with a gauge factor for both rosettes of $k_g = 2.08$ [18]. Each strain gauge was wired to a differential analog channel input on a wireless data transmitter, which was a V-Link-200 Node[®] device manufactured by LORD Sensing Systems Corporation. The sensor node was interfaced to a laptop through a WSDA-200-USB[®] gateway and it was set up and controlled by the software SensorConnect[®]. For this experiment, we set a $\pm 2.44\ \text{V}$ range for the measured voltage and a wireless transmission power of 10 dBm. Fig. 3.11 shows the layout of the experimental instrumentation and the equipment setup installed on one shaft. Each differential channel of the Node transmitter incorporated an anti-aliasing, 2nd-order Butterworth filter, with cutoff frequency equals to 128 Hz.

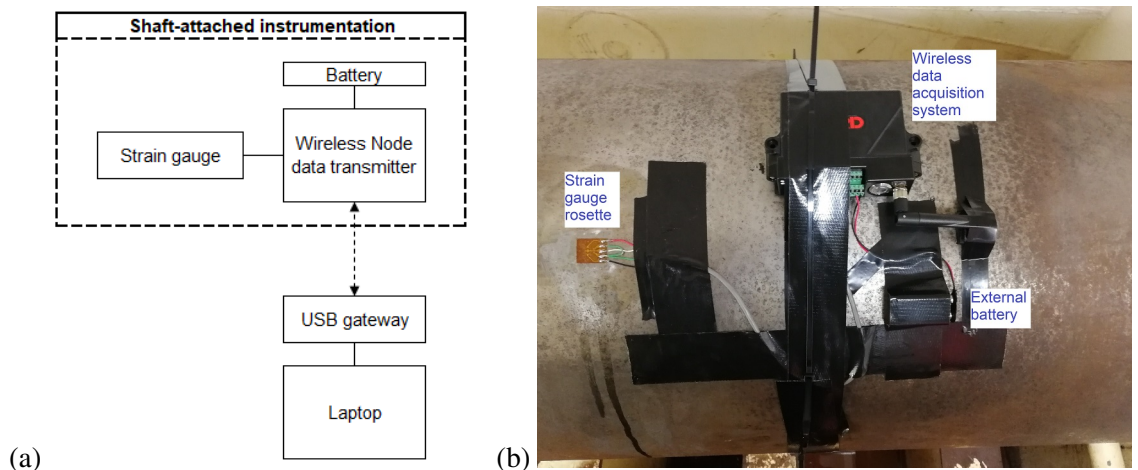


Figure 3.11: Experimental apparatus scheme (a); strain gauge rosette and wireless data transmitter on the shaft (b).

3.3.2.2 Measurement procedure

Before starting the measurements, we calibrated the sensors by using the internal shunt circuit of the sensor node. Data was acquired with a sampling frequency (f_s) of 256 Hz when the engine was operating in steady-state conditions. Multiple engine operation loads (ℓ_p) and corresponding CPP configurations (Φ) were analyzed. The acquired data was then processed in MATLAB®. For each Φ , we calculated the average $\bar{\varepsilon}(\Phi)$ from the measured linear microstrain ($\mu\varepsilon(t)$). Under the assumption of homogeneous and linear elastic material, we can calculate the shaft torque $Q_s(\Phi)$ as shown in Eq. 3.21 [18, 32]:

$$Q_s(\Phi) = \frac{\pi E (d_o^4 - d_i^4)}{16 d_o (1 + \nu)} \bar{\varepsilon}(\Phi) \quad (3.21)$$

where E and ν are the material Young's Modulus and Poisson's ratio respectively, d_o and d_i are the outer and inner shaft diameters respectively.

From Eq. 3.21, we can calculate the shaft power ($P_s(\Phi)$, Eq. 3.22):

$$P_s(\Phi) = Q_s(\Phi) \omega_{\text{prop}} \quad (3.22)$$

3.3.3. Numerical model's validation process

3.3.3.1 Propeller hydrodynamic torque curve and engine's model validation

The hydrodynamic characteristic curves of the CCGS *Terry Fox's* propellers were not available. So, we estimated the hydrodynamic torque absorbed by the propellers from

the results of the full-scale measurements. Since the strain gauges were placed at a short distance from the propeller tailshaft, we assumed that the transmission efficiency associated to that shafting segment equals 1; therefore, we can write Eq. 3.23:

$$Q_h(\Phi, n_{\text{prop}}) = Q_s(\Phi) \quad (3.23)$$

To calculate the power delivered by each engine ($P_{\text{eng}}(\Phi)$), we can write the energy balance on the two sides of the shaftline:

$$2 P_{\text{eng}}(\Phi) \eta_s = P_s(\Phi) + P_m(\Phi) \quad (3.24)$$

where $P_m(\Phi)$ the total power drawn by external machinery units, which are connected to the shaftline, and $\eta_s = 0.98$ is the transmission efficiency of the whole shaftline. We assume that both engines deliver the same power.

Thus:

$$P_{\text{eng}}(\Phi) = \frac{1}{2} \frac{1}{\eta_s} \left(P_s(\Phi) + P_m(\Phi) \right) \quad (3.25)$$

From $P_{\text{eng}}(\Phi)$, we can calculate $\ell_P(\Phi)$ according to Eq. 3.6, and so the four quantities that constitute the parameter set $S_{\text{eng}}(\ell_P(\Phi))$ and are used to create the model of the diesel engine. Using this model, we can calculate the output power ($P_{\text{eng}}^*(\Phi)$) and validate it against the $P_{\text{eng}}(\Phi)$ from Eq. 3.25. Fig. 3.12 illustrates the procedure in flowchart form.

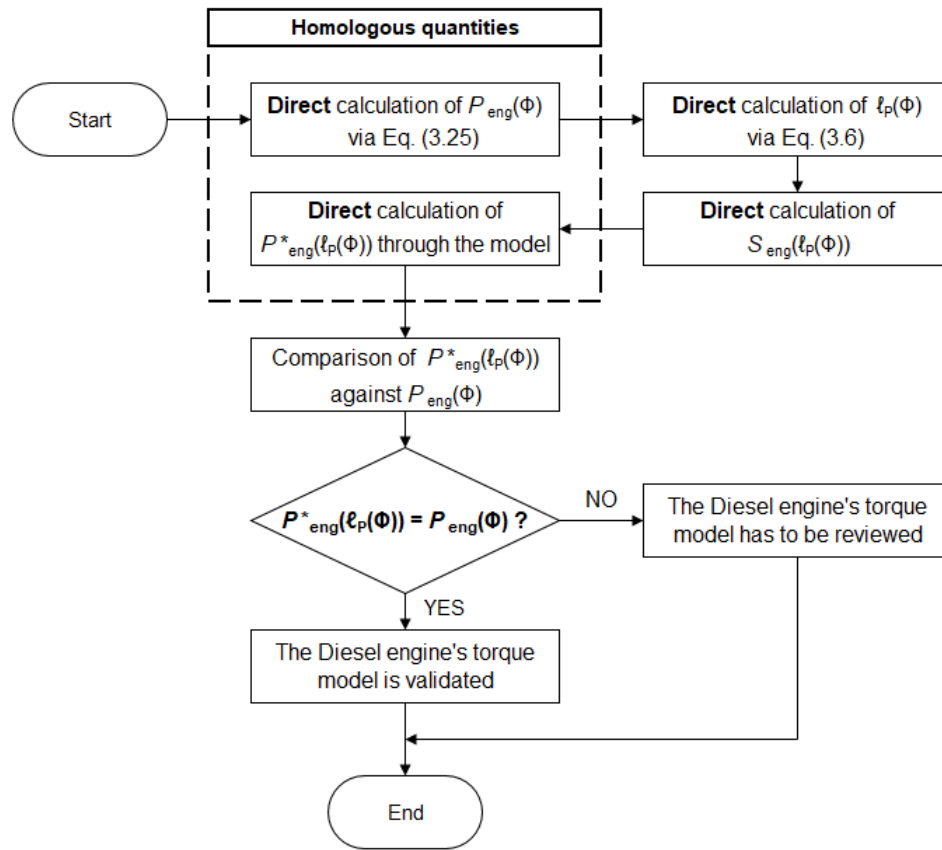


Figure 3.12: Procedure to validate the Diesel engine's mathematical model.

3.3.3.2 Model updating procedure of the lumped-element shaftline model

Fig. 3.13 shows a longitudinal view of CCGS *Terry Fox's* shafting system and the corresponding lumped-parameter model, which is composed of 5 DOFs. The properties of both Diesel engines are merged into the DOF θ_5 .

The model was created by using information on the geometry and material of the shaft system provided by CCG and reported in 3.A. The provided data did not include the gearbox's torsional inertia and the engine-gearbox clutch's stiffness. Therefore, we followed the iterative procedure built on a sensitivity analysis, presented in [6], to update the entries of

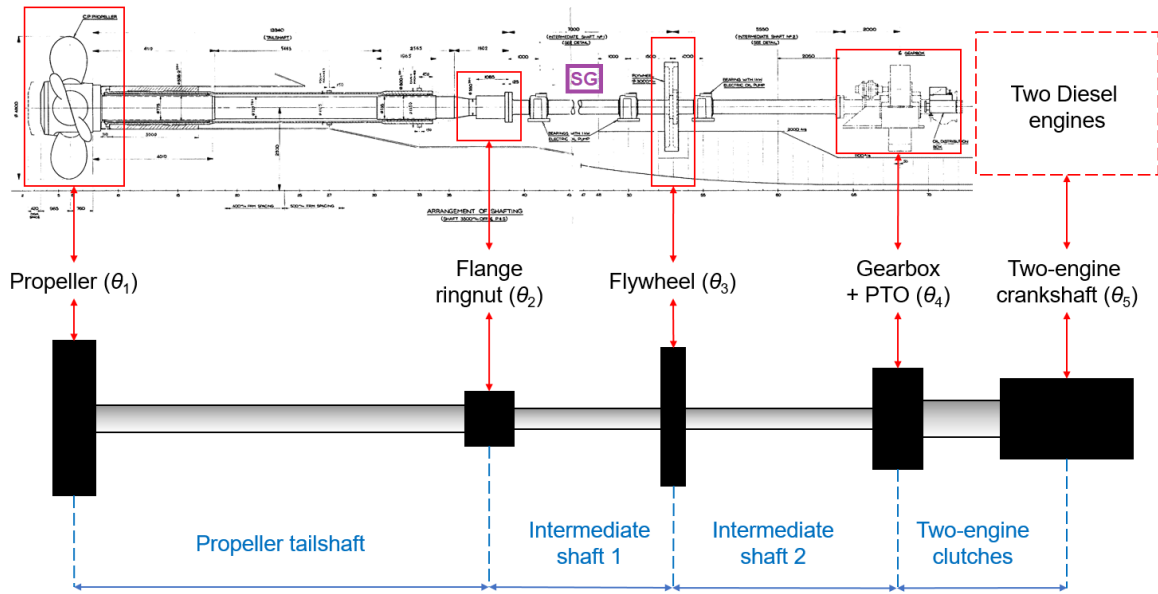


Figure 3.13: Outline of the shaftline model of the case study. The label “SG” indicates the location along the shaftline where the strain gauge was attached.

[**I**] and [**K**] (Eq. 3.1) and make the numerical eigenfrequencies (f_i) match the experimental resonance frequencies (\bar{f}_i) of the shaftline at each Φ step.

3.4. Validation of the numerical models

3.4.1. Shaft torque and power: experimental outcomes

Table 3.4 reports the torque values ($Q_s(\Phi)$) calculated via Eq. 3.21 from both shafts’ experimental data, in six runs during open-water, constant advancement speed conditions.

In the Table, $Q_s(\Phi)$ is the average torque value and $P_s(\Phi)$ is the corresponding average power (Eq. 3.22).

Table 3.4: Measurement-based shaft torque and power values at different CPP scenarios.

Run	Φ [%]	$Q_{s,Port}$ [kNm]	$Q_{s,Stbd}$ [kNm]	Q_s [kNm]	P_s [kW]
1	0	71.66	78.19	74.93	1,020.0
2	15	106.46	90.98	98.72	1,343.9
3	37	132.48	113.73	123.11	1,675.9
4	45	150.57	124.42	137.50	1,871.8
5	50	165.79	150.04	157.92	2,149.8
6	70	231.01	215.58	223.30	3,039.8

3.4.1.1 Propeller's hydrodynamic torque curve

Fig. 3.14 shows the propeller torque curve ($Q_{prop}(\Phi, n_{prop})$, black line) calculated according to Eq. 3.23. The plot also shows the torque values of the two shaftlines (Table 3.4, red and green curves). For $\Phi[\%] = 100\% = \Phi_{max}$, we assumed that the hydrodynamic torque equals the value for the overload condition ($110\% P_{eng,max}$).

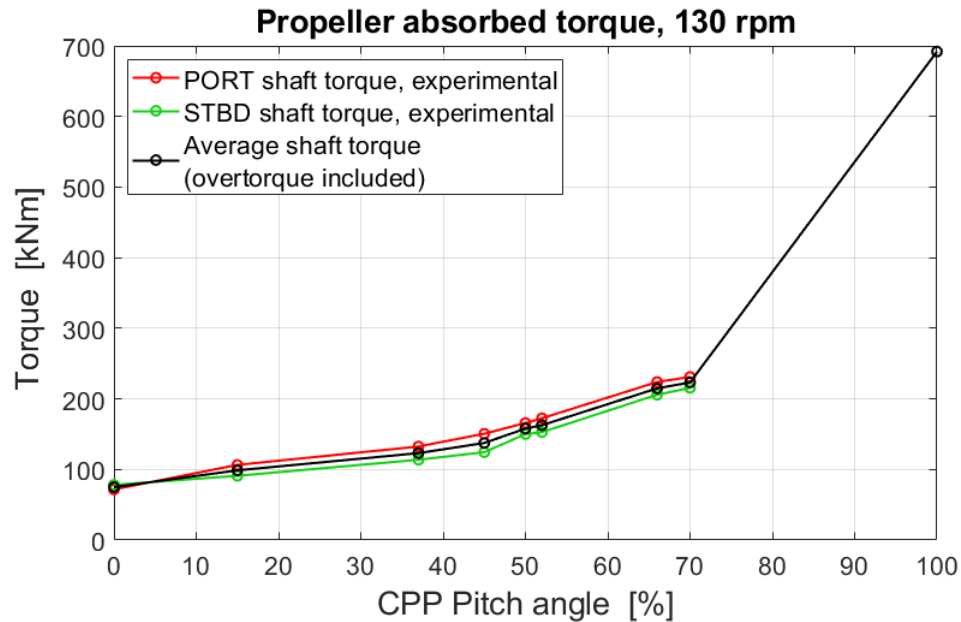


Figure 3.14: Torque absorbed by the propeller at n_{prop} , as a function of Φ ($100\% = \Phi_{max}$).

3.4.2. Validation of the Diesel-engine torque mathematical model

Following the procedure presented in Subsection (3.2.2.4) and Fig. 3.7, we calculated the parameter set $S_{\text{eng}}(\ell_P)$. We used the values of $p_{0,\text{spec}}$ and $p_{\text{peak},\text{spec}}$ provided by the engine manufacturer (Table 3.5) to create regression curves for the cylinder pressure quantities ($p_0(\ell_P)$ and $p_{\text{peak}}(\ell_P)$) and then calculate the other parameters ($\alpha(\ell_P)$ and $\varphi_{\text{peak}}(\ell_P)$). The statistical parameter R^2 was used to select the mathematical pattern that best fitted $p_0(\ell_P)$ and $p_{\text{peak}}(\ell_P)$. Equations 3.26a, 3.26b, 3.26c, 3.26d, 3.26e are the resulting functions.

Table 3.5: Values of $p_{0,\text{spec}}$ and $p_{\text{peak},\text{spec}}$ from the Diesel engine specifications; the data points are provided for 7 $\ell_{P,\text{spec}}$ operating loads.

$\ell_{P,\text{spec}}$	[-]	0.10	0.25	0.50	0.75	0.90	1.00	1.10
$p_{0,\text{spec}}$	[bar]	0.18	0.38	0.76	1.25	1.54	1.72	1.90
$p_{\text{peak},\text{spec}}$	[bar]	51	65	87	110	120	126	133

$$p_{\text{BMEP}}(\ell_P) \text{ [bar]} = 17.183 \ell_P \quad (3.26a)$$

$$p_0(\ell_P) \text{ [bar]} = 0.3285 \ell_P^2 + 1.360 \ell_P + 0.02752 \quad (3.26b)$$

$$p_{\text{peak}}(\ell_P) \text{ [bar]} = -19.16 \ell_P^2 + 105.6 \ell_P + 40.14 \quad (3.26c)$$

$$\alpha(\ell_P) \text{ [-]} = \frac{-19.489 \ell_P^2 + 104.24 \ell_P + 40.112}{-0.3285 \ell_P^2 + 15.823 \ell_P - 0.02752} - 1 \quad (3.26d)$$

$$\varphi_{\text{peak}}(\ell_P) \text{ [deg past TDC]} = -2.172 \ell_P^2 + 10.39 \ell_P + 8.440 \quad (3.26e)$$

For the six data points in Table 3.4, we determined the values of P_{eng} through Eq. 3.25,

and, from them, the corresponding ℓ_P using the values of P_m measured in the case study. We had $P_m = 400$ kW for $\Phi = 0\%$ (run 1), and $P_m = 100$ kW otherwise. Then, we used the model to calculate P_{eng}^* for each ℓ_P value. The data in Table 3.4 refers to low ℓ_P rates. We considered four additional data points characterized by higher ℓ_P rates to validate the Diesel engine model (Table 3.6). This data was acquired during manoeuvring operations, with only one engine engaged to the gearbox. For this reason, this data was not uniquely associated to corresponding Φ values and therefore they were not included in Table 3.4.

Table 3.6 reports the sets $S_{eng}(\ell_P)$ that produce the respective output $P_{eng}^*(\ell_P)$ values through the Diesel engine mathematical model, for the 10 experimental runs. The P_{eng}^* outcomes match very closely the experimental P_{eng} ; $|\Delta P_{eng}|$ falls below the 1% margin of error. The correspondence between $P_{eng}^*(\ell_P)$ and $P_{eng}(\ell_P)$ validates the methodology to determine the Diesel engine's dynamic torque (Subsection 3.2.2).

Table 3.6: Parameters and results from the Diesel-engine model for all CPP scenarios (runs 1-6) and additional operation points (runs 7-10). φ_{peak} is expressed in degrees past TDC; $|\Delta P_{eng}|$ is the absolute value of the relative deviation between $P_{eng}^*(\ell_P)$ and $P_{eng}(\ell_P)$.

Run	ℓ_P [%]	p_0 [bar]	p_{peak} [bar]	α [-]	φ_{peak} [deg _{TDC}]	P_{eng} [kW]	P_{eng}^* [kW]	$ \Delta P_{eng} $ [%]
1	17.0	0.268	57.5	20.6	10.1	723.4	725.7	0.32
2	17.2	0.271	57.7	20.4	10.2	735.3	734.2	0.15
3	21.2	0.331	61.7	17.5	10.6	904.3	902.9	0.15
4	23.5	0.365	63.9	16.3	10.8	1,004.0	998.7	0.53
5	26.9	0.417	67.2	14.9	11.1	1,145.6	1,141.7	0.34
6	37.5	0.584	77.1	12.1	12.0	1,598.7	1,588.7	0.63
7	45.2	0.709	84.0	10.8	12.7	1,917.4	1,928.2	0.56
8	53.4	0.847	91.1	9.8	13.4	2,270.7	2,278.6	0.35
9	70.6	1.151	105.1	8.5	14.7	3,017.2	3,009.2	0.27
10	83.1	1.385	114.7	7.8	15.6	3,557.0	3,545.9	0.31

3.4.3. Model updating

Fig. 3.15 shows the $\mu\epsilon$ spectra for all six CPP configurations. \bar{f}_1 to \bar{f}_4 indicate the four non-zero resonance frequencies of the shaftline.

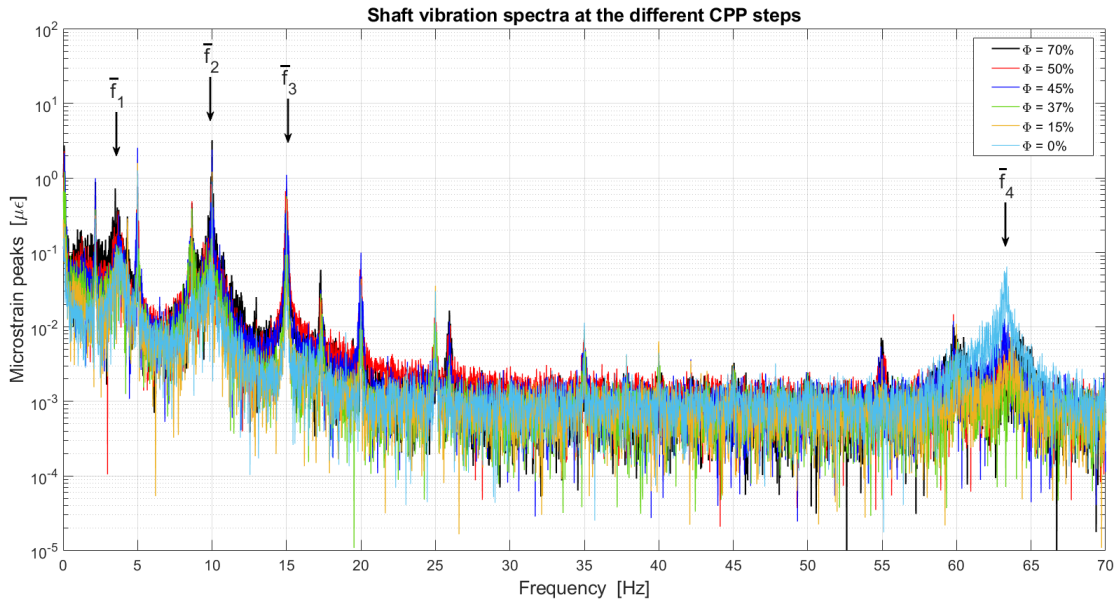


Figure 3.15: Measured microstrain spectra, for all Φ scenarios.

Measured spectra for two relevant operating conditions are shown in Fig. 3.16: $\Phi = 0\%$ (zero-thrust condition), and $\Phi = 45\%$ (the most common operating condition). In the graphs, the rises and peaks of \bar{f}_i are indicated with rectangles in the plots. We also checked that in each Φ step the resonance frequencies of both shaftlines coincide; thereby, the vibration data sets from the two shafts could be considered indiscriminately to characterize the shaftline's numerical model.

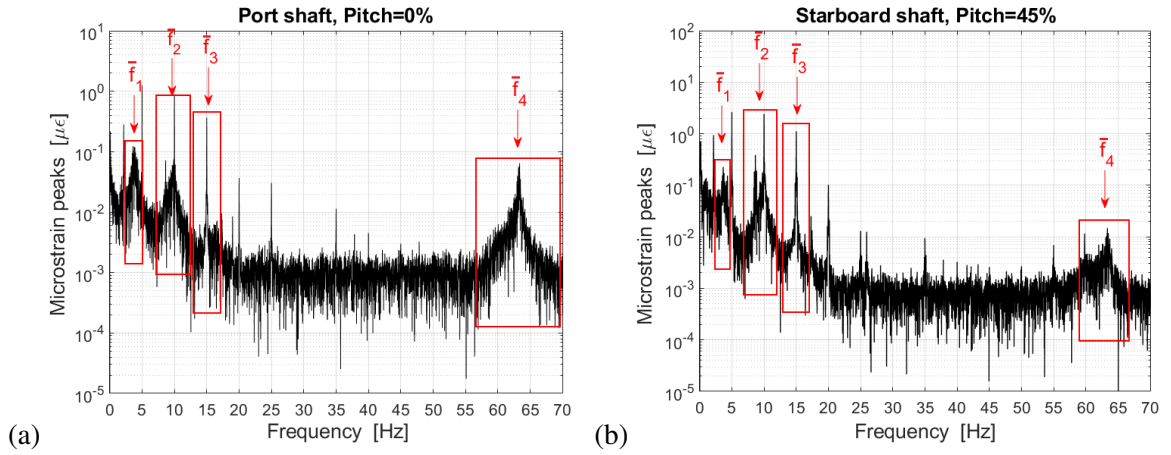


Figure 3.16: Measured microstrain spectra. Port-side, $\Phi = 0\%$ (a); Stbd-side, $\Phi = 45\%$ (b).

Table 3.7 shows the model’s parameters prior and after the updating process. In the Table 3.7, the apex indicates that the inertia value is referred to the single node, without the contribution from the adjacent shaft segments. These are added later to define the terms I_i . $I_{1,\text{add},\Phi}$ is the water added inertia ($I_{1,\text{add},\Phi}$).

Table 3.8 reports the eigenfrequencies for both numerical models—before and after the updating process, the experimental results, and the difference in percentage between updated numerical results and experimental ones (Δf_i). The updating procedure was considered completed when Δf_i the maximum discrepancy between two homologous frequency values not to exceed 5% in order to accept the updated parameters of the numerical model.

Fig. 3.17 shows the five modal shapes of the numerical model for $\Phi = 45\%$. From the results of Table 3.8, we observe that f_1 and f_2 are the two frequencies that change as Φ increases. In Fig. 3.18, the sets of values for f_1 and f_2 are plotted for both the experimental and numerical cases. We notice that as $I_{1,\text{add}}(\Phi)$ increases, both groups of frequencies

Table 3.7: Torsional inertia and stiffness properties of the shaftline model.

Element	Symbol	Initial	Updated
<i>Torsional inertia parameters: nodes [kg.m²]</i>			
Propeller (in air)	$I'_{1,dry}$	33,028	=
Added inertia ($\Phi = 0\%$)	$I_{1,add,0}$	47	=
Added inertia ($\Phi = 15\%$)	$I_{1,add,15}$	637	=
Added inertia ($\Phi = 37\%$)	$I_{1,add,37}$	5,318	=
Added inertia ($\Phi = 45\%$)	$I_{1,add,45}$	8,204	=
Added inertia ($\Phi = 50\%$)	$I_{1,add,50}$	10,357	=
Added inertia ($\Phi = 70\%$)	$I_{1,add,70}$	21,844	=
Flange ringnut	I'_2	520.2	=
Flywheel	I'_3	21,538	=
Gearbox	I'_4	23,892	14,993
Two engines' rotating assembly	I'_5	162,661	=
<i>Torsional inertia parameters: shafting segments [kg.m²]</i>			
Propeller tailshaft	I_{12}	3,362.4	=
Intermediate shaft 1	I_{23}	228.7	=
Intermediate shaft 2	I_{34}	160.1	=
Gearbox-engines connection	I_{45}	28,870	16,241
<i>Torsional stiffness parameters: shafting segments [Nm.rad⁻¹]</i>			
Propeller sterntube and tailshaft	k_{12}	240,366,213	288,439,455
Intermediate shaft 1	k_{23}	57,517,389	60,393,256
Intermediate shaft 2	k_{34}	72,544,452	68,917,229
Gearbox-engines connection	k_{45}	17,091,359	73,994,736

decrease monotonically.

The results shown in Subsection 3.4.3 and summarized in Table 3.8 indicate that updating the uncertain inertial and stiffness terms in the shaftline system led to a f_i correspondence for every vibration mode and Φ step. The fact that only the uncertain parameters were necessary to be significantly updated to tune the experimental \bar{f}_i indicates that the overall modelling process of the propulsion line is reliable.

Table 3.8: Measured resonance frequencies vs. numerical model eigenfrequencies.

Quantity		$(f, \bar{f})_1$	$(f, \bar{f})_2$	$(f, \bar{f})_3$	$(f, \bar{f})_4$
CPP $\Phi = 0\%$					
Numerical, initial	[Hz]	2.44	6.62	13.54	58.43
Numerical, updated	[Hz]	3.93	9.64	15.25	63.27
Experimental (Fig. 3.16(a))	[Hz]	3.80	9.97	14.98	63.37
Δf_i	[%]	3.42	3.31	1.80	0.16
CPP $\Phi = 15\%$					
Numerical, initial	[Hz]	2.43	6.59	13.54	58.40
Numerical, updated	[Hz]	3.91	9.63	15.25	63.24
Experimental	[Hz]	3.77	9.95	15.00	63.20
Δf_i	[%]	3.71	3.22	1.67	0.06
CPP $\Phi = 37\%$					
Numerical, initial	[Hz]	2.38	6.42	13.49	58.26
Numerical, updated	[Hz]	3.76	9.51	15.23	63.08
Experimental	[Hz]	3.73	9.92	15.08	63.15
Δf_i	[%]	0.80	4.13	0.99	0.11
CPP $\Phi = 45\%$					
Numerical, initial	[Hz]	2.35	6.34	13.47	58.19
Numerical, updated	[Hz]	3.69	9.45	15.22	63.00
Experimental (Fig. 3.16(b))	[Hz]	3.71	9.90	15.03	63.33
Δf_i	[%]	0.54	4.55	1.25	0.52
CPP $\Phi = 50\%$					
Numerical, initial	[Hz]	2.32	6.28	13.45	58.14
Numerical, updated	[Hz]	3.63	9.41	15.21	62.95
Experimental	[Hz]	3.67	9.85	15.07	63.40
Δf_i	[%]	1.09	4.47	0.93	0.87
CPP $\Phi = 70\%$					
Numerical, initial	[Hz]	2.22	6.03	13.39	57.95
Numerical, updated	[Hz]	3.39	9.25	15.18	62.73
Experimental	[Hz]	3.50	9.72	15.07	64.87
Δf_i	[%]	3.14	4.84	0.73	3.30

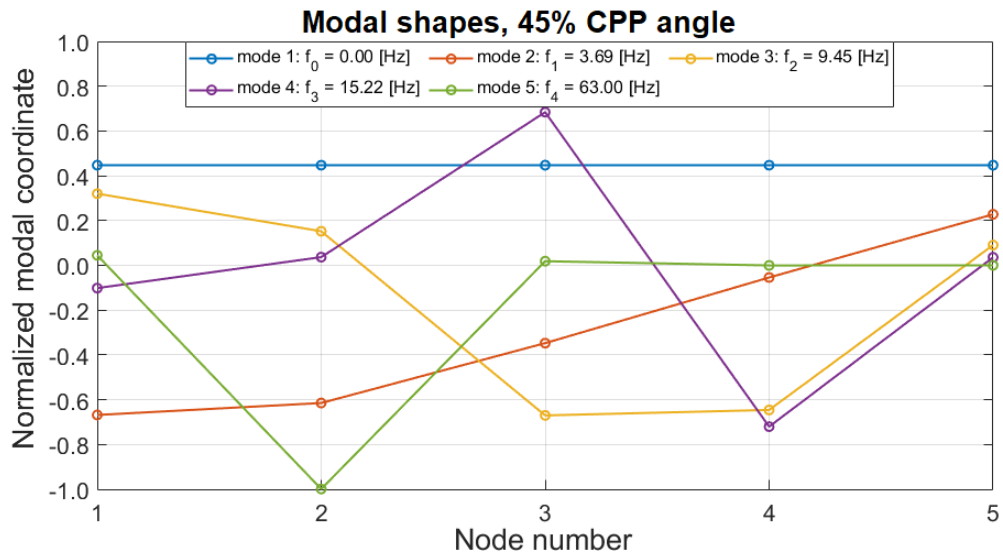


Figure 3.17: Modal shapes of the updated shaftline's model, at $\Phi = 45\%$.

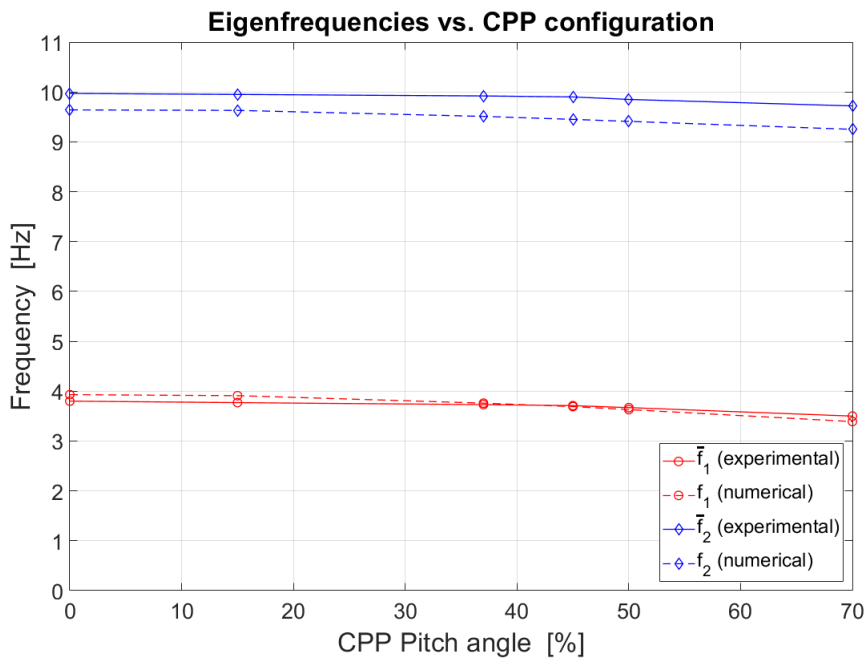


Figure 3.18: Variation of $(f, \bar{f})_1$ and $(f, \bar{f})_2$ as Φ changes.

3.5. Ice-propeller interaction: TVA simulations

To test the effectiveness of the model in simulating TVA, we used the validated model to calculate the shaft's response torque $Q_{\text{resp}}(t)$ under the excitation of an ice-propeller interaction torque ($Q_{\text{ice}}(t)$). The characteristics of the ice-induced propeller torque are included in the IACS Polar Rules [22] and summarized herein in 3.B.

3.5.1. Ice-induced torque

The IACS Polar Rules [22] require that the amplitude of the ice-propeller impact torque (Q_{max}) shall be proportional to the pitch-to-diameter ratio as for the relation below (from Eq. 3.31):

$$Q_{\text{max}} \propto \left(\frac{P_{0.70R,\text{base}}}{D_{\text{prop}}} \right)^{0.16} \quad (3.27)$$

which does not take into account the effect of the variation of Φ , hence $P_{0.70R}$, during the ice-milling event. To overcome this simplification, we determined $Q'_{\text{ice}}(t)$ as follows (Eq. 3.28):

$$Q'_{\text{ice}}(t) = Q_{\text{ice}}(t) \underbrace{\left(\frac{P_{0.70R}(\Phi(t))}{P_{0.70R,\text{base}}} \right)^{0.16}}_{q_{\Phi}(t)} \quad (3.28)$$

The dynamic response torque occurring in the shaft segment between the nodes i and $i + 1$ ($Q_{\text{resp},i,i+1}(t)$) is calculated as follows [47] (Eq. 3.29):

$$Q_{\text{resp},i,i+1}(t) = c_{i,i+1} [\dot{\theta}_i(t) - \dot{\theta}_{i+1}(t)] + k_{i,i+1} [\theta_i(t) - \theta_{i+1}(t)] \quad (3.29)$$

3.5.2. Implementation to the case study vessel

In the simulations, the ice-induced torque applied to the propeller node is characterized by the $PC = 4$ grade and $IC = 2$ type, calculated as per 3.B; this configuration corresponds to the worst-case scenario torque that can be exerted to CCGS *Terry Fox*'s propulsion line.

The simulated event of ice-induced perturbation is 20 seconds long. In particular, during the initial 4 seconds the shaftline is spinning in steady-state conditions; then, at $t = 0$ the ice-propeller excitation takes place. We set the start CPP configuration at $\Phi = 80\%$ of the blade angle range, with $\Delta t_m = 1.50$ [s] and $\Delta t_s = 0.50$ [s] (Subsection 3.2.4) [34]. The gain factor in the $p_{\text{peak}}(t)$ control (Eq. 3.15) is $k_p = 0.025$ [s/rad]. Concerning the superposition of Q_{cyl} from both engines (Eq. 3.8), we assume that the cylinders of the two engines are in phase.

We run two simulations: the first one takes into account the dynamic variation of $\Phi(t)$ (CPP mode), whereas the second one is performed considering the pitch angle locked (FPP mode), as per the IACS Polar Rules, and then we compare the results.

3.5.3. Results

Fig. 3.19 shows the evolution of $\Phi(t)$ and $q_{\Phi}(t)$ —sub-plots (a) and (b), respectively; the actual ice-propeller impact torque ($Q'_{\text{ice}}(t)$) as a result of Eq. 3.28—sub-graphs (c); the variations of the propeller's hydrodynamic torque $Q_h(t)$ and the rotational speed of the

engine node $\omega_{\text{eng}}(t)$ —sub-graphs (d) and (e), respectively. The outcomes are shown for the FPP and CPP modes.

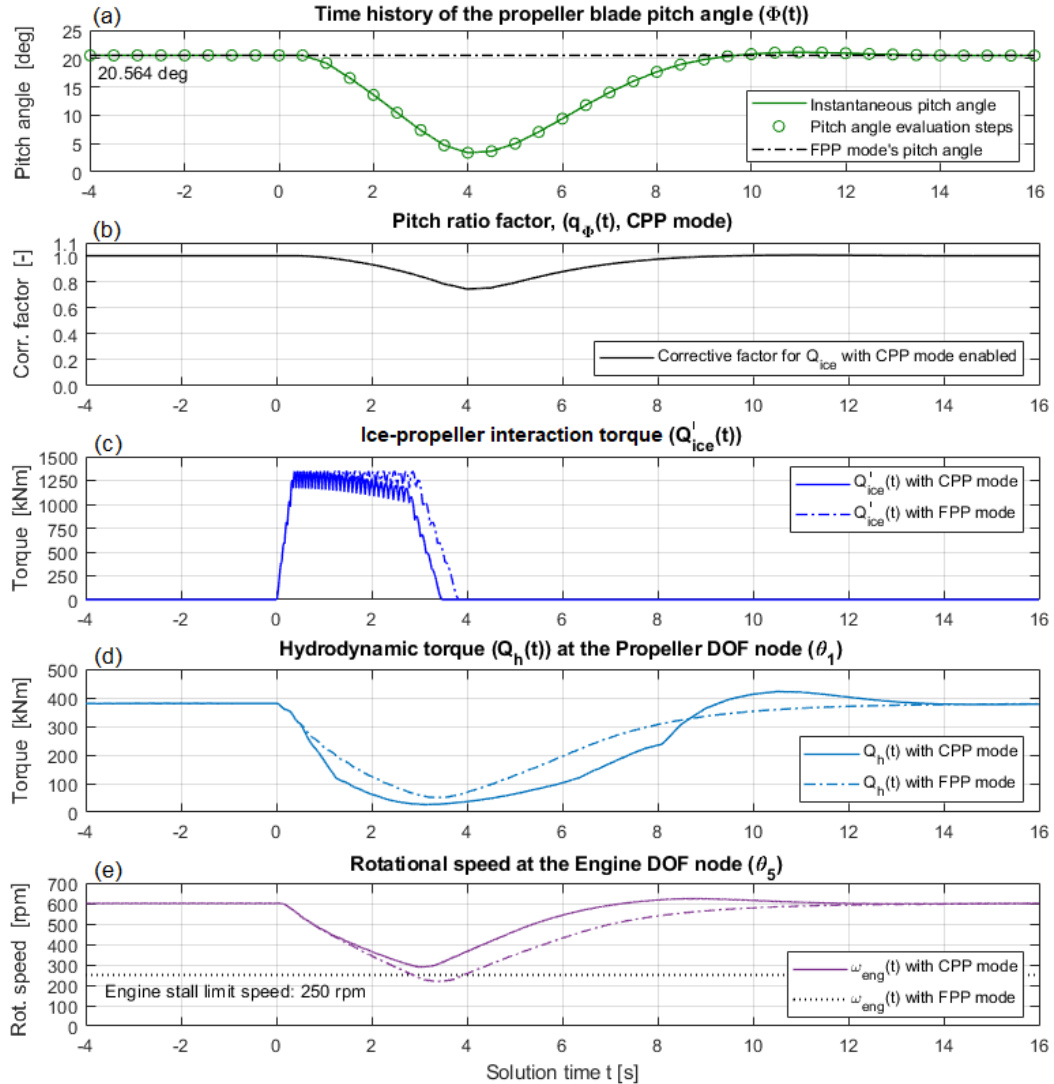


Figure 3.19: Comprehensive plot showing: CPP pitch angle evolution ($\Phi(t)$, (a)), ratio $q_{\Phi}(t)$ (b), propeller torques ($Q'_{\text{ice}}(t)$, (c) and $Q_h(t)$, (d)), engine node speed ($\omega_{\text{eng}}(t)$, (e)).

Fig. 3.20 shows the superposition of $Q_h(t)$ and $Q'_{\text{ice}}(t)$ on the propeller node (blue curves), and the overall Diesel engine torque $Q_{\text{eng}}(t)$ (red curves) for both CPP and FPP modes.

Fig. 3.21 shows the response torques ($Q_{\text{resp}}(t)$) of the three shafting segments between

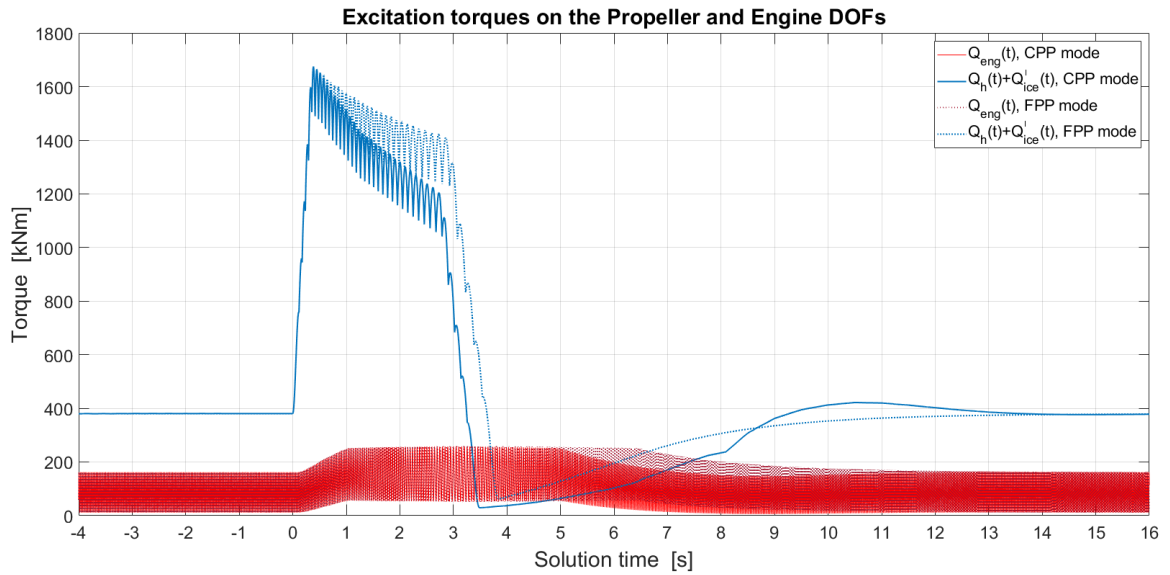


Figure 3.20: Time evolution of the torques acting on the propeller and engine nodes.

the propeller and the gearbox.

Table 3.9 shows the absolute values of the ranges between the maximum and minimum $Q_{\text{resp}}(t)$ in the three shafts, for both simulations. The deviation between each pair of outcomes is also shown. In particular, the $Q_{\text{resp}}(t)$ range is an important parameter that is required by IACS and the Classification Societies, when the shaft torsional strength analysis is concerned.

Table 3.9: Ranges between maximum and minimum shaft response torque.

Shafting segment	DOFs	CPP mode	FPP mode	Difference
		[kNm]	[kNm]	
Propeller tailshaft	1 – 2	1,307	1,318	0.8
Intermediate shaft 1	2 – 3	1,299	1,310	0.9
Intermediate shaft 2	3 – 4	1,171	1,236	5.6

The evolution of $\Phi(t)$ when the CPP mode is enabled is shown in Fig. 3.19(a). Overall, a 16.5-degree excursion of $\Phi(t)$ occurs from the steady-state condition to the minimum pitch

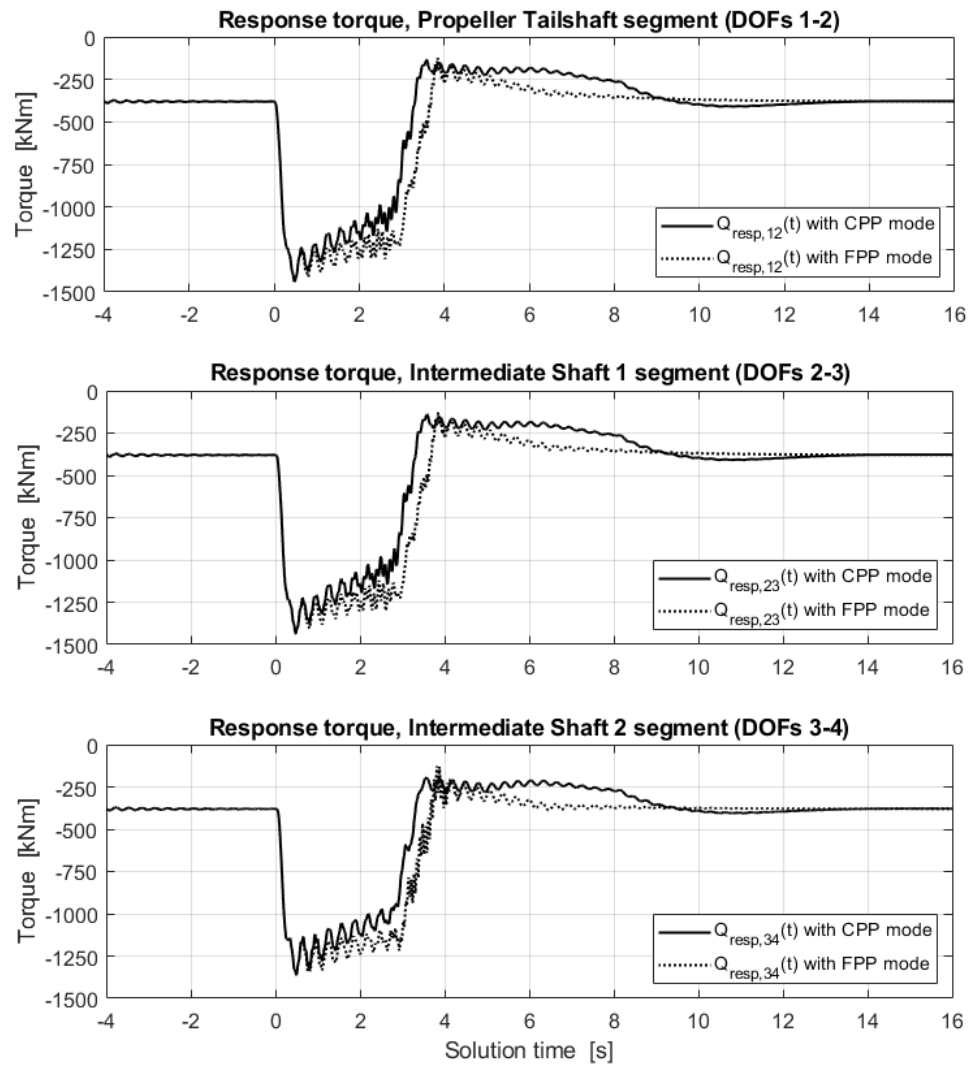


Figure 3.21: Shaft response torque in the segments 1 – 2, 2 – 3, 3 – 4 from both simulations.

angle reached during the ice-propeller interaction. The $q_{\Phi}(t)$ ratio (Fig. 3.19(b)) drops to 0.74 when Φ is at its minimum, and this shows the influence of the CPP variation on the actual ice-propeller load (Fig. 3.19(c)). Fig. 3.19(e) shows the shaft speed drop; here, a crucial difference between the two modes can be noticed: in the FPP mode simulation, the engine speed drops below the stall limit (250 rpm for the simulated diesel engines), whereas when the CPP mode is enabled, the engine speed remains above the limit. Therefore,

during ice-related transient states, taking into account the dynamic evolution of Φ in CPPs is essential to model the ice-propeller excitation and obtain reliable TVA results correctly. An overshoot takes place when the system restores the initial equilibrium, and it is visible for $\Phi(t)$, $Q_h(t)$, and $\omega_{\text{prop}}(t)$ in Figs. 3.19(a),(d),(e). In all cases, the convergence to the equilibrium state is eventually reached without oscillations; this also indicates the good modelling of the engine and CPP controllers.

From Fig. 3.20, we can evaluate the reaction of the engine-delivered torque to counter the ice-induced perturbation on the propeller. The engines reach the maximum combustion pressure state in about 1 second for both simulations; then, when the propeller pitch is locked (FPP mode), the engines maintain the maximum operating point for approximately 1.5 seconds longer than the case with the CPP mode enabled. Afterwards, when the ice-propeller impact process is over, the engine load decreases accordingly until the initial equilibrium with the propeller hydrodynamic load is restored. In the plot, the difference between the two modes' curves for the total torque on the propeller node ($Q_1(t) = Q_h(t) + Q'_{\text{ice}}(t)$) remark the significance of the $\Phi(t)$ effect on the TVA outcomes.

Fig. 3.21 shows the time histories of $Q_{\text{resp}}(t)$ for the three segments of the propeller-side branch of the shaftline. In the initial stages of the ice-propeller excitation, the response torque in the three shafts is approximately the same for both CPP and FPP modes. Subsequently, the $Q_{\text{resp}}(t)$ curves differ significantly between the two simulations; in particular, we can observe that in all three shafts the response torque is more severe in the FPP mode simulation, in which the ice-propeller excitation is higher, coherently. At the end of the transient state, the equilibrium is reached almost simultaneously in both simulations. Concerning the $Q_{\text{resp}}(t)$

ranges, the results reported in Table 3.9 show that no significant differences arise from the two simulations for the first two shafting segments, whereas the range differs by more than 5% in the third segment.

3.6. Discussion

3.6.1. Strengths and limitations

The procedure to model Diesel-driven ship-propulsion systems demonstrated to be effective. To simulate a Diesel-drive marine shaftline, the lumped-element approach guarantees high versatility regarding model development and processing time. In addition, our model to calculate $Q_{\text{eng}}(\varphi)$ can be implemented without the need for exclusive experimental data. Therefore, this modelling approach represents an advantage that improves the tool's flexibility when employed in the ship design process, while maintaining a reliable representation of the Diesel engine delivered torque. As shown in Fig. 3.20, simulating the Diesel engine excitation through a dynamic model maintains the exact relation between each crank's displacement and the time-domain torque phase, as the rotational speed drops. Indeed, modelling Q_{eng} simply through the delivered indicated torque would entail the distortion of the frequency content for the engine output torque.

Besides, we determined the CPP hydrodynamic torque curve ($Q_h(\Phi)$) experimentally because no data concerning the open-water performance of the case study propellers were available. Hence, the $Q_h(\Phi)$ determined in this work can be considered as reference data to simulate analogous CPPs. However, our $Q_h(\Phi)$ curve is limited to the pitch angle range

below $\Phi_{c/o} = 70\%$, and the linear trend in the values $70\% \leq \Phi_{c/o} \leq 100\%$ has been assumed for simplicity. Further measurements would be important to define the curve over the missing range.

Two controls are implemented in the model: the engine cylinder combustion pressure (Subsection 3.2.2.5) and the CPP pitch angle value (Subsection 3.2.4). Both controls have proven essential to model the reaction of the propulsion system against transient perturbations. In the future, additional measurements should be conducted to refine the expression for the engine's combustion pressure control (Eq. 3.15).

The inclusion of the Φ evolution through the CPP controller during transient conditions constitutes a novel concept in the field of ice-propeller interaction TVA. In addition, the CPP control that we introduced features an algorithm easy to be implemented. Specifically, our CPP controller shows a plausible evolution through time, but it has not been validated yet, during real ice-induced perturbations.

Limitations of the lumped-element model of the shaftline include the reduced number of DOFs to represent its dynamics, plus the disregard of the local torsional effects in correspondence of the flanges and bearings. These two aspects of the shaftline dynamics can be achieved through FEA, which is more suitable to simulate structural details.

In our system, we represent the combined engines' inertia through a single node, namely one rigid body with no deformations within the crankshafts. A more detailed comprehension of the torsional dynamics in a crankshaft can be achieved by subdividing it into separate DOFs, as carried out in [35] and [23]. However, the correspondence between the experimental resonance frequencies of the shaftline and the eigenfrequencies of our 5-DOF

model demonstrates that simulating the engine pair into one inertial node is effective when the low-frequency range is concerned.

The pattern of the cylinder's combustion pressure curve ($p_{\text{cyl}}(\varphi)$) produced by the mathematical formulation in Eq. 3.5 has not been validated against specific full-scale measures with the case study engines; this topic constitutes an extension of the work presented in this paper. Nonetheless, considering a plausible shape pressure rise—as $p_{\text{cyl}}(\varphi)$ per Eq. 3.5—over an engine cycle guarantees the representation of the proper harmonics in the spectrum of the Diesel engine excitation.

3.6.2. Future developments

In order to improve the model, full-scale measurements to be acquired during icebreaking operations are necessary. Measuring shaft torsional vibrations induced by ice-propeller impacts leads to two goals: firstly, studying the full-scale, transient $Q_{\text{resp}}(t)$ during ice-milling processes would be useful to compare the experimental data with the predictions of our numerical simulations; secondly, the torsional measures would indicate whether the IACS recommendations provided in [22] are consistent with the full-scale ice-propeller load, and thus if they need to be updated. Furthermore, the numerical simulation of the ice-induced torque can be extended from one single-layer milling to a sequence of multiple ice layers with different thickness values; this would represent the case when separate ice floes impact the propeller in close succession.

Additionally, on-board measurements during icebreaking operations would characterize the engine's and CPP's responses to transient propeller-ice loads. We also aim to improve

the Diesel engine simulation concept: we plan to augment the single Diesel engine node by representing the engine's rotating block as a series of lumped elements corresponding to the piston-crank assemblies of each cylinder. Thereby, the results on the crankshaft nodes produced by the ice-propeller interaction excitation would be useful in predicting critical stresses that could lead to engine failure.

3.7. Conclusions

In this work, we presented a methodology to model Diesel-drive propulsion systems and simulate the torsional dynamics of the shaftline in transient conditions. Specifically, we focused our attention on the ice-induced impact load applied to the propeller. We introduced a novel mathematical model to simulate the dynamic driving torque delivered by Diesel engines; the CPP controller was also modelled. The procedure was applied to the CCGS *Terry Fox*, which was considered as a case study, and validated against experimental data. Finally, we tested the model under an ice-propeller interaction perturbation. The results show the importance of properly simulating the CPP control during the ice-milling and proof the flexibility of the Diesel-engine drive's and shaftline's modelling procedure, which makes the methodology efficient to be employed in the early design stages of new ships.

Acknowledgements

The authors thank Mr. Daniel Oldford from the American Bureau of Shipping (ABS) and Mr. Wayne Lambert from the Canadian Coast Guard (CCG) for their important and kind

contribution to this research activity, which would not have been possible without their support. We also acknowledge the courtesy of the crew members of CCGS *Terry Fox*. This work was supported by the American Bureau of Shipping (ABS) and the Department of Industry, Energy and Technology (IET) of the Government of Newfoundland and Labrador.

Appendices

3.A. Shaftline's main specifications

Table 3.10 reports the primary properties of the shaftline's components and materials.

Table 3.10: Shaftline components: specification, properties, dimensions.

Quantity	Symbol	Value	U.M.
<i>Materials' characteristics</i>			
Steel density	ρ_{steel}	7,850	[kg.m ⁻³]
Steel Young modulus	E	210.0	[GPa]
Steel Poisson ratio	ν	0.27	[-]
Steel shear modulus	G	82.7	[GPa]
Shaft damping factor [1]	S_1	0.005	[-]
Gearbox-engine clutch: relative damping ²	ψ_{clutch}	1.5	[-]
Gearbox-engine clutch: viscous damping ratio	ζ_{clutch}	0.232	[-]
Clutch's nominal stiffness	k_{clutch}	1,750	[kNm.rad ⁻¹]
<i>Shafting segments' dimensions</i>			
Propeller tailshaft: length	L_{1-2}	12.138	[m]
Propeller tailshaft: outer diameter	$d_{o,1-2}$	0.775	[m]
Propeller tailshaft: inner diameter	$d_{i,1-2}$	0.190	[m]
Intermediate shaft 1: length	L_{2-3}	7.000	[m]
Intermediate shaft 1: outer diameter	$d_{o,2-3}$	0.475	[m]
Intermediate shaft 1: inner diameter	$d_{i,2-3}$	0.190	[m]
Intermediate shaft 2: length	L_{3-4}	5.550	[m]
Intermediate shaft 2: outer diameter	$d_{o,3-4}$	0.475	[m]
Intermediate shaft 2: inner diameter	$d_{i,3-4}$	0.190	[m]

²Definition: $\psi = 2\pi \left(\zeta / \sqrt{1 - \zeta^2} \right)$

3.B. Ice-propeller interaction torque

The IACS Polar Rules [22] provide the mathematical characteristics of the ice-induced impact torque ($Q_{ice,IACS}$) exerted on the propeller blades. The pattern outlined by IACS is then adopted by the Classification Societies American Bureau of Shipping (ABS) and Det Norske Veritas (DNV) with minor variants [2, 12]. In this paper, we refer to the ABS-DNV definitions and nomenclature.

$Q_{ice,IACS}$ is a function of the propeller rotational angle φ , and it is obtained by superposing single ice-block impacts, each of those corresponding to the milling process of one propeller blade against an ice layer. One blade passage through the ice is modelled as a semi-sinusoidal function [56]:

$$Q_{ice}(\varphi) = C_q(IC) Q_{max}(PC) \sin\left(\varphi \frac{180^\circ}{\alpha_{ice}(IC)}\right) \quad (3.30)$$

where C_q is a coefficient that depends on the Impact Case (IC , ranging from 1 to 4) and α_{ice} is also based on IC to define the angular span through which the single ice-blade milling process occurs; Fig. 3.22 shows the values of C_q and α_{ice} as IC varies. Q_{max} is the torque amplitude that depends on the main propeller properties and the Polar Class grade (PC , ranging from 1 to 7), as expressed by the following formulae:

$$Q_{\max} = \begin{cases} k_{o,d} \left(1 - \frac{d}{D}\right) \left(\frac{P_{0.7}}{D}\right)^{0.16} (nD)^{0.17} D^3, & D < D_{\text{limit}} \\ 1.9 k_{o,d} \left(1 - \frac{d}{D}\right) \left(\frac{P_{0.7}}{D}\right)^{0.16} H_{\text{ice}}^{1.1} (nD)^{0.17} D^{1.9}, & D \geq D_{\text{limit}} \end{cases} \quad (3.31)$$

where $k_{o,d}$ is a coefficient that depends on both the *PC* notation and whether the propeller is open or ducted; D and d are the propeller's disc and hub diameters, respectively; $P_{0.7}$ is the pitch length at 70% disc radius blade section; n indicates the propeller rotational speed in [rps], or $85\%n$ is taken in case of Diesel-drive FPP; H_{ice} is the design ice layer thickness, which is determined by the *PC* grade. The parameter D_{limit} is proportional to H_{ice} by a coefficient that equals 1.81 or 1.80 whether the propeller is open or ducted, respectively.

The number of modular impacts that compose the full ice-propeller interaction process depends on the ice layer thickness, which in turn is determined by the *PC* grade. Fig. 3.22 shows an example pattern with the 4 Impact Cases of $Q_{\text{ice}}(\varphi)$ for a 4-blade propeller [22]. Additionally, the ABS and DNV introduced the application of a linear rise and descent over the initial and final 270° of the ice-propeller torque impact sequence, respectively [2, 12].

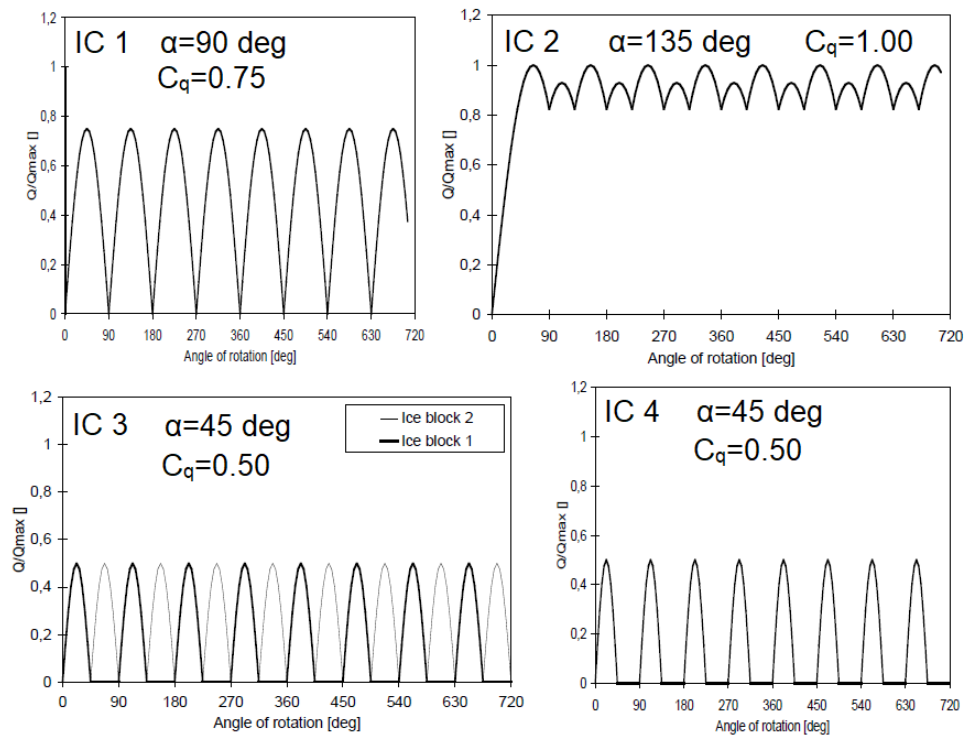


Figure 3.22: Ice-induced torque on a 4-blade propeller. The ABS-DNV notations for the *IC* patterns are used [2, 12, 22].

References

- [1] ABS (2011). ABS Torsional Vibration software - V2.1 - Users Manual. Technical report, American Bureau of Shipping. Updated Nov 2011. 99, 126
- [2] ABS (2019). *Part 6: Specialized Items and Systems, Chapter 1: Strengthening for Navigation in Ice, Section 3: Machinery Requirements for Polar Class Vessels*. Rules for Building and Classing - Marine vessels, American Bureau of Shipping, Edition July 2019. xix, 127, 128, 129
- [3] Adams, M. L. (2010). *Rotating Machinery Vibrations*. Taylor & Francis, 2nd edition. 98
- [4] Batrak, Y. A., Serdjuchenko, A. M., and Tarasenko, A. I. (2012). Calculation of propulsion shafting transient torsional vibration induced by ice impacts on the propeller blades. In *Proceedings of World Maritime Technology Conference (WMTTC)*, Saint Petersburg, Russia. 82

- [5] Bond, J., Hindley, R. J., Kendrick, A., Kämäräinen, J., Kuuliala, L., et al. (2018). Evaluating Risk and Determining Operational Limitations for Ships in Ice. In *OTC Arctic Technology Conference*, Houston, TX, USA. Offshore Technology Conference. 81
- [6] Burella, G., Moro, L., and Oldford, D. (2018). Analysis and validation of a procedure for a lumped model of Polar Class ship shafting systems for transient torsional vibrations. *Journal of Marine Science and Technology*, 23(3):633–646. 82, 84, 96, 106
- [7] Carlton, J. S. (2007). *Marine Propellers and Propulsion*. Butterworth-Heinemann, Elsevier, 2nd edition. 94, 95
- [8] Carrera, G. and Rizzuto, E. (1997). Simulation of mechanical and thermodynamic performances of a ship propulsion plant in transient conditions. In *ASME 1997 Turbo Asia Conference*. American Society of Mechanical Engineers (ASME). 79
- [9] de Waal, R. J. O., Bekker, A., and Heyns, P. S. (2017). Bi-Polar Full Scale Measurements of Operational Loading on Polar Vessel Shaft-lines. In *Proceedings of the 24th International Conference on Port and Ocean Engineering under Arctic Conditions (POAC 2017)*, Busan, South Korea. 81, 82
- [10] de Waal, R. J. O., Bekker, A., and Heyns, P. S. (2018). Indirect load case estimation for propeller-ice moments from shaft line torque measurements. *Cold Regions Science and Technology*, 151:237–248. 82
- [11] Dien, R. and Schwanecke, H. (1973). Die propellerbedingte Wechselwirkung zwischen Schiff und Maschine. *Motortechnische Zeitschrift*, 34(12):425–430. 97
- [12] DNV (2021). *Part 6: Additional Class Notations, Section 7: Polar Class, Par. 11: Ice interaction loads – machinery*, chapter 6: Cold climate. Det Norske Veritas, Edition July 2021. xix, 127, 128, 129
- [13] Dullens, F. P. M. (2009). Modeling and Control of a Controllable Pitch Propeller. Master's thesis, Technische Universiteit Eindhoven. 95
- [14] Gold, P. W., Philipp, T., Schelenz, R., and Buehren, M. (2003). Application of process calculation of the internal combustion engine for the analysis of torsional vibrations in marine drives. In *ASME 2003 Internal Combustion Engine Division Spring Technical Conference*, volume 36789, pages 329–337. American Society of Mechanical Engineers (ASME). 80
- [15] Guerrero, D. P. and Jiménez-Espadafor, F. J. (2019). Torsional system dynamics of low speed diesel engines based on instantaneous torque: Application to engine diagnosis. *Mechanical Systems and Signal Processing*, 116:858–878. 80
- [16] Guzzomi, A. (2007). *Torsional vibration of powertrains: an investigation of some common assumptions*. PhD thesis, University of Western Australia. 80, 86
- [17] Hafner, K. E. (1974). Torsional Stresses of Shafts Caused by Reciprocating Engines Running through Resonance Speeds. In *Mechanical Engineering*, volume 96, pages 58–58. American Society of Mechanical Engineers (ASME). 79

- [18] Hoffmann, K. (2001). Applying the Wheatstone Bridge Circuit. Technical report, Hottinger Baldwin Messtechnik (HBM) GmbH. Version W1569en-1.0. 103, 104
- [19] Huang, Q., Yan, X., Wang, Y., Zhang, C., and Jin, Y. (2016). Numerical and experimental analysis of coupled transverse and longitudinal vibration of a marine propulsion shaft. *Journal of Mechanical Science and Technology*, 30(12):5405–5412. 79
- [20] Huang, Q., Yan, X., Wang, Y., Zhang, C., and Wang, Z. (2017). Numerical modeling and experimental analysis on coupled torsional-longitudinal vibrations of a ship's propeller shaft. *Ocean Engineering*, 136:272–282. 80
- [21] Ikonen, T., Peltokorpi, O., and Karhunen, J. (2015). Inverse ice-induced moment determination on the propeller of an ice-going vessel. *Cold Regions Science and Technology*, 112:1–13. 82
- [22] International Association of Classification Societies (IACS) (2006). Requirements concerning Polar Class - Polar Rules. Rev. 1 Jan 2007, Corr. 1 Oct 2007. xix, 116, 124, 127, 128, 129
- [23] Jenzer, J. and Keller, H. (2003). Torsional vibration and admissible limits in marine propulsion installations. In *ASME 2003 Internal Combustion Engine Division Spring Technical Conference*, pages 289–296. American Society of Mechanical Engineers (ASME). 123
- [24] Kagawa, K., Fujita, K., Hirayama, T., Kokawa, H., and Nagamoto, R. (1986). Vibration of Long-stroke Type Marine Diesel Engine. *Naval Architecture and Ocean Engineering*, 24:211–222. 79
- [25] Khan, A. G., Hisette, Q., Streckwall, H., and Liu, P. (2020). Numerical investigation of propeller-ice interaction effects. *Ocean Engineering*, 216:107716. 81, 94
- [26] Kitagawa, H. et al. (2011). Safety and Regulations of Arctic Shipping. In *The Twenty-first International Offshore and Polar Engineering Conference*. International Society of Offshore and Polar Engineers. 81
- [27] Kujala, P., Goerlandt, F., Way, B., Smith, D., Yang, M., Khan, F., and Veitch, B. (2019). Review of risk-based design for ice-class ships. *Marine Structures*, 63:181–195. 81
- [28] Larsen, O. C. (1981). Some considerations of marine shafting design. *Industrial Lubrication and Tribology*. 78
- [29] Lee, S.-K. (2006). Rational approach to integrate the design of propulsion power and propeller strength for ice ships. *ABS Technical Papers*. Originally presented at the 2006 SNAME ICETECH conference; Banff, Canada, July 16-19, 2006. 81
- [30] Lee, S.-K. (2007). Engineering practice on ice propeller strength assessment based on IACS polar ice rule-URI3. In *10th International Symposium on Practical Design of Ships and Other Floating Structures, ABS Technical Papers*. Citeseer. 94
- [31] Li, W., Guo, Y., Lu, X., Ma, X., He, T., and Zou, D. (2015). Tribological effect of piston ring pack on the crankshaft torsional vibration of diesel engine. *International Journal of Engine Research*, 16(7):908–921. 86

- [32] Lubliner, J. and Papadopoulos, P. (2014). *Introduction to Solid Mechanics - An Integrated Approach*. Springer, New York, USA. 104
- [33] MAN (2011). *Basic Principles of Ship Propulsion*. Frederikshavn, Denmark. MAN Diesel & Turbo. 94
- [34] Martelli, M., Figari, M., Altosole, M., and Vignolo, S. (2014). Controllable pitch propeller actuating mechanism, modelling and simulation. *Journal of Engineering for the Marine Environment*, 228(1):29–43. 117
- [35] Mendes, A. S., Meirelles, P. S., and Zampieri, D. E. (2008). Analysis of torsional vibration in internal combustion: modelling and experimental validation. In *Proceedings of the Institution of Mechanical Engineers Part K Journal of Multi-body Dynamics*, volume 222, pages 155–178. xviii, 79, 80, 89, 123
- [36] Mollenhauer, K. and Tschöke, H. (2010). *Handbook of Diesel Engines*. Springer. 80, 86, 88, 90, 93, 98
- [37] Murawski, L. and Charchalis, A. (2014). Simplified method of torsional vibration calculation of marine power transmission system. *Marine structures*, 39:335–349. 79, 80, 84
- [38] Murawski, L. and Dereszewski, M. (2020). Theoretical and practical backgrounds of monitoring system of ship power transmission systems' torsional vibration. *Journal of Marine Science and Technology*, 25(1):272–284. 79
- [39] Nikolaidis, E., Perakis, A. N., and Parsons, M. G. (1989). Probabilistic torsional vibration analysis of a marine diesel engine shafting system: the level crossing problem. *Journal of Applied Mechanics*, 56:953–959. 79
- [40] Parsons, M. G., Srinivas, J., and Raju, V. (1983). Mode coupling in torsional and longitudinal shafting vibration. *Marine Technology*, 20(3):257–271. 78, 84
- [41] Parsons, M. G., Vorus, W. S., and Richard, E. M. (1980). Added mass and damping of vibrating propellers. Technical report, The University of Michigan. No. 229. 97
- [42] Polić, D., Æsøy, V., and Ehlers, S. (2016). Transient simulation of the propulsion machinery system operating in ice—modeling approach. *Ocean Engineering*, 124:437–449. 80
- [43] Polić, D., Ehlers, S., and Æsøy, V. (2017). Propeller Torque Load and Propeller Shaft Torque Response Correlation During Ice-propeller Interaction. *Journal of Marine Science Applications*, 16(1):1–9. 80, 82, 94
- [44] Polić, D., Ehlers, S., and Æsøy, V. (2019). Inverse modeling approach for transformation of propeller shaft angular deformation and velocity to propeller torque load. *Marine Structures*, 67. 82
- [45] Rakopoulos, C. D. and Giakoumis, E. G. (2009). *Diesel Engine Transient Operation*. Springer. 86, 93

- [46] Rao, D. K. and Sanyal, A. (1980). Torsional vibration of ship engine shafts. *Shock and Vibration Digest*, 12(12):3–8. 78
- [47] Rao, S. S. (2011). *Mechanical Vibrations*. Pearson, 5th edition. 116
- [48] Schiffer, W. and Jenzer, J. (2003). 3-D shafting calculations for marine installations: static and dynamic. In *ASME 2003 Internal Combustion Engine Division Spring Technical Conference*, pages 297–303. American Society of Mechanical Engineers (ASME). 79
- [49] Senjanović, I., Ančić, I., Magazinović, G., Alujević, N., Vladimir, N., and Cho, D.-S. (2019a). Validation of analytical methods for the estimation of the torsional vibrations of ship power transmission systems. *Ocean Engineering*, 184:107–120. 79
- [50] Senjanović, I., Hadžić, N., Murawski, L., Vladimir, N., Alujević, N., and Cho, D.-S. (2019b). Analytical procedures for torsional vibration analysis of ship power transmission system. *Engineering Structures*, 178:227–244. 78, 79, 80, 84, 96
- [51] Sinha, R. P. and Balaji, R. (2018). A mathematical model of marine diesel engine speed control system. *Journal of the Institution of Engineers (India): Series C*, 99(1):63–70. 93
- [52] Suominen, M., Karhunen, J., Bekker, A., Kujala, P., Elo, M., Enlund, H., Saarinen, S., et al. (2013). Full-scale measurements on board PSRV SA Agulhas II in the Baltic Sea. In *Proceedings of the International Conference on Port and Ocean Engineering Under Arctic Conditions*, Espoo, Finland. 81
- [53] Tang, B. and Brennan, M. J. (2013). On the influence of the mode-shapes of a marine propulsion shafting system on the prediction of torsional stresses. *Journal of Marine Science and Technology*, 21(2):209–214. 79
- [54] Tavares, H. F. and Prodonoff, V. (1986). A new approach for gearbox modelling in finite element analyses of torsional vibration of gear-branched propulsion systems. *The Shock and Vibration Bulletin*, (56):117–125. 98
- [55] Tsitsilonis, K.-M. and Theotokatos, G. (2021). A novel method for in-cylinder pressure prediction using the engine instantaneous crankshaft torque. *Proceedings of the Institution of Mechanical Engineers, Part M: Journal of Engineering for the Maritime Environment*. 80
- [56] Veitch, B. (1995). *Predictions of Ice Contact Forces on a Marine Screw Propeller During the Propeller-Ice Cutting Process*. PhD thesis, Helsinki University of Technology, Finland. Acta Polytechnica Scandinavica, Mechanical Engineering Series. 81, 127
- [57] Wang, J., Akinturk, A., and Bose, N. (2006). Numerical prediction of model podded propeller-ice interaction loads. In *25th International Conference on Offshore Mechanics and Arctic Engineering (OMAE2006)*, pages 667–674, Hamburg, Germany. American Society of Mechanical Engineers Digital Collection. 81
- [58] Zhou, X., Qin, L., Chen, K., Niu, W., Jiang, X., Xiong, Y., Quan, J., and Wang, X. (2014). Vibrational Characteristics of a Marine Shaft Coupling System Excited by Propeller Force. In *The 21st International Congress on Sound and Vibration (ICSV21)*, Beijing, China. 78, 79

- [59] Zweiri, Y. H., Whidborne, J. F., and Seneviratne, L. D. (1999). Dynamic simulation of a single-cylinder diesel engine including dynamometer modelling and friction. *Proceedings of the Institution of Mechanical Engineers, Part D: Journal of Automobile Engineering*, 213(4):391–402. 86

Chapter 4

Torsional vibrations of Polar-Class

shaftlines: correlating ice-propeller

interaction torque to sea ice thickness

Abstract

During ship operations in ice-covered waters, propellers often collide with sea ice pieces. This phenomenon represents a severe hazard that affects the torsional stress state of shafting systems and, ultimately, the ship propulsion-system reliability. Even though Classification Societies provide ship designers with design loads and criteria to simulate these events, there are still uncertainties on the actual characteristics of the impacts that ice-class propellers undergo. This paper presents the results of a research activity that combines experimental measurements and numerical analysis to identify the correlation between ice-induced pro-

propeller loads and sea ice conditions. The Canadian Coast Guard (CCG) icebreaker *Henry Larsen* is considered as a case study; we simulate its propulsion shaftline as a lumped-element system and validate this model against full-scale data. A series of numerical simulations to predict the ice-induced impact loads on the propeller were performed by using measured dynamic torque data as the analysis' input. Finally, the resulting values were correlated with the ice thickness data acquired while the ship was navigating. We compare this ice-propeller torque distribution with the homologous quantities calculated as per the current Polar Class framework. The results show that for the study case of this work the torque values obtained from the current regulatory guidelines risk to underestimate the actual ice-propeller interaction torque.

Keywords

Torsional Vibration Analysis; Arctic; Ice-propeller interaction; Ship propulsion systems; Polar Class; Full-scale measurements.

4.1. Introduction

4.1.1. Ice-going vessel design: an overview

Over the last few decades, the expansion of ship operations across the Arctic region has driven the growth in the demand of ice-going vessels [9, 44, 61]. Navigation in Polar regions poses diverse challenges that must be addressed during the ship design and construction processes. Therefore, technical regulations must keep evolving to provide the industry

updated design tools and guidelines [34, 38]. In particular, research has been advancing on risk-based analysis methods: this branch aims to support the design process by assessing the ship's operational reliability, which is connected to the environmental scenario where the vessel is operating [8, 20, 39]. The increase of marine traffic across the Arctic Ocean has also arisen concerns regarding pollution and exhaust emission issues, whose effects have been worsening over the last decades [10, 22, 54]. Reviews on the evolution of the environmental sustainability requirements for ice-going vessels can be found in [26] and [48]. Overall, the concurrent evolution of on-board safety requirements, ship design methodologies, and pollutant emission criteria aim at the common goal of improving the economic sustainability of Arctic shipping [59].

The Polar Code developed by the International Maritime Organization (IMO), together with the Polar Rules by the International Association of Classification Societies (IACS), shapes the primary regulatory framework in which ice-going vessels are currently classified [30, 31]. In particular, the IACS Polar Rules are more focused on regulations to be applied to ship structures and machinery design. Propulsion plants play a role of foremost importance among the systems on-board vessels, as their reliability is crucial for the vessels' safety. On this matter, the studies [32] and [24] discuss recent applications of the azimuthing propulsors for expedition ships and cruise vessels intended to operate in polar environments, showing that such propulsive solution enhances the reliability of the system during manoeuvring operations in ice-covered waters [24, 32].

Full-scale measurements and ice monitoring aboard Polar vessels play a significant role for the development of regulatory frameworks and the ship-design standards [26, 35, 38].

4.1.2. Experimental works on board ice-going ships

Over the recent decades, research has been conducted to study the effects of ice-induced perturbations on marine propellers, shafting systems, and ship structures through full-scale measurements. Experimental campaigns on different types of ice-going vessels took place to investigate multiple aspects of ship-ice interaction phenomena. In particular, Jussila and Koskinen arranged a novel long-running, full-scale measurement system to study the ice-induced impact loads on the blades of a Controllable-Pitch type propeller (CPP) [33]. Williams et al. considered the CCG icebreaker *Henry Larsen* during level ice navigation; in their work, the authors monitored the propulsion performance of the ship during different operational conditions [58]. Also, Dahler et al. investigated the case of an Arctic-Class bulk carrier; the authors used their experimental results to calibrate a simulation tool for the shaftline's vibration analysis, which included the dynamics of the vessel's two-stroke engine [14]. More recently, de Waal et al. carried out an extensive vibration measurement campaign on two Antarctic-going ships; torsional strain gauges and accelerometers were employed to detect short-term, isolated ice-propeller crushing events [15, 16]. A statistical analysis on the ice load peak distribution was performed in [15], and the authors analyzed in detail the shaft torque data to estimate the ice-propeller excitation [16]. In addition, the authors studied the contribution of the propeller-blade cavitation on the ice-induced rotational dynamics of the shafting system [17].

In-the-field measurements of the ice's main physical properties are essential to frame the environmental conditions during ice navigation. High-precision equipment and software

were often employed to achieve three-dimensional images of the ice floes [46, 57]. On the other hand, Lensu et al. focused more on the sole thickness parameter to characterize different ice scenarios [40]. Multiple ice properties such as type, shape, age, concentration were measured and analyzed in [42] and [57]. Hughes developed a monitoring system that integrates radar sensors and satellite imaging to provide real-time information to assist navigation in ice-covered waters [28]. However, the ice-ship interaction measurements are disregarded in these works: the ice-induced loads calculated are not linked to the concurrent sea ice monitoring.

Experimental data has also been used to validate numerical models that simulate propeller-shaft torsional vibration.

4.1.3. Ice-propeller interaction and shaftline modeling

In the research activity by de Waal et al., the authors employed shaft vibration data in numerical simulations to calculate the ice-induced excitation on propeller's blades. The shafting system of the vessel was simulated as a lumped-element model with limited Degrees Of Freedom (DOF); then, the dynamic matrix equation of the system was manipulated to test the effectiveness of selected time-domain numerical algorithms—originally presented and investigated in [29]—with experimental data [16]. The implementation of time-domain methods may require a high computational effort, both for the equation-solving process and for the tuning process of the numerical solvers [25, 29]. Besides, Kinnunen et al. investigated the case of a Z-drive propeller system connected to an Electric motor; MATLAB® Simscape was used to simulate the transmission system, and the numerical outcomes were compared

with the torque and speed readings acquired during full-scale measurements [37].

Polić et al. modeled a Diesel-drive shafting system and its torsional excitation by using Bond-Graph (BG) elements [50, 51]. The assumed ice-propeller torque referred to the IACS formulations [30]. Then, the BG-based model was validated with Finite Element Analysis (FEA), which provided additional indications on the model setup [49]. Hence, the authors presented an inverse algorithm to transform the measured torsional displacement vibration signals into the ice-induced transient load [52].

Other studies approached the ice-shaftline TVA problem purely numerically. Examples can be found in [6] and [7], where the authors employed a specific CAE software to simulate the response of a Diesel-drive shaftline to ice-propeller loads. Also, Burella et al. performed a sensitivity analysis via FEA on the structural properties of CCGS *Henry Larsen*'s electric-drive shaftline, in relation to the ice-induced shaft torsional response [11, 12].

4.1.4. Contribution of the present work

This paper aims to determine a correlation between ice-induced torque peaks on marine propellers and the average ice block thickness during ice navigation. As a case study, we consider the CCG icebreaker *Henry Larsen*, which is equipped with an integrated measurement system that synchronously acquires visual imaging of sea ice scenarios as well as shaft thrust, torque, and speed data. The system arrangement was devised throughout a joint research collaboration that involves Memorial University of Newfoundland (MUN, St. John's NL, Canada) and National Research Council - Ocean, Coastal and River Engineering Research Centre (NRC-OCRE, St. John's NL, Canada).

First, we finalize the preliminary work done in [12] by refining a lumped-element numerical model to simulate the torsional dynamics of the vessel's shaftline. The model is updated via full-scale vibration data acquired in open-water, steady-state conditions. Next, we develop a procedure that uses the experimental shaft torque data and the numerical model to calculate the full-scale ice-propeller interaction torque.

Finally, the resulting ice-propeller torque peaks are matched to the simultaneous ice thickness data, determined from the video recording processing; hence, we conduct a statistical analysis to seek their correlation. Afterwards, our findings are compared with the IACS characterization of the ice-propeller interaction as a function of ice layer thickness [30].

4.2. Methods

Fig. 4.1 shows the layout of the present work.

First, we delineate the procedure to model the case study shaftline; then, we describe the experimental equipment utilized for the full-scale measurements in open-water sea trials and the procedure to update the shaftline model's properties (Subsection 4.2.2).

In Subsection 4.2.3, we outline the characteristics of the integrated measurement system installed on board the vessel. Afterwards, the methodology to process the experimental dataset is described.

In Subsection 4.2.4, we present our mathematical algorithm that delivers the actual ice-propeller interaction torque as output by using experimental shaft response torque data as input.

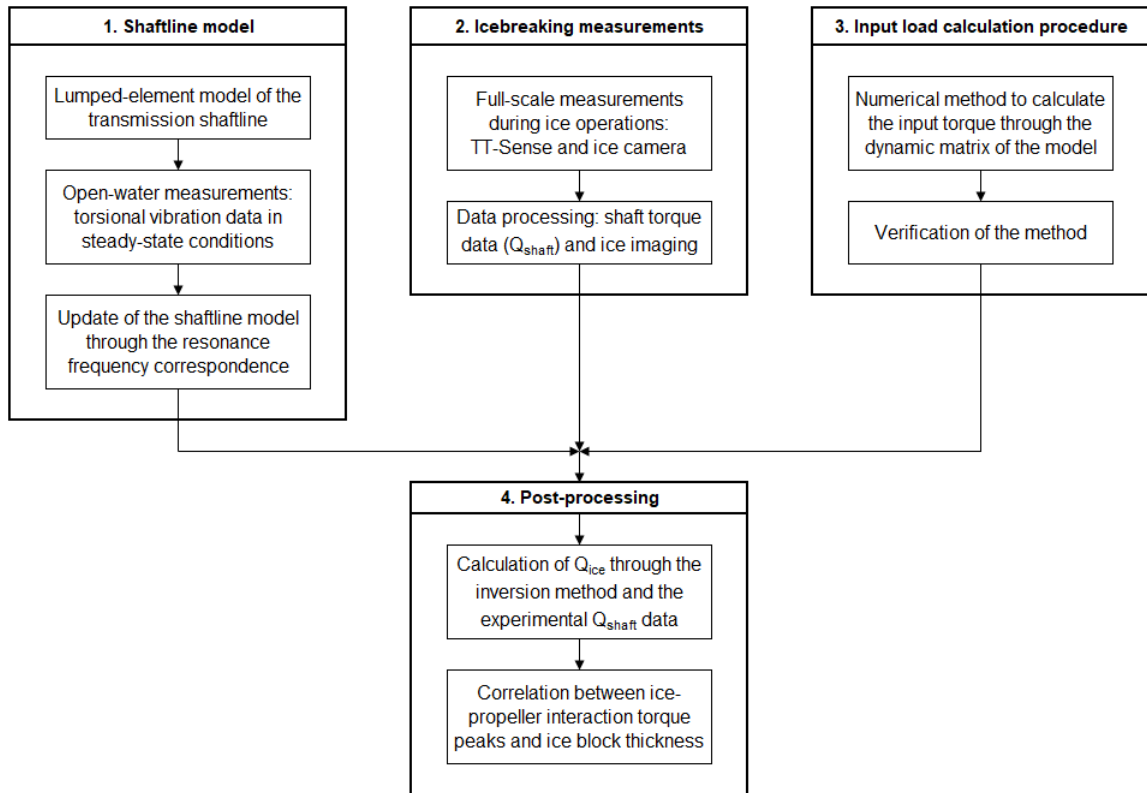


Figure 4.1: Flowchart illustrating the paper outline.

In Subsection 4.2.5, the full-scale, ice-propeller torque data are calculated by means of the method described in Subsection 4.2.4. Finally, we work out the correlation between ice-induced propeller torque peaks and average ice block thickness. The outcomes are then discussed in relation to the current Rules' recommendations.

4.2.1. Case study

The vessel considered in this work is the medium icebreaker CCG Ship (CCGS) *Henry Larsen* (Fig. 4.2). The ship is equipped with two 4-blade Fixed-Pitch propellers (FPPs); the propulsion plant is a Diesel-Electric system that consists of three Wärtsilä Vasa 16V32 Diesel engines and two General Electric synchronous motors, which are the prime movers

of the two shaftlines. Table 4.1 summarizes the main characteristics of the ship.

Table 4.1: Main specifications of the CCG icebreaker *Henry Larsen*.

Quantity		Value	Unit
Length OA	L_{OA}	99.8	[m]
Beam	B	19.6	[m]
Service draft	d	7.3	[m]
Gross Tonnage	GT	6,167	[GT]
Maximum speed	$V_{S,max}$	16.0	[kn]
Nominal propulsion power	$P_{ED,max}$	12.2	[MW]
Propeller diameter	D	4.120	[m]
Propeller blade number	Z	4	[-]
Arctic Class	AC	4	[-]



Figure 4.2: CCGS *Henry Larsen* at sea.

4.2.2. Shaftline model: development and validation

4.2.2.1 Numerical model outline: structural elements

We adopted the lumped-element approach to develop a MATLAB numerical model that simulates CCGS *Henry Larsen*'s shaftline torsional dynamics [11, 12]. Specifically, the

nodes are associated with the major structural components of the shafting system [45, 47]. The shafting segments between the nodes incorporate linear torsional stiffness and damping properties.

The subdivision of the shaftline considered herein was first introduced in [12]. Fig. 4.3 outlines the icebreaker's shaftline model, which is simulated with 9 DOFs. Also, the drawing shows the locations of the torsional strain gauge and the optical thrust-torque meter, both employed for the on-board measurement sessions.

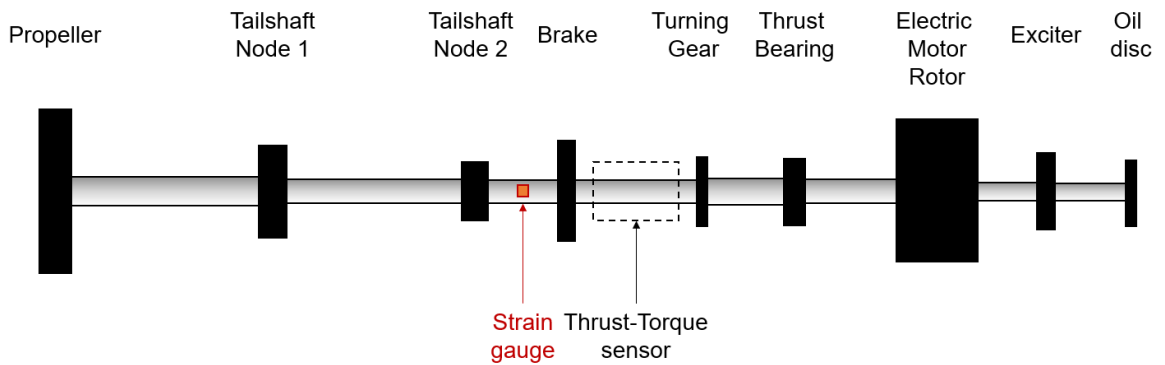


Figure 4.3: Lumped-element system for CCGS *Henry Larsen*'s shaftline.

Since our numerical model is linear, the dynamic matrix equation of the system can be formulated as follows:

$$[\mathbf{I}]\ddot{\vec{\theta}} + [\mathbf{C}]\dot{\vec{\theta}} + [\mathbf{K}]\vec{\theta} = \vec{Q} \quad (4.1)$$

where $[\mathbf{I}]$, $[\mathbf{C}]$, $[\mathbf{K}]$ are the torsional inertia, damping, stiffness matrices respectively; $\vec{\theta} = [\theta_1, \dots, \theta_9]^T$ and $\vec{Q} = [Q_1, \dots, Q_9]^T$ are the DOF and excitation torque vectors, respectively.

The propeller is simulated as a single node (θ_1), which includes both its mass moment of

inertia in air and the water's added inertia. We used the formula provided in [18] to calculate the added mass, as it was implemented in [55] and [60]. Similarly, the rotor block of the electric motor is simulated as a single node (θ_7). The other inertial nodes were modeled as done in [12].

The inertia of each shaft is evenly split: the two half-inertia values are incorporated into the moments of inertia of the two adjacent nodes. Regarding the determination of the shafts' stiffness coefficients, the characteristics of each segment's material are assumed to be linear elastic [3]. The equivalent viscous damping coefficient of the shaft connections are calculated by adopting the expression related to the material's hysteresis. Therefore, the torsional stiffness ($k_{i,i+1}$) and damping ($c_{i,i+1}$) constants of the i -th shaft, which connects the nodes i and $i + 1$, are modeled as follows:

$$k_{i,i+1} = G \frac{J_{P,i,i+1}}{l_{i,i+1}} \quad c_{i,i+1} = S_1 \frac{k_{i,i+1}}{\omega_{\text{prop}}} \quad (4.2)$$

where G is the shear modulus of the material, $J_{P,i,i+1}$ is the polar moment of inertia of the shaft sectional area, $l_{i,i+1}$ is the shaft length, ω_{prop} is the shaft nominal angular speed. S_1 is the uni-dimensional damping factor, whose dimensionless value can be assumed as 0.005 for all shafts [1].

4.2.2.2 Numerical model outline: external loads

The curve to describe the hydrodynamic torque absorbed by the propeller (Q_{hydro}) can be modeled as a function of the rotational speed (n , [rps]) at a fixed pitch angle. Precisely, we

use the following expression [13, 43]:

$$Q_{\text{hydro}}(n) = K_Q(n) \rho n^2 D^5 \quad (4.3)$$

where ρ is the water density and $K_Q(n)$ is defined as the open-water torque coefficient of the propeller. In particular, we assume $K_Q(n)$ to be constant for the FPPs in free-running, steady-state conditions, since in such scenario the propeller's advance coefficient does not fluctuate significantly [12, 13].

To model the torque output of the Electric Drive (ED) configuration, we adopted a constant-power torque curve, as a function of n . The torque curve ($Q_{\text{ED}}(n)$) is capped at the threshold value ($Q_{\text{ED,max}}$), determined by the motor manufacturer. With P_{ED} indicating the motor power, the maximum torque is reached at the limit speed of n_0 and below; The power delivered by the motor is considered to be stable throughout a TVA simulation with external loads perturbing the steady-state equilibrium of the system. At higher speeds, the function in Eq. 4.4 holds:

$$Q_{\text{ED}}(n) = \begin{cases} Q_{\text{ED,max}} = \frac{P_{\text{ED}}}{2\pi n_0} & \text{for } 0 \leq n \leq n_0 \\ \frac{P_{\text{ED}}}{2\pi n} & \text{for } n_0 < n \leq n_{\text{max}} \end{cases} \quad (4.4)$$

where n_{max} is the upper-threshold speed of the propulsion line. The schematic curve in Fig. 4.4 shows the pattern of the ED torque [12].

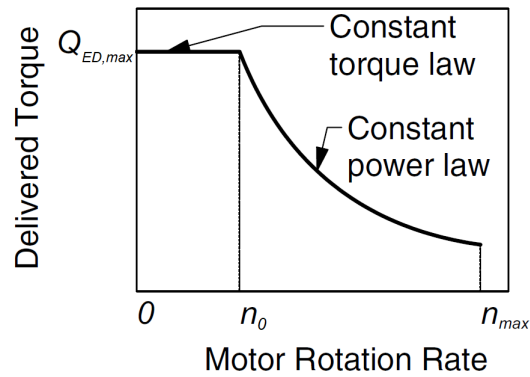


Figure 4.4: Characteristic curve of the ED-delivered torque.

4.2.2.3 Open-water, full-scale measurements

A series of vibration measurements was conducted during the open-water sea trials of the vessel, which took place on August 10, 2019, off the shore of the Avalon Peninsula in Newfoundland, Canada. In detail, we employed one Wheatstone-bridge rosette to measure the shear strain vibration on the shaft surface. Fig. 4.5 shows the instrumentation outline and its arrangement on the shaft.

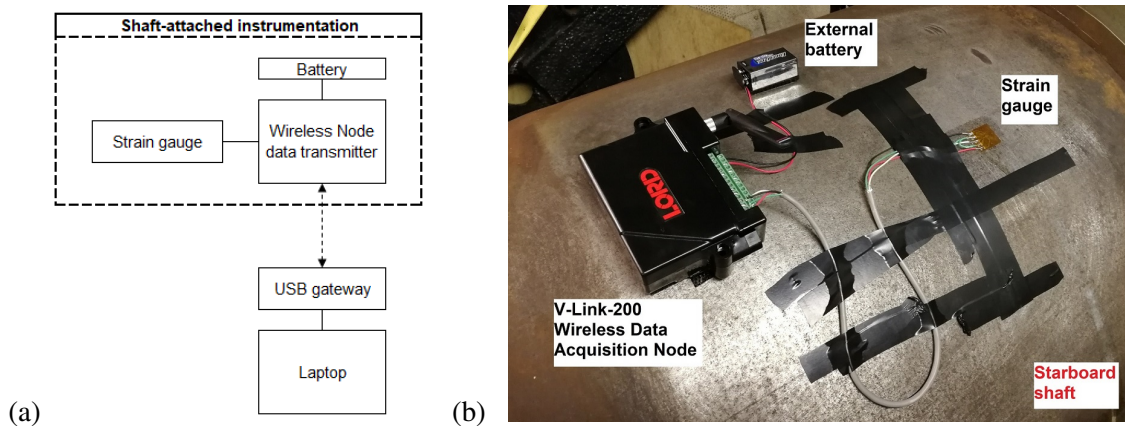


Figure 4.5: Layout of the equipment (a); instrumentation attached to the shaft (b).

The strain gauge employed was a full-bridge rosette, model CEA-06-250US-350, manufactured by VPG Sensors. We positioned the grid pattern on the shaft surface according

to [27]. The measurement output is the linear strain (ε), along the 45-degree direction with respect to the shaft sectional plane. The strain gauge terminals were wired to a differential analog channel input on a wireless data transmitter, namely a V-Link-200 Node® device supplied by LORD Sensing Systems Corp. A WSDA-200-USB® gateway interfaced the node to a laptop. The analog voltage input from the gauge is converted into microstrain units ($1 \mu\varepsilon = 10^{-6}\varepsilon$), and the voltage-microstrain relation could be calibrated through the shunt calibration circuit incorporated in the node. We employed the software “SensorConnect”® to set up the node and perform the measurement runs, which were carried out using a sampling frequency of 256 Hz. Each differential channel incorporates an anti-aliasing, 2nd-order Butterworth filter, whose cutoff frequency was set at 128 Hz.

4.2.2.4 Shaftline’s model updating

The torsional inertia and stiffness properties of the lumped-element model were determined from some general drawings of the propulsion line [12]. However, due to the unavailability of some structural details, we carried out a model updating procedure to determine the matrices $[\mathbf{I}]$ and $[\mathbf{K}]$, by matching the numerical and experimental shaftline’s eigenfrequencies.

A frequency range up to 150 Hz was considered; indeed, frequencies beyond that limit are not significant for large marine shaftline applications [12, 23, 55]. Besides, the frequency components of the ice-propeller interaction loads are of the same order of the shaft’s rotation rate and blade passing frequency ($BPF = Z n_{\text{prop}}$), which usually do not exceed 10-15 Hz.

Additionally, it was necessary to verify that the blade’s natural frequencies did not overlap with the shaftline model’s lower eigenfrequencies, which correspond to its main

vibration modes [4, 21]. To this end, we performed a FE modal analysis on the propeller’s hub-blade assembly simulated as a solid-element model through the FEA software “LS-Dyna”®. So, after confirming that the eigenfrequencies did not coincide, we could keep the propeller representation as a single DOF in the shaftline model.

4.2.3. Full-scale measurements during icebreaking operations

4.2.3.1 Instrumentation and experimental campaigns

An integrated measurement system to be installed on board the ship was designed and implemented through a research collaboration with NRC, to achieve concurrent monitoring of shaft dynamics and sea ice scenarios during navigation. Table 4.2 outlines the system’s components and their respective operations. Fig. 4.6 presents the equipment that composes the measurement system, whereas Fig. 4.7 provides a graphical representation of the scenario in which the shaftline sensors operate.

Table 4.2: Summary of the measurement system components.

Item	Manufacturer	Description	Operation
TT-Sense® meter	VAF Instruments	Optical-LED, rotating sensor	Low-frequency dataset of shaft torque, thrust, speed.
Laser tachometer	Brüel & Kjær	CCLD laser probe	High-frequency measurements of shaft rotational speed.
Outdoor HD Camera	HIK Vision	Weatherproof IP-PoE ¹ camera	Video recordings of the sea surface close to the hull, Port side.

¹Internet Protocol, Power-on-Ethernet.

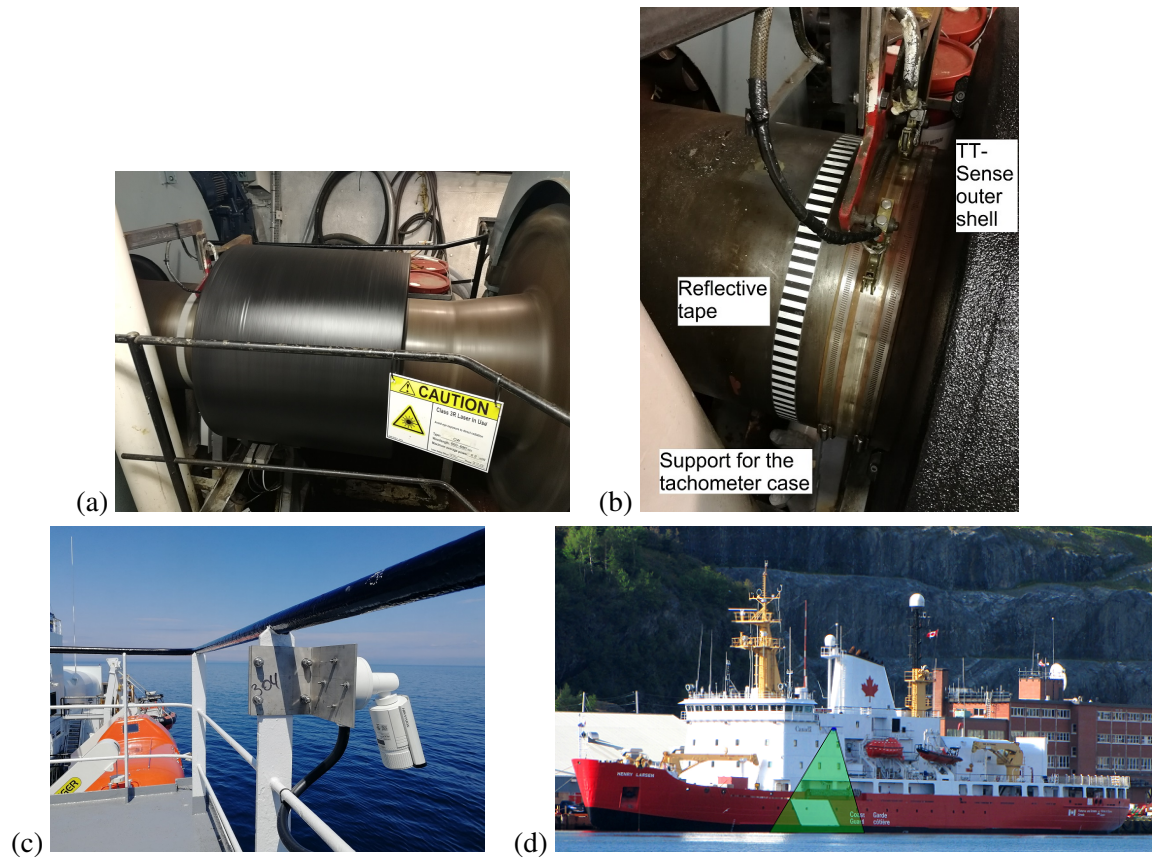


Figure 4.6: Starboard-side TT-Sense apparatus (a); Tachometer tape and support around the shaft (b); Camera mounting on the Upper Deck (c); Camera's angle of view (d).

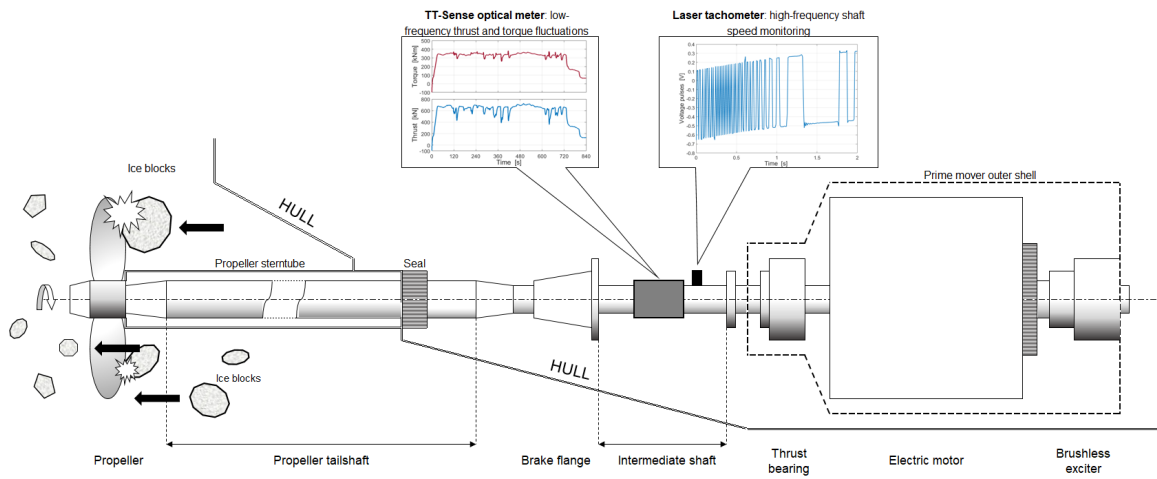


Figure 4.7: Configuration of the shaft sensors on board CCGS *Henry Larsen*.

One TT-Sense® thrust-torque meter was mounted on the intermediate shaft segment between the brake (θ_4) and the turning gear (θ_5) of each shaftline (Fig. 4.3). The principle of operation of the meter is based on the detection via LED optical sensors of the relative motions between two rings fixed on the shaft, in both axial and radial directions. The fluctuating laser pulses generate corresponding voltage signals, which are converted into the output quantities—shaft’s thrust (T_s), torque (Q_s), and rotational speed (n_s)—with a frequency of 5 Hz.

The laser tachometers were set to acquire a 12.8-kHz pulse signal to measure shaft rotational speed data. Each sensor was connected to a National Instruments® data acquisition system, and the Pulse Timing Method was implemented to process the output pulse signal [53]. Then, the pulse signal was under-sampled at 100 Hz to optimize the data handling.

A high-definition, weatherproof IP-PoE camera was fixed to the Port-side railing of the Upper Deck. The camera was used to estimate the ice block thickness from the video recordings. Hence, we considered the occurrences when ice floes turned over against the hull during ice operations. The camera’s line of view was arranged to be perpendicular to the water surface in order to visualize the ice thickness dimension on the frame (Fig. 4.6-d). To calculate the real-scale lengths from the recorded video frames, we used a marked floating ruler to set the ratio between pixels and sea-level distance.

In this paper, we consider the dataset acquired during two ice operation voyages of the *CCGS Henry Larsen*.

On October 17-18, 2019 the ship undertook icebreaking trials in ice-covered waters from Franklin Strait to the Gulf of Boothia, by passing through the Bellot Strait (NU) (Fig.

4.8-a). Heavy ice conditions were encountered until the end of the Bellot Strait passage, whereas the remainder of the voyage was characterized by milder ice scenarios.

On March 15-18, 2020 the vessel sailed from St. John's NL to the Northern Newfoundland strait, to perform icebreaking operations on the ferry route between Saint Barbe (NL) and Blanc Sablon (QC) (Fig. 4.8-b). The vessel encountered highly-concentrated ice conditions firstly across the sea region between Twillingate and Fogo Island (NL), and secondly in the strait between Labrador and Newfoundland.

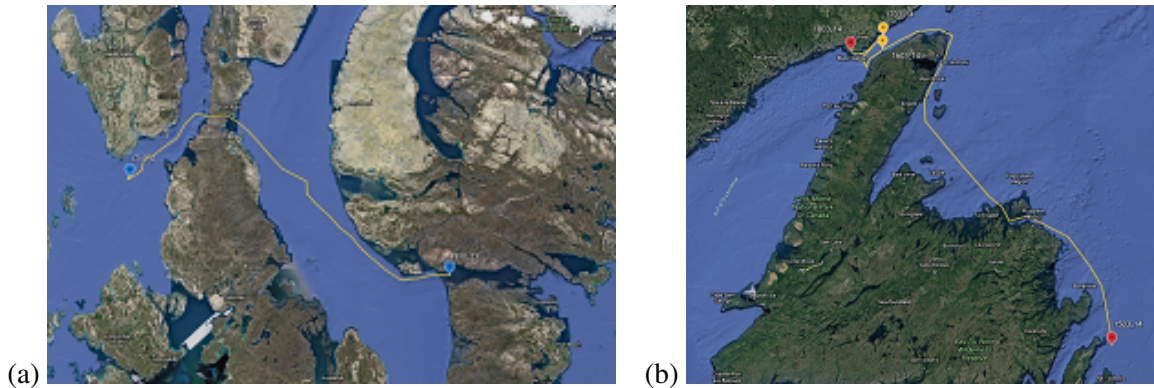


Figure 4.8: CCGS *Henry Larsen*'s routes: October 17-18, 2019 (a); March 15-18, 2020 (b).

4.2.3.2 Data processing

We analyzed the dataset produced by the TT-Sense sensors to identify time windows and corresponding T_s , Q_s , n_s data series, which included significant and distinguishable ice-breaking operations or transit navigation in ice-covered waters. Overall, 131 data clips were determined, of which 32 referred to backward direction manoeuvring.

The Q_s data were used to calculate the relative torsional displacement in the TT-Sense's shaft segment (DOFs 4 – 5). Since the $c_{i,i+1}$ term for all shafting segments is smaller than

$k_{i,i+1}$ by some orders of magnitude (Eq. 4.2), the torsional damping term is neglected in the calculation of the experimental torsional displacement. Thus, the angular torsional twist ($\Delta\theta_s(t)$) between the nodes 4 and 5 was calculated through the torsional stiffness term only:

$$\Delta\theta_s(t) = \theta_4(t) - \theta_5(t) = \frac{Q_s(t)}{k_{45}} \quad (4.5)$$

Concurrently, the video recordings were examined over the time lapses corresponding to the operations in ice. Hence, we gathered all the frames in which ice floes and blocks' thicknesses were viewed transversely by the camera. The thickness of the ice blocks were then determined by employing the imaging manipulation software "IC Measure".

Additionally, we cross-checked the ice's average thickness and qualitative concentration with the corresponding sea ice charts provided by the governmental agency Environment Canada. In this work, we considered the sole ice layer thickness quantity to characterize the sea ice scenarios.

4.2.4. Calculation of the ice-propeller interaction torque

The N -DOF matrix equation in Eq. 4.1 can be expressed in the frequency domain (f); thereby, we obtain the complex, dynamic stiffness matrix of the system ($[\mathbf{Z}(\omega)]$) as follows:

$$\left[-\omega^2[\mathbf{I}] + i\omega[\mathbf{C}] + [\mathbf{K}] \right] \vec{\theta}(\omega) = \vec{Q}(\omega) \quad \iff \quad [\mathbf{Z}(\omega)] \vec{\theta}(\omega) = \vec{Q}(\omega) \quad (4.6)$$

where ω is the angular frequency (rad/s) and equals $2\pi f$; i is the imaginary unit. In Eqs. 4.1 and 4.6, \vec{Q} constitutes the user-defined input, whereas $\vec{\theta}$ is the output variable vector

that results from the TVA simulation of the model. Hereinafter, we indicate this process as Direct Simulation (DS). Conversely, in this work we seek to calculate the input—ice-induced torque on the propeller (Q_{ice})—from the experimental data.

The measured Q_s data determines the corresponding torsional angular shift, $\Delta\theta_s(t) = \theta_s(t) - \theta_{s+1}(t)$, via Eq. 4.5. Therefore, the $\Delta\theta_s$ expression constitutes an additional equation to the system of Eq. 4.6. Consequently, θ_s can be eliminated from $\vec{\theta}(\omega)$ in the DS equation system, and we can write the new vector of the unknown variables $\vec{\eta}$ as follows:

$$\vec{\eta} = [\theta_1, \dots, \theta_{s-1}, \theta_{s+1}, \dots, \theta_N, Q_{\text{ice}}]^T \quad (4.7)$$

To establish a new matrix equation that takes $\vec{\eta}$ as the unknown-variable vector, $[\mathbf{Z}(\omega)]$ and $\vec{Q}(\omega)$ in Eq. 4.6 have to be properly rewritten. Precisely, we indicate with z_{jk} the generic entry of $[\mathbf{Z}(\omega)]$ at the j -th row and k -th column (Eq. 4.6); the j -th row of the equation system is shown in Eq. 4.8:

$$z_{j1}\theta_1 + \dots + z_{j,s-1}\theta_{s-1} + z_{js}\theta_s + z_{j,s+1}\theta_{s+1} + \dots + z_{jN}\theta_N = Q_j \quad (4.8)$$

If we add and subtract the term $z_{js}\theta_{s+1}$ to the left-hand side in Eq. 4.8, we obtain Eq. 4.9:

$$z_{j1}\theta_1 + \dots + z_{j,s-1}\theta_{s-1} + (z_{js} + z_{j,s+1})\theta_{s+1} + \dots + z_{jN}\theta_N = Q_j - z_{js}\Delta\theta_s \quad (4.9)$$

where the known terms have been moved to the right-hand side of the equation.

Finally, the new N -order equation system is completed by including the terms related to Q_{ice} . Specifically, the first row's equation in Eq. 4.6 corresponds to the propeller-node torque (Q_1), which is the superposition of the hydrodynamic (Q_{hydro}) and ice-induced (Q_{ice}) components: $Q_1 = Q_{\text{hydro}} + Q_{\text{ice}}$. We can write the first row's equation as follows:

$$\begin{aligned} z_{11}\theta_1 + \dots + z_{1,s-1}\theta_{s-1} + (z_{1s} + z_{1,s+1})\theta_{s+1} + \dots + z_{1N}\theta_N - Q_{\text{ice}} = \\ = Q_{\text{hydro}} - z_{1s}\Delta\theta_s \end{aligned} \quad (4.10)$$

Only the first equation in the N -order system involves Q_{ice} , therefore we can write the following system (Eq. 4.11):

$$\begin{aligned} \begin{bmatrix} z_{11} & \dots & z_{1,s-1} & (z_{1s} + z_{1,s+1}) & z_{1,s+2} & \dots & z_{1N} & -1 \\ z_{21} & \dots & z_{2,s-1} & (z_{2s} + z_{2,s+1}) & z_{2,s+2} & \dots & z_{2N} & 0 \\ \vdots & \ddots & \vdots & \vdots & \vdots & \ddots & \vdots & \vdots \\ z_{N1} & \dots & z_{N,s-1} & (z_{Ns} + z_{N,s+1}) & z_{N,s+2} & \dots & z_{NN} & 0 \end{bmatrix} \vec{\eta} = \\ = \begin{bmatrix} Q_{\text{hydro}} - z_{1s}\Delta\theta_s \\ Q_2 - z_{2s}\Delta\theta_s \\ \vdots \\ Q_N - z_{Ns}\Delta\theta_s \end{bmatrix} \end{aligned} \quad (4.11)$$

We use $[\mathbf{Y}(\omega)]$ to indicate the $N \times N$ matrix at the left-hand side of Eq. 4.11; in turn,

$\vec{R}(\omega)$ is the vector at the right-hand side. Thus, for each frequency value ($\bar{\omega}$), the solution $\vec{\eta}$ is found by inverting $[\mathbf{Y}(\bar{\omega})]$:

$$\vec{\eta}(\bar{\omega}) = [\mathbf{Y}(\bar{\omega})]^{-1} \vec{R}(\bar{\omega}) \quad (4.12)$$

The last entry of the vector $\vec{\eta}$ is the component of the complex spectrum of Q_{ice} corresponding to $\bar{\omega}$. Therefore, iterating the $[\mathbf{Y}(\bar{\omega})]$ calculation and inversion for multiple values of $\bar{\omega}$ delivers the full complex spectrum of the ice-propeller interaction torque ($Q_{\text{ice}}(\omega)$). Then, the application of the Inverse Fast Fourier Transform (IFFT) to $Q_{\text{ice}}(\omega)$ leads to the time-domain ice-propeller torque curve. The procedure just outlined, which utilizes the experimental $\Delta\theta_s(t)$ to provide $Q_{\text{ice}}(t)$, will be indicated as “Inverse Method” (IM) hereinafter.

The experimental $\Delta\theta_s$ data series is not the sole input quantity that is needed to obtain $\vec{\eta}(\omega)$. In fact, the hydrodynamic and prime mover torques ($Q_{\text{hydro}}(\omega)$ and $Q_{\text{ED}}(\omega)$) inside $\vec{Q}(\omega)$ are also included in the term $\vec{R}(\omega)$ of Eq. 4.11. Since those torques were not directly monitored during the on-board measurements, we estimated them by considering the TT-Sense’s shaft speed data and the mathematical relations for $Q_{\text{hydro}}(n)$ and $Q_{\text{ED}}(n)$ in Eqs. 4.3 and 4.4, respectively. In particular, the delivered power ($P_{\text{ED}}(n)$) was determined from the observation of the shaft power and steady-state shaft speed just before each ice-propeller interaction occurrence.

To verify the reliability of the IM algorithm, we carried out a verification procedure to check the correspondence between a known ice-propeller torque as DS-input and the

solution torque as IM-output.

4.2.5. Post-processing of the data

The updated properties of the shaftline model (Subsection 4.2.2.4) composed the matrix $[\mathbf{Z}(\omega)]$ of the system, to be employed in the IM (Subsection 4.2.4). Hence, the $\Delta\theta_s(t)$ data series were processed through the IM algorithm, to obtain the corresponding ice-propeller interaction $Q_{ice}(t)$ profiles. The data sets were separated into forward (F) and backward (B) direction operations. For each resulting $Q_{ice}(t)$ curve, we identified its most significant and delineated peaks, and then considered their average value (\bar{Q}_{ice}) as the representative torque peak magnitude of that $Q_{ice}(t)$ clip.

Besides, we subdivided all the ice-thickness camera frames into groups with reference to the time intervals corresponding to the $Q_{ice}(t)$ sequences. The average ice thickness value (\bar{h}_{ice}) was then calculated for each group of images, and thereby we defined \bar{h}_{ice} as the characteristic ice block thickness for that respective time window.

Additionally, we studied the correlation between ice thickness and mean shaft power peaks. For each $Q_s(t)$ data clip, the instantaneous shaft power ($P_s(t)$) was calculated through the product between $Q_s(t)$ and $\omega_s(t)$. Hence, we determined the mean peak values (\bar{P}_s) through the same procedure to determine \bar{Q}_{ice} . Finally, in correspondence of the i -th data clip, we obtained the following two pairings:

$$C_{(F,B),i} = \left\{ \left\{ \bar{Q}_{ice,(F,B),i}, \bar{h}_{ice,(F,B),i} \right\}, \left\{ \bar{P}_{s,(F,B),i}, \bar{h}_{ice,(F,B),i} \right\} \right\} \quad (4.13)$$

The aggregation of all $C_{(F,B),i}$ pairs constituted the data distributions of ice-propeller peak torque and shaft power against the concurrent sea ice thickness, for the F and B cases respectively. Hence, we performed regression analyses on the C_F and C_B data sets separately to study their trends.

4.3. Results

4.3.1. Shaftline model validation

4.3.1.1 Experimental results

During the open-water sea trials of the vessel, multiple vibration measurements were carried out at different shaft speeds. We examined the vibration spectra acquired at 126, 148, 159, 169 rpm to get the readings of the full-scale resonance frequencies. The frequency range in our analysis tops the measurements' Nyquist frequency, namely 128 Hz.

As an example, Fig. 4.9 shows the vibration spectrum acquired at the speed 159 rpm (n_s). Three torsional resonance modes could be clearly identified, and their respective frequencies are indicated with red arrows in the graph. The minor peaks at approximately 80 and 105 Hz are caused to the influence of the shaftline's axial and bending modes. We also highlight the sharp peaks corresponding to n_s and the BPF —the Z -th harmonic of n_s .

4.3.1.2 Model updating

Table 4.3 reports the three resonance frequencies visible in each one of the four vibration spectra at the different n_s steps. The data was used to update $[\mathbf{I}]$ and $[\mathbf{K}]$ (Eq. 4.1)

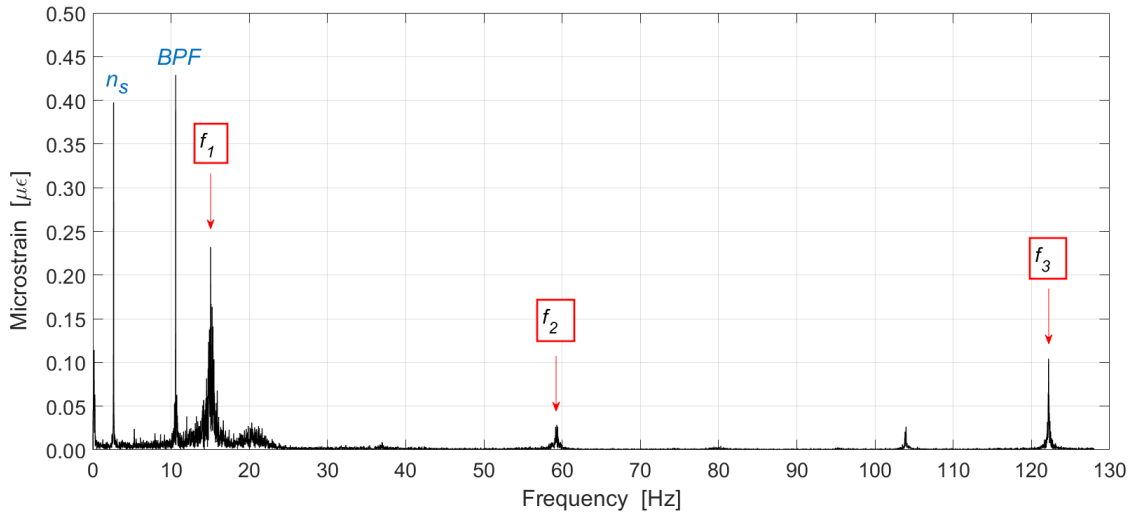


Figure 4.9: Microstrain ($\mu\epsilon$) vibration spectrum at 159 rpm.

as described in Subsection 4.2.2.4 [5]. The percent deviations between the two sets of frequencies are also reported.

Table 4.3: Resonance frequencies and eigenfrequencies for the torsional modes 1 to 3.

	f_1 [Hz]	f_2 [Hz]	f_3 [Hz]
$n_s = 126$ rpm	15.05	59.28	122.28
$n_s = 148$ rpm	15.02	59.40	122.37
$n_s = 159$ rpm	15.05	59.32	122.18
$n_s = 169$ rpm	15.07	59.30	122.24
Average exp. f_i	15.05	59.33	122.27
Numerical f_i	14.98	59.13	123.36
$ \Delta f_i $ [%]	0.47 %	0.34 %	0.89 %

Fig. 4.10 shows the normalized modal shapes resulting from the modal analysis of the updated model; the lower vibration modes concerned in our analysis are plotted in solid lines. In 4.B, we summarize the structural properties of the shaftline lumped-element model that were obtained through the model updating process.

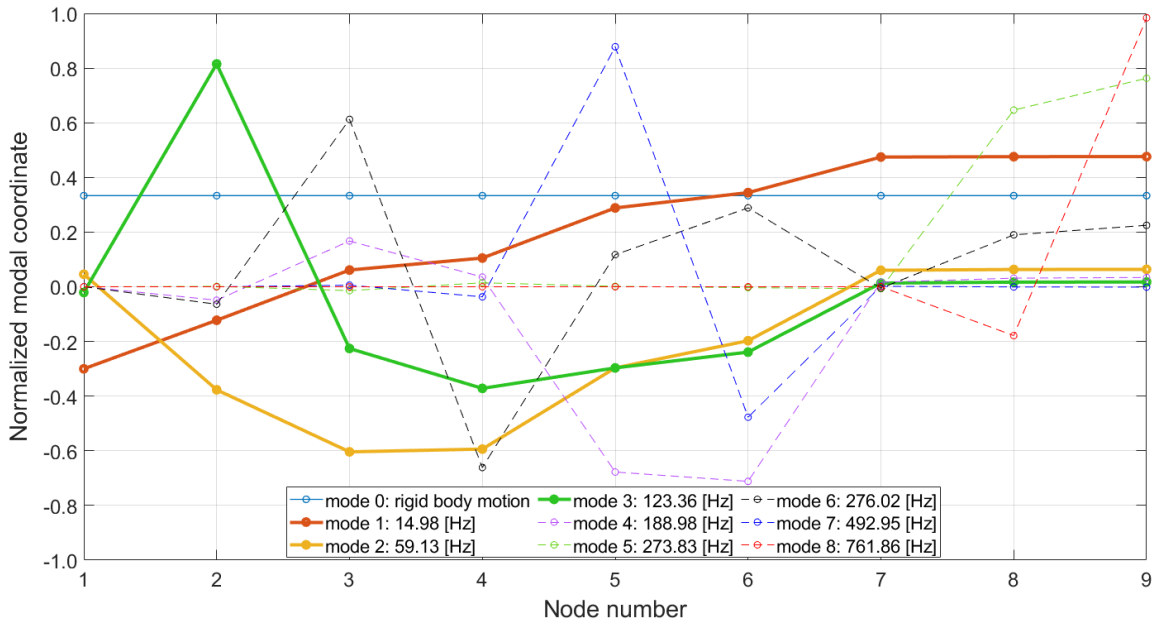


Figure 4.10: Torsional modal shapes of the shaftline's 9-DOF system.

4.3.1.3 Modal analysis of the propeller blade

To evaluate the propeller blade's natural frequencies, we performed an FE modal analysis of the hub-blade assembly, which was simulated with solid tetrahedral elements. Fig. 4.11 shows two views of the FE model. The model's geometry and mesh were developed in HyperMesh®, while the analysis was done in LS-Dyna®.

The model material was the alloy CuNiAl (UNS C95500), whose mass density, Young Modulus, and Poisson Ratio were set at 8,500 [kg.m⁻³], 120 [GPa], 0.32, respectively. Afterwards, we applied a 6-DOF, zero-motion constraint to each FE node on the propeller hub's inner cylindrical surface. A total number of 191,702 solid elements composed the model; the length of all sides in each element is set to be shorter than 50 mm.

We carried out an implicit modal analysis on the FE model. Table 4.4 reports the natural

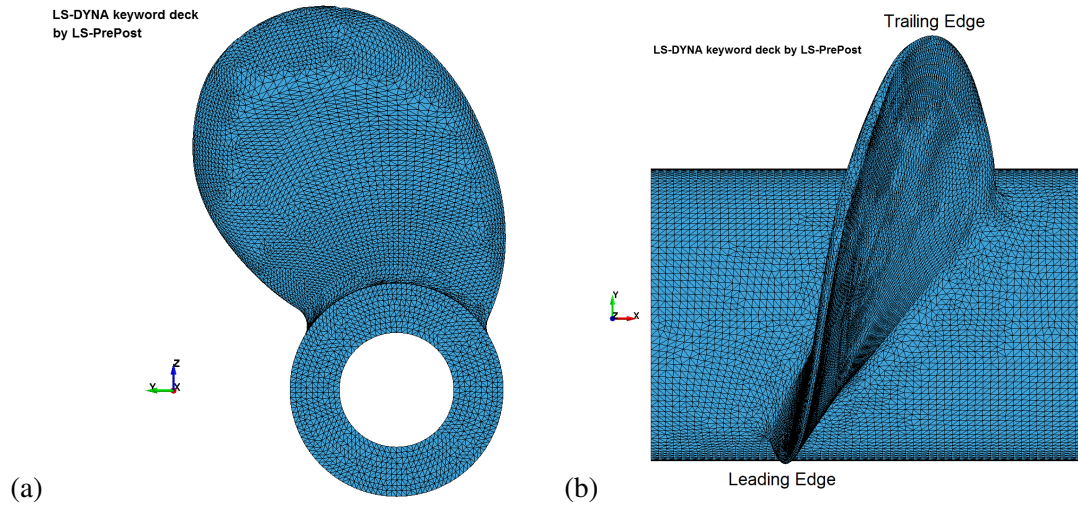


Figure 4.11: Front view (a) and Top view (b) of the propeller's hub-blade FE model.

frequencies of the first three assembly's vibration modes, compared against the first three natural frequencies of the shaftline system.

Table 4.4: First three eigenfrequencies of the propeller blade and the shaftline model.

	Mode I [Hz]	Mode II [Hz]	Mode III [Hz]
Hub-blade FE model	75.63	162.97	196.65
Shaftline system (with dry propeller)	15.21	59.23	123.40

Table 4.4 shows that the two sets of eigenfrequencies did not coincide at any value. Also, only the first blade's vibration mode fell into our frequency range of interest; that frequency is higher than the *BPF*—12 Hz at 180 rpm—and its first harmonics, which constitute the spectrum of the ice-induced and hydrodynamic excitation. Therefore, this allowed us to simulate the overall propeller as a single inertial node in the shaftline's lumped-element model.

4.3.2. Full-scale measurements

4.3.2.1 Icebreaking scenarios vs. Ice Charts

During the icebreaking operations in the October 2019 voyage, the ship encountered both multi-year and grey ice types, with floe dimensions ranging from medium to vast². The Egg Code diagrams in the Ice Charts provided by Environment Canada indicate total ice concentrations of 9/10ths to 10/10ths; the corresponding Stage-of-Development codes are 4, 5, 9, 8, 9 to denote the presence of ice floes more than 1.20-metre thick. This agrees with our ice imaging observations, which include several layers thicker than 1.50 metres. Beyond Franklin Strait, the ship sailed eastward through new, thin grey ice (Oct. 18), without significant ice-propeller interaction occurrences.

For the March 2020 voyage, the Egg Code data indicate grey ice type with an 8/10ths to 9/10ths total concentration in the region between Twillingate and Fogo Island (NL); in the strait between Labrador and Newfoundland, the encountered ice was thin, first-year ice with a total concentration of 9/10ths to 10/10ths. In both scenarios, the Stage-of-Development codes are 4, 5, 7, which indicate layer thickness ranges up to 0.70 metres. Correspondingly, we found average thickness values between 0.40 and 0.60 metres throughout our ice image processing.

²“Interpreting ice charts”, documentation provided by the Government of Canada weather services: <https://www.canada.ca/en/environment-climate-change/services/ice-forecasts-observations/publications/interpreting-charts/chapter-1.html>

4.3.2.2 Experimental data: examples

During the icebreaking operations in both voyages, shaft dynamics data and sea ice video recordings were acquired continuously. Fig. 4.12 shows a 10-minute dataset excerpt as an example of the output data format that is produced by the TT-Sense shaft sensors. The peaks and drops of T_s , Q_s , n_s are visible in the graphs, as well as the substantial differences between the two shaftlines' time-domain signals.

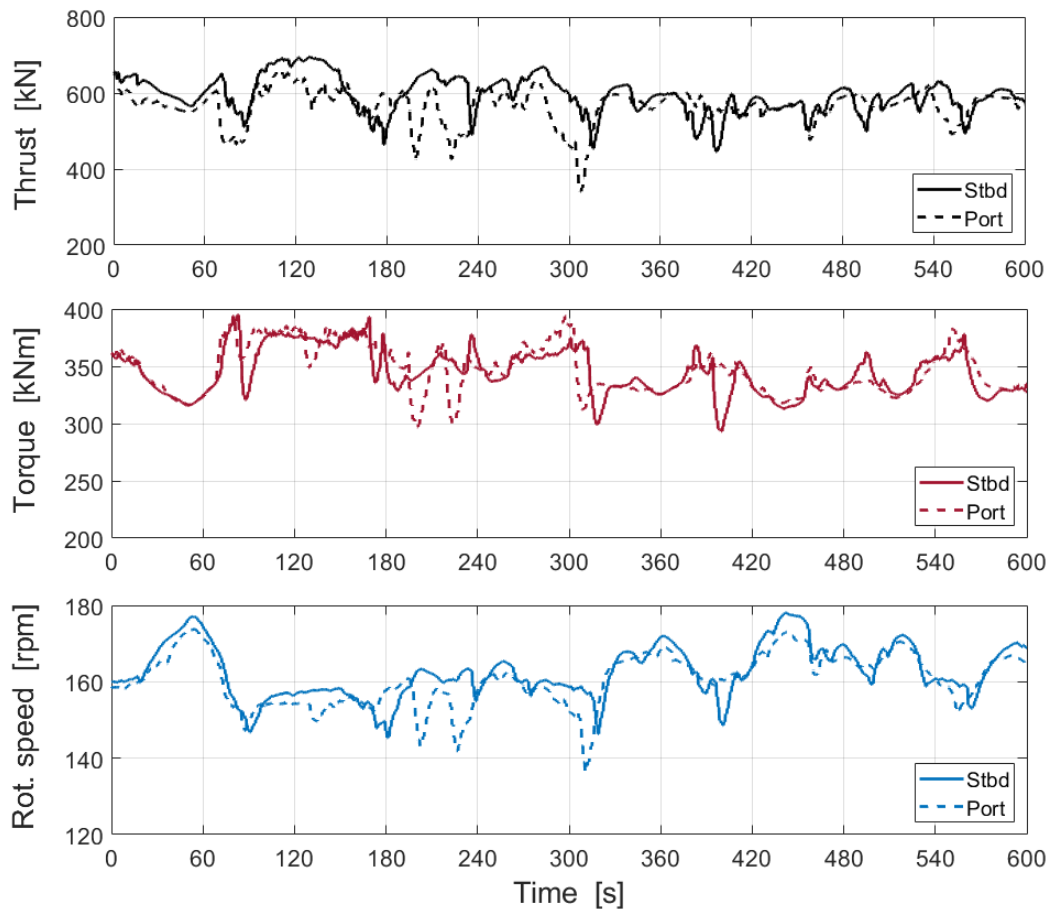


Figure 4.12: Data series clip from both TT-Sense meters, acquired on March 16, 2020.

Fig. 4.13 shows two screenshots from the camera video recordings, which were processed through imaging software to measure ice thickness values at sea level. Overall, in the entire

dataset we gathered about 500 frames that displayed vertically-flipped ice floes distinctly.

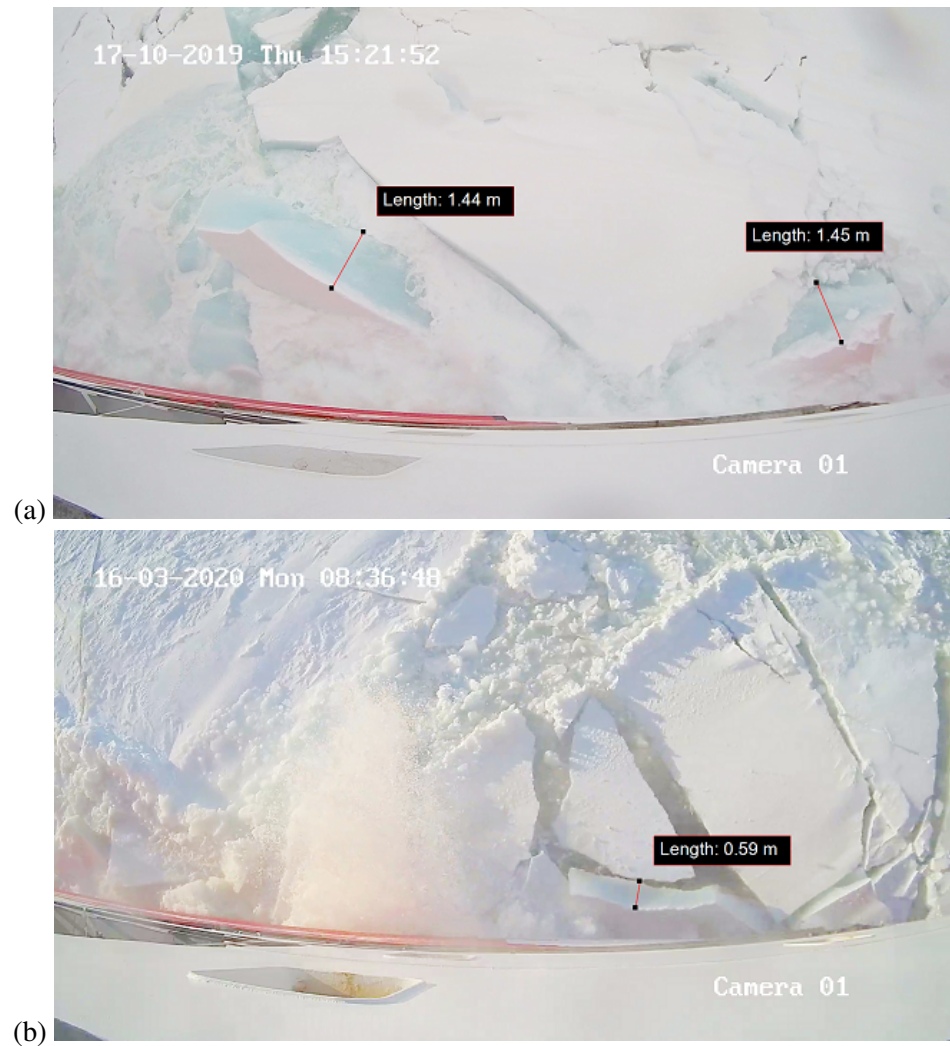


Figure 4.13: Camera frames in icebreaking operations: Oct. 17, 2019 (a); Mar. 16, 2020 (b).

4.3.3. Verification of the IM algorithm

Fig. 4.14 outlines the steps that compose the verification procedure.

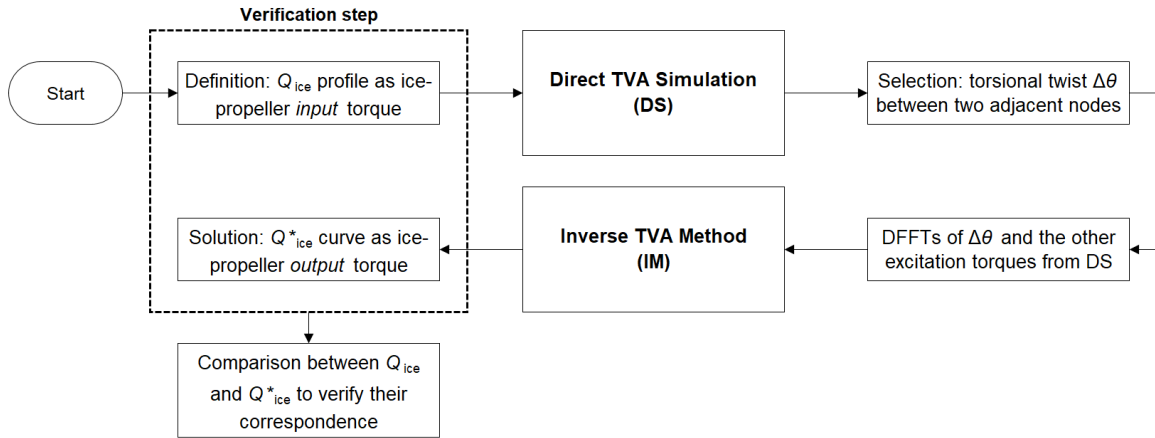


Figure 4.14: Flowchart outlining the IM verification process.

Firstly, a DS run was performed with a user-defined ice-propeller torque (Q_{ice}). The output quantities of the DS process included $\vec{\theta}(t)$ plus the instantaneous excitation torques $Q_{hydro}(t)$ and $Q_{ED}(t)$; those terms were then transformed into the frequency domain to establish the vector \vec{R} in Eq. 4.11. We implemented the IM algorithm to calculate the output torque $Q_{ice}^*(t)$. At this point, the comparison between the DS-input ($Q_{ice}(t)$) and the IM-output ($Q_{ice}^*(t)$) determined whether the IM process worked correctly.

Specifically, a *PC4*, *IC1* ice-induced torque was applied to the propeller (Eqs. 4.19, 4.20). We set the transient TVA to simulate 15 seconds of the shaftline dynamics, with an initial shaft speed of 170 [rpm]. A time-domain resolution of 1 [ms] was used in the simulation. Fig. 4.15-a shows the nominal, input ice-propeller torque ($Q_{ice,IACS}$); besides, Fig. 4.15-b shows the actual, time-domain $Q_{ice}(t)$ as it evolved throughout the DS run.

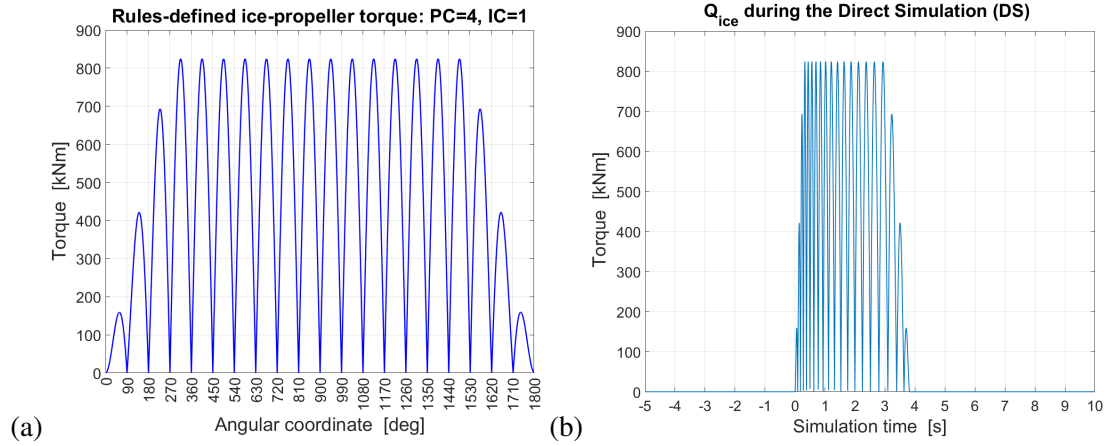


Figure 4.15: Plots of: nominal $Q_{ice,IACS}(PC = 4, IC = 1)$ (a); actual $Q_{ice}(t)$ (b).

Fig. 4.16 show the time-domain excitation torques ($Q_{hydro}(t)$ and $Q_{ED}(t)$) and the Intermediate shaft's torsional twist ($\Delta\theta_{45}(t)$).

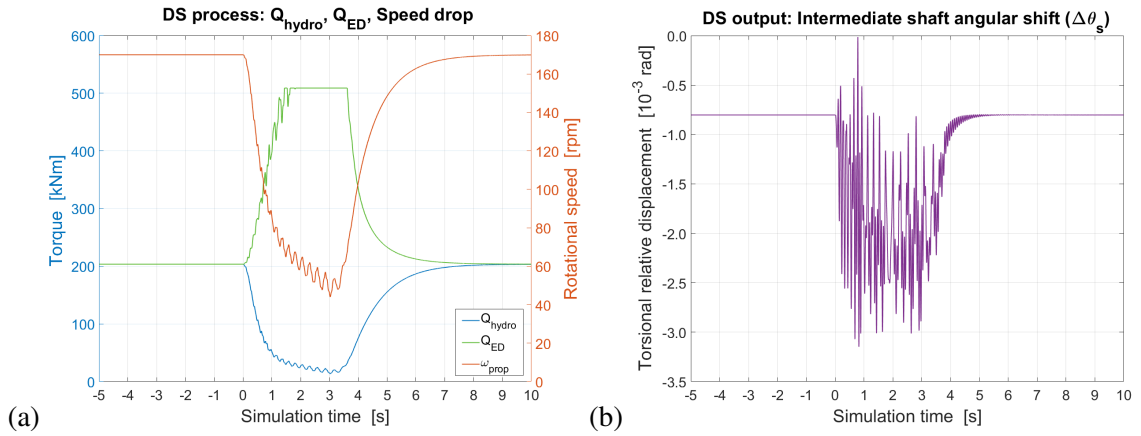


Figure 4.16: Plots of: $Q_{hydro}(t)$, $Q_{ED}(t)$, $\dot{\theta}_1(t)$ (a); $\Delta\theta_{45}(t)$ (b).

Finally, Fig. 4.17-a shows the IM-output, $Q_{ice}^*(t)$, with the primary peaks that correspond to the ones of $Q_{ice,IACS}$ and $Q_{ice}(t)$; Fig. 4.17-b shows the two homologous profiles superposed.

In $Q_{ice,IACS}$ and $Q_{ice}(t)$, the maximum torque value equals 824.3 kNm, which is reached at the 14 central impacts (Fig. 4.15-a). In $Q_{ice}^*(t)$ from Fig. 4.17-a, the maximum and

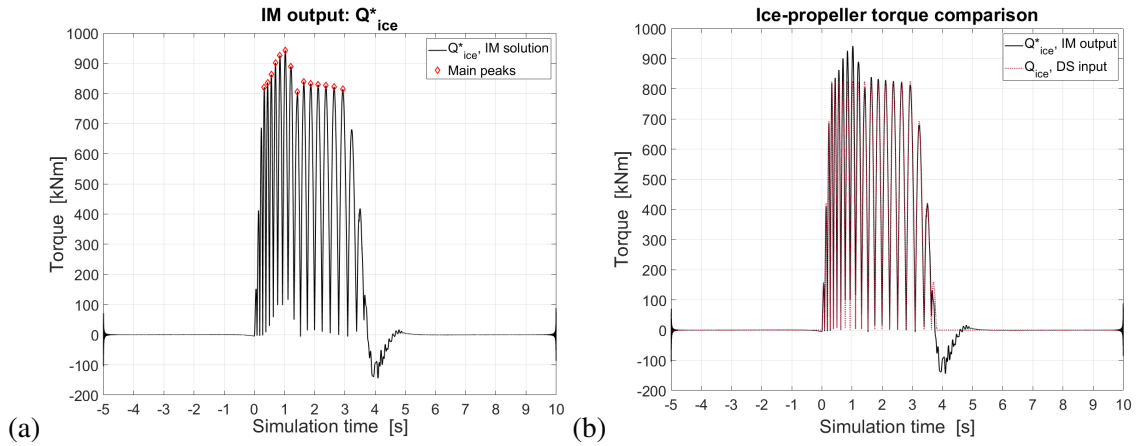


Figure 4.17: Plots of: IM-output $Q_{ice}^*(t)$ (a); overlay of the two curves (b).

minimum peaks in those 14 impact pulses reach 942.2 and 805.7 kNm, respectively. The average value of the 14 highest peaks in $Q_{ice}^*(t)$ equals 853.3 kNm, which deviates by 3.5% from the nominal value. In detail, the initial impacts immediately after the perturbation onset result magnified ($t = 0$ to 1 s), whereas the ending part ones ($t \approx 4, 5$ s) are correspondingly abated. On the other hand, the peaks in the middle portion of the impact series coincide in both curves (Fig. 4.17-b). Also, the time-span widths of all impacts are correctly reproduced in $Q_{ice}^*(t)$.

Overall, $Q_{ice}^*(t)$ deviates from $Q_{ice}(t)$ because of numerically-related factors, such as the frequency resolution of the processed spectra, DFFT-IFFT spectral distortions, and the numerical errors arising from the solving process of Eq. 4.12. Therefore, we affirm the IM algorithm to be verified.

In this work, we considered the average value of multiple peaks among the highest and most clearly delineated ones from the resulting ice-propeller torque curves (\bar{Q}_{ice} , Subsection 4.2.5). Therefore, possible local distorting effects throughout the signal's numerical reconstruction became attenuated.

4.3.4. Data analysis results: correlations between shaft data and ice thickness

4.3.4.1 C_F dataset: ice-induced torque

We implemented the procedure outlined in Subsection 4.2.5, to obtain the mean ice-propeller torque set (\bar{Q}_{ice}) and the average ice thickness value (\bar{h}_{ice}) associated to all data series. Overall, 99 Q_s data sequences were acquired during forward direction operations; 56 clips were obtained from the Starboard-side TT-Sense meter, 43 from the Port-side one.

Afterwards, we used the MATLAB Curve Fitting toolbox to perform statistical analyses on the $\{\bar{Q}_{ice}, \bar{h}_{ice}\}$ data. We found that the single-term power function ($y(x) = ax^b$ pattern) was the most efficient fit formulation.

Fig. 4.18 shows the data distribution, fitting curves, and regression outcomes of the C_F data set. The fit function associated to all data points is indicated by the solid curve in Fig. 4.18-a and is presented in Eq. 4.14:

$$\bar{Q}_{ice,F,all} = 356.5 (\bar{h}_{ice})^{1.105} \quad [\text{kNm}] \quad (4.14)$$

The dashed line in Fig. 4.18-a draws the fit curve for the whole distribution except for the 7 circled points. Those points refer to data from the operations conducted through Franklin and Bellot straits, where particularly heavy ice conditions were encountered; those values associate high ice thickness to lower ice-propeller torque peaks, and this fact is due to the different manoeuvring procedures applied during icebreaking in that scenario. Specifically, the ED power and shaft speed were kept at lower levels to avoid high impact shocks between

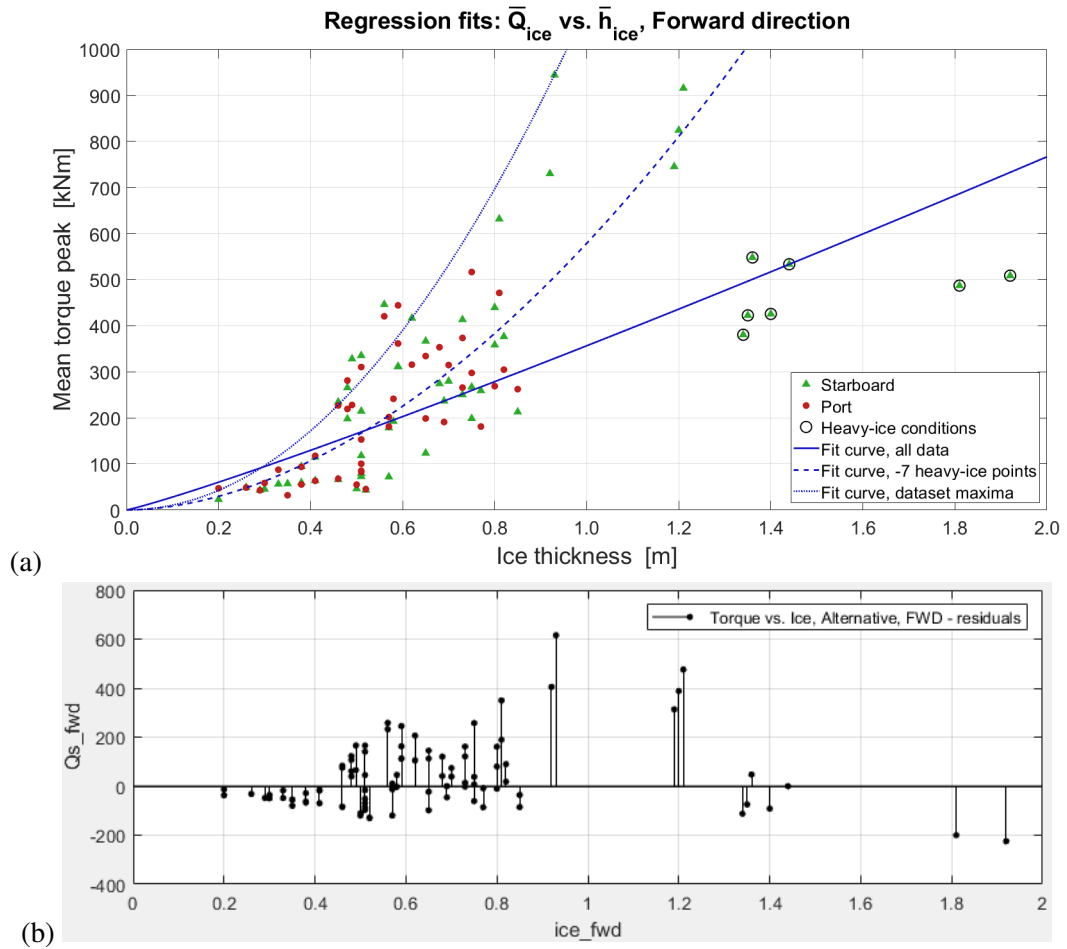


Figure 4.18: Forward direction C_F dataset: distribution and correlation curves between propeller torque and ice thickness (a); residuals plot of the regression that generates $\bar{Q}_{ice,F,all}$. The adjusted R^2 value of the fit equals 0.9803 (b).

the propeller blades and the ice layers. Therefore, to separate this different operational use of the prime movers, we determined an intermediate-ice curve without those specific points ($\bar{Q}_{ice,F,int}$). Fig. 4.19 shows the residual plot of the regression analysis, which generates the formula in Eq. 4.15.

$$\bar{Q}_{ice,F,int} = 579.0 (\bar{h}_{ice})^{1.848} \quad [\text{kNm}] \quad (4.15)$$

Additionally, the dotted line in Fig. 4.18-a depicts the “severe” case loads; this profile

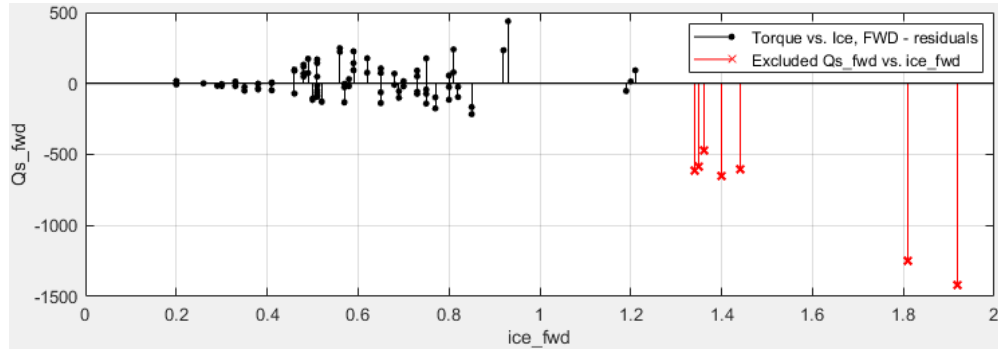


Figure 4.19: Forward direction C_F dataset: residuals plot of the regression that generates $\bar{Q}_{ice,F,int}$ (7 heavy-ice points excluded). The adjusted R^2 value of the fit equals 0.7087.

was determined by fitting the maximum \bar{Q}_{ice} points that correspond to each 0.05-metre-wide \bar{h}_{ice} data bin. Namely, this selection criterion considers the upper boundary of the data distribution region. Equation 4.16 reports the curve's expression and Fig. 4.20 shows the residuals plot.

$$\bar{Q}_{ice,F,max} = 1094 (\bar{h}_{ice})^{2.019} \quad [\text{kNm}] \quad (4.16)$$

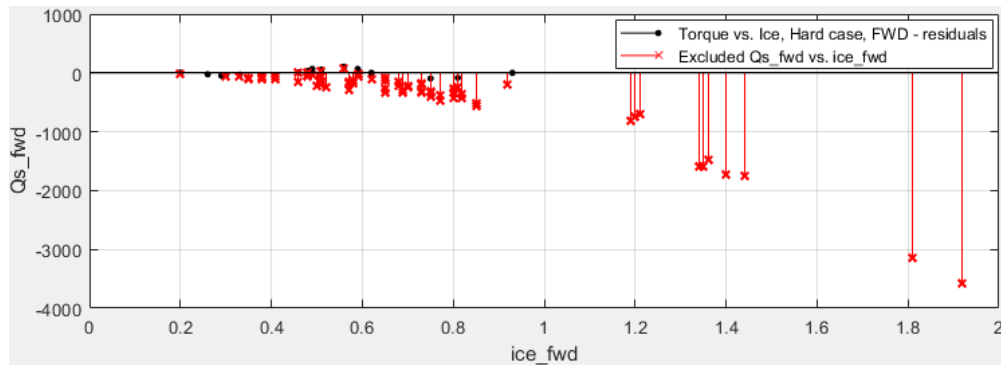


Figure 4.20: Forward direction C_F dataset: residuals plot of the regression that generates $\bar{Q}_{ice,F,max}$ (severe case points). The adjusted R^2 value of the fit equals 0.9469.

4.3.4.2 C_F dataset: shaft power

Analogously to what was done for $\bar{Q}_{ice,F}$, we carried out a regression analysis on the $\{\bar{P}_{s,F}, \bar{h}_{ice}\}$ data. The same 7 heavy-ice data points disregarded to determine Eq. 4.15 were excluded here; the regression fit function is reported in Eq. 4.17.

$$\bar{P}_{s,F,int} = 6615 (\bar{h}_{ice})^{0.699} \quad [\text{kW}] \quad (4.17)$$

Fig. 4.21-a shows the data scattering and the resulting curve, together with the ED Bollard Condition power limit; the statistical analysis outcomes are reported in Fig. 4.21-b.

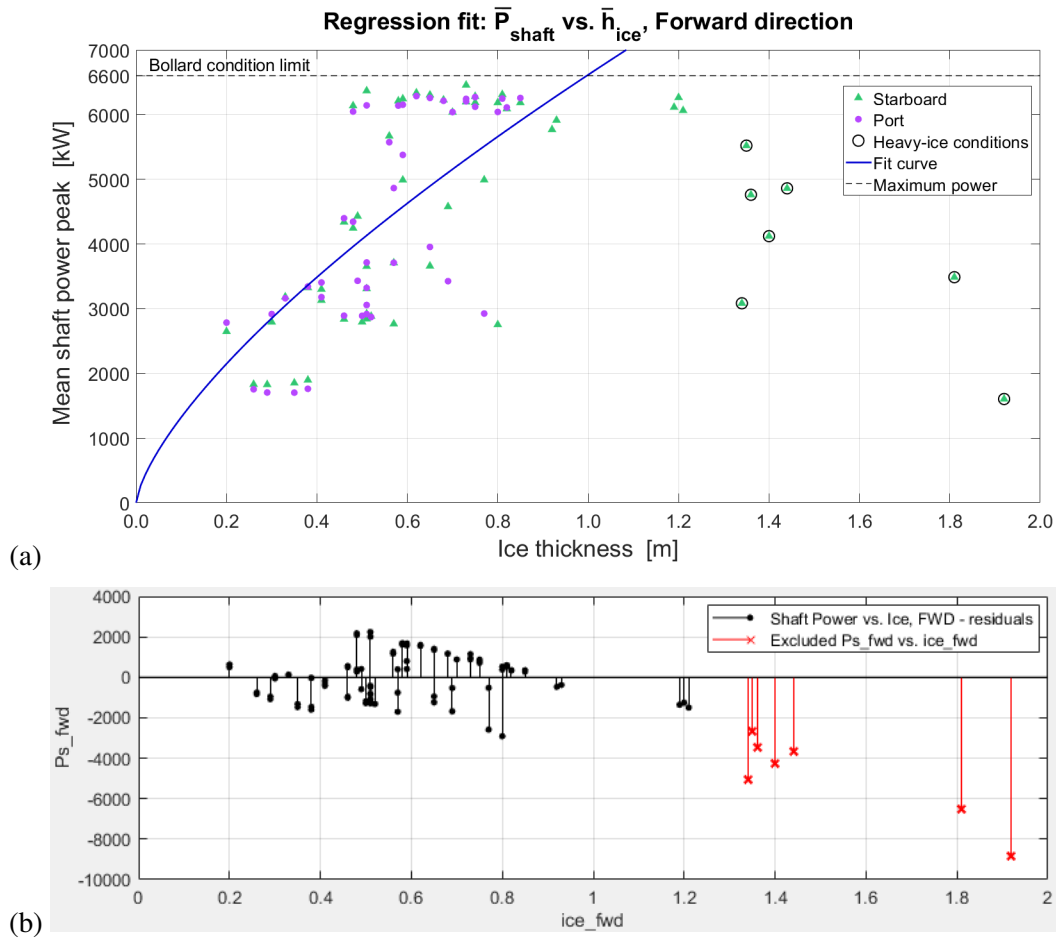


Figure 4.21: Forward direction C_F dataset: distribution and correlation curves between shaft power and ice thickness (a); residual plot of the regression that generates $\bar{P}_{s,F,int}$. The adjusted R^2 value of the fit equals 0.5056 (b).

4.3.4.3 C_B dataset: ice-induced torque and shaft power

With regard to the backward direction operations, we identified 32 Q_s data sequences; 24 were obtained from the Starboard-side TT-Sense meter, 8 from the Port-side one. Fig. 4.22 shows the data distributions of both $\bar{Q}_{ice,B}$ and $\bar{P}_{s,B}$ data sets, with two and one outliers discarded, respectively. Both plots indicate that no significant trends in relation to \bar{h}_{ice} were found.

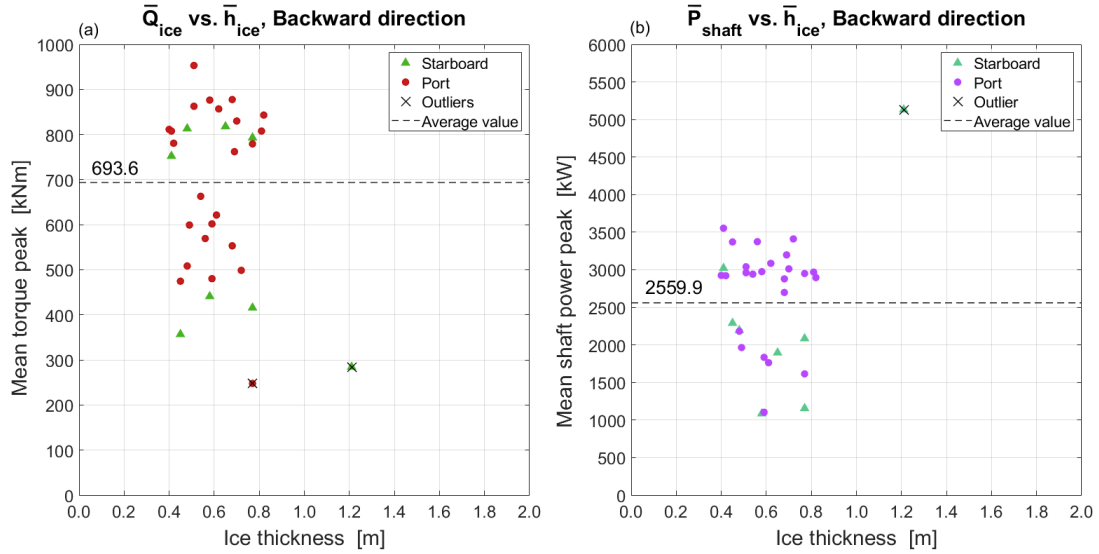


Figure 4.22: Backward direction C_B dataset: data distributions of $\bar{Q}_{ice,B}$ (a) and $\bar{P}_{s,B}$ (b).

4.4. Discussion

4.4.1. Comments on the results

4.4.1.1 Ice-torque and ice-shaft power correlations

The C_F regression curves as per Figs. 4.18-b, 4.19, 4.20 feature high R^2 values to confirm the goodness of their fits. The abundance of data points in the range $\bar{h}_{ice} < 1$ metre makes the relations $\bar{Q}_{ice,F,int}$ and $\bar{Q}_{ice,F,max}$ robust; conversely, the opposite outcome arises for $\bar{Q}_{ice,F,all}$ due to the scarcity of C_F data points in the heavy ice range.

Concerning the shaft power regression (Eq. 4.17), we notice from Fig. 4.21-a that several data points lie in the range between 6.0 MW and 6.6 MW, namely the ED power output exceeding the nominal value and below the Bollard Condition point. Moreover, we observe that the exponent of the shaft power fit curve (Eq. 4.17) is significantly smaller

than the exponents of the three $\bar{Q}_{ice,F}(\bar{h}_{ice})$ fits. This means that the shaft power features a lower variability with respect to \bar{h}_{ice} than the ice-propeller torque does. Hence, from the design perspective, the Bollard propulsive point should be considered disregarding from the $\bar{P}_{s,F,int}(\bar{h}_{ice})$ curve.

Regarding the backward-direction data (Fig. 4.22), the main reasons why no correlations were found for $\bar{Q}_{ice,B}$ and $\bar{P}_{s,B}$ are three: firstly, the C_B data series are remarkably less numerous than the ones in C_F ; secondly, the data we obtained are included into a range of \bar{h}_{ice} that is too narrow to make potential relations identifiable; thirdly, during the backward-icebreaking operations the ED-delivered power was frequently set to a fixed level, independently from the ice conditions.

4.4.1.2 C_F regression outcomes vs. Rules' recommendations

We aim to compare our findings—specifically the $\bar{Q}_{ice,F}(\bar{h}_{ice})$ correlation curves—versus the ice-propeller torque amplitudes that are obtained in accordance with the current Rules.

The determination of the ice-propeller torque amplitude according to the IACS Polar Rules is based on the definition of the Polar Class (PC), the Impact Case type (IC), and the propeller's characteristics [30]. In 4.A, we outline the IACS formulae plus the corrective variants adopted by the American Bureau of Shipping (ABS) and Det Norske Veritas (DNV) [2, 19]. Throughout this paper, the ABS-DNV version of the formulations is considered. In Eq. 4.18 we introduce $Q_{peak,Rules}$, which corresponds to the amplitude of the $Q_{ice,IACS}(\varphi)$ curve (Eq. 4.19) calculated as per the ABS-DNV corrections:

$$Q_{\text{peak,Rules}}(PC, IC) = C_q(IC) Q_{\text{max}}(PC) \quad (4.18)$$

We determined the peak values $Q_{\text{peak,Rules}}(PC, IC)$ with the specifications of CCGS *Henry Larsen's* propeller type and with its maximum rotational speed ($n = 3$ rps). In particular, since the design thickness of the ice layer (H_{ice}) is involved in the mathematical expression for $Q_{\text{peak,Rules}}$ and depends to the PC notation, $Q_{\text{peak,Rules}}(PC, IC)$ is also a function of H_{ice} . We implemented Eqs. 4.20 and 4.18, and these results are named “actual” $Q_{\text{peak,Rules}}(PC, IC, H_{\text{ice}})$; they are plotted with black marks in Fig. 4.23.

Equation 4.20 has two formulae: one of the two mathematical expressions of Eq. 4.20 is chosen whether D is larger or smaller than the threshold value $D_{\text{limit}}(PC)$. Here we want to study how the application of the switch-value $D_{\text{limit}}(PC)$ affects the final values of $Q_{\text{peak,Rules}}$; therefore, in addition to the “actual” $Q_{\text{peak,Rules}}(PC, IC, H_{\text{ice}})$, we first calculated both values of Q_{max} in Eq. 4.20, and then selected the maximum one disregarding from the $D_{\text{limit}}(PC)$ condition. These values are indicated as “max” $Q_{\text{peak,Rules}}(PC, IC, H_{\text{ice}})$; they are plotted with red marks in 4.23.

Fig. 4.23 shows the two series of $Q_{\text{peak,Rules}}(PC, IC, H_{\text{ice}})$ points plus the three regression curves presented in Eqs. 4.14, 4.15, 4.16.

In Fig. 4.23 we can notice the analogy between the $Q_{\text{peak,Rules}}$ trend and the $\bar{Q}_{\text{ice},F,\text{all}}$ curve with respect to \bar{h}_{ice} ; the “max” series results to be substantially parallel to $\bar{Q}_{\text{ice},F,\text{all}}$ because the exponents in the respective mathematical expression are very close (Eqs. 4.14 and 4.20). The slope of $\bar{Q}_{\text{ice},F,\text{all}}$ is driven by the C_F data points that lie in the heavy-ice

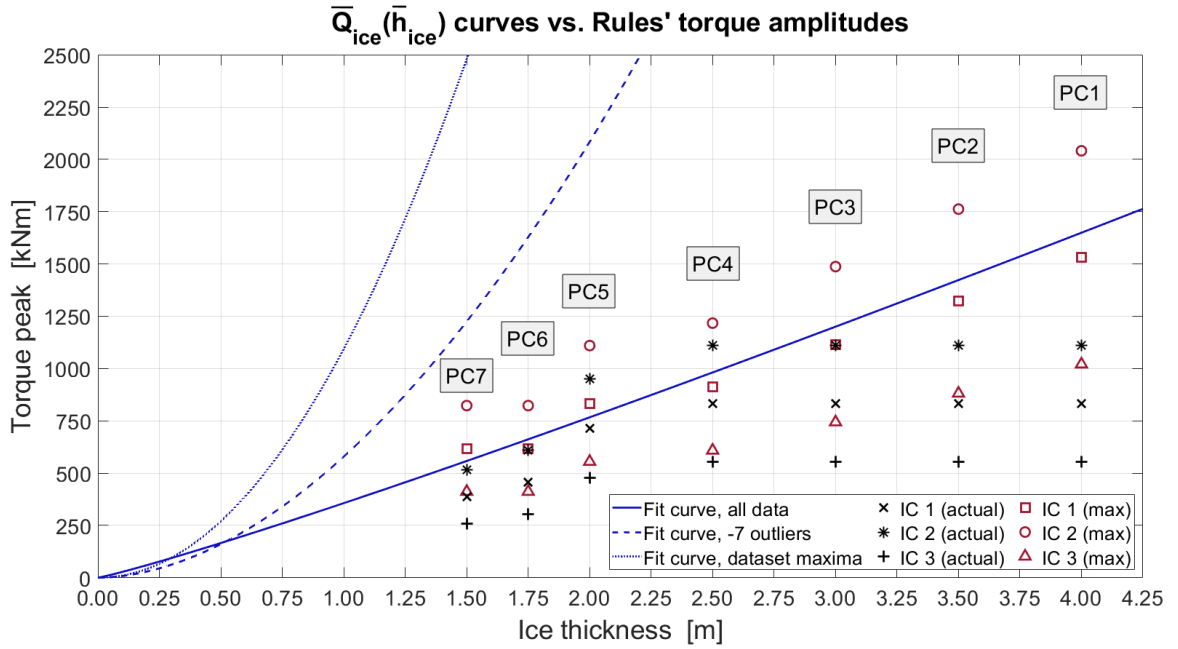


Figure 4.23: Comparison between the different $\bar{Q}_{ice,F}(\bar{h}_{ice})$ regression curves and the two series of $Q_{peak,Rules}(PC, IC, H_{ice})$ outcomes by considering the open propeller case with the *Henry Larsen's* properties. In detail, the “actual” points are derived from the outcomes of the Eq. 4.20, whereas the “max” points are obtained from calculating both values in the subequations of Eq. 4.20 first, and then taking the maximum among them.

region, which are notably rarer than the light-ice observations. A larger number of data points in ice conditions similar to the ones encountered in the October 2019 voyage would improve the reliability of $\bar{Q}_{ice,F,all}$; however, ice thickness levels similar to the design values are unlikely to be observed, due to the conservative approach adopted to define H_{ice} .

Concerning the difference between the “actual” and “max” torque peaks, it can be noticed from the plotted series in Fig. 4.23 that when the D_{limit} threshold criterion is applied as per Eq. 4.20, for each PC the “actual” $Q_{peak,Rules}$ values are always the lowest ones. Specifically, for CCGS *Henry Larsen's* FPP case, $D > D_{limit}$ for the PC s 5, 6, 7; consequently, the “actual” $Q_{peak,Rules}$ results for PC s from 1 to 4 are constant even if $H_{ice}(PC)$ changes (Fig. 4.23). The comparison of the $Q_{peak,Rules}(PC, IC)$ distribution against $\bar{Q}_{ice,F,all}(\bar{h}_{ice})$ shows

that among the “actual” values only the ones at $PC = 4, 5$ and $IC = 2$ exceed the fit curve; conversely, among the “max” values all $IC = 2$ outcomes, plus the $IC = 1$ at $PC = 5, 7$, exceed $\bar{Q}_{ice,F,all}(\bar{h}_{ice})$.

Therefore, the combination of our experimental results and data analysis (Subsection 4.3.4.1) with the outcomes via the Rules’ formulae suggests that the design correlation between ice-propeller peak torque and mean ice layer thickness could be split in two formulations: the curve $\bar{Q}_{ice,F,max}$ is more appropriate to model the torque amplitudes for the light-medium ice thickness range, up to $\bar{h}_{ice} = 1$ metre; above this threshold, the curve $\bar{Q}_{ice,F,all}$ should be applied with a correction factor of at least 1.5 to make it overcome the highest $Q_{peak,Rules}(PC, IC)$ points.

4.4.2. Strengths and limitations of this work

The development and implementation of the IM algorithm proved efficient and accurate. Indeed, avoiding time-domain inverse simulations on the $Q_s(t)$ data series could save significant computational time. As shown in Subsection 4.3.3, the reconstructed signal was demonstrated to be congruent to the homologous known input.

The integration between ice-propeller torque outcomes and sea ice visual observations, as conducted through the methods and instruments we employed, constitutes a unique analysis within the field of ice-shaftline TVA. We found notable correlations between ice-propeller interaction loads and ice thickness in the gray, thin-medium ice type range; this information might be significant for the design of propulsion systems on board cargo vessels, which are more vulnerable to light-medium ice conditions. Since we showed that high ice-induced

torque peaks can happen for light-medium ice thickness values (Fig. 4.18-a), the curves $\bar{Q}_{ice,F,int}(\bar{h}_{ice})$ and $\bar{Q}_{ice,F,max}(\bar{h}_{ice})$ represent important findings to be applied to navigation in grey, thin, first-year ice conditions.

In Subsection 4.4.1.2, we highlighted that the scattering of the Rules' $Q_{peak,Rules}$ results is coherent with the trend of the $\bar{Q}_{ice,F,all}(\bar{h}_{ice})$ curve (Eq. 4.14). Besides, we showed that the IC definition and the D_{limit} threshold in the implementation of Eq. 4.20 play crucial roles in determining $Q_{peak,Rules}$, as the different “actual” and “max” point distributions can assume very distant values (Fig. 4.23). Hence, these findings suggest that the functions of IC and D_{limit} may need to be reviewed and possibly redefined.

On the other hand, some remarks need to be made in order to characterize our results' boundaries. In this work, the definition of the ice thickness variable (\bar{h}_{ice}) is related to ice observations in the surroundings of the ship hull, and it is intended to represent the average dimension of the ice blocks colliding with the propeller blades over the observation time intervals. Instead, the IACS Polar Class Rules [30] are based on past empirical studies, and settled the $H_{ice}(PC)$ thresholds for each PC with a conservative standpoint. Hence, the C_F and C_B data points shown in Figs. 4.18-a, 4.21, 4.22 have to be considered with a reasonable uncertainty margin about the \bar{h}_{ice} values. Also, the torque data were acquired with a sampling frequency of 5 Hz, which is too low to detect distinctly the actual peak value of each single ice-blade impact. In our analysis, the quantity \bar{Q}_{ice} represents the average torque peak that characterizes a longer ice-propeller interaction (Subsection 4.2.5); namely, the prominent peaks in each $Q_{ice}(t)$ data clip—used to determine the corresponding \bar{Q}_{ice} value—incorporate the information of several ice-induced pulses.

Finally, the torque-ice correlations we obtained are valid for propellers similar to the case study ones since the characteristics of the ice-propeller loads are closely related to the propeller's geometry [36, 41, 56]. A more comprehensive correlation of data would be achieved from a broader measurement campaign involving diverse sea ice conditions, multiple vessels, and different propeller types. About the data distributions that support our statistical analysis, the C_F dataset does not include several data points over the ice thickness interval beyond 1 metre; consequently, the outcomes via the overall curve $\bar{Q}_{ice,F,all}$ (Eq. 4.14) for high values of \bar{h}_{ice} result to be more uncertain, and require further validation.

4.4.3. Future work

In the next steps of this research project, we will continue to collect data from the measurement system on board CCGS *Henry Larsen*. Further measurements in heavy-ice scenarios and during backing-ramming operations will be used to extend the findings presented in this paper. We also aim to conduct high-frequency measurements through the laser tachometers plus additional vibration sensors, in order to study the short-term ice-induced excitation and hence detect the signals produced by single ice-propeller pulses. The results achieved through our data analysis need also to be elaborated and thereby extended to diverse ice-breaker propulsion systems and propeller types, in order to identify a more comprehensive correlation between ice conditions and ice-propeller interaction. Moreover, especially for the thin-ice range, further studies shall be conducted on board different types of vessels with no icebreaking capability.

4.5. Conclusions

This paper presented the results of an integrated experimental and numerical data analysis to investigate the correlation between sea ice conditions and the ice-induced torsional excitation on marine propellers. The CCG medium icebreaker *Henry Larsen* constituted the case study for our work. We developed a lumped-element numerical model to simulate the torsional dynamics of the vessel's shaftline, and its properties were updated via full-scale vibration measures. On board the ship, a multi-device measurement system was arranged with the scope of providing concurrent monitoring of the shaft torsional vibration response and the sea ice scenario during icebreaking operations. We also developed a mathematical algorithm to calculate the ice-propeller interaction excitation using the experimental shaft torque data and the shaftline numerical model. Afterwards, on-board measurements were conducted during two voyages of the ship in ice-covered waters. We analyzed the dataset and studied how the distribution of ice-induced propeller torque peaks and shaft power were related to the mean ice layer thickness. The outcomes of the analysis showed that significant interdependence between those variables exists in forward-direction operations. Finally, our numerical correlations were compared against the ABS-DNV design torque amplitudes as a function of the Polar Class notation and design ice thickness. As a result, our research has shown that the application of the current regulatory framework defining the design ice-propeller torque may produce lower ice-induced loads for an icebreaker like the CCGS *Henry Larsen*. Important results have been found concerning the correlation between ice-induced torque and thin-gray ice, which can be of interest for commercial cargo vessels

encountering light ice. For those types of vessels and propellers, as well as for icebreaker applications, further full-scale data measurements and research are required.

Acknowledgements

The authors thank Mr. Michael Chaisson from the Canadian Coast Guard (CCG), the technicians of the National Research Council of Canada (NRC), and the American Bureau of Shipping (ABS) for their important and kind contribution to this research project, which would not have been possible without their support and availability. We also acknowledge the collaboration of the crew members of CCGS *Henry Larsen*.

This work was supported by the American Bureau of Shipping (ABS) and the Department of Industry, Energy and Technology (IET) of the Government of Newfoundland and Labrador, Canada.

Appendices

4.A. Characteristics of the ice-propeller interaction torque in the IACS

Polar Rules

The IACS Polar Rules [30] provide the mathematical characteristics of the ice-induced impact torque ($Q_{ice,IACS}$) exerted on the propeller blades. In detail, $Q_{ice,IACS}$ is a function of the propeller rotational angle φ , and it is obtained by superposing single ice-block impacts, which correspond to the cutting process of one propeller blade crushing through an ice layer.

One blade passage through the ice is modeled as a semi-sinusoidal function:

$$Q_{\text{ice,IACS}}(\varphi) = C_q(IC) Q_{\text{max}}(PC) \sin\left(\varphi \frac{180}{\alpha_{\text{ice}}(IC)}\right) \quad (4.19)$$

where C_q is a coefficient that depends on the Impact Case (IC) and α_{ice} is also based on IC to define the angular span through which the single ice-blade interaction occurs. Major Classification Societies as the American Bureau of Shipping (ABS) and Det Norske Veritas (DNV) adopt the IACS guidelines with minor variants concerning the formulae terms [2, 19]; in this paper, our calculations are performed with respect to the ABS nomenclature. Fig. 4.24 reports the values of C_q and α_{ice} corresponding to the three IC patterns [2]. $Q_{\text{max}}(PC)$ is the torque amplitude that depends on the propeller's main properties and the Polar Class grade (PC , ranging from 1 to 7), as expressed by the following formula:

$$Q_{\text{max}} = \begin{cases} k_{o,d} \left(1 - \frac{d}{D}\right) \left(\frac{P_{0.7}}{D}\right)^{0.16} \left(\frac{t_{0.7}}{D}\right)^{0.6} (nD)^{0.17} D^3, & D < D_{\text{limit}} \\ 1.9 k_{o,d} \left(1 - \frac{d}{D}\right) \left(\frac{P_{0.7}}{D}\right)^{0.16} \left(\frac{t_{0.7}}{D}\right)^{0.6} H_{\text{ice}}^{1.1} (nD)^{0.17} D^{1.9}, & D \geq D_{\text{limit}} \end{cases} \quad (4.20)$$

where $k_{o,d}$ is a coefficient that depends on both the PC notation and whether the propeller is open or ducted; D and d are the propeller's disc and hub diameters, respectively; $P_{0.7}$ and $t_{0.7}$ are the pitch length and the maximum blade thickness at 70% propeller radius blade section, respectively; n indicates the propeller rotational speed in [rps], or 85% n is taken in case of Diesel-drive FPP; H_{ice} is the design ice layer thickness, which is determined by the PC notation. The parameter D_{limit} is proportional to H_{ice} by a coefficient that varies

between the open and ducted propeller cases.

The number of modular impacts that compose the full ice-propeller interaction process depends on the ice layer thickness, which in turn is determined by the Polar Class grade.

Fig. 4.24 shows an example with the 4 Impact Cases of $Q_{ice}(\varphi)$ for a 4-blade propeller [30].

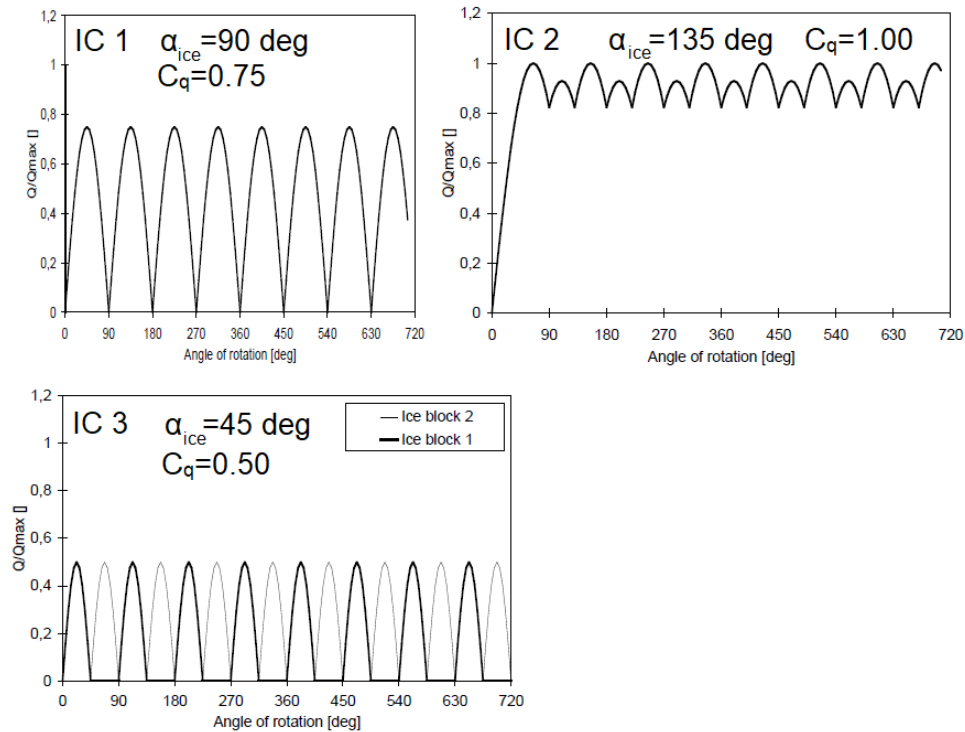


Figure 4.24: Ice-induced torque on a 4-blade propeller. Three impact cases are shown, with the ABS nomenclature concerning *IC* [2, 30].

Additionally, the ABS and DNV introduced the application of a linear rise and descent over the initial and final 270° of the ice-propeller torque impact sequence, respectively [2, 19]. Also, they set the term containing $t_{0.7}$ in Eq. 4.20 to be equal to 1. In this paper, we consider this specific variant when ice-propeller torque calculations are concerned. Fig. 4.25 shows the three *IC* types modified with the two ramps.

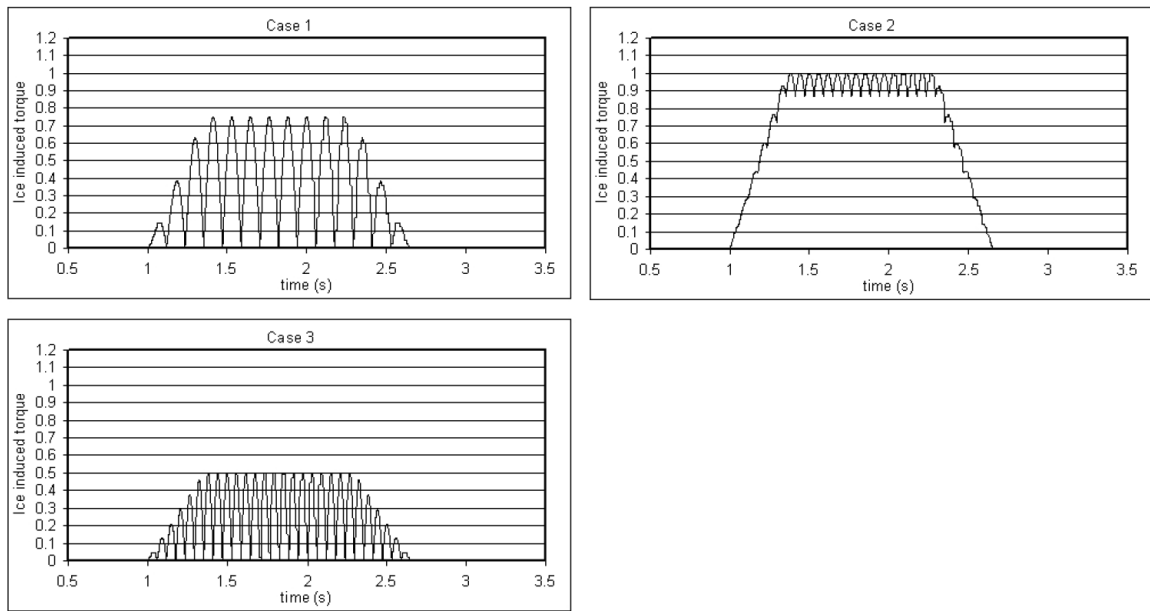


Figure 4.25: Ice-induced torque sequences for the three *IC* cases, with ramps applied [2].

4.B. Structural properties of the case study's shaftline numerical model

The following Tables report the main parameters and characteristics that define the lumped-element model of the shaftline. The structural properties refer to the model updating procedure outcomes. Table 4.5 introduces the shaft material properties employed in the modeling process.

The nodal mass moments of inertia shown in Table 4.6 include also the half-inertia portions from the two adjacent shaft segments. Also, the propeller node (θ_1) includes the contribution of the added inertia due to the water mass, which was calculated as per [18].

Table 4.7 lists the linear stiffness and damping properties of the shafting segments between each adjacent couple of nodes.

Table 4.5: Shaftline material properties.

Parameter		Value	Unit
Steel density	ρ_s	7,850	[kg.m ⁻³]
Steel Young modulus	E	210.3	[GPa]
Steel Poisson ratio	ν	0.27	[-]
Steel shear modulus	G	82.8	[GPa]
Shaft damping factor [1]	S_1	0.005	[-]

Table 4.6: Mass moments of inertia of the model's nodes.

Element	DOF	I_i
	θ_i	[kg.m ²]
Propeller plus added water inertia	θ_1	17,509.0
Tailshaft Node 1	θ_2	999.4
Tailshaft Node 2	θ_3	837.2
Coupling brake	θ_4	786.3
Turning gear	θ_5	160.0
Thrust bearing	θ_6	280.0
Electric motor's rotor	θ_7	10,634.0
Motor exciter	θ_8	98.6
Oil disc	θ_9	15.2

Table 4.7: Torsional stiffness and damping.

Shaft segment	DOFs	$k_{i,i+1}$	$c_{i,i+1}$
	$i, i + 1$	[MNm.rad ⁻¹]	[kNm.(rad/s) ⁻¹]
Tailshaft 1	1, 2	262.3	74.10
Tailshaft 2	2, 3	259.5	73.32
Tailshaft 3	3, 4	1,072.9	303.11
Intermediate shaft	4, 5	253.6	71.65
ED Motor shaft input	5, 6	823.2	232.57
Motor shaft 1	6, 7	347.4	98.14
Motor shaft 2	7, 8	341.2	96.40
Motor shaft 3	8, 9	294.8	83.28

References

- [1] ABS (2011). ABS Torsional Vibration software - V2.1 - Users Manual. Technical report, American Bureau of Shipping. Updated Nov 2011. 145, 185
- [2] ABS (2019). *Part 6: Specialized Items and Systems, Chapter 1: Strengthening for Navigation in Ice, Section 3: Machinery Requirements for Polar Class Vessels*. Rules for Building and Classing - Marine vessels, American Bureau of Shipping, Edition July 2019. xxi, 174, 182, 183, 184
- [3] Adams, M. L. (2010). *Rotating Machinery Vibrations*. Taylor & Francis, 2nd edition. 145
- [4] Al-Bedoor, B. O., Aedwesi, S., and Al-Nassar, Y. (2006). Blades condition monitoring using shaft torsional vibration signals. *Journal of Quality in Maintenance Engineering*. 149
- [5] Bagchi, A. (2005). Updating the mathematical model of a structure using vibration data. *Journal of Vibration and Control*, 11(12):1469–1486. 159
- [6] Batrak, Y. A., Serdjuchenko, A. M., and Tarasenko, A. I. (2012). Calculation of propulsion shafting transient torsional vibration induced by ice impacts on the propeller blades. In *Proceedings of World Maritime Technology Conference (WMTC)*, Saint Petersburg, Russia. 140
- [7] Batrak, Y. A., Serdjuchenko, A. M., and Tarasenko, A. I. (2014). Calculation of torsional vibration responses in propulsion shafting system caused by ice impacts. In *Torsional Vibration Symposium*, Salzburg, Austria. 140
- [8] Bond, J., Hindley, R. J., Kendrick, A., Kämäräinen, J., Kuuliala, L., et al. (2018). Evaluating Risk and Determining Operational Limitations for Ships in Ice. In *OTC Arctic Technology Conference*, Houston, TX, USA. Offshore Technology Conference. 137
- [9] Borch, O. J., Westvik, M. H., Ehlers, S., and Berg, T. E. (2012). Sustainable Arctic field and maritime operation. In *OTC 2012*, pages 1–10. Offshore Technology Conference. OTC23752. 136
- [10] Browse, J., Carslaw, K. S., Schmidt, A., and Corbett, J. J. (2013). Impact of future Arctic shipping on high-latitude black carbon deposition. *Geophysical research letters*, 40(16):4459–4463. 137
- [11] Burella, G. and Moro, L. (2017). Transient torsional analysis of polar class vessel shafting systems using a lumped model and finite element analysis. In *The 27th International Ocean and Polar Engineering Conference*, San Francisco, USA. 140, 143
- [12] Burella, G., Moro, L., and Oldford, D. (2018). Analysis and validation of a procedure for a lumped model of Polar Class ship shafting systems for transient torsional vibrations. *Journal of Marine Science and Technology*, 23(3):633–646. 140, 141, 143, 144, 145, 146, 148
- [13] Carlton, J. S. (2007). *Marine Propellers and Propulsion*. Butterworth-Heinemann, Elsevier, 2nd edition. 146

- [14] Dahler, G., Stubbs, J. T., and Norhamo, L. (2010). Propulsion in ice – Big ships. In *International conference and exhibition on performance of ship and structure in ice - ICETECH*, Anchorage, AK, USA. 138
- [15] de Waal, R. J. O., Bekker, A., and Heyns, P. S. (2017). Bi-Polar Full Scale Measurements of Operational Loading on Polar Vessel Shaft-lines. In *Proceedings of the 24th International Conference on Port and Ocean Engineering under Arctic Conditions (POAC 2017)*, Busan, South Korea. 138
- [16] de Waal, R. J. O., Bekker, A., and Heyns, P. S. (2018). Indirect load case estimation for propeller-ice moments from shaft line torque measurements. *Cold Regions Science and Technology*, 151:237–248. 138, 139
- [17] de Waal, R. J. O., Soal, K., Bekker, A., and Heyns, P. S. (2016). Rotational dynamic characteristics of the shaft line of a Polar supply and research vessel during open water, cavitation and ice navigation. In *Proceedings of ISMA 2016 - International Conference on Noise and Vibration Engineering and USD2016 - International Conference on Uncertainty in Structural Dynamics*, pages 2183–2197. ISMA. 138
- [18] Dien, R. and Schwanecke, H. (1973). Die propellerbedingte Wechselwirkung zwischen Schiff und Maschine. *Motortechnische Zeitschrift*, 34(12):425–430. 145, 184
- [19] DNV (2021). *Part 6: Additional Class Notations, Section 7: Polar Class, Par. 11: Ice interaction loads – machinery*, chapter 6: Cold climate. Det Norske Veritas, Edition July 2021. 174, 182, 183
- [20] Ehlers, S., Kujala, P., Veitch, B., Khan, F., and Vanhatalo, J. (2014). Scenario based risk management for arctic shipping and operations. In *ASME 2014 33rd International Conference on Ocean, Offshore and Arctic Engineering*. American Society of Mechanical Engineers (ASME). 137
- [21] Firouzi, J., Ghassemi, H., and Shadmani, M. (2021). Analytical model for coupled torsional-longitudinal vibrations of marine propeller shafting system considering blade characteristics. *Applied Mathematical Modelling*, 94:737–756. 149
- [22] Granier, C., Niemeier, U., Jungclaus, J. H., Emmons, L., Hess, P., Lamarque, J.-F., Walters, S., and Brasseur, G. P. (2006). Ozone pollution from future ship traffic in the Arctic northern passages. *Geophysical Research Letters*, 33(13). 137
- [23] Han, H. S., Lee, K. H., and Park, S. H. (2016). Parametric study to identify the cause of high torsional vibration of the propulsion shaft in the ship. *Engineering Failure Analysis*, 59:334–346. 148
- [24] Hanninen, S., Viherialehto, S., Maattanen, P., and Heideman, T. (2020). Propulsion Solutions for Large Arctic Offshore Vessels. In *SNAME 25th Offshore Symposium*. Society of Naval Architects and Marine Engineers (SNAME). TOS-2020-001. 137

- [25] Hansen, P. C. (1994). Regularization tools: a Matlab package for analysis and solution of discrete ill-posed problems. *Numerical Algorithms*, 6(1):1–35. Update: Version 4.1, March 2008. 139
- [26] Hindley, R. J., Tustin, R. D., and Upcraft, D. S. (2007). Environmental protection regulations and requirements for ships for Arctic sea areas. In *RINA International Conference - Design and Construction of Vessels Operating in Low Temperature Environments*, pages 107–118, United Kingdom. Royal Institution of Naval Architects. 137
- [27] Hoffmann, K. (2001). Applying the Wheatstone Bridge Circuit. Technical report, Hottinger Baldwin Messtechnik (HBM) GmbH. Version W1569en-1.0. 148
- [28] Hughes, N. E. (2001). Ice Cam: For the Polar Seas, an environmental monitoring solution with implications for navigation and safety. *Sea Technology*, 42(11):36–40. 139
- [29] Ikonen, T., Peltokorpi, O., and Karhunen, J. (2015). Inverse ice-induced moment determination on the propeller of an ice-going vessel. *Cold Regions Science and Technology*, 112:1–13. 139
- [30] International Association of Classification Societies (IACS) (2006). Requirements concerning Polar Class - Polar Rules. Rev. 1 Jan 2007, Corr. 1 Oct 2007. xxi, 137, 140, 141, 174, 178, 181, 183
- [31] International Maritime Organization (IMO) (2017). International Code for Ships Operating in Polar Waters (Polar Code). MEPC 68/21. 137
- [32] Irgens, O.-J., Kokkila, K., Hänninen, S., et al. (2018). Propulsion Technology for Polar Expedition Ships. In *OTC Arctic Technology Conference*. Offshore Technology Conference. 137
- [33] Jussila, M. and Koskinen, P. (1989). Ice loads on CP-propeller and propeller shaft of small ferry and their statistical distributions during winter '87. In *Proceedings of the 8th International Conference on Offshore Mechanics and Arctic Engineering*, volume IV. 138
- [34] Kendrick, A. and Santos-Pedro, V. (2010). The future of polar shipping rules. In *International Conference and Exhibition on Performance of Ships and Structures in Ice - ICETECH 2010*, pages 31–35. 137
- [35] Kendrick, A. M. (2014). Polar ship design standards - state of the art, and way forward. In *Transactions - Society of Naval Architects and Marine Engineers (SNAME)*, volume 122, pages 428–433, Houston, TX, USA. 137
- [36] Khan, A. G., Hissette, Q., and Streckwall, H. (2018). Numerical Investigation of Propeller-Ice Interaction Effects. In *The 28th International Ocean and Polar Engineering Conference*, Sapporo, Japan. International Society of Offshore and Polar Engineers. 179
- [37] Kinnunen, A., Turunen, T., Koskinen, P., and Heinonen, J. (2017). Propulsion Shaft Line Ice-Induced Dynamic Torque Response. In *Proceedings of the 24th International Conference on Port and Ocean Engineering under Arctic Conditions (POAC 2017)*, Busan, South Korea. 139, 140

- [38] Kitagawa, H. et al. (2011). Safety and Regulations of Arctic Shipping. In *The Twenty-first International Offshore and Polar Engineering Conference*. International Society of Offshore and Polar Engineers. 137
- [39] Kujala, P., Goerlandt, F., Way, B., Smith, D., Yang, M., Khan, F., and Veitch, B. (2019). Review of risk-based design for ice-class ships. *Marine Structures*, 63:181–195. 137
- [40] Lensu, M., Kujala, P., Kulovesi, J., Lehtiranta, J., and Suominen, M. (2015). Measurements of Antarctic sea ice thickness during the ice transit of SA Agulhas II. In *Proceedings of the International Conference on Port and Ocean Engineering Under Arctic Conditions (POAC 2015)*, Trondheim, Norway. 139
- [41] Liu, P., Bose, N., and Veitch, B. (2015). Evaluation, design and optimization for strength and integrity of polar class propellers. *Cold Regions Science and Technology*, 113:31–39. 179
- [42] Lu, W., Zhang, Q., Lubbad, R., Løset, S., Skjetne, R., et al. (2016). A shipborne measurement system to acquire sea ice thickness and concentration at engineering scale. In *Arctic Technology Conference*, St. John's, NL, Canada. OTC. 139
- [43] MAN (2011). Basic Principles of Ship Propulsion. Frederikshavn, Denmark. MAN Diesel & Turbo. 146
- [44] Melia, N., Haines, K., Hawkins, E., and Day, J. J. (2017). Towards seasonal Arctic shipping route predictions. *Environmental Research Letters*, 12(8). 084005. 136
- [45] Murawski, L. and Charchalis, A. (2014). Simplified method of torsional vibration calculation of marine power transmission system. *Marine structures*, 39:335–349. 144
- [46] Niioka, T. and Kohei, C. (2010). Sea ice thickness measurement from an ice breaker using a stereo imaging system consisted of a pairs of high definition video cameras. *International Archives of the Photogrammetry, Remote Sensing and Spatial Information Science, Kyoto Japan*, 38(8):1053–1056. 139
- [47] Parsons, M. G., Srinivas, J., and Raju, V. (1983). Mode coupling in torsional and longitudinal shafting vibration. *Marine Technology*, 20(3):257–271. 144
- [48] Pietri, D., Soule I V, A. B., Kershner, J., Soles, P., and Sullivan, M. (2008). The Arctic shipping and environmental management agreement: a regime for marine pollution. *Coastal Management*, 36(5):508–523. 137
- [49] Polić, D., Æsøy, V., and Ehlers, S. (2016). Transient simulation of the propulsion machinery system operating in ice—modeling approach. *Ocean Engineering*, 124:437–449. 140
- [50] Polić, D., Æsøy, V., Ehlers, S., and Pedersen, E. (2014). Shaft response as a propulsion machinery design load. In *Proceedings of the ASME 2014 33rd International Conference on Ocean, Offshore and Arctic Engineering (OMAE2014)*, San Francisco, California, USA. 140
- [51] Polić, D., Ehlers, S., and Æsøy, V. (2017). Propeller Torque Load and Propeller Shaft Torque Response Correlation During Ice-propeller Interaction. *Journal of Marine Science Applications*, 16(1):1–9. 140

- [52] Polić, D., Ehlers, S., and Æsøy, V. (2019). Inverse modeling approach for transformation of propeller shaft angular deformation and velocity to propeller torque load. *Marine Structures*, 67. 140
- [53] Remond, D. (1998). Practical performances of high-speed measurement of gear transmission error or torsional vibrations with optical encoders. *Measurement Science and Technology*, 9(3):347. 151
- [54] Schröder, C., Reimer, N., and Jochmann, P. (2017). Environmental impact of exhaust emissions by Arctic shipping. *Ambio*, 46(3):400–409. 137
- [55] Senjanović, I., Hadžić, N., Murawski, L., Vladimir, N., Alujević, N., and Cho, D.-S. (2019). Analytical procedures for torsional vibration analysis of ship power transmission system. *Engineering Structures*, 178:227–244. 145, 148
- [56] Veitch, B. (1995). *Predictions of Ice Contact Forces on a Marine Screw Propeller During the Propeller-Ice Cutting Process*. PhD thesis, Helsinki University of Technology, Finland. Acta Polytechnica Scandinavica, Mechanical Engineering Series. 179
- [57] Weissling, B., Ackley, S., Wagner, P., and Xie, H. (2009). EISCAM—Digital image acquisition and processing for sea ice parameters from ships. *Cold Regions Science and Technology*, 57(1):49–60. 139
- [58] Williams, F. M., Spender, D., Mathews, S. T., and Bayly, I. (1992). Full Scale Trials in Level Ice with Canadian R-Class Icebreaker. In SNAME, editor, *SNAME Transactions*, volume 100, pages 293–313. 138
- [59] Yumashev, D., van Hussen, K., Gille, J., and Whiteman, G. (2017). Towards a balanced view of Arctic shipping: estimating economic impacts of emissions from increased traffic on the Northern Sea Route. *Climatic Change*, 143(1-2):143–155. 137
- [60] Zambon, A. and Moro, L. (2022). Torsional vibration analysis of diesel driven propulsion systems: The case of a polar-class vessel. *Ocean Engineering*, 245:110330. 145
- [61] Zhang, Z., Huisingh, D., and Song, M. (2019). Exploitation of trans-Arctic maritime transportation. *Journal of cleaner production*, 212:960–973. 136

Chapter 5

Impact of different characteristics of the ice-propeller interaction torque on the torsional vibration response of a Polar-Class shaftline

Abstract

During navigation in Polar regions, ice-induced torque excitation endanger the operation and integrity of ship propulsion systems. Predicting these dynamic phenomena through proper numerical models is therefore essential. This paper studies the influence of different properties of the ice-propeller torque on the transient torsional dynamics of a Polar-Class shafting system. To this end, we initially considered the ice torque pattern defined by the

current regulatory framework. Hence, we examined variants of four ice impact properties—(i) rise shape; (ii) angular span; (iii) ramps up-down feature; (iv) number of ice impacts—to study the transient and steady-state conditions induced by the ice-propeller excitation. We performed a series of torsional vibration analyses, using the numerical model of the shaftline of the Canadian Coast Guard (CCG) icebreaker *Terry Fox*. Furthermore, we tested the system with Diesel engine and electric motor excitation models interchangeably; the electric drive solution proved to counter ice-induced transient perturbations more effectively. The results indicate that the ice impact span, the ramps up-down application, and the number of impacts are the most important factors to affect the shaftline’s rotational speed drop and response torque. In particular, the significance of the ice impact ramps is such that it might entail a review of the in-force regulatory guidelines.

Keywords

Torsional Vibration Analysis; Ice-propeller interaction; Ship propulsion systems; Polar Class; Icebreakers.

5.1. Introduction

5.1.1. Background

Over the recent decades, the hazard posed by the interaction between sea ice and ship propulsion systems has become more and more significant, as the volume of marine traffic and operations across the Arctic region has increased [15, 42, 53]. This involved all

types of vessels; therefore, the International Maritime Organization (IMO) and the various Classification Societies have had to evolve shipbuilding standards and regulations constantly [22, 23, 24]. The ship-design process within the Polar Class framework needs to satisfy concurrently multiple goals, which may be challenging to integrate. Specifically, propulsion and machinery systems are required to be highly reliable while meeting stringent emission criteria and safety standards [17, 27, 50]. To accomplish these requirements, assessing the risks associated with the scenarios in which ice-going vessels are supposed to operate has acquired great importance [5, 14, 28]. In this approach, the proper design methodology of ship propulsion systems is one of the most relevant processes [16, 21].

5.1.2. Ice-propeller interaction loads: modelling and applications

Several research works have been conducted to simulate the dynamic loads induced by ice-milling phenomena on marine propellers. Realistic models to simulate this excitation are fundamental for two main reasons: (i) determine the propeller blade strength and investigate the impact on propulsion efficiency; (ii) study the ice-induced dynamic effects on the shafting system components through vibration analysis.

Concerning Polar-Class propeller design, Liu et al. integrated advanced Finite Element (FE) techniques to evaluate the blade robustness with optimization strategies to reduce the propeller's weight [32]. Similarly, Wang et al. used FE Analysis (FEA) to investigate the time-domain, ice-milling process to obtain the corresponding dynamic loading and propeller blade response [47]. Scale-model test experiments in ice towing tanks were also conducted, aiming to validate numerical methods for the ice-propeller loading and

to observe the corresponding drop in propulsive efficiency [6, 25, 48]. In particular, the combined experimental-numerical results obtained by Veitch represented a groundbreaking work regarding the characterization of the ice-milling loads as a function of propellers' geometry [46]. Furthermore, Lee applied the investigation on ice-propeller interaction loads to the powering design and propulsion performance assessment [30]. These studies highlighted that the overall loads on the propellers can be decoupled into two components: ice-propeller load and hydrodynamic load. This assumption is adopted in the Polar Rules by the International Association of Classification Societies (IACS) for all degrees of freedom (DOF) of the ice-propeller excitation [20]. Specifically, the IACS rules require that the torsional load is modelled as a sequence of superposed impacts, each having a semi-sinusoidal pulse shape[20]; this modelling guideline is straightforward to be implemented, but it approximates the actual ice-impact curve.

Accurate modelling of the ice-propeller interaction allows ship designers to estimate the corresponding dynamic response of ship propulsion systems, subject to high torsional stresses in the shafting segments and abrupt torque reactions of prime movers. To study these processes, Torsional Vibration Analysis (TVA) represents the primary design tool; experimental campaigns have proven fundamental to support the development of TVA methods connected with ice-induced excitation.

A joint Finnish and South-African research team conducted vibration measurements aboard two Antarctic-going ships; torsional strain gauges and accelerometers were employed to detect short-term ice-propeller milling occurrences [10, 11]. Firstly, a statistical analysis on the distribution of the shaft response torque peaks was performed [10]; afterwards,

the authors analyzed the shaft torque vibration data to obtain the ice-propeller excitation numerically, also discussing the effectiveness of different algorithms [11, 19, 35]. The authors achieved remarkable results; however, the prime mover excitation influence on the shaft dynamics was not considered in detail.

On this matter, the approach undertaken by Polić et al. focused on the propulsion drive excitation modelling; Bond-Graph (BG) elements were used to simulate the torsional dynamics of a Diesel-driven shafting system under ice-induced loads [36, 37, 39]; the authors used the DNV guidelines to implement numerically the ice-propeller excitation [13]. The BG-based model was validated against FE simulations [36]. Hence, the authors developed an inverse algorithm to estimate ice-induced transient loads from torsional vibration measures [38]. The analyses in the studies by Polić et al. did not involve full-scale experimental measurements.

Other studies focused on shaftlines' vibration response and modelling approaches more in detail, while considering the IACS guidelines to simulate the ice-induced excitation on the propeller. Kinnunen et al. investigated the case of a Z-drive propeller system connected to an Electric motor; MATLAB® Simscape was used to simulate the transmission system, and the numerical outcomes were compared with the torque and speed readings acquired during full-scale measurements [26]. Burella et al. performed a sensitivity analysis through FEA on the shaft structural properties of an Electric-drive shaftline to determine its response to ice-induced loads as a function of different shaft properties [7, 8]. Lecourt Jr analyzed the mathematical models for the complete powering system of a Diesel-Electric icebreaker; all components and control systems of the propulsion plant are integrated [29]. Batrak et al.

developed a design tool to simulate the torsional dynamics of shaftlines. They simulated the ice-induced TVA of a Diesel-driven shaftline using the Kujawski-Gallager algorithm [4]. Yang et al. used the Newmark method to perform a time-domain TVA for the shaftline of an Ice-Class bulk carrier; the analyzed propulsion system featured a 2-stroke Diesel engine drive, which was simulated through a simplified model [49].

5.1.3. Contribution of this work

The scope of the present paper is studying (i) to what extent different patterns of the ice-propeller interaction torque affect the transient, torsional vibration response of an icebreaker propulsion system, and (ii) the response to ice-propeller interaction of two different prime movers—Diesel engine (DE) and electric motor (EM).

The CCG heavy icebreaker *Terry Fox* is considered as a case study. In [51], we developed and validated a numerical model to simulate the torsional dynamics of the vessel's shaftline. In this paper, we present a more detailed model of the DE and benchmark it against experimental data. Then, the validated model is used to perform a series of TVA simulations, where we vary four properties of the Polar Rules' ice-propeller torque.

In addition, we consider the case of equivalent-power EMs in place of the DEs to investigate the influence of diverse prime movers on the shaftline dynamic response.

5.2. Methods

5.2.1. Overview

Fig. 5.1 outlines the organization of the present paper.

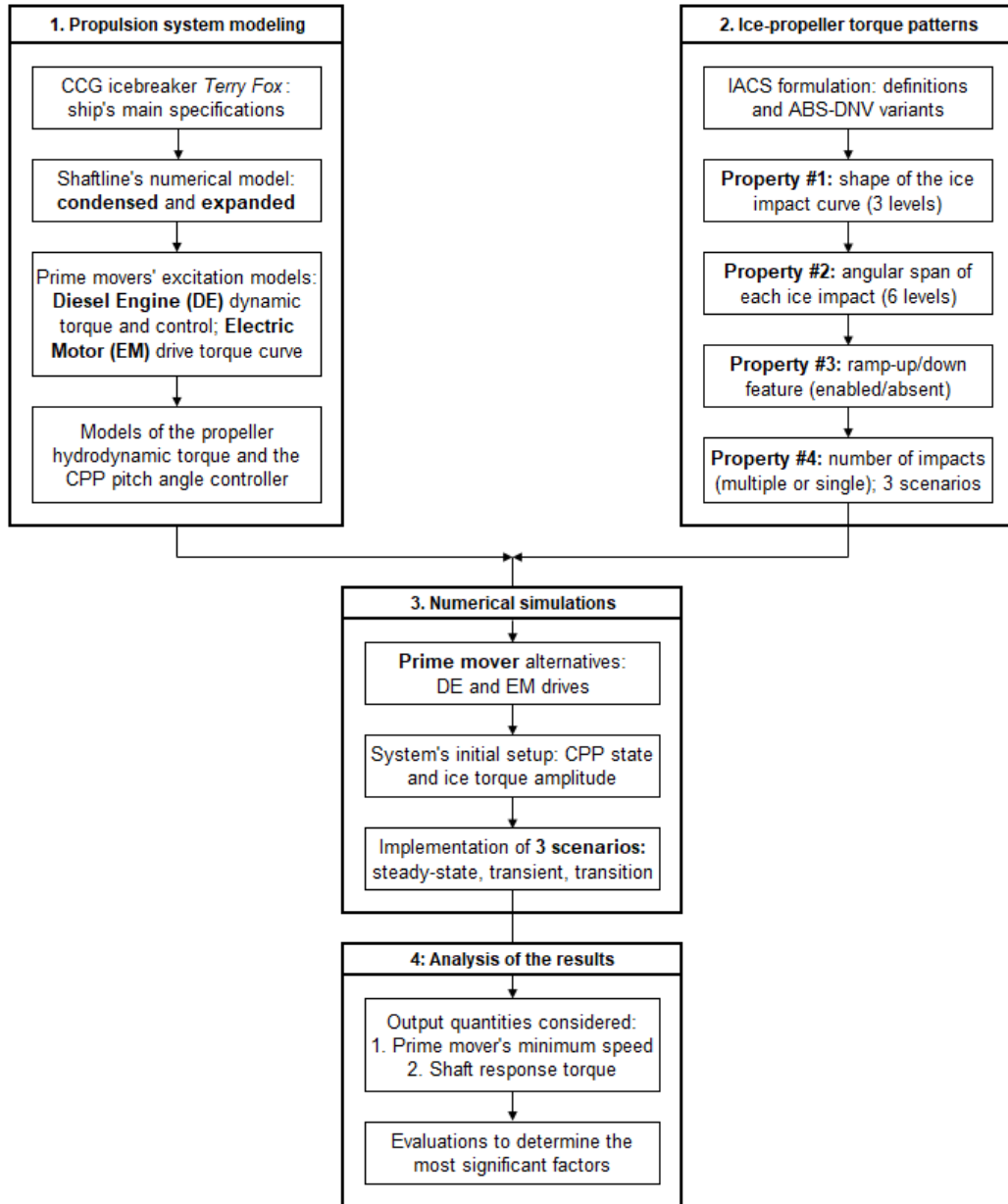


Figure 5.1: Flowchart illustrating the paper structure.

Firstly, we resume the methodology to model the case study shaftline and the corresponding excitation torques [51], and we introduce a more elaborate version of the shaftline's model we used in [51]. The DE torque and control modelling are outlined, together with the model of the alternative EM excitation (Subsection 5.2.2).

After recalling the ice-propeller torques as per the IACS Polar Rules [20] and the variations by the American Bureau of Shipping (ABS) and Det Norske Veritas (DNV) [2, 13], we introduce the modifications on the ice impact model that we implemented (Subsection 5.2.3). The overall analysis is subdivided into three scenarios, which differ in the number of consecutive impacts.

Subsections 5.2.4.1 and 5.2.4.2 present the three sets of TVA simulations, with also the alternative EM-drive option. Finally, we analyze and discuss the results (Section 5.3).

5.2.2. Numerical model of the case study shaftline

5.2.2.1 Case study vessel

Table 5.1 outlines the main properties of the CCG Ship (CCGS) *Terry Fox*, which is shown in Fig. 5.2. The propulsion plant of the icebreaker includes two shafting systems, which drive two Controllable Pitch Propellers (CPP). Each shaftline is powered by two 4-stroke Diesel engines (Stork-Werkspoor, model 8TM410) connected to the shaft through a reduction gearbox. A power take-off (PTO) electric generator can be engaged with the slow gear of each gearbox. Table 5.2 shows the main specifications of the system.



Figure 5.2: CCGS *Terry Fox* in ice-covered waters.

Table 5.1: Main specifications of the CCG heavy icebreaker *Terry Fox*.

Quantity		Value	Unit
Length OA	L_{OA}	88.0	[m]
Beam	B	17.8	[m]
Service draft	d	8.3	[m]
Gross Tonnage	GT	4,234	[GT]
Maximum speed	$V_{S,max}$	16.0	[kn]
Nominal propulsion power	$P_{eng,tot}$	17.3	[MW]
Arctic Class	AC	4	[-]

5.2.2.2 Shaftline model: condensed version

The CCGS *Terry Fox*'s propulsion line was modelled as a lumped-element system in MATLAB [51]. Fig. 5.3 shows a longitudinal view of the icebreaker's transmission line and the corresponding lumped system, which is composed of 5 inertial nodes associated with torsional DOFs. The hydrodynamic torque (Q_h) and the ice-induced torque (Q_{ice}) are exerted on the propeller node, while the total DE-delivered torque (Q_{eng}) is applied to the engine node.

Table 5.2: Main specifications of the CCGS *Terry Fox*'s propulsion system components.

Quantity		Value	Unit
<i>Machinery</i>			
Engine nominal power, at 100% load	$P_{\text{eng,max}}$	4,265	[kW]
Number of cylinders	N_{cyl}	8	[-]
Engine nominal speed	n_{eng}	600	[rpm]
Gearbox reduction ratio	γ	4.625	[-]
<i>Controllable Pitch Propeller</i>			
Diameter	D_{prop}	4.800	[m]
Number of blades	Z	4	[-]
Nominal rotational speed	n_{prop}	129.73	[rpm]
Zero-thrust pitch angle at 70% R	Φ_{min}	-0.86	[deg]
Maximum pitch angle at 70% R	Φ_{max}	25.92	[deg]

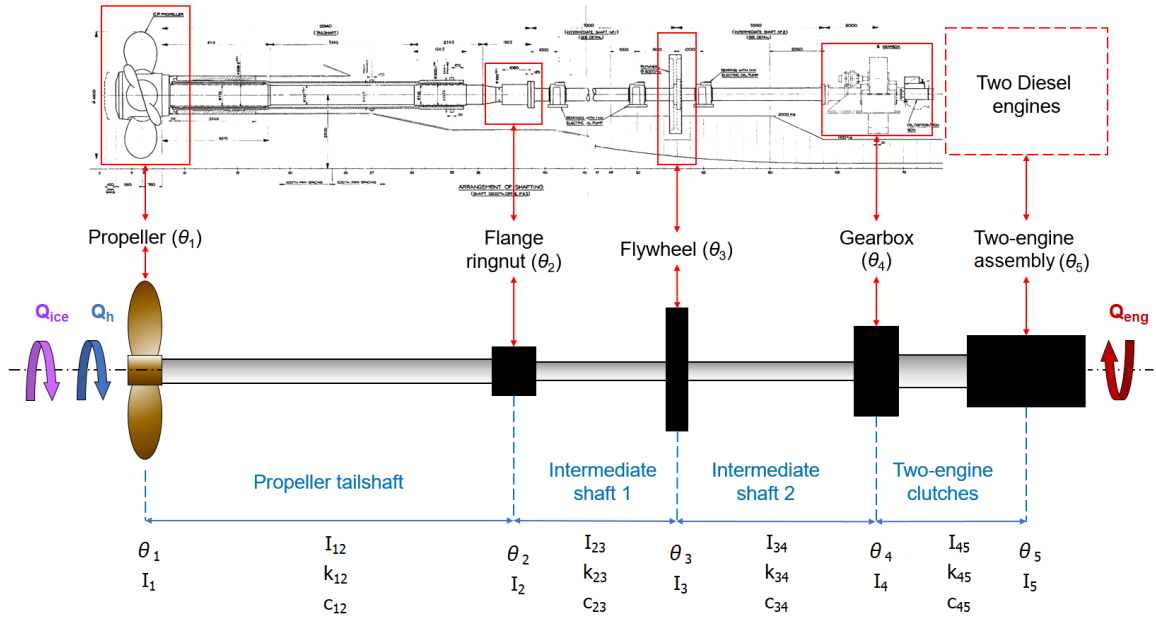


Figure 5.3: Outline of the shaftline's condensed model of the case study [51].

Given the linearity of the system, its dynamic equation of motion is as follows:

$$[\mathbf{I}]\ddot{\vec{\theta}} + [\mathbf{C}]\dot{\vec{\theta}} + [\mathbf{K}]\vec{\theta} = \vec{Q} \quad (5.1)$$

where $[\mathbf{I}]$, $[\mathbf{C}]$, $[\mathbf{K}]$ are the torsional inertia, damping, stiffness matrices respectively; $\vec{\theta} = [\theta_1, \dots, \theta_5]^T$ and $\vec{Q} = [Q_1, \dots, Q_5]^T$ are the torsional DOFs and excitation torque vectors, respectively.

5.2.2.2.1 Node modelling

The mass moment of inertia of the propeller node (θ_1) is the sum of the mass moment of inertia of the propeller (dry condition), and the contribution of the water's added mass.

The added torsional inertia is calculated with the empirical formula of Eq. 5.2 [12]:

$$I_{\text{prop,add}} = 0.0703 g \frac{\rho D_{\text{prop}}^5}{\pi Z} \left(\frac{P_{0.70R}}{D_{\text{prop}}} \right)^2 \left(\frac{A_E}{A_0} \right)^2 \quad [\text{kg.m}^2] \quad (5.2)$$

where g is the gravity acceleration, Z is the number of blades, A_E/A_0 is the expanded area ratio, and $P_{0.70R}$ is the pitch length at the blade section at 70% of the propeller radius.

The two transmission line's branches connected through the gearbox rotate at different speeds. In our model, we consider the entire shaftline to rotate according to the propeller-branch, slow speed. Consequently, the inertia, stiffness, damping properties of the fast-speed, engine branch (subscript F) are converted into the corresponding slow-speed equivalents (subscript S) as per the relations in Eq. 5.3 [3, 34, 45]:

$$I_S = \gamma^2 I_F \quad k_S = \gamma^2 k_F \quad c_S = \gamma^2 c_F \quad Q_S = \gamma Q_F \quad (5.3)$$

where γ is the reduction ratio between the F-speed and the S-speed branches.

In the condensed version of the shaftline model, the torsional inertia of the fast-speed

rotating parts in the Diesel engines are lumped into a single element, represented by the DOF θ_5 .

5.2.2.2.2 *Shafting segment properties*

Each shaft connection's inertia is split into two halves, which are incorporated into the two adjacent nodes. The equivalent viscous damping coefficient of the shaft connections refers to the material's hysteresis formulation [41]. Therefore, the torsional stiffness ($k_{i,i+1}$) and damping ($c_{i,i+1}$) coefficients of the i -th shaft—which is comprised between the nodes i and $i + 1$ —are calculated according to Eq. 5.4:

$$k_{i,i+1} = G \frac{J_{P,i,i+1}}{l_{i,i+1}} \quad c_{i,i+1} = S_1 \frac{k_{i,i+1}}{\omega_{\text{prop}}} \quad (5.4)$$

where G is the shear modulus of the material, $J_{P,i,i+1}$ is the polar moment of inertia of the shaft sectional area, $l_{i,i+1}$ is the shaft length, ω_{prop} is the shaft nominal angular speed. S_1 is the uni-dimensional damping factor, whose dimensionless value can be assumed as 0.005 for all shafts [1].

5.A includes the overall inertia, stiffness, and damping coefficients of the condensed numerical model [51].

5.2.2.3 **Shaftline model: expanded version**

5.2.2.3.1 *Model's description*

We developed an augmented lumped-element system (“expanded model”), including the DE rotating elements. This model allows us to: (i) evaluate the reaction of multiple system

components to transient perturbations; (ii) account for the mutual dynamic interaction between adjacent cylinder-crank nodes. Fig. 5.4 shows its configuration, in which all DE crank arms and the torsional vibration damper (TVD) of each engine are modelled as separate lumped elements; overall, the expanded model is composed of 22 DOFs. The total inertia of the DE items and TVDs coincides with the θ_5 -node inertia in the condensed model. In particular, $Q_{cyl,i}$ indicates the torque produced by the i -th DE cylinder on the i -th crank arm.

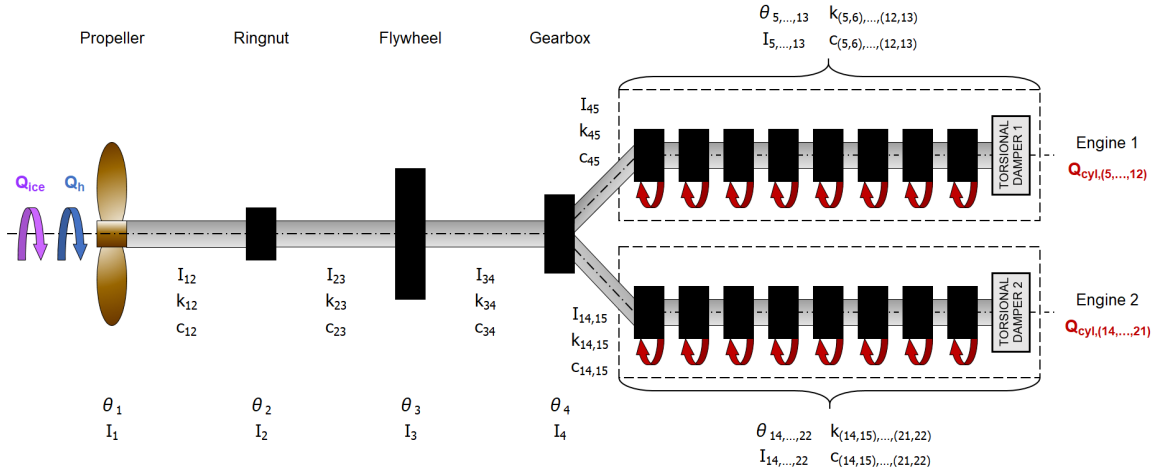


Figure 5.4: Outline of the shaftline's expanded model of the case study.

Concerning the crankshaft connections between the crank arms, the value $S_1 = 0.0001$ was employed for the damping determination (Eq. 5.4, [1]). We determined the stiffness and damping coefficients of each TVD connection through the relations that characterize the vibration absorbers, with respect to the engine nominal speed (ω_{eng}) [41]:

$$k_{TVD} = \tau I_{TVD} \omega_{eng}^2 \quad c_{TVD} = 2 \zeta_{TVD} \sqrt{k_{TVD} I_{TVD}} \quad (5.5)$$

where I_{TVD} is the overall moment of inertia of the TVD and ζ_{TVD} is the equivalent viscous damping ratio, which was estimated to be equal to 0.10 [43]. The coefficient τ is the damper's tuning factor which is used to calibrate k_{TVD} and therefore the vibration damper [41]. To determine τ , we adjusted its value by iterating numerical modal analyses of the expanded model.

5.2.2.3.2 *Model validation via full-scale measurements*

In December 2019, a series of shaft vibration measurements were carried out on board the icebreaker during her sea trials in free-running conditions, and the obtained data was employed to validate the condensed version of the shaftline model [51]. We utilized Wheatstone-bridge, torsional strain gauges connected to wireless data acquisition systems to acquire shaft torsional vibration data at different DE operation points, with a sampling frequency of 256 Hz. VPG Sensors Corp. manufactured the gauges, and they were positioned on the shaft surface according to [18]. The gauge's single coils presented a 350Ω resistance, with a gauge factor for both rosettes of $k_g = 2.08$ [18]. Each sensor was wired to a differential analog channel input on a wireless data transmitter: a V-Link-200 Node® device manufactured by LORD Sensing Systems Corporation. The sensor node was interfaced to a laptop through a WSDA-200-USB® gateway and it was set up and controlled by the software SensorConnect®. For this experiment, we set a ± 2.44 V range for the measured voltage and a wireless transmission power of 10 dBm. Each differential channel of the Node transmitter incorporated an anti-aliasing, 2nd-order Butterworth filter, with cutoff frequency equal to 128 Hz.

Fig. 5.5 outlines the equipment, which was attached to the “Intermediate Shaft 1” segment of each shaftline (Fig. 5.3).

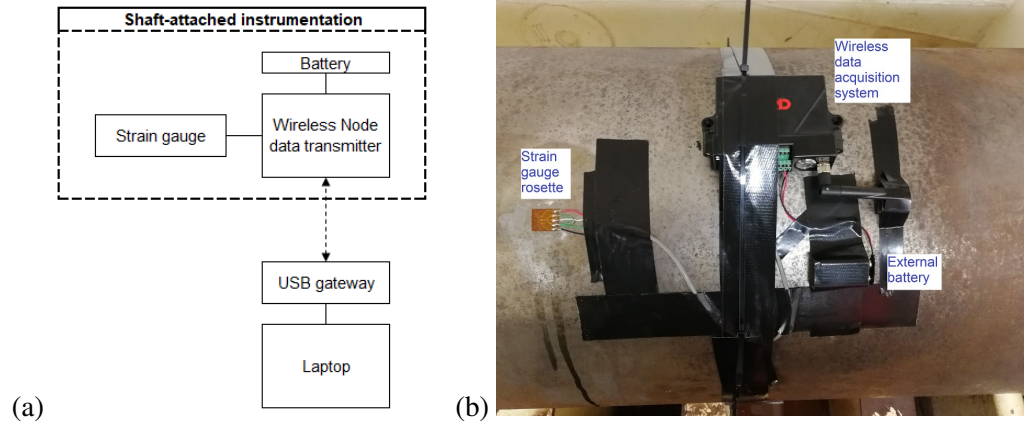


Figure 5.5: Experimental apparatus scheme (a); shaft’s strain gauge and wireless data transmitter (b) [51].

We compare its first four nonzero eigenfrequencies with the corresponding resonance frequencies that are visible in the measured torsional vibration spectra, to validate the expanded model of the shaftline. Those four vibration modes are homologous to the condensed model’s ones: they correspond to the modal shapes associated to the propeller-gearbox branch, which is the same in both models. In the validation, we consider the zero-thrust condition of the propeller, when the CPP angle was set to zero and thus the propeller’s torsional added inertia could be neglected (Eq. 5.2). The dynamics of the model is then validated disregarding the additional effects of the added inertia.

5.2.2.4 Excitation torques

5.2.2.4.1 DE dynamic torque

The torque produced by one c -stroke, DE cylinder (Q_{cyl}) is composed of the reciprocating assembly part (Q_{rec}) and the combustion pressure part (Q_p), as shown in Eq. 5.6 and

Fig. 5.7(a):

$$Q_{cyl}(\varphi) = Q_{rec}(\varphi) + Q_p(\varphi) \quad (5.6)$$

where φ is the angular coordinate of the connected crank arm. Fig. 5.6 shows the general configuration of a cylinder assembly system.

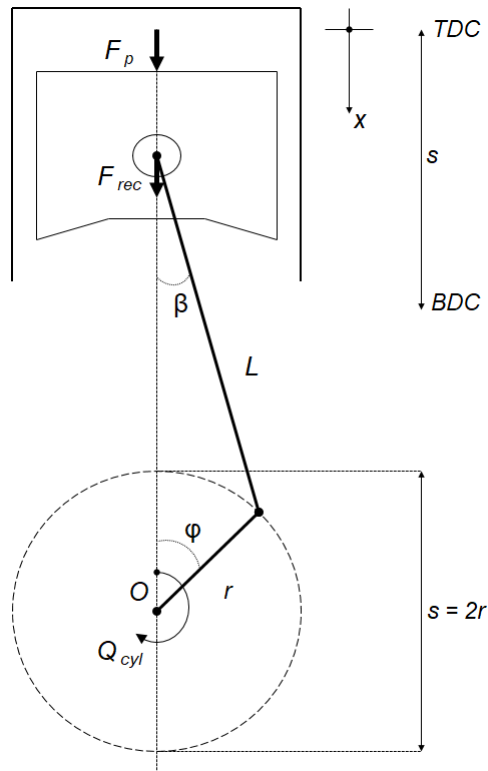


Figure 5.6: Simplified diagram of a piston, connecting rod, crank arm assembly. x is the piston's coordinate, L is the connecting rod's length, $s = 2r$ is the stroke length and r is the crank radius. φ is the crank angle, and β is the angle between the connecting rod and the vertical direction. $\vec{F}_{rec}(\varphi)$ and $\vec{F}_p(\varphi)$ are the forces generated by the reciprocating parts and the combustion pressure, respectively [51].

In detail, the analytical expression of $Q_{rec}(\varphi)$ is reported in Eq. 5.7:

$$\begin{aligned}
Q_{\text{rec}}(\varphi) &= \left(\vec{F}_{\text{rec}}(\varphi) \wedge \vec{r} \right) \cdot \hat{z} \\
&= -m_{\text{rec}} (\omega_{\text{eng}} r)^2 \left[\cos \varphi \left(1 + \frac{\lambda \cos \varphi}{\xi} \right) + \lambda \sin^2 \varphi \left(\frac{\lambda^2 \cos^2 \varphi}{\xi^3} - \frac{1}{\xi} \right) \right] \frac{\sin(\varphi + \beta)}{\cos \beta}
\end{aligned} \tag{5.7}$$

where \vec{r} is a vector of origin O and magnitude r , \hat{z} is a unitary vector which lays on the crankshaft rotational axis, according to a right-handed coordinate system, $\lambda = r/l$, and $\xi = \sqrt{1 - \lambda^2 \sin^2 \varphi}$.

$Q_{\text{p}}(\varphi)$ is determined via Eq. 5.8:

$$\begin{aligned}
Q_{\text{p}}(\varphi) &= \left(\vec{F}_{\text{p}}(\varphi) \wedge \vec{r} \right) \cdot \hat{z} \\
&= p_{\text{cyl}}(\varphi) A_{\text{cyl}} r \frac{\sin(\varphi + \beta)}{\cos \beta}
\end{aligned} \tag{5.8}$$

where $p_{\text{cyl}}(\varphi)$ is the combustion pressure curve and A_{cyl} is the cylinder sectional area, which has the bore as diameter. $p_{\text{cyl}}(\varphi)$ is described through the following expression [51]:

$$p_{\text{cyl}}(\varphi) = \begin{cases} p_0 + \frac{p_{\text{peak}} - p_0}{\varphi_{\text{peak}}^\alpha} \varphi^\alpha & \text{for } \varphi \in [0, \varphi_{\text{peak}}] \\ p_0 + \frac{p_{\text{peak}} - p_0}{(c\pi - \varphi_{\text{peak}})^\alpha} (c\pi - \varphi)^\alpha & \text{for } \varphi \in]\varphi_{\text{peak}}, c\pi] \end{cases} \tag{5.9}$$

where the parameters $\{p_0, p_{\text{peak}}, \alpha, \varphi_{\text{peak}}\}$ compose the set $S_{\text{eng}}(\ell_{\text{p}})$, which identifies the curve $p_{\text{cyl}}(\varphi)$ at a specific engine load rate (ℓ_{p}). The procedure to tune S_{eng} is based on the energy balance of the engine at steady-state operations and is described in detail in [51].

Finally, the total torque delivered by a Diesel engine ($Q_{\text{eng}}(\varphi)$, Eq. 5.10) is the superpo-

sition of all $Q_{\text{cyl}}(\varphi)$ contributions of the N_{cyl} cylinders.

$$Q_{\text{eng}}(\varphi) = \sum_{i=1}^{N_{\text{cyl}}} Q_{\text{cyl}}(\varphi + \delta_i), \quad \delta_i = \left\{ 0, \frac{c\pi}{N_{\text{cyl}}}, \dots, \frac{c\pi}{N_{\text{cyl}}}(N_{\text{cyl}} - 1) \right\} \text{ [rad]} \quad (5.10)$$

where δ_i is the phase offset, determined by the engine firing sequence. Fig. 5.7 shows examples of the curves for $Q_{\text{cyl}}(\varphi)$ and $Q_{\text{eng}}(\varphi)$.

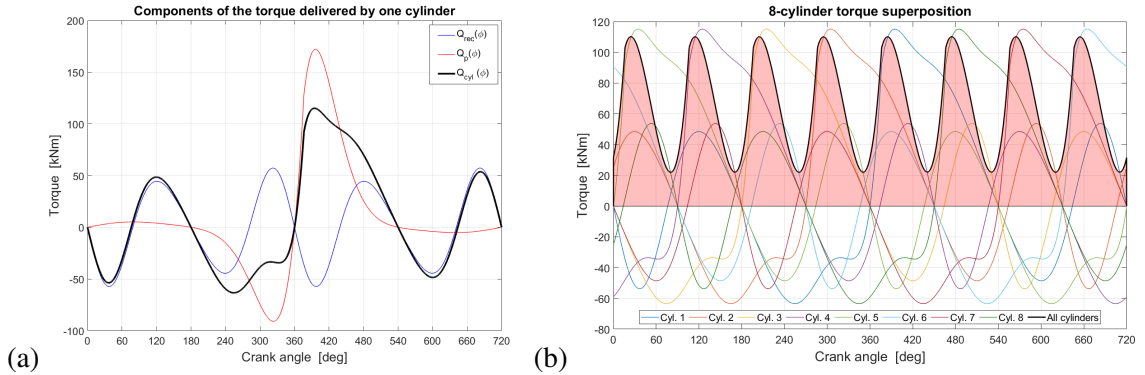


Figure 5.7: (a) Cylinder torque as per Eq. 5.6; (b) DE overall torque as per Eq. 5.10 [51].

In the condensed model of the shaftline (Fig. 5.3), $Q_{\text{eng}}(\varphi)$ from Eq. 5.10 is applied to the θ_5 node (Fig. 5.3). In the expanded model (Fig. 5.4), $Q_{\text{cyl}}(\varphi + \delta_i)$ from Eq. 5.6 is applied to each i -th crank arm node with the corresponding phase offset, which is superposed on top of the instantaneous DOF angular position; thereby, the torsional twist between adjacent crank arms is accounted in each cylinder's cycle.

The DE fuel governor is simulated through a proportional control that acts on the steady-state combustion peak pressure (\bar{p}_{peak}) [40, 44]. The update of the instantaneous peak pressure value ($p'_{\text{peak}}(t)$) is based on the difference between the engine's instantaneous rotational speed ($\omega(t)$) and the nominal speed (ω_{eng}) ($\Delta\omega(t) = \omega(t) - \omega_{\text{eng}}$):

$$p'_{\text{peak}}(t) = \bar{p}_{\text{peak}} [1 + k_p \Delta\omega(t)] \quad (5.11)$$

where k_p is the instantaneous pressure corrective factor ((rad/s)⁻¹).

5.2.2.4.2 EM torque characteristics

The alternative EM drive replaces the DE in the shaftline's condensed model (θ_5). The EM torque output is modelled through a constant-power curve as a function of the speed (n). The torque curve ($Q_{EM}(n)$) is capped at the limit value ($Q_{EM,\text{max}}$), determined by the EM manufacturer; in this work, we set $Q_{EM,\text{max}} = 2.5 Q_{EM}(\gamma n_{\text{prop}})$, where n_{prop} (rps) is the propeller's nominal speed at steady-state operations [7, 8]. The function in Eq. 5.12 holds:

$$Q_{EM}(n) = \begin{cases} Q_{EM,\text{max}} = \frac{P_{EM}}{2\pi n_0} & \text{for } 0 \leq n \leq n_0 \\ \frac{P_{EM}}{2\pi n} & \text{for } n_0 < n \leq n_{\text{max}} \end{cases} \quad (5.12)$$

where P_{EM} is the EM power at a fixed operation, n_{max} is the maximum reachable speed, and n_0 is the limit speed at which $Q_{EM,\text{max}}$ is delivered. The schematic curve in Fig. 5.8 delineates the pattern of $Q_{EM}(n)$ [8, 52].

The inertia of the EM is considered equal to the inertia of the DE and applied to the prime mover node (θ_5).

5.2.2.4.3 Propeller hydrodynamic torque

Q_h represents the open-water, hydrodynamic excitation applied to the CPP node in the shaftline models (θ_1). In detail, we set Q_h to be a function of the propeller blades' pitch angle

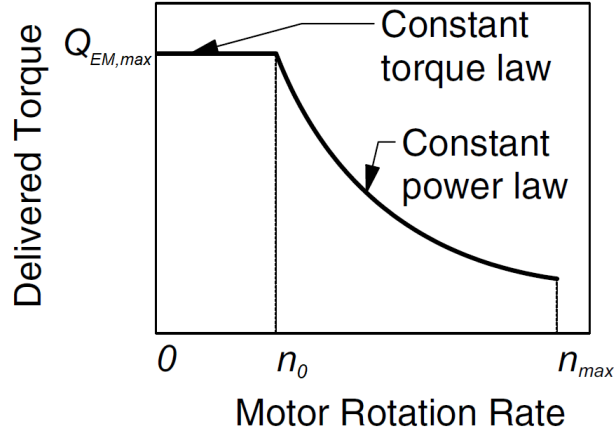


Figure 5.8: Characteristic curve of the EM-delivered torque.

(Φ) and the rotational speed (n); in turn, n is a function of time (t). At n_{prop} , the propeller's hydrodynamic torque $Q_h(\Phi, n_{\text{prop}})$ can be expressed as follows (Eq. 5.13) [9, 33]:

$$Q_h(\Phi, n_{\text{prop}}) = K_Q(\Phi) \rho n_{\text{prop}}^2 D_{\text{prop}}^5 \quad (5.13)$$

where ρ is the water's mass density, D_{prop} is the propeller diameter, and $K_Q(\Phi)$ is defined as the torque coefficient of the propeller in open water conditions [9, 33]. In [51], we determined $Q_h(\Phi, n_{\text{prop}})$ through full-scale vibration measurements acquired at different Φ operational steps. Fig. 5.9 shows the propeller torque curves at the system's nominal speed ($Q_{\text{prop}}(\Phi, n_{\text{prop}})$) [51]. For $\Phi = 100\%$, we assumed that the hydrodynamic torque equals the value for the overtorque condition (110% $P_{\text{eng,max}}$).

In addition, to account for transient perturbations on the propulsion system, we correct $Q_h(\Phi, n_{\text{prop}})$ by considering the instantaneous rotational speed ($n(t)$) and the relation Eq. 5.13. Thus, we can write:

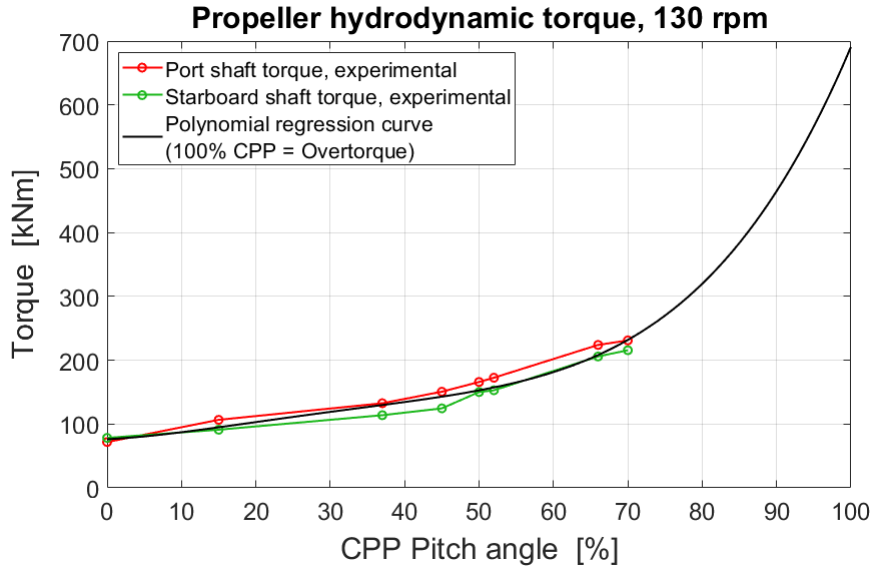


Figure 5.9: Torque absorbed by the propeller at n_{prop} , as a function of Φ . The torque curve (black line) was determined through polynomial regression of the experimental points plus the overtorque operation point [51].

$$Q_h(\Phi, t) = Q_h(\Phi, n(t)) = Q_h(\Phi, n_{\text{prop}}) \left(\frac{n(t)}{n_{\text{prop}}} \right)^2 \quad (5.14)$$

5.2.2.4.4 CPP controller

In this work, we use a proportional controller to govern the pitch angle of the CPP blades (Φ) during perturbations of the dynamic equilibrium [51]; the variation of Φ is based on the propeller's rotational speed drop from the nominal value. Two quantities need to be considered: the sampling interval of the propeller's discrete controller (Δt_s), and the delay time that is required by the CPP mechanism to effectuate the pitch angle variation from the current state to the future state (Δt_m). Every Δt_s time intervals, the path to reach the target Φ is determined and it overrides the previous one. Hence, the actual time-domain evolution of $\Phi(t)$ that ultimately takes place is the result of superposed linear Φ variations [51].

5.2.3. Ice torque patterns

5.2.3.1 IACS formulation and ABS-DNV variants

The IACS Polar Rules define the ice-propeller interaction torque ($Q_{ice,IACS}$) as a function of the propeller rotational angle (ϕ) [20]. In detail, $Q_{ice,IACS}$ is obtained by superposing single ice-induced impacts, each of those corresponding to the milling process of one propeller blade against an ice layer. Each impact of a propeller blade with the ice is described with a semi-sinusoidal curve ($Q_{ice}(\phi)$), as per Eq. 5.15:

$$Q_{ice}(\phi) = C_q(IC) Q_{max}(PC) \sin\left(\phi \frac{180^\circ}{\alpha_{ice}(IC)}\right) \quad (5.15)$$

where C_q is a coefficient that depends on the Impact Case (IC), whereas α_{ice} is also based on IC and it defines the angular span (in degrees) through which the single ice-blade milling process occurs.

ABS and DNV both adopt the IACS guidelines with some adjustments [2, 13]. In this paper, we use the ABS nomenclature. Fig. 5.10 shows the values of C_q and α_{ice} corresponding to the three IC -defined patterns [2]. Q_{max} is the torque amplitude that is related to the propeller's main properties and the Polar Class grade (PC , ranging from 1 to 7), as expressed by the following formulae:

$$Q_{\max} = \begin{cases} k_{o,d} \left(1 - \frac{d}{D}\right) \left(\frac{P_{0.7}}{D}\right)^{0.16} \left(\frac{t_{0.7}}{D}\right)^{0.6} (nD)^{0.17} D^3, & D < D_{\text{limit}} \\ 1.9 k_{o,d} \left(1 - \frac{d}{D}\right) \left(\frac{P_{0.7}}{D}\right)^{0.16} \left(\frac{t_{0.7}}{D}\right)^{0.6} H_{\text{ice}}^{1.1} (nD)^{0.17} D^{1.9}, & D \geq D_{\text{limit}} \end{cases} \quad (5.16)$$

where $k_{o,d}$ is a coefficient that depends on the specific *PC* notation and whether the propeller is open or ducted; D and d are the propeller's disc and hub diameters, respectively; $P_{0.7}$ and $t_{0.7}$ are the pitch length and the blade thickness at 70% propeller radius blade section, respectively; n indicates n_{prop} in rps, or 85% n_{prop} is taken in case of DE-drive Fixed-Pitch Propeller (FPP); H_{ice} is the design ice layer thickness, which is determined by the *PC* grade. D_{limit} is set to be proportional to H_{ice} .

The ice-milling process is composed of multiple superposed impacts, whose number depends on H_{ice} and the *PC* notation. Each impact starts at a $2\pi/Z$ shift after the previous one. Fig. 5.10 shows example patterns of the 3 *IC* cases of $Q_{\text{ice}}(\phi)$ for a 4-blade propeller [20].

ABS and DNV introduced the application of a linear rise and descent over the initial and final 270° of the ice-propeller torque series, respectively [2, 13]. Hereinafter, these two slopes at the extremities of the impact sequence are named “ramp up” and “ramp down”; they can be observed in the examples shown in Fig. 5.11. Also, ABS and DNV set the term $t_{0.7}/D$ in Eq. 5.16 equal to 1.

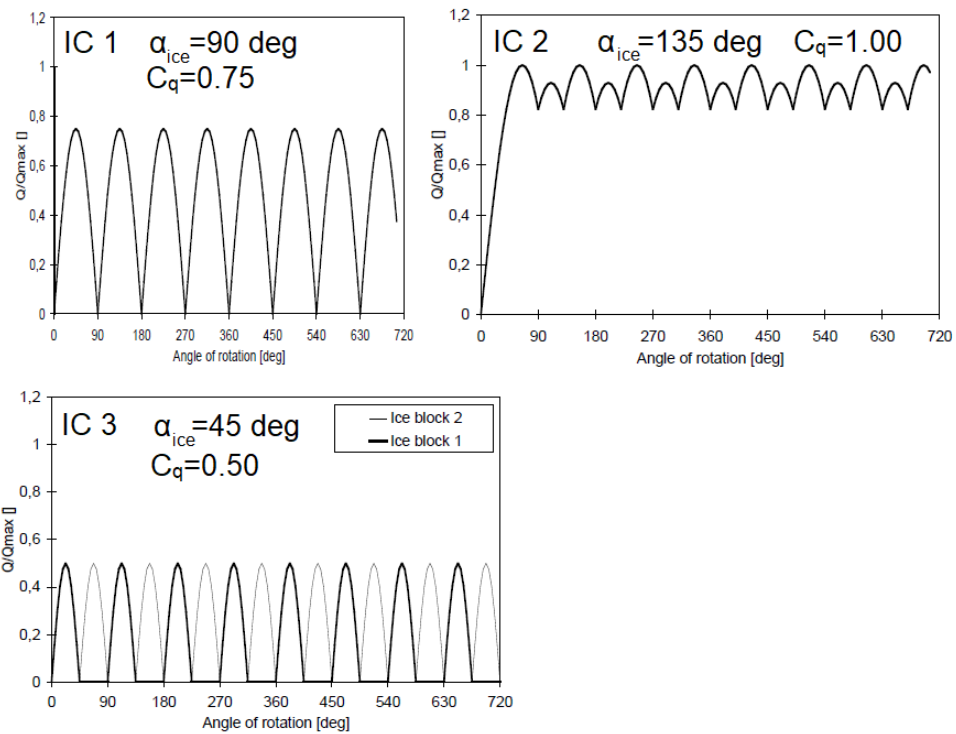


Figure 5.10: Ice-induced torque on a 4-blade propeller. Three ICs are shown: the images are taken as per the IACS Polar Rules [20], whereas the IC notations refer to the ABS-DNV nomenclature [2, 13].

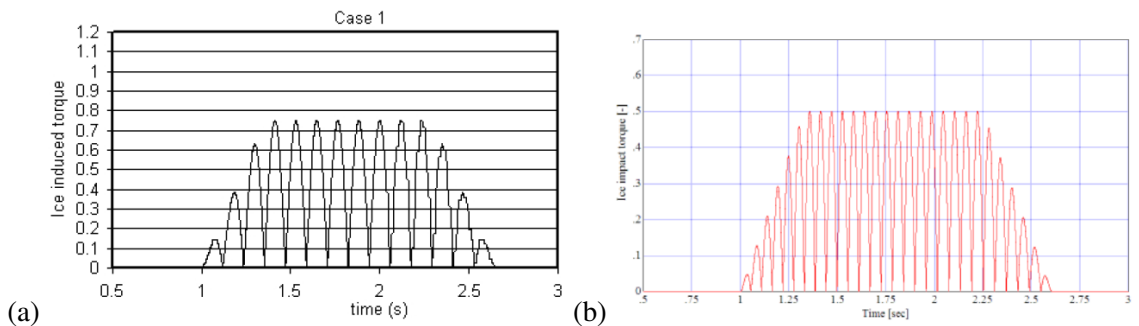


Figure 5.11: Examples of ice-propeller torque patterns, with $Z = 4$. (a) Impacts with $IC = 1$ as per the ABS rules [2]; (b) impacts with $IC = 3$ as per the DNV rules [13].

5.2.3.2 Modifications of the ice impact configuration

In this part, we introduce the four modifications of the ice-propeller torque pattern that are going to be analyzed.

5.2.3.2.1 Ice impact shape

In addition to the semi-sinusoidal pulse of Eq. 5.15, we consider an alternative formulation that allows us to vary the shape of the ice-impact. The studies by Veitch and Wang et al. achieved experimental representations of the ice-propeller torque excitation; Fig. 5.12 shows examples of torque profiles obtained in those works.

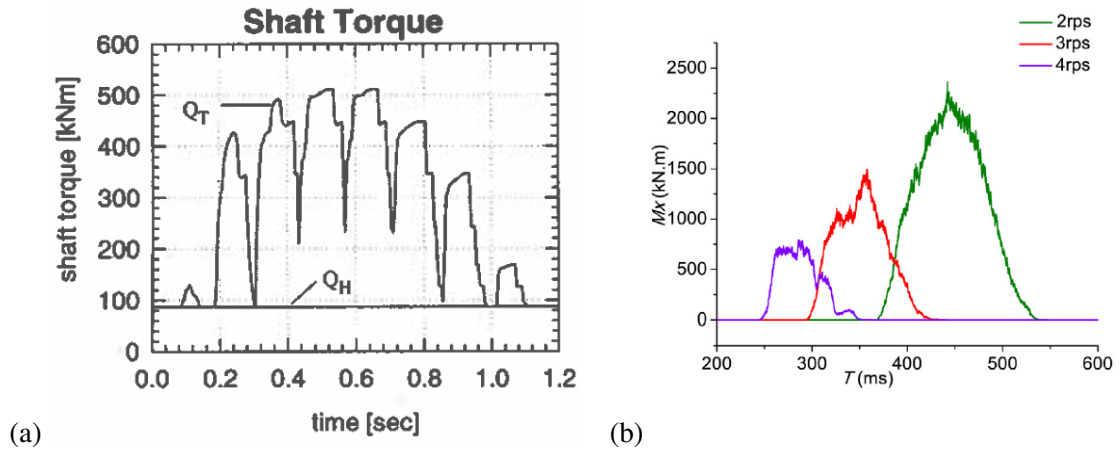


Figure 5.12: Shaft torque profiles induced by ice-propeller milling processes, obtained in the studies by Veitch (a) and Wang et al. (b).

As shown in Fig. 5.12 shows, in numerous loading cases, the single ice-blade impacts resulted in rising and declining with steeper slopes than in the sinusoidal pulse's curve [46, 47]. To simulate these different load patterns, we employ the following polynomial expression:

$$Q_{ice,\epsilon}(\phi) = Q_{\max} \left(1 - \left| \frac{2\phi - \alpha_{ice}}{\alpha_{ice}} \right|^{\epsilon} \right), \quad 0 \leq \phi \leq \alpha_{ice} \quad (5.17)$$

where the exponent ϵ can be adjusted to produce different curves and Q_{\max} is the pulse amplitude. Fig. 5.13 shows the sinusoidal shape (S) (solid red curve), which results to be

close to $Q_{ice,2}(\phi)$ (dashed red curve). In the simulation space of this work, we consider two additional impact shapes, which are obtained by setting $\epsilon = 4$ (curve M) and $\epsilon = 8$ (curve H).

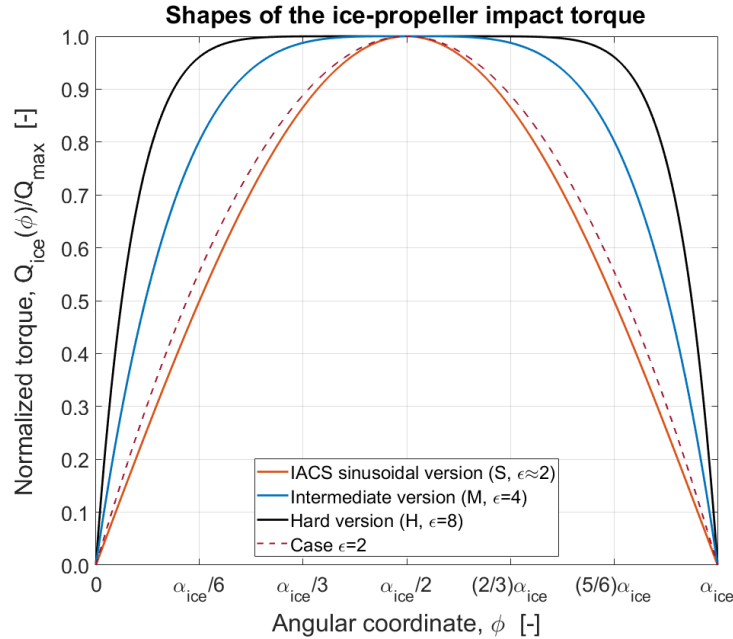


Figure 5.13: Three different curves to represent the torque of one ice-propeller impact. In this paper we use the S-shape curve plus the pulses obtained with $\epsilon = 4, 8$ in Eq. 5.17.

Different shapes describing the ice-induced pulse entail the excitation of different frequency ranges, as shown in Fig. 5.14. The spectra of the three Q_{ice} pulses are plotted; their angular span is set to $\alpha_{ice} = 90^\circ$, and its expression in the time domain is obtained by considering the propeller's nominal speed (n_{prop} , Table 5.2). As ϵ increases, the excitation of lower frequencies gets enhanced.

5.2.3.2.2 Ice impact's angular span

The IC parameter in the IACS recommendations identifies the angle α_{ice} (Fig. 5.10, Eq. 5.15, [20]), and the values it can assume are three: 45° , 90° , 135° degrees. In our work, we

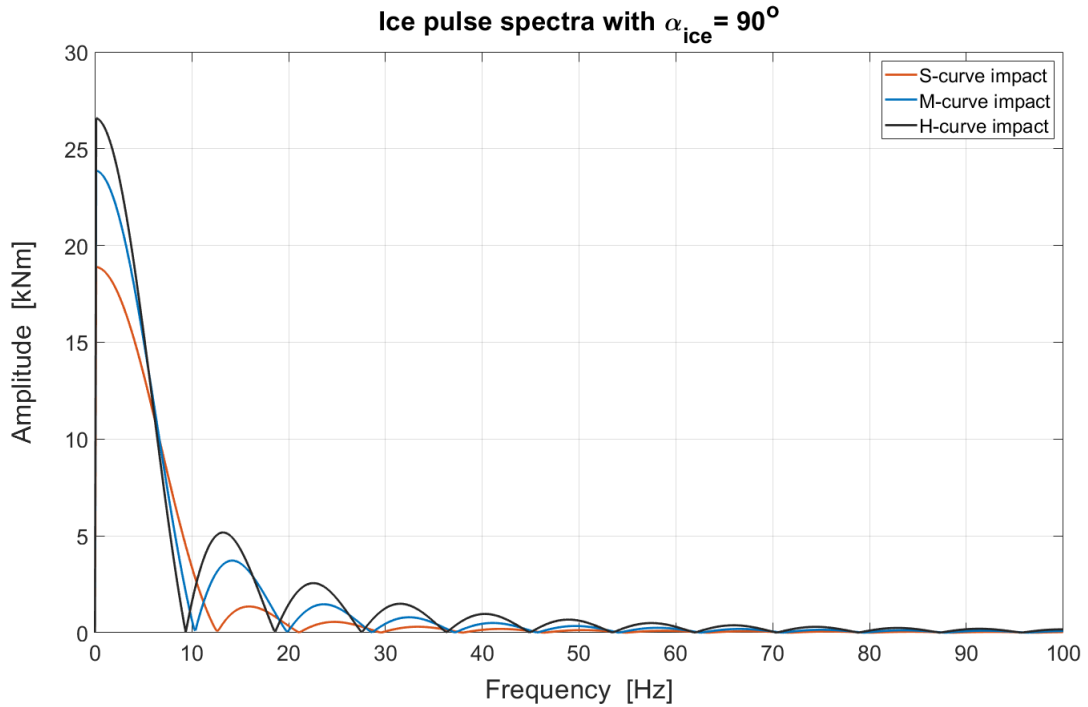


Figure 5.14: Three different curves to represent the torque of one ice-propeller impact. In this paper we use the S-shape curve plus the pulses obtained with $\epsilon = 4, 8$ in Eq. 5.17.

test a wider range of values, going from 30° to 180° with steps of 30° :

$$\alpha_{\text{ice}} = \{30, 60, 90, 120, 150, 180\} \text{ [deg]} \quad (5.18)$$

We do not consider α_{ice} values beyond 180° because such a scenario would physically mean that the encountered ice layer is milled through more than half propeller disc, and this event is extremely unlikely to occur.

5.2.3.2.3 Ramp-up Ramp-down

In our work, we test both configurations—ice excitation with and without ramps (Sub-section 5.2.3.1)—to investigate their effects on the shaftline’s dynamic response.

Fig. 5.15 shows six examples obtained by combining the above characteristics into

multiple-impact sequences. When the α_{ice} angle is larger than $2\pi/Z$ —namely 120° , 150° , 180° in the examples shown in Fig. 5.15—consecutive impacts overlap. Therefore, in those cases the $Q_{ice}(\phi)$ peaks in the overall ice-propeller excitation exceed Q_{max} .

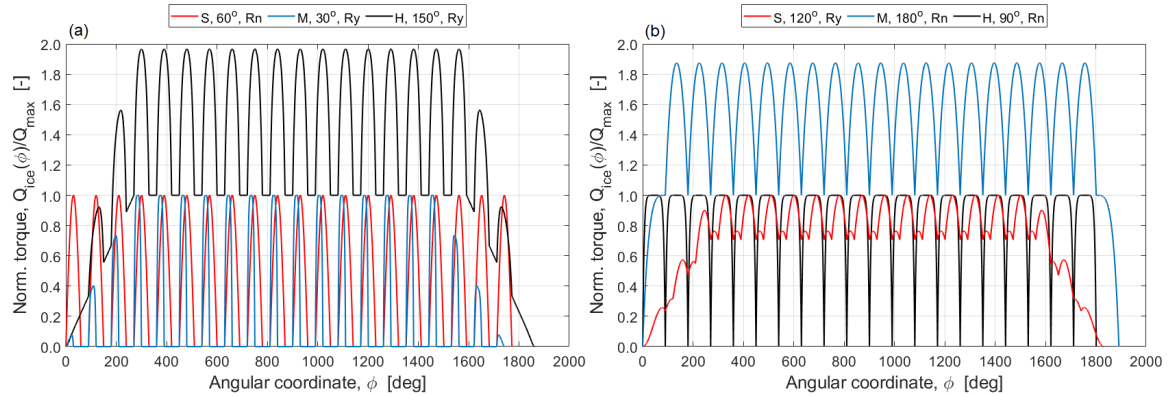


Figure 5.15: Examples of different ice-induced torque sequences, with several impacts. The application or not of the up-down ramps is indicated by “Ry” and “Rn”, respectively. The angular shift between the onset of one impact and the next one is set to be 90° , namely the shift obtained with a 4-blade propeller.

5.2.3.2.4 Number of impacts

The rules determine the specific number of consecutive impacts to compose the overall ice-milling sequence [2, 13, 20]. When the ice-propeller interaction load does not halt the system, the application of several impacts to the propeller node makes the propulsion line settle at a new steady-state condition, in which the increased driving torque delivered by the prime mover balances the combined hydrodynamic-ice torque on the propeller. Conversely, applying a single ice-propeller impact induces a transient response of the system. To study how the number of ice impacts affects the TVA outcomes, we examine the three following scenarios:

1. **Ice-induced steady-state response:** application of a 30-impact ice-impact sequence

to the model. We implement this number of impacts because we determined through multiple preliminary simulations that the system reaches and maintains an equilibrium point at approximately 30 consecutive pulses. This quantity is coherent with the most severe conditions according to the IACS guidelines [20]. All combinations of impact shapes, α_{ice} , and ramps' presence/absence are independently implemented.

2. **Single-impact transient response:** application of one ice-propeller torque impact to the model. All combinations of impact shapes and α_{ice} are independently implemented.
3. **Transition between transient and steady-state conditions:** separate TVAs with a variable number of impacts, ranging from 1 to 30, with selected combinations of impact shape and α_{ice} . In this case, we are able to observe how the system responds as we progressively increase the number of impacts, in order to study the evolution from transient-state dynamics to steady-state response.

5.2.4. Simulation series and analysis of the results

5.2.4.1 Numerical analysis setup

Overall, 72 configurations compose the simulation space of Scenario 1 (3 impact shapes, 6 angular span values, 2 options to apply or not the ramps, 2 prime mover excitation models) and 36 configurations for Scenario 2 (since in the latter case the ramp up-down feature is not applicable). Regarding the simulations composing Scenario 3, we selected the pairing prime mover–impact shape that yields the most severe results in terms of shaft's speed drop and response torque fluctuations. For that combination, we considered the no-ramp option

and all α_{ice} cases.

The initial conditions of the shaftline are kept the same for each TVA simulation; Table 5.3 outlines both the fixed parameters of the ice-propeller excitation and the propulsion system's initial setup. In particular, the torque amplitude of each ice-blade impact (Q_{max}) is determined through the ice-torque peak correlation we presented in [52], assuming a design ice layer thickness of 2.5 metres; this value corresponds to the thickness associated to the *PC4* grade, which is the Polar Class notation of the CCGS *Terry Fox* [2, 20].

Table 5.3: Fixed parameters and initial conditions of the TVA simulation series.

Quantity		Value	Unit
Ice impact torque amplitude	Q_{max}	1.0	[MNm]
Ice impact angular shift ($2\pi/Z$)	α_{shift}	90	[deg]
CPP initial pitch angle	Φ_{start}	90	[°]
CPP controller's sample time	Δt_s	0.50	[s]
CPP controller's delay time	Δt_m	1.50	[s]
Combustion pressure gain	k_p	0.025	[s/rad]
Steady-state propulsion power	P_{start}	6, 513	[kW]
Steady-state propulsion torque	Q_{start}	468.6	[kNm]
Steady-state DE load ratio	$\ell_{P,\text{start}}$	74.0	[%]

In the simulation sets, the PTO was assumed to be disengaged from the gearbox drive.

In the numerical analyses, we simulated 11 seconds of the model's response; the ice-propeller excitation was set to begin after 1 seconds of steady-state conditions with the dynamic balance established between $Q_h(\Phi, t)$ and the prime mover's torque (Q_{start}). We used 0.5 milliseconds as the maximum time step in the time-domain solver.

Before the onset of the ice-propeller perturbation, open-water conditions are assumed to be in place to define $Q_h(\Phi, t)$ (Fig. 5.9); we assume the icebreaker to navigate with steady

heading and speed in uniform wake field [31, 39]. During the ice-milling process, $Q_h(\Phi, t)$ is considered to be a separable load, as treated in [25].

The effect of the CPP dynamic evolution on Q_{ice} during the transient perturbation is taken into account, as implemented in [51]. Equation 5.19 introduces the instantaneous pitch length ($P'_{0.7}(\Phi(t))$) to define the correction factor ($q_\Phi(t)$), which updates $Q_{ice}(t)$ into $Q'_{ice}(t)$, through the propeller's pitch relation defined by Eq. 5.16.

$$Q'_{ice}(t) = Q_{ice}(t) \underbrace{\left(\frac{P'_{0.7}(\Phi(t))}{P_{0.7}} \right)^{0.16}}_{q_\Phi(t)} \quad (5.19)$$

5.2.4.2 Output quantities

To evaluate the result set from the TVA combinations, we consider (i) the minimum rotational speed of the prime mover reached during the ice-propeller perturbation, and (ii) the dynamic response torque of the three shafting segments between the propeller and the gearbox nodes.

In detail, we select the minimum value of the rotational speed reached by the prime mover ($\omega_{PM,min}$) during the entire process, in each TVA simulation. For the DE-drive case, we calculate $\omega_{PM,min}$ as the minimum of the average speed of all 16 crank element nodes.

Concerning the dynamic response torque ($Q_{resp}(t)$), it is determined for each shaft segment—between the nodes i and $i + 1$ —as follows [41]:

$$Q_{resp,i,i+1}(t) = c_{i,i+1} [\dot{\theta}_i(t) - \dot{\theta}_{i+1}(t)] + k_{i,i+1} [\theta_i(t) - \theta_{i+1}(t)] \quad (5.20)$$

To evaluate the maximum torsional stress intensity affecting each shaft segment, the Rules consider $Q_{\text{peak},i,i+1}$, which corresponds to the maximum absolute value assumed by $Q_{\text{resp}}(t)$ [2, 13]:

$$Q_{\text{peak},i,i+1} = \max \left\{ \text{abs} \left[Q_{\text{resp},i,i+1}(t) \right] \right\} \quad (5.21)$$

Moreover, we consider the range between the highest and the lowest peaks of $Q_{\text{resp},i,i+1}(t)$; this is a key quantity for the torsional fatigue calculations of each shafting segment ($Q_{\text{range},i,i+1}$) as per the rules [2, 13]:

$$Q_{\text{range},i,i+1} = \max \left\{ Q_{\text{resp},i,i+1}(t) \right\} - \min \left\{ Q_{\text{resp},i,i+1}(t) \right\} \quad (5.22)$$

The outputs $Q_{\text{peak},i,i+1}$ and Q_{range} are fundamental to determine if the shafting segments are compliant with the requirements of each target *PC* notation, on the matter of shaft structural integrity [2, 13, 20]. Similarly, considering the lowest rotational speed reached by the prime mover during ice-induced perturbations is crucial in relation to the stall speed threshold.

5.3. Results and discussion

5.3.1. Equivalence between the condensed and expanded models

Fig. 5.16 shows the modal shapes and the corresponding eigenfrequencies of the two systems. In the two plots, the homologous modal shapes are drawn with corresponding colours and thicker lines. In addition, in the expanded model's diagram, the dashed modal shapes indicate the two eigenvectors associated with the TVDs. Their eigenfrequencies are 9.98 Hz and 10.13 Hz, which were obtained by tuning the TVD torsional stiffness with $\tau = 0.925$ (Eq. 5.5). The remaining thin-drawn modal shapes are associated with the relative motions of the engine crank nodes; their contribution to the propeller-gearbox shafting line is negligible.

Fig. 5.17 shows the spectrum of the shaft vibration measure at the zero- Φ configuration of the Port-side shaftline. Table 5.4 reports the experimental resonance frequency values and the four nonzero homologous eigenfrequencies of the two models ($f_{1,\dots,4}$), and the corresponding percentage difference ($\Delta f_{1,\dots,4}$). We can notice that the f_3 and f_4 pairs coincide, whereas there are slight deviations for f_1 and f_2 . Those discrepancies are due to the superposition of all the additional modal shapes in the expanded model. The correspondence of the two sets of modal shapes and natural frequencies is verified; also the experimental frequencies correspond to the respective numerical counterparts.

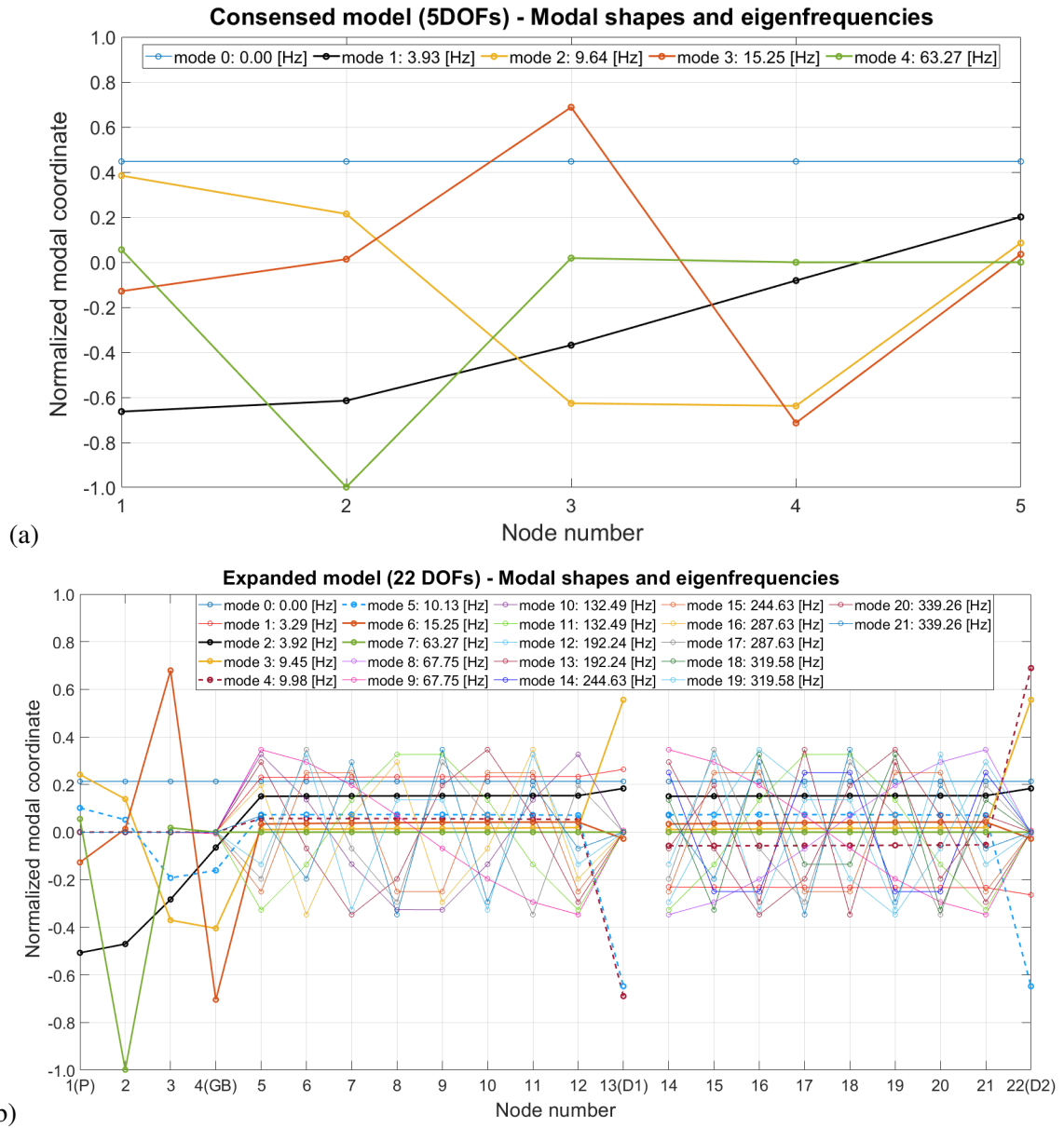


Figure 5.16: Normalized modal shapes and natural frequencies: (a) condensed model; (b) Expanded model, where P, GB, D1, D2 indicate the nodes of the propeller, gearbox, TVD 1 and 2, respectively.

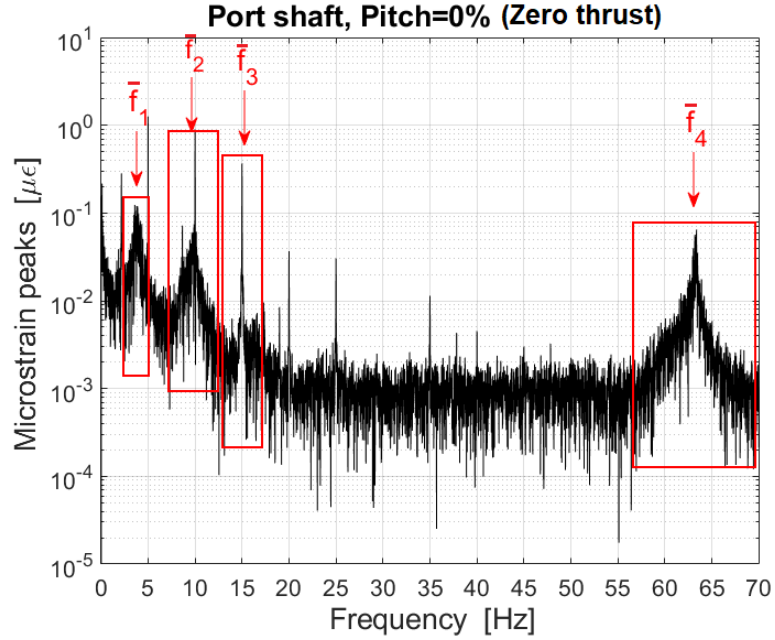


Figure 5.17: Spectrum of the measured microstrain ($\mu\epsilon$) at CPP $\Phi = 0\%$ and zero-thrust condition. The quantity ϵ is defined as the linear strain along the shaft's circumferential dimension.

Table 5.4: Common eigenfrequencies of the condensed and expanded models, plus the resonance frequencies obtained through the full-scale measurements.

Quantity		f_1	f_2	f_3	f_4
Condensed model	[Hz]	3.93	9.64	15.25	63.27
Expanded model	[Hz]	3.92	9.45	15.25	63.27
Measurements	[Hz]	3.80	9.97	14.98	63.37
$ \Delta f_i $ (Exp. vs. Meas.)	[%]	3.16	5.22	1.80	0.16

Then, we applied an ice-induced torque on the propeller node of each model and performed a TVA simulation to investigate the difference in $Q_{\text{resp}}(t)$, $\omega_{\text{prop}}(t)$, and $\omega_{\text{eng}}(t)$ between the two systems. We implemented the ABS-defined ice load with the parameters $PC = 4$ and $IC = 2$ [2]. In particular, for the expanded model, the speed $\omega_{\text{eng}}(t)$ is determined as the average rotational speed of the 16 nodes corresponding to the cylinder-crank assemblies—DOFs 5 to 12 and 14 to 21 (Fig. 5.4). Fig. 5.18 shows the results in terms of shaft response torque in the three shafting segments between the propeller and the gearbox nodes.

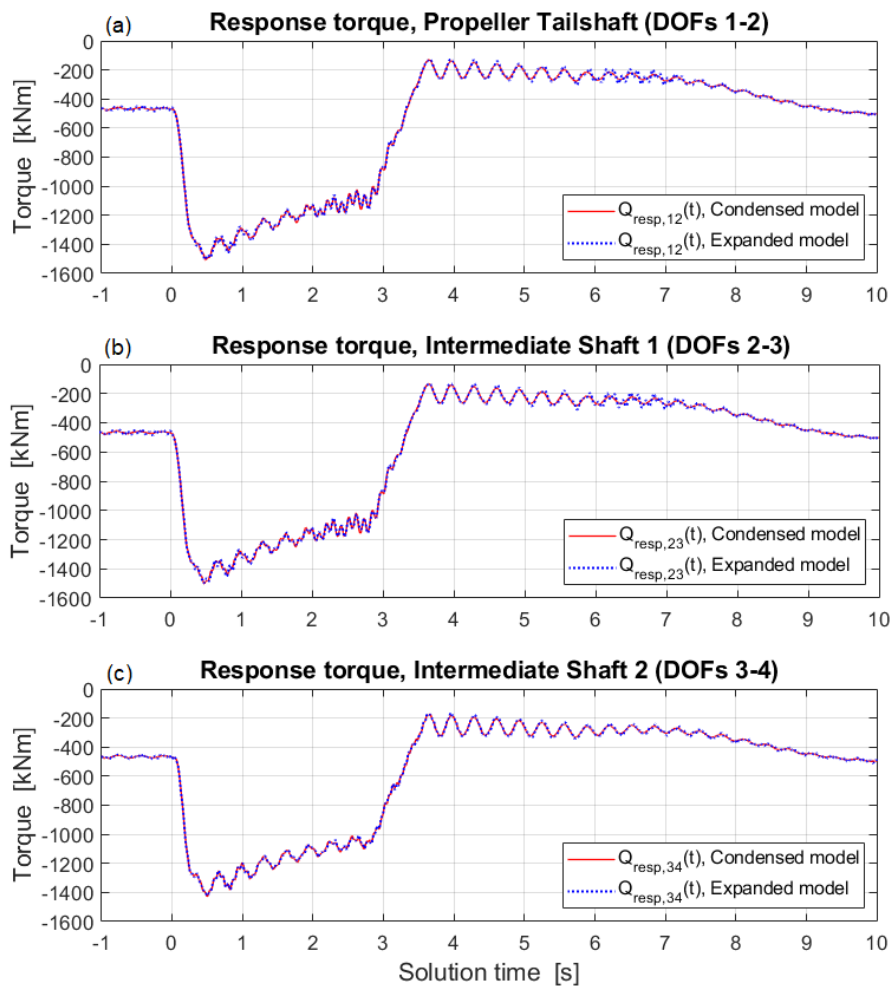


Figure 5.18: $Q_{\text{resp},12,23,34}(t)$ from the TVA applied to the two models.

The three pairs of curves visibly coincide. Table 5.5 reports the minimum, maximum, and amplitude torque values from the three plots, plus the corresponding percentage deviations.

Table 5.5: Main characteristics of the shaft response torque from the condensed and expanded models' TVAs.

Quantity		Shaft 1–2	Shaft 2–3	Shaft 3–4
Maximum torques: $\max \{Q_{\text{resp},i,i+1}(t)\}$				
Condensed model	[kNm]	-128.7	-132.2	-175.1
Expanded model	[kNm]	-127.7	-131.1	-164.0
$ \Delta Q_{\text{resp,max},i,i+1} $	[%]	0.74	0.81	6.35
Minimum torques: $\min \{Q_{\text{resp},i,i+1}(t)\}$				
Condensed model	[kNm]	-1505.7	-1501.2	-1428.2
Expanded model	[kNm]	-1504.7	-1498.6	-1422.3
$ \Delta Q_{\text{resp,min},i,i+1} $	[%]	0.07	0.17	0.41
Torque ranges: $\max \{Q_{\text{resp},i,i+1}(t)\} - \min \{Q_{\text{resp},i,i+1}(t)\}$				
Condensed model	[kNm]	1377.1	1369.0	1253.1
Expanded model	[kNm]	1377.0	1367.5	1258.3
$ \Delta Q_{\text{range},i,i+1} $	[%]	0.00	0.11	0.42

The discrepancies between the two sets of values shown in Table 5.5 are all below the 1% with the exception of $\max \{Q_{\text{resp},34}(t)\}$. The coincidence of the outcomes of the two models is verified. Fig. 5.19 and Table 5.6 shows the time series of the propeller and engine node speed.

Table 5.6: Minimum speeds at the propeller and engine nodes from the condensed and expanded models.

Quantity		$\min \{\omega_{\text{prop}}\}$	$\min \{\omega_{\text{eng}}\}$
Condensed model	[rpm]	58.87	269.74
Expanded model	[rpm]	58.86	269.73
$ \Delta f_i $	[%]	0.02	0.00

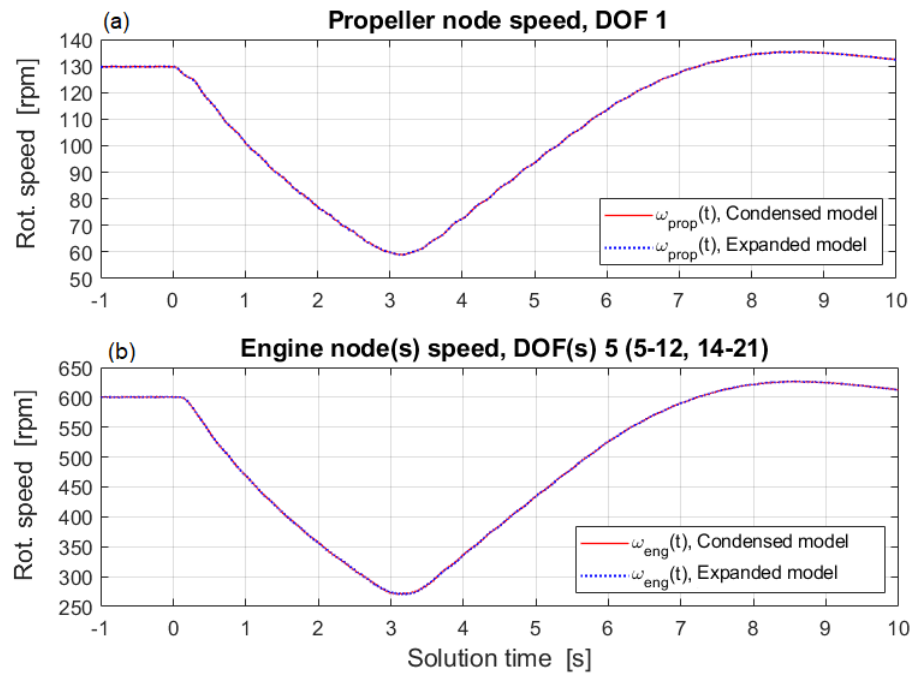


Figure 5.19: $\omega_{\text{prop}}(t)$ and $\omega_{\text{eng}}(t)$ from the TVA applied to the two models.

Also in the $\omega(t)$ case, the coincidence between the two groups of values demonstrate the consistency of results that both models deliver.

5.3.2. Scenario 1: ice-induced steady-state

We sequentially performed the 72 30-impact simulations characterized by the different configurations of Scenario 1 (Section 5.2.4.1).

Fig. 5.20 shows an example of the excitation torques as they evolve during one of the TVA simulations.

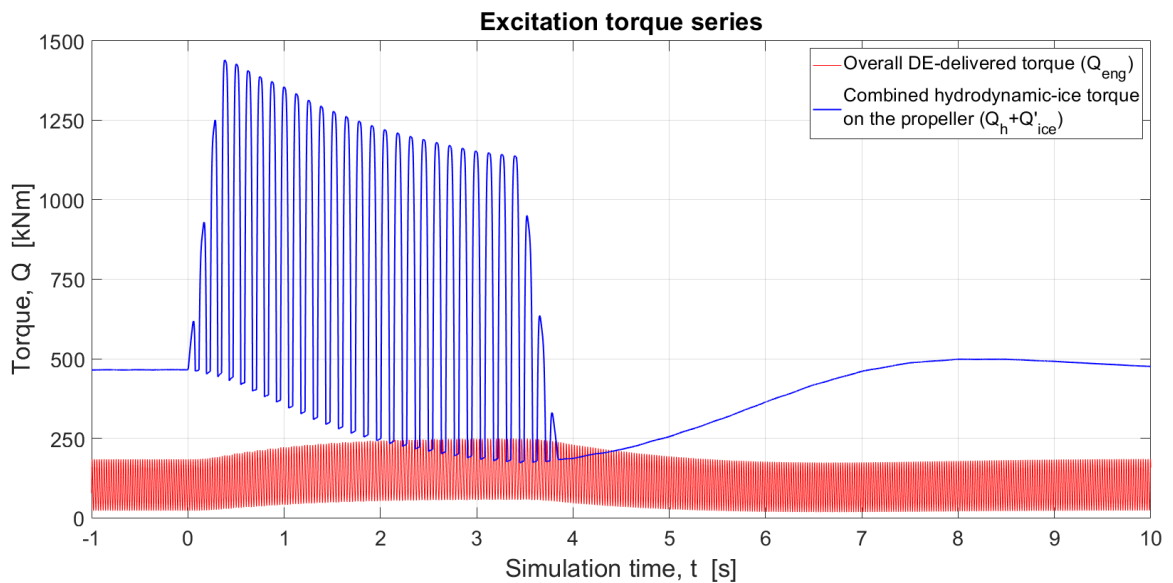


Figure 5.20: Combined propeller torques and DE driving torque throughout a simulation, with the Q_{ice} combination identified by M -shape, $\alpha_{ice} = 60^\circ$, ramps applied.

Fig. 5.21 shows the concurrent evolution of multiple parameters throughout a simulation. By observing subplots (c), (d), and (e) in Fig. 5.21, we can see that a dynamic equilibrium between $Q_h(t) + Q_{ice}(t)$ and $Q_{EM}(t)$ is achieved as the rotational speed gets steady for about half the duration of the ice-propeller interaction process.

Fig. 5.22 outlines the set of comprehensive plots showing how the prime mover speed minima ($\omega_{PM,min}$) change across the 72 system configurations. The threshold limit speed of

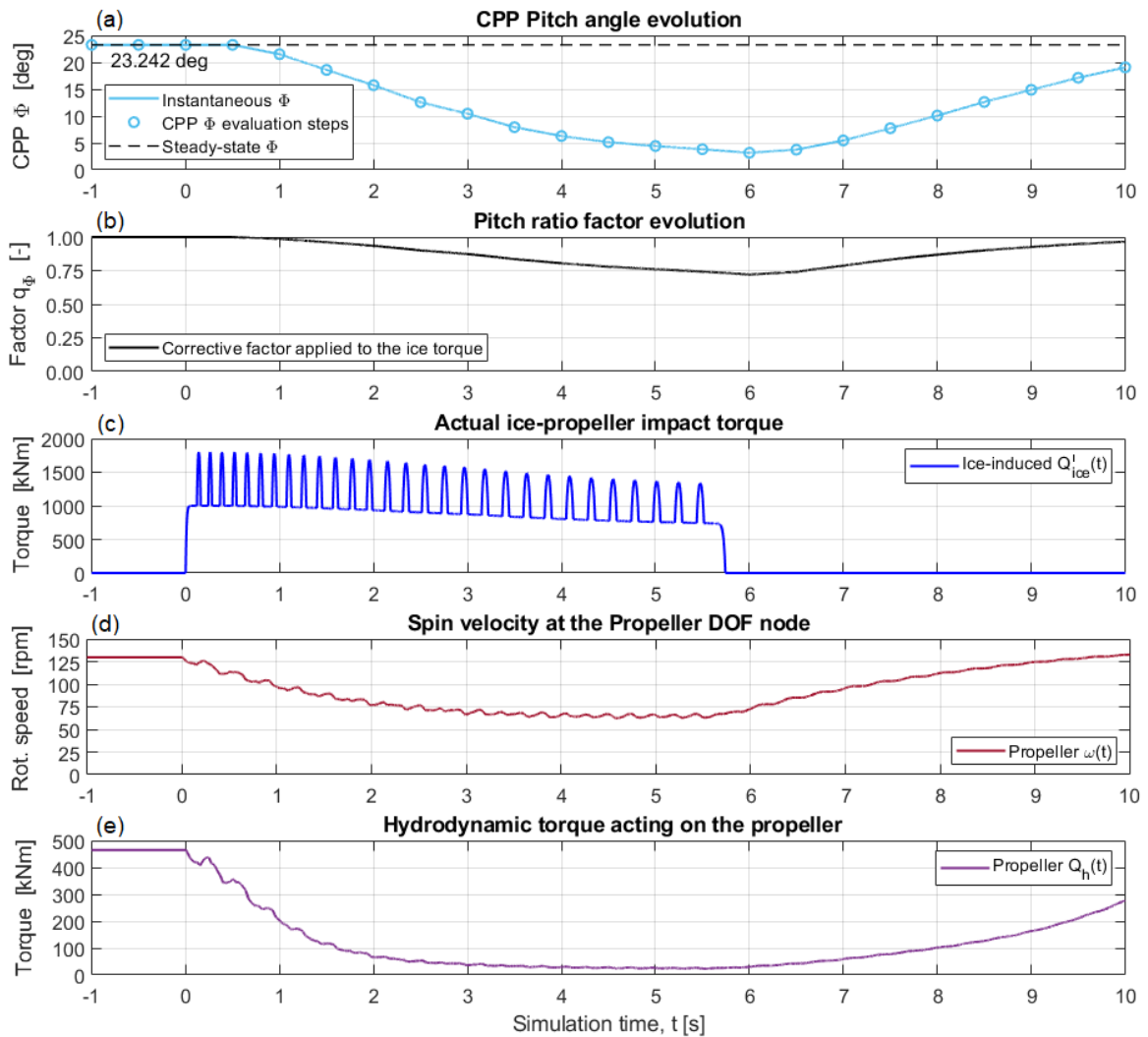


Figure 5.21: (a) CPP Pitch angle evolution (Φ); (b) pitch corrective factor (q_Φ), (c) Ice-propeller torque (Q_{ice}); (d) propeller node speed (ω_{prop}); (e) hydrodynamic torque on the propeller (Q_h), for the combination identified by EM prime mover, H -shape, $\alpha_{ice} = 120^\circ$, no ramps.

the CCGS *Terry Fox*'s propulsion plant is 250 rpm; below this speed, the prime movers stall.

We can notice a substantial difference between the DE and EM drives, with the latter being more efficient in countering the ice-propeller loading. The drop of the curves with the EM option is close to linear—whereas, in the DE-drive case, it is distinctly more than linear.

Overall, the presence or not of the ramps up-down does not constitute a significant parameter

for the results; $\omega_{PM,min}$ slightly deviates in the intermediate α_{ice} cases with the DE-drive prime mover. The DE-drive cases characterized by $\alpha_{ice} = 180^\circ$ and M, H shapes produce minimum speeds below zero (Fig. 5.22-b,c), which means that the propulsion system is ineffective to withstand the ice-propeller torque even below the threshold speed limit.

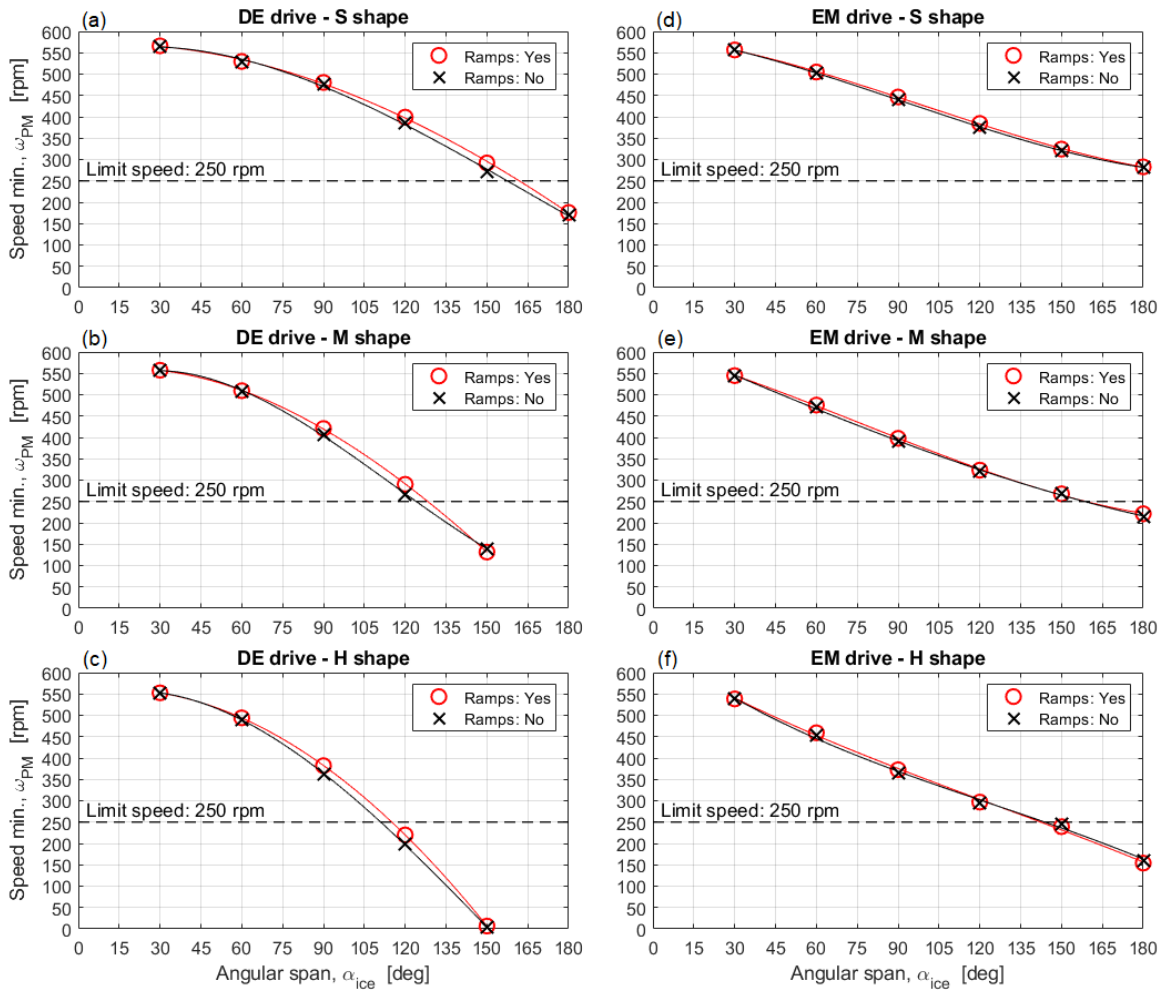


Figure 5.22: Minimum rotational speeds reached by the prime mover node(s) in each model configuration of the Scenario 1. In particular, a polynomial fit curve is associated to each data series to show its trend as a function of α_{ice} . The outcomes from the simulations in which the shaftline's speed is negative are disregarded in the fit curve calculations.

Fig. 5.23 shows the contour plots of the dataset, where the influence of α_{ice} and the shape exponent (ϵ , Eq. 5.19) can be observed. α_{ice} represents the most important factor to affect

$\omega_{PM,min}$, whereas the impact shape type results significant especially for the low- ϵ region.

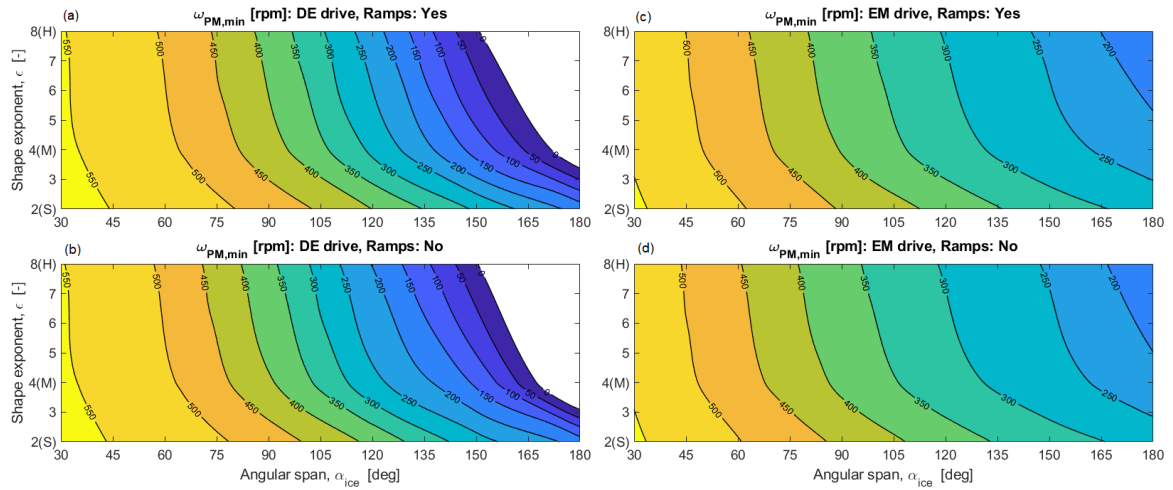


Figure 5.23: Contour plots of the $\omega_{PM,min}$ distribution for the configurations of the Scenario 1. The impact shape types are characterized by the exponent ϵ as per Eq. 5.19, and the S -type shape is considered to correspond to the case $\epsilon = 2$ (Fig. 5.13).

Concerning the shaft response torque results, we will consider the data related to the “Intermediate Shaft 1” segment (DOFs 2 – 3, Table 5.14), since it is the shafting segment equally distant from both the propeller node and the gearbox. The results of the other two shafts are analogous in terms of qualitative patterns of the curves.

Fig. 5.24 shows the results for $Q_{peak,23}$; we can see how the application of the ramps up-down affects the numerical outcomes remarkably. The no-ramps simulations visibly produce higher torque peaks since the ice pulse magnitude does not increase as gradually as it happens with the ramps. Also, we can notice that the no-ramps $Q_{peak,23}$ curves follow a close to linear rise. This is more evident in the cases with the EM-drive option. The curve patterns between the two prime mover models are similar until $\alpha_{ice} = 120^\circ$; they diverge beyond that point, primarily due to the different outcomes in terms of $\omega_{PM,min}$.

Fig. 5.25 shows the contour plots of $Q_{peak,23}$. The significance of the shape type exponent

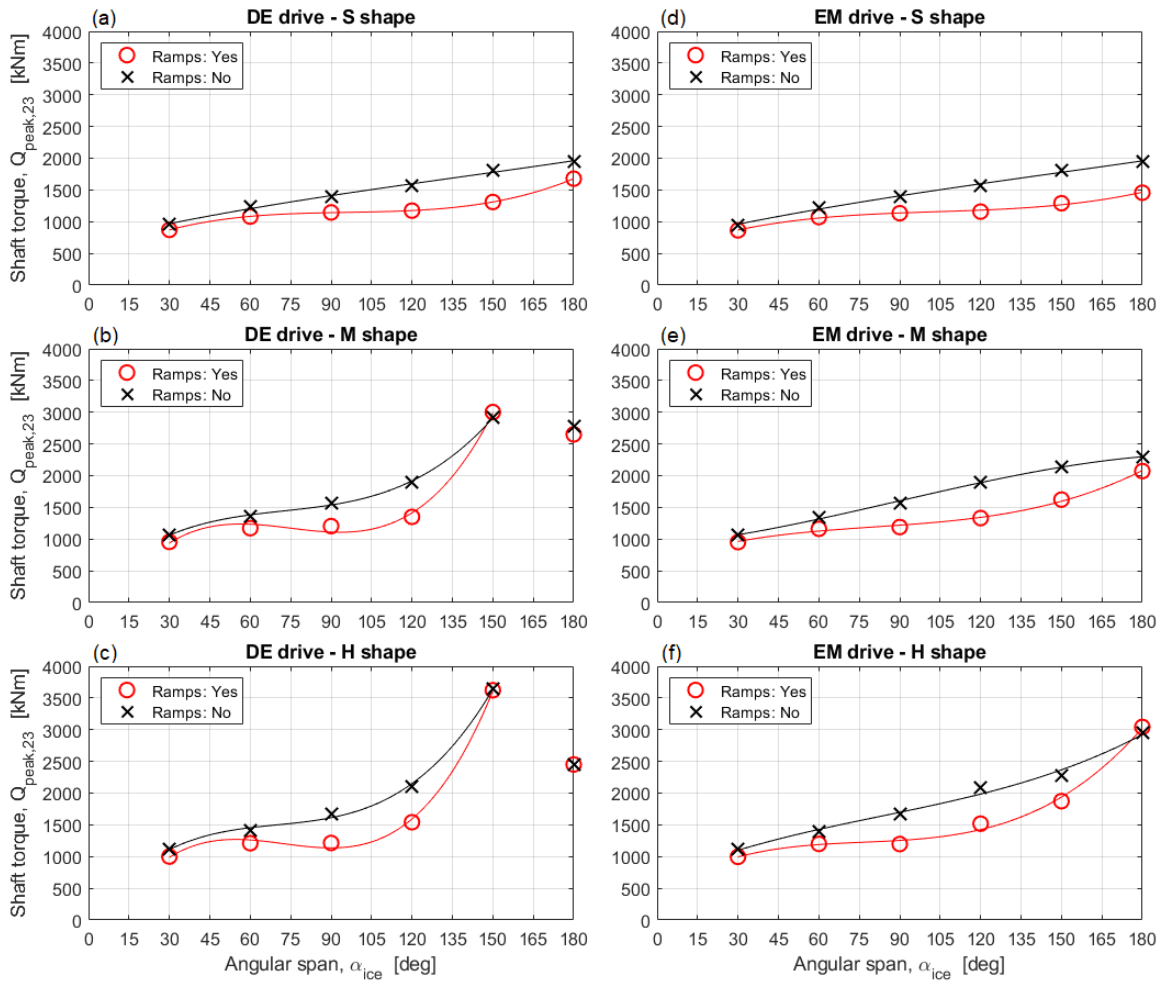


Figure 5.24: Peak torques ($Q_{\text{peak},23}$) in the shaft segment between the nodes 2 and 3, in each model configuration of the Scenario 1. A polynomial fit curve is associated to each data series to show its trend as a function of α_{ice} . The outcomes from the simulations in which the shaftline's speed is negative are disregarded in the calculation of the fit curves.

(ϵ) in correspondence of high α_{ice} values is clear.

Table 5.7 reports the ratios between the data pairs from Fig. 5.24 that differ by the sole ramp factor. The layout of Table 5.7 is analogous with the subplots in Fig. 5.24. In detail, the ratios are low in the α_{ice} region until 60° , and then they increase up to about 140% for the intermediate-high α_{ice} values. The ice impact shape is not a significant parameter until $\alpha_{\text{ice}} = 120^\circ$, coherently with the $\omega_{\text{PM},\text{min}}$ outcomes below the threshold speed limit.

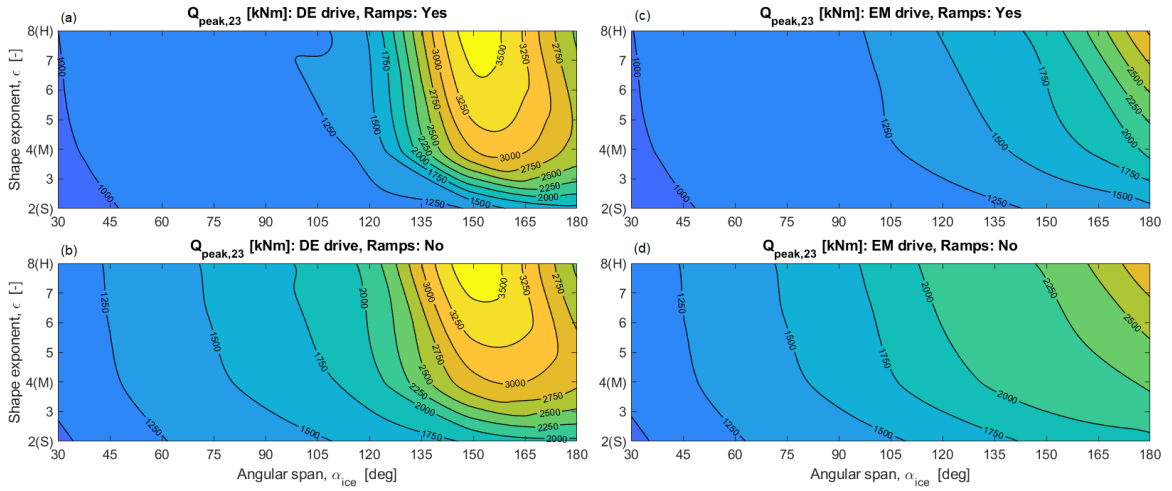


Figure 5.25: Contour plots of the $Q_{\text{peak},23}$ distribution for the configurations of the Scenario 1. The impact shape types are characterized by the exponent ϵ as per Eq. 5.19, and the S -type shape is considered to correspond to the case $\epsilon = 2$ (Fig. 5.13).

Table 5.7: Ratios between the $Q_{\text{peak},23}$ results obtained without and with ramps up-down.

Shape	DE drive						EM drive					
	30°	60°	90°	120°	150°	180°	30°	60°	90°	120°	150°	180°
S	1.10	1.15	1.21	1.34	1.38	1.16	1.10	1.14	1.22	1.36	1.40	1.34
M	1.12	1.16	1.30	1.40	0.97	n/a	1.11	1.16	1.32	1.42	1.32	1.11
H	1.12	1.17	1.38	1.37	1.01	n/a	1.12	1.17	1.40	1.37	1.22	0.97

Similarly, Figs. 5.26 and 5.27 show the results regarding $Q_{\text{range},23}$ for the 72 simulations. The significance of the ramp parameter is likewise evident, especially for the intermediate region of the α_{ice} interval. For a fixed ice impact setup, the absence of the ramps up-down can cause discrepancies in Q_{range} values even up to 90-100%, as shown in Table 5.8. The ratios between the $Q_{\text{range},23}$ pairs result to be remarkably larger than the homologous ones for $Q_{\text{peak},23}$ (Table 5.7). Overall, as the contour plot show, the relations between the simulation parameters are analogous for both $Q_{\text{peak},23}$ and $Q_{\text{range},23}$.

As an example, in Fig. 5.28 we compare the $Q_{\text{resp},23}(t)$ curves from two simulations

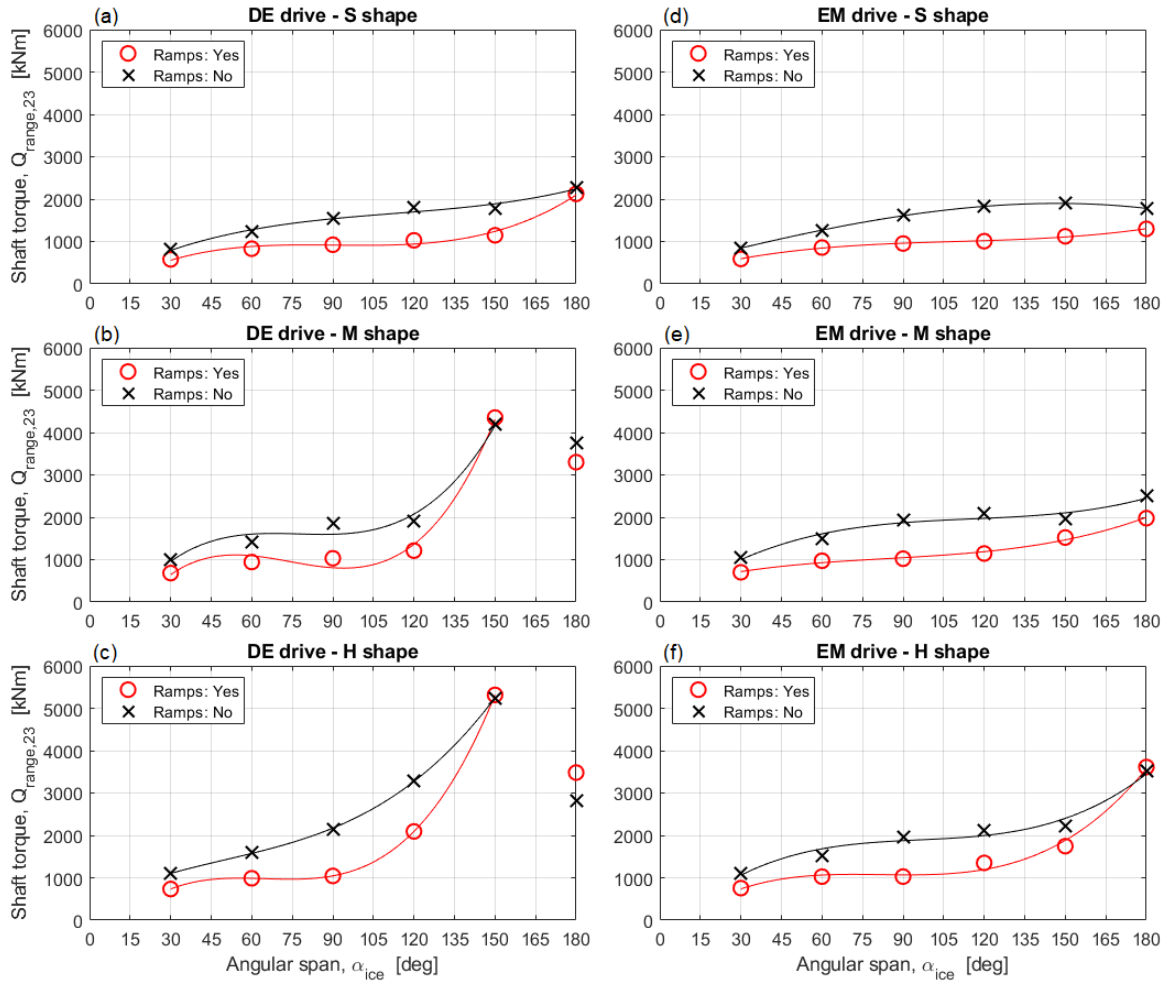


Figure 5.26: Amplitude torques ($Q_{range,23}$) in the shaft segment between the nodes 2 and 3, in each model configuration of the Scenario 1. A polynomial fit curve is associated to each data series to show its trend as a function of α_{ice} . The outcomes from the simulations in which the shaftline's speed goes below zero are disregarded in the fit curve calculations.

Table 5.8: Ratios between the $Q_{range,23}$ results obtained without and with ramps up-down.

Shape	DE drive						EM drive					
	30°	60°	90°	120°	150°	180°	30°	60°	90°	120°	150°	180°
<i>S</i>	1.41	1.48	1.66	1.75	1.56	1.07	1.44	1.47	1.70	1.81	1.69	1.37
<i>M</i>	1.47	1.51	1.81	1.56	0.97	n/a	1.49	1.53	1.90	1.82	1.29	1.26
<i>H</i>	1.50	1.61	2.05	1.57	0.99	n/a	1.47	1.49	1.91	1.57	1.28	0.97

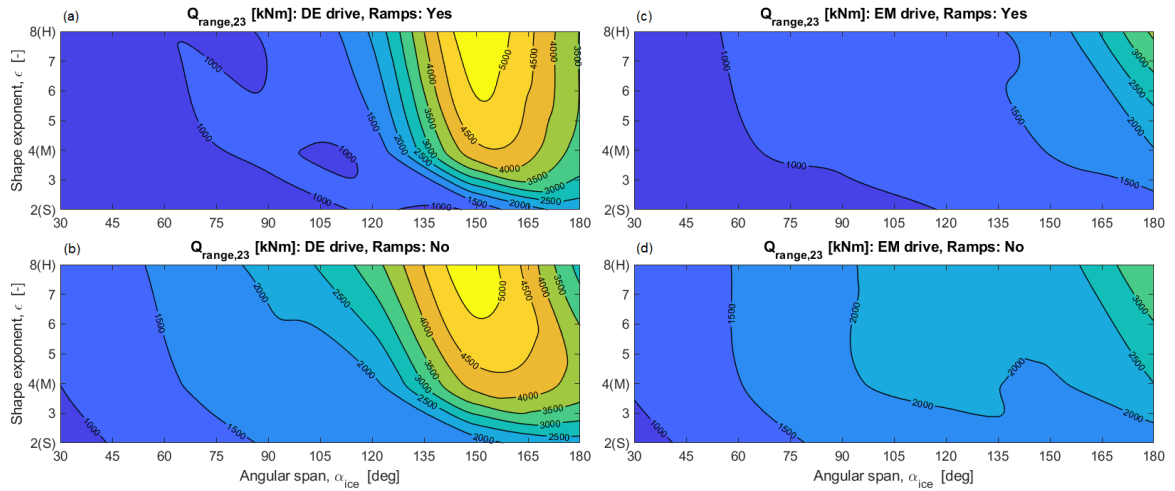


Figure 5.27: Contour plots of the $Q_{\text{range},23}$ distribution for the configurations of the Scenario 1. The impact shape types are characterized by the exponent ϵ as per Eq. 5.19, and the S -type shape is considered to correspond to the case $\epsilon = 2$ (Fig. 5.13).

having the same configuration apart from the ramps' application. $Q_{\text{resp},23}(t)$ of the shaft does not differ by just the Q_{peak} and Q_{range} values, but also the secondary torsional oscillations are visibly different. Specifically, when the ramps up-down are applied, the amplitude of the $Q_{\text{resp}}(t)$ oscillations get attenuated throughout the entire process; this fact might be crucial when fatigue analysis is involved, especially in this loading mode with several consecutive impacts causing ample fluctuations repeatedly.

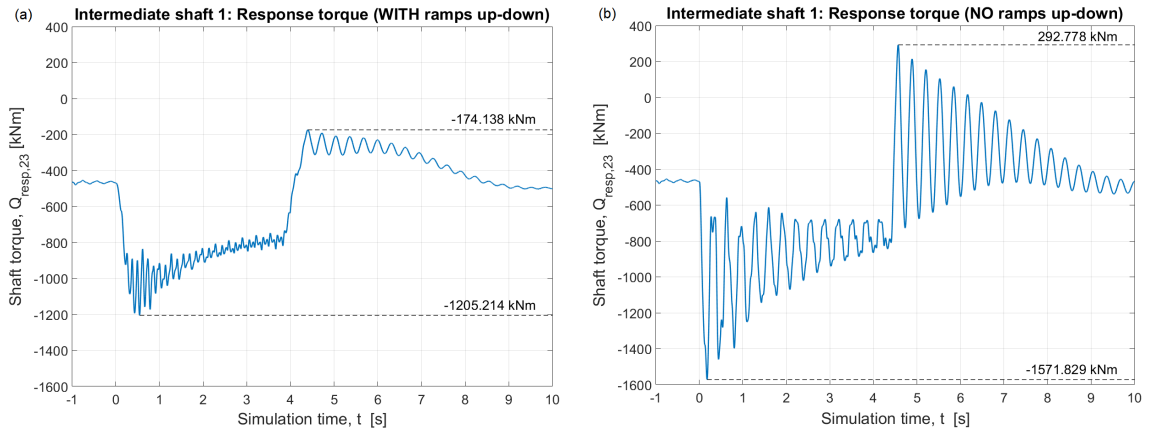


Figure 5.28: Examples of $Q_{\text{resp},23}(t)$ torque curves, with DE prime mover, M -shape, $\alpha_{\text{ice}} = 90^\circ$. The same scale range is used in both vertical axes. (a) Simulation with ramps up-down applied; (b) Simulation with ramps up-down absent.

The results presented in Tables 5.7 and 5.8, plus the curves shown in Fig. 5.28 highlight the influence of the application of the ramps up-down to the Q_{ice} sequence. The application of the IACS pattern [20] or the ABS-DNV one [2, 13] may produce very different outcomes that could affect the design recommendations of shaft strength and fatigue. Modelling Q_{ice} with or without the ramps corresponds to simulate different ice-propeller milling phenomena; without ramps, the ice-blade collisions represent the worst-case scenario with ice-blade impacts occurring against a large and fixed layer of ice.

5.3.3. Scenario 2: single-impact transient response

Fig. 5.29 shows an example of the time-domain excitation torques acting on the propeller and prime mover—in this case the EM drive—when the propeller is excited by a single impact (Scenario 2). The initial equilibrium is resumed in few seconds.

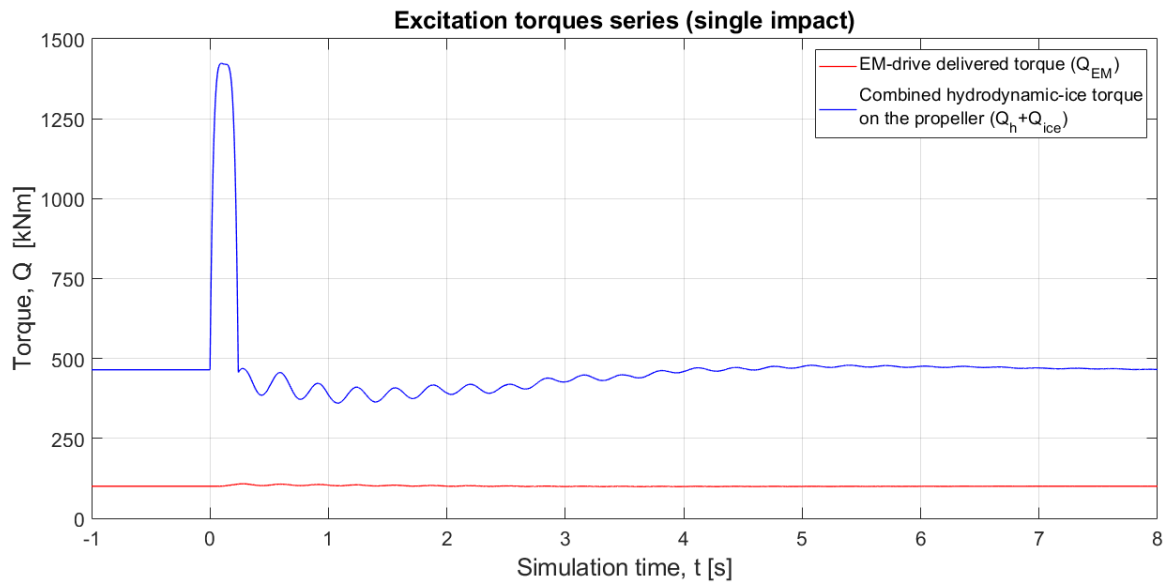


Figure 5.29: Combined propeller torques and EM driving torque throughout a simulation, with the Q_{ice} combination identified by M -shape, $\alpha_{ice} = 180^\circ$.

In Scenario 2, we do not examine $\omega_{PM,min}$ because a single ice-induced impact does not produce results of significant interest.

Fig. 5.30 shows the Q_{peak} outcomes in the “Intermediate shaft 1” (Fig. 5.3). The curves indicate that $Q_{peak,23}$ is linear with respect to α_{ice} until 120° or 150° , and subsequently it reaches a plateau; in particular, the extent of the curve flatness increases as the ice impact shape passes from S to H . Different prime mover types do not affect the results.

Fig. 5.31 shows the contour plots of the results; the high variability of $Q_{peak,23}$ is clear

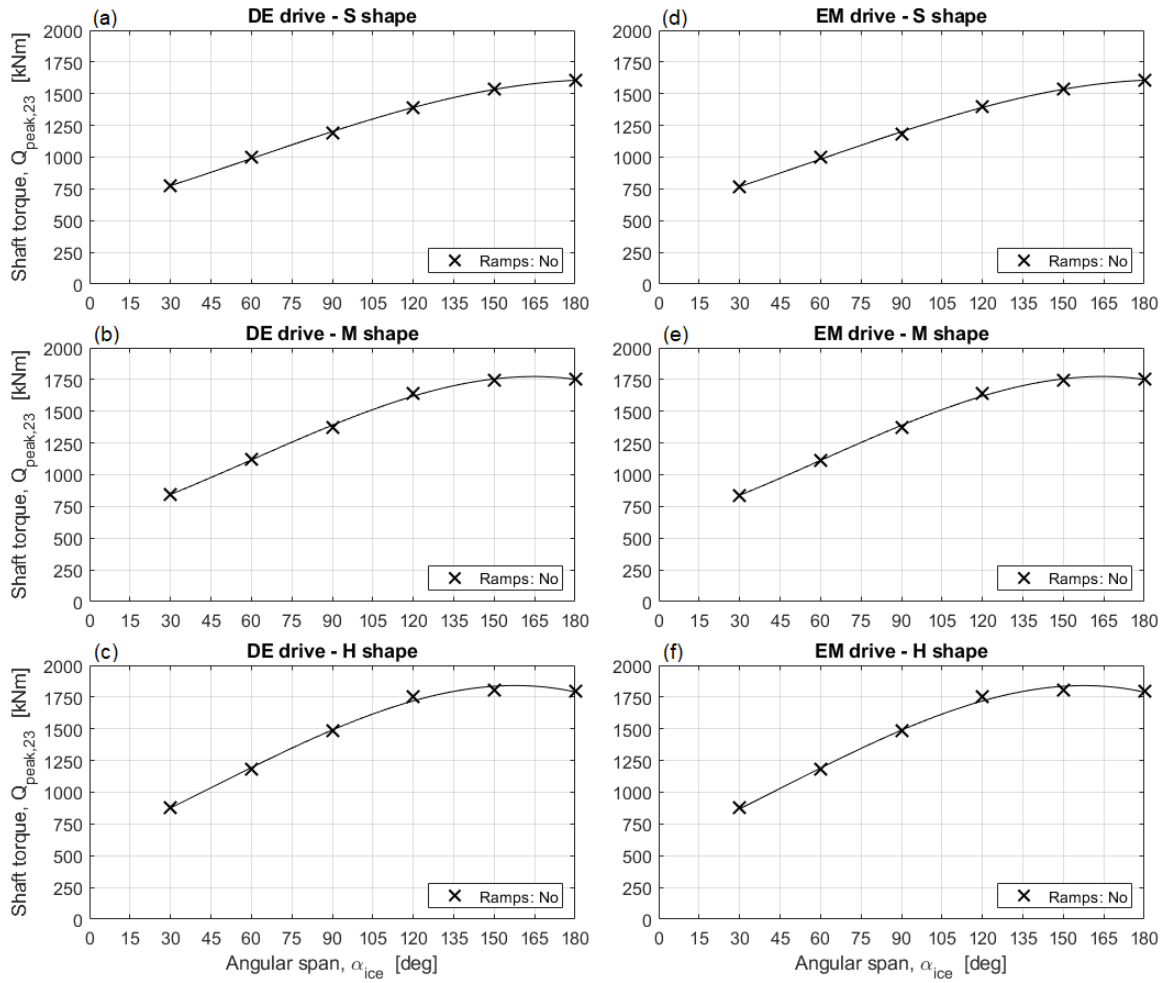


Figure 5.30: Peak torques ($Q_{\text{peak},23}$) in the shaft segment between the nodes 2 and 3, in each model configuration of the Scenario 2. A polynomial fit curve is associated to each data series to show its trend as a function of α_{ice} .

over the low values of ϵ .

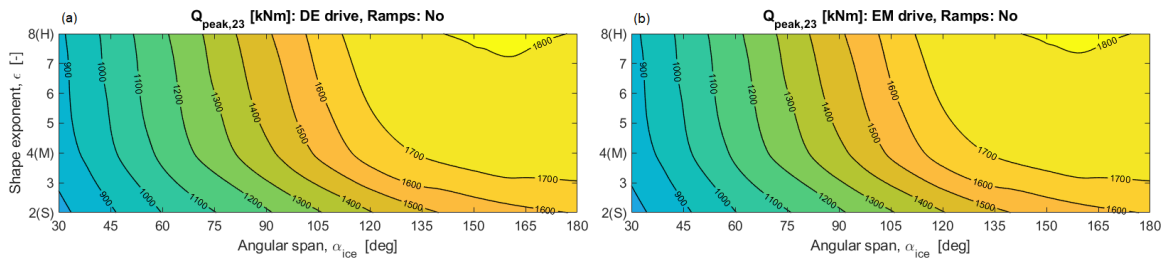


Figure 5.31: Contour plots of the $Q_{\text{peak},23}$ distribution for the configurations of the Scenario 2. The impact shape types are characterized by the exponent ϵ as per Eq. 5.19, and the S-type shape is considered to correspond to the case $\epsilon = 2$ (Fig. 5.13).

Table 5.9 presents the ratios of the $Q_{\text{peak},23}$ values obtained with the M -curve and H -curve cases to the corresponding S -curve values; the ratios are determined for each prime mover and α_{ice} combination. These outcomes indicate how $Q_{\text{peak},23}$ changes as the exponent ϵ —hence the ice impact steepness—increases (Eq. 5.17). The ratio series indicate that no actual differences exist between the application of the DE-drive or the EM option; also, the distance between the M and H shapes’ results is smaller than the difference between the S and M shapes’ outcomes. Therefore, as ϵ increases to define squarer ice impact shapes, the resulting $Q_{\text{peak},23}$ values increase with a less-than-linear trend.

Table 5.9: Ratios between the $Q_{\text{peak},23}$ results obtained with the M , H shape types to the S -shape homologous outcomes, for the Scenario 2.

Shape ratio	DE drive						EM drive					
	30°	60°	90°	120°	150°	180°	30°	60°	90°	120°	150°	180°
M/S	1.09	1.12	1.16	1.17	1.13	1.09	1.09	1.12	1.16	1.17	1.13	1.09
H/S	1.14	1.18	1.25	1.26	1.17	1.12	1.14	1.18	1.25	1.26	1.17	1.12

Figs. 5.32 and 5.33 show the $Q_{\text{range},23}$ outcomes: in this case, differently from the $Q_{\text{peak},23}$ case (Fig. 5.30), $Q_{\text{range},23}$ exhibits a concave trend. As a result, $Q_{\text{range},23}$ as a function of α_{ice} has a maximum value at approximately $\alpha_{\text{ice}} = 150^\circ$. The non-monotonic behaviour of the curves takes place in correspondence of the plateaus in the $Q_{\text{peak},23}$ curves. Therefore, the magnitude of $Q_{\text{range},23}$ is ultimately determined by the overshoot peak value, which is the $Q_{\text{resp},23}$ peak taking place at the opposite oscillation side from $Q_{\text{peak},23}$. The overshoot peak occurs immediately after the ice-induced excitation ceases, and its intensity depends on the torsional vibration status of the shaft in that moment. Specifically, the transient angular position of $\vec{\theta}$ in place at the end of Q_{ice} constitutes the initial condition of the system after

the pulse, which undergoes a free oscillation. The variable α_{ice} determines the ice impact's duration, hence the free oscillation evolution after it. As Fig. 5.32 shows, this effect causes $Q_{range,23}$ to drop beyond $\alpha_{ice} = 150^\circ$.

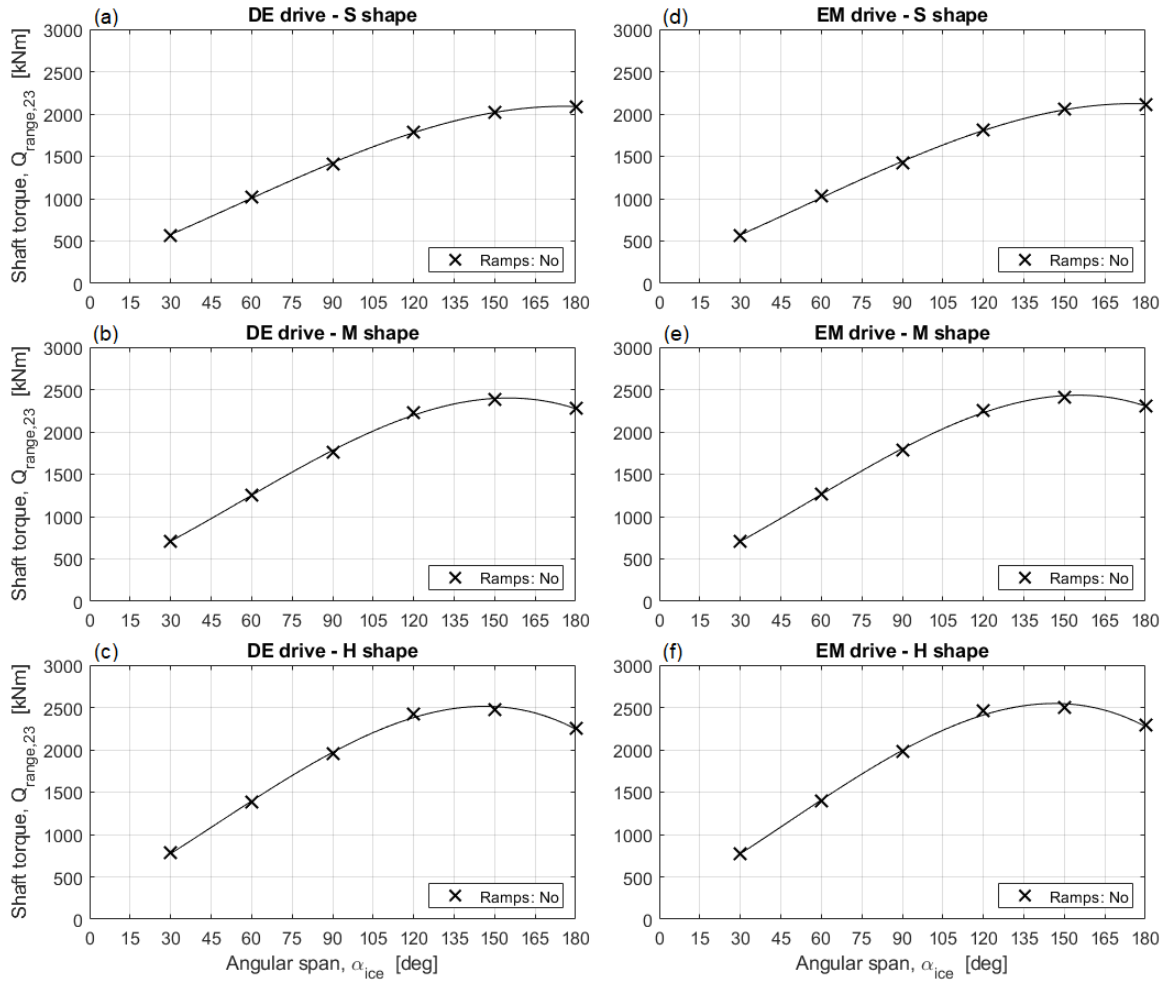


Figure 5.32: Range torques ($Q_{range,23}$) in the shaft segment between the nodes 2 and 3, in each model configuration of the Scenario 2. A polynomial fit curve is associated to each data series to show its trend as a function of α_{ice} .

Table 5.10 shows the $Q_{range,23}$ shape ratios calculated as we did for Table 5.9. The main difference with the outcomes we obtained for $Q_{peak,23}$ is that in the case of $Q_{range,23}$ the ratios are significantly larger up to the $\alpha_{ice} = 120^\circ$ value. Therefore, the impact shape type affects

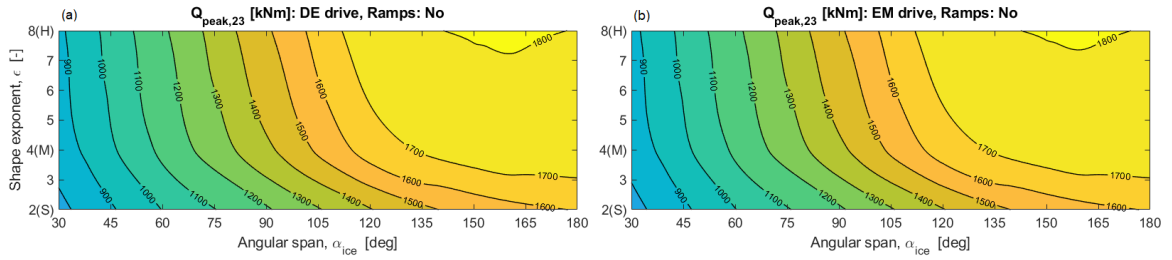


Figure 5.33: Contour plots of the $Q_{\text{range},23}$ distribution for the configurations of the Scenario 2. The impact shape types are characterized by the exponent ϵ as per Eq. 5.19, and the S -type shape is considered to correspond to the case $\epsilon = 2$ (Fig. 5.13).

$Q_{\text{range},23}$ more than it influences $Q_{\text{peak},23}$. With an analogous pattern, $Q_{\text{range},23}$ changes with a less-than-linear trend with respect to ϵ ; besides, the prime mover model does not affect the $Q_{\text{range},23}$ ratios, and also the torque magnitudes result to be approximately equal.

Table 5.10: Ratios between the $Q_{\text{range},23}$ results obtained with the M , H shape types to the S -shape homologous outcomes, for the Scenario 2.

Shape ratio	DE drive						EM drive					
	30°	60°	90°	120°	150°	180°	30°	60°	90°	120°	150°	180°
M/S	1.24	1.23	1.26	1.25	1.17	1.09	1.24	1.23	1.26	1.25	1.17	1.09
H/S	1.37	1.35	1.40	1.36	1.22	1.08	1.37	1.35	1.40	1.36	1.22	1.08

As an example, Fig. 5.34 shows $Q_{\text{resp},23}$ resulting from two simulations with different excitation shapes. In the plots, we chose the $\alpha_{\text{ice}} = 150^\circ$ case, as it maximizes the $Q_{\text{range},23}$ curves. The discrepancies in $Q_{\text{peak},23}$ and $Q_{\text{range},23}$ between the examples are close to 20% (as per Tables 5.9 and 5.10).

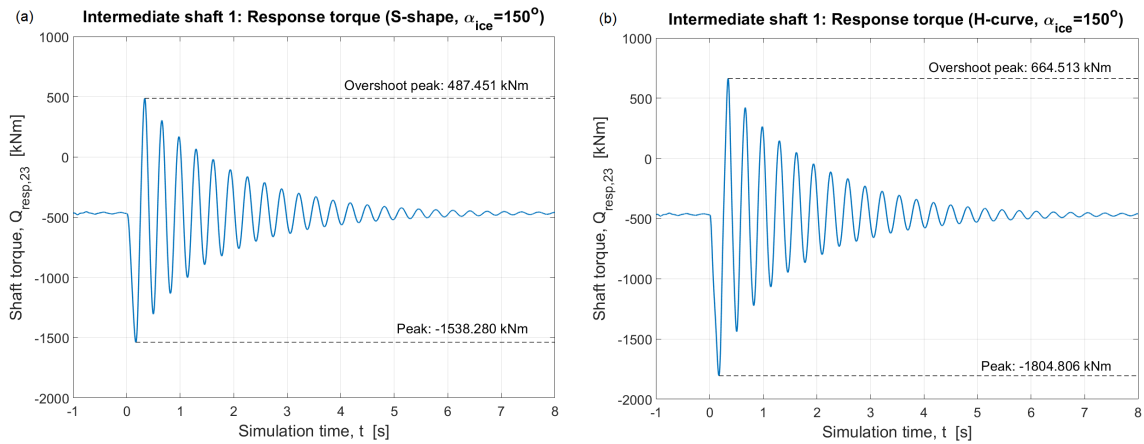


Figure 5.34: Examples of $Q_{\text{resp},23}(t)$ torque curves during a single ice-propeller impact, with DE prime mover, $\alpha_{\text{ice}} = 150^\circ$. The same scale range is used in both vertical axes. (a) Simulation with *S*-shape impact; (b) Simulation with *H*-shape impact.

5.3.4. Scenario 3: transition between transient and steady-state conditions

We examine how the shaftline response evolves as the number of ice-propeller impacts gradually increases from 1 to 30. From the analysis in Subsection 5.3.2, the combination prime mover–impact shape that produces the most severe outcomes is identified by the subplots (c) in Figs. 5.22, 5.24, 5.26 (DE-drive and *H*-shape pair). In it, we consider the four α_{ice} cases up to 120° , since in the 150° and 180° cases the system halts.

Fig. 5.35 shows the results of the four simulation series, plotted against the impacts’ number. The “Intermediate shaft 1” segment is considered to evaluate $Q_{\text{peak},23}$ and $Q_{\text{range},23}$, as done in Subsections 5.3.2 and 5.3.3.

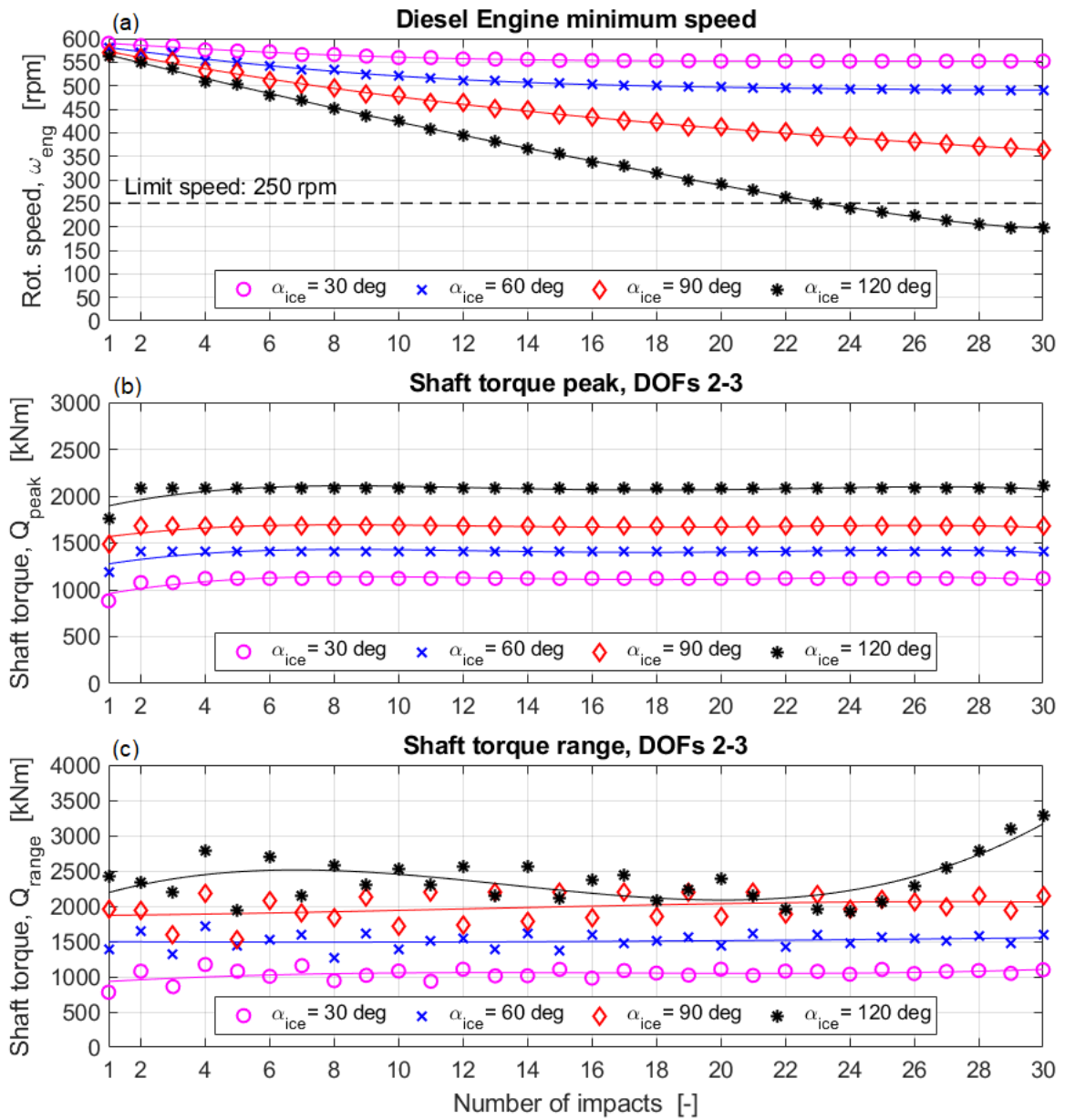


Figure 5.35: Quantities $\omega_{eng,min}$, $Q_{peak,23}$, and $Q_{range,23}$ for four system configurations, as the number of the ice-propeller interaction impacts ranges from 1 to 30. A polynomial fit curve is associated to each data series to show its trend (solid thin lines).

Regarding $\omega_{eng,min}$, the $\alpha_{ice} = 30^\circ$ case reaches its stabilized level at about 18-20 impacts; the 60° one stabilizes at about 22-24 impacts, and the 90° , 120° simulations reach

the steady-state speed at around 28 impacts. The 120° case falls below the stall limit speed when the ice-propeller sequence counts 23 impacts. The curves follow a linear trend until $\omega_{\text{eng,min}}$ settles.

On the other hand, the $Q_{\text{peak},23}$ series converge to their respective levels starting from the 2-impact case. This fact means that to evaluate the shafts' Q_{peak} no difference arises when the number of consecutive impacts increases.

Very different patterns result in the $Q_{\text{range},23}$ case: the asymptotical values of the simulations with 30° , 60° , 90° are reached after ample fluctuations of the respective $Q_{\text{range},23}$ outcomes corresponding to low numbers of impacts. The higher α_{ice} , the larger the deviations from the final, stabilized $Q_{\text{range},23}$ level. This fact means that in order to evaluate Q_{range} , ice-propeller torque series with a limited number of impacts may produce significantly higher values; therefore, the shaftline's fatigue criteria according to the rules [2, 13] would get crucially affected. We can also observe that the values included in the $Q_{\text{range},23}$ data series lay approximately on two levels: one for the even-number impacts, one for the odd-number ones. This particular behaviour is due to the overshoot peak phenomenon discussed in the single-impact series (Subsection 5.3.3): the torsional oscillation position of the shaftline is different when the impacts are odd or even, hence the alternating trend of the resulting points.

The case with $\alpha_{\text{ice}} = 120^\circ$ shows a different pattern, because even if its $Q_{\text{peak},23}$ values converge, $Q_{\text{range},23}$ diverge. We carried out additional simulations up to 50 impacts to test whether the $Q_{\text{range},23}$ curve settles eventually; the plots are shown in Fig. 5.36.

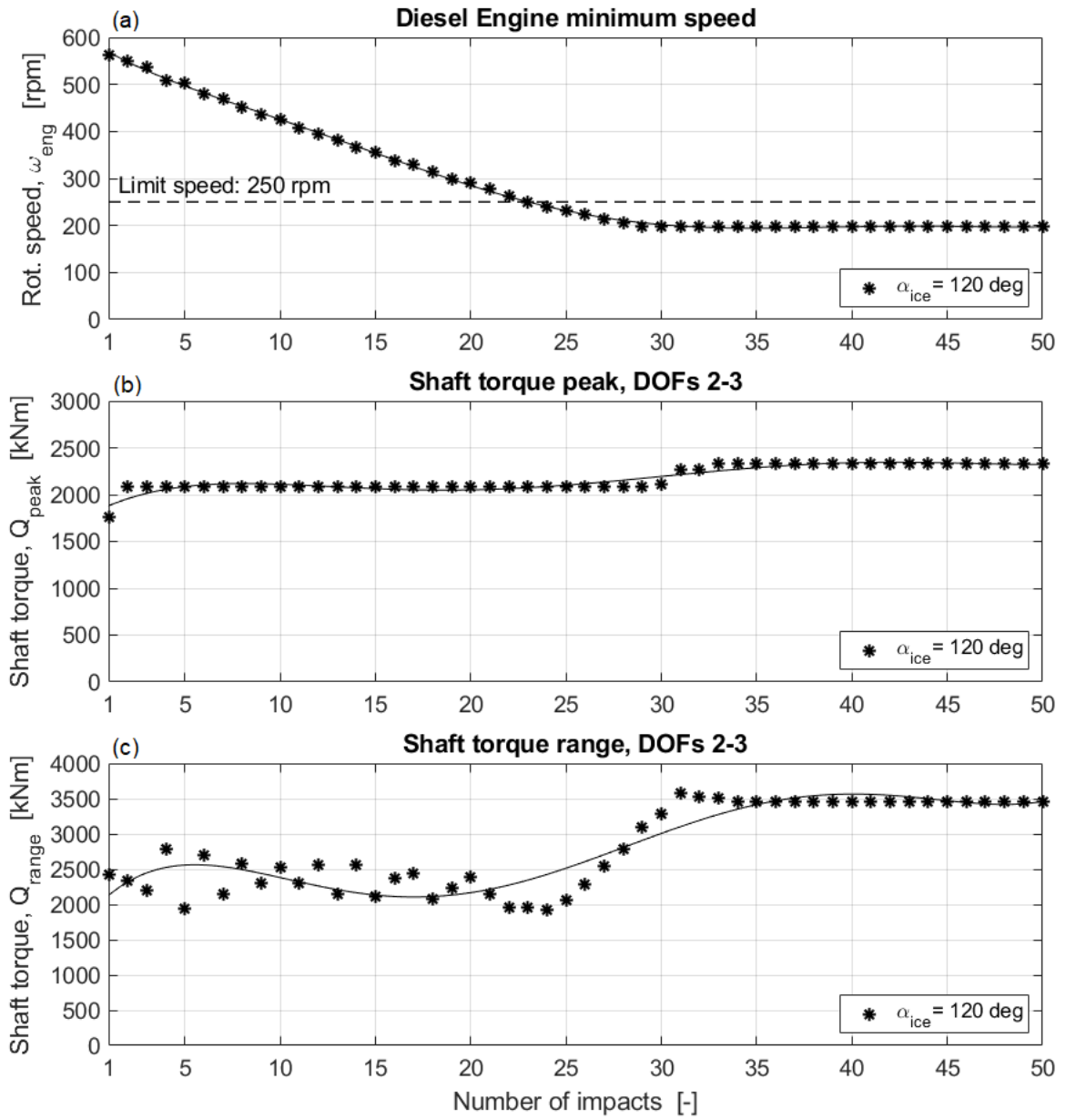


Figure 5.36: Quantities $\omega_{eng,min}$, $Q_{peak,23}$, and $Q_{range,23}$ for the *H*-shape, $\alpha_{ice} = 120^\circ$ configuration, as the number of the ice-propeller interaction impacts ranges from 1 to 50. A polynomial fit curve is associated to each data series to show its trend (solid thin lines).

This behaviour is due to a numerical occurrence related to the CPP effect on $Q_{ice}(t)$.

Indeed, the system's $\omega_{eng,min}$ falls below the stall limit after 23 impacts; hence, the CPP

blade pitch angle reaches its minimum value (Φ_{\min} , Table 5.2), crossing the 0° mark. As a result, the factor q_Φ (Eq. 5.19) becomes null for a time instant, and this consequently makes the ice-induced excitation zero. The numerical outcome of this event is a very high overshoot peak value that induces $Q_{\text{range},23}$ to increase. Fig. 5.36 shows that a new level of $Q_{\text{peak},23}$ is ultimately reached, while maintaining the same $\omega_{\text{eng},\min}$ asymptote, and that between 27 and 33 impacts $Q_{\text{range},23}$ —hence $Q_{\text{peak},23}$ and $Q_{\text{range},23}$ —becomes unstable.

From the standpoint of the shaftline’s design, the propulsion system is considered to fail as soon as $\omega_{\text{PM}}(t)$ crosses the stall speed limit disregarding the Q_{peak} and Q_{range} outcomes. However, even if $\omega_{\text{PM},\min}$ resulted higher than the prime mover’s stall limit, the effects of q_Φ at $\Phi \approx 0$ would constitute a numerical concern that requires caution in the results’ analysis.

5.4. Final remarks

5.4.1. Summary of the results

The outcomes of the three analyses are commented below.

- **Scenario 1.** All four simulation parameters concur to affect the responses $Q_{\text{peak},23}$ and $Q_{\text{range},23}$. Regarding $\omega_{\text{PM},\min}$, the application of the ramps up-down is not significant. Conversely, the ramps’ presence represents a crucial factor to affect $Q_{\text{resp}}(t)$ both in terms of $Q_{\text{peak},23}$ and $Q_{\text{range},23}$, and concerning the intermediate torque fluctuations during the ice-induced perturbation. This fact highlights how critical is choosing between applying the IACS guidelines (no ramps up-down applied, [20]) or the ABS-DNV recommendations (ramps up-down applied, [2, 13]). Also, since the ramps’ application results to be

particularly important for intermediate values of α_{ice} , the cases with 90° and 135° in the rules are the most affected ones. About the prime mover type, the results show that the EM option prevents the shaftline system to stall in 30 configurations out of 36, whereas the DE drive sustains the ice-induced load only in 24 cases (Fig. 5.22). The effectiveness of the EM drive model is based on the coefficient that determines $Q_{EM,max}$ from the EM steady-state torque (Eq. 5.12): adjusting this factor influences the system's capability to oppose the ice-propeller torque in relation to the lowest allowable speed.

- **Scenario 2.** Only α_{ice} and the impact shape (through ϵ , Eq. 5.19) are the significant parameters to influence the responses $Q_{peak,23}$ and $Q_{range,23}$. A single impact is not sufficient to make the effects of the two prime movers types clearly distinct in the $Q_{resp}(t)$ results. In this part, a relevant result is the non-monotonic trend of the $Q_{range,23}$ curves as a function of α_{ice} (Fig. 5.32). The particular behaviour of $Q_{resp}(t)$ at the end of the ice-induced pulse is the key factor that affects $Q_{range,23}$ during transient states. This fact needs to be considered when the rules' fatigue assessment is concerned [2, 13], in the case of single impacts occurring in time-distant sequences.
- **Scenario 3.** The progressive addition of consecutive impacts points out the importance of considering the ice-propeller excitation sequences with a low number of impacts. Indeed, the transient character of the shaftline's response through few ice-propeller pulses makes $Q_{range,23}$ assume unexpected values before stabilizing asymptotically towards the steady-state condition (Fig. 5.35). Therefore, to achieve worst-case scenario evaluations of $Q_{range,23}$ —hence increasing the safety level of the shaftline's design—multiple simulations

with different numbers of impacts should be carried out. Our results also highlight the numerical anomalies that arise from the CPP zero-pitch effect (Fig. 5.36), which occurs when the propulsion system settles on a speed level close to the stall speed limit of the prime mover.

5.4.2. Strengths and limitations of this work

We considered alternative impact shapes of the ice-propeller torque pulse that could simulate heavier loads than the ones recommended by the rules. Likewise, we examined a more comprehensive set of impact's angular span values, exceeding the rule-defined maximum width [2, 13, 20]. A remarkable result of this work regards the difference in the TVA outcomes when the “ramps up-down” feature is applied or not. This fact might induce a review of the ramps' application according to the current design rules, in order to evaluate whether this element reduces too much the ice-propeller excitation and thus the shaft segments' response. Besides, the fixed magnitude of every single ice-induced pulse is realistic, as it has been derived from the ice-torque correlation we achieved in [52].

The Polar Rules' formulation of the ice-propeller torque pattern refers to the process of ice milling through a uniform ice layer, with a constant penetration depth of the propeller blades; this scenario simulates the worst-case situation when icebreaking operations are conducted in heavy packed ice. A limitation of our analysis is the lack of knowledge on how to simulate the ice-propeller interaction after many consecutive impacts. In that situation, the chaotic motion and blockage of the milled ice debris affect the actual excitation [25, 46, 47]. However, the assumption of applying identical loads for 30-pulse sequences (Scenario 1,

Subsection 5.3.2) is here considered as a safety-side implementation. We simulated the dynamic effect of the CPP reaction to sudden loads and included the cases in which the pitch angle approaches zero; in those particular conditions, the mathematical definition of $q_{\Phi}(t)$ may follow a different pattern.

5.4.3. Future developments

The following steps in the research project involve measurement campaigns during ice-breaking operations to acquire torsional vibration data on the CCGS *Terry Fox*'s shafts; such measures would then be processed to determine the actual ice-propeller excitation and its magnitude through the procedure presented in [52]. In particular, obtaining high-frequency signals would contribute to characterize the shape of single ice-induced torque pulses, also in relation to diverse icebreaking manoeuvres and ice type. Besides the ice impact properties analyzed in this paper, the effects of the propeller's geometry needs to be investigated more thoroughly, in order to possibly integrate the works [32, 46, 47]. Concerning the numerical simulations of the prime mover excitation and the dynamic controllers, a more sophisticated model may have to be developed to correctly reproduce the EM-drive power control and the effect of the CPP motion on the ice-induced load for low CPP angles.

5.4.4. Conclusions

Our study aims to provide a systematic view of the TVA results obtained by applying multi-variable alterations of the ice-propeller interaction torque to the numerical model of a propulsion shaftline. Initially, we developed and verified an expanded version of our DE-

drive lumped-element model, which simulates the torsional dynamics of the shafting system of the CCG icebreaker *Terry Fox*. Then, we considered the mathematical formulation of the ice-induced torque on marine propeller blades, as per the IACS Polar Rules [20] and the ABS-DNV guidelines [2, 13]. Different variants of the main properties that characterize this excitation were considered, and then arranged into a simulation space including all their combinations. We examined three excitation sets having: (i) a fixed number of consecutive ice impacts; (ii) a single ice-propeller pulse; (iii) an increasing number of ice impacts. Additionally, we implemented the EM-drive excitation on the shaftline's condensed model as an alternative prime mover plant.

Our findings point out the higher significance of the ice impact's angular span and the ramps up-down to affect both the system's minimum speed and the shaft response torques during the multiple-impact scenarios. On the other hand, the ice pulse shape and the prime mover type entailed minor effects on the shaftline's TVA results. Besides, we highlighted how relevant is the difference in the system's response between simulating several impacts or a single pulse as ice-propeller excitation; the transient dynamic behaviour of the system under few consecutive impacts may induce more severe results than the ones obtained by augmenting the number of impacts. These findings suggest the need for detailed ice-induced torque measurements on polar-class vessels to better characterize these loads.

Acknowledgements

The authors thank Mr. Wayne Lambert from the Canadian Coast Guard (CCG) and the crew members of CCGS *Terry Fox* for their availability and courtesy in accommodating our experimental activity on board the vessel.

This work was supported by the American Bureau of Shipping (ABS) and the Department of Industry, Energy and Technology (IET) of the Government of Newfoundland and Labrador.

Appendices

5.A. Numerical model of the case study's shaftline: structural properties

We report the main characteristics that define the lumped-element model of the CCGS *Terry Fox*'s shaftline. The shaft material properties employed in the modelling process are shown in Table 5.11.

Table 5.11: Shaftline material properties.

Parameter		Value	Unit
Steel density	ρ_s	7,850	[kg.m ⁻³]
Steel Young modulus	E	210.3	[GPa]
Steel Poisson ratio	ν	0.27	[-]
Steel shear modulus	G	82.8	[GPa]
Shaft damping factor [1]	S_1	0.005	[-]
Crankshaft damping factor [1]	$S_{1,cr}$	0.0001	[-]

Table 5.12 lists the main properties of the icebreaker's DE components.

Table 5.12: Detailed specifications of the engine components.

Parameter		Value	Unit
Cylinder bore	b	410	[mm]
Stroke (in-line)	s	470	[mm]
Crank throw radius	r	235	[mm]
Connecting rod length	L	1,140	[mm]
Connecting rod mass	m_{connrod}	427	[kg]
Piston mass	m_{piston}	223	[kg]
Crankshaft mass (whole)	$m_{\text{crankshaft}}$	7,700	[kg]

Table 5.13 lists the mass moments of inertia of the shaftline model nodes, including the expanded model; in particular, each nodal inertia also includes the half-inertia portions from the two adjacent shaft segments. The speed ratio transformations as per Eq. 5.3 are applied to the concerned items.

Besides, the propeller node (θ_1) includes the contribution of the added inertia at 90% CPP angle, which was calculated as per [12]. Likewise, the global inertia of the DE condensed node and the DE crank arms in the expanded variant include the moment of inertia given by the portion of connecting rod considered to be lumped in the crankpin [34].

Table 5.14 reports the torsional stiffness and damping coefficients of the nodal connections. The transformations as per Eq. 5.3 are included.

Table 5.13: Mass moments of inertia of both models' nodes.

Element	DOF θ_i	I_i [kg.m ²]
Propeller plus added water inertia ($\Phi = 90\%$)	θ_1	73,384.0
Flange ringnut	θ_2	2,315.8
Flywheel	θ_3	21,732.4
Gearbox	θ_4	23,193.0
<i>Condensed model</i>		
DE (and EM) overall rotating assembly	θ_5	170,781.1
<i>Expanded model</i>		
DE crank arm(s)	$\theta_{5,\dots,12;14,\dots,21}$	9,962.6
Torsional vibration damper(s)	$\theta_{13;22}$	5,689.9

Table 5.14: Torsional stiffness and damping coefficients.

Connecting segment	DOFs $(i, i + 1)$	$k_{i,i+1}$ [MNm.rad ⁻¹]	$c_{i,i+1}$ [kNm.(rad/s) ⁻¹]
Propeller tailshaft	(1, 2)	288.4	106.2
Intermediate shaft 1	(2, 3)	60.39	22.23
Intermediate shaft 2	(3, 4)	68.92	25.36
<i>Condensed model</i>			
Gearbox-DE(or EM) coupling	(4, 5)	73.99	249.5
<i>Expanded model</i>			
Gearbox-DE coupling(s)	(4, 5)	37.00	124.7
	(4, 14)	=	=
Crank throw connection(s)	(5, 6); ... ; (11, 12)	11,765	18.72
	(14, 15); ... ; (20, 21)	=	=
DE-TVD connection(s)	(12, 13)	22.46	71.50
	(21, 22)	=	=

References

- [1] ABS (2011). ABS Torsional Vibration software - V2.1 - Users Manual. Technical report, American Bureau of Shipping. Updated Nov 2011. 202, 203, 252
- [2] ABS (2019). *Part 6: Specialized Items and Systems, Chapter 1: Strengthening for Navigation in Ice, Section 3: Machinery Requirements for Polar Class Vessels*. Rules for Building and Classing - Marine vessels, American Bureau of Shipping, Edition July 2019. xxii, 198, 212, 213, 214, 218, 220, 222, 226, 237, 245, 247, 248, 249, 251
- [3] Adams, M. L. (2010). *Rotating Machinery Vibrations*. Taylor & Francis, 2nd edition. 201
- [4] Batrak, Y. A., Serdjuchenko, A. M., and Tarasenko, A. I. (2014). Calculation of torsional vibration responses in propulsion shafting system caused by ice impacts. In *Torsional Vibration Symposium*, Salzburg, Austria. 195, 196
- [5] Bond, J., Hindley, R. J., Kendrick, A., Kämäräinen, J., Kuuliala, L., et al. (2018). Evaluating Risk and Determining Operational Limitations for Ships in Ice. In *OTC Arctic Technology Conference*, Houston, TX, USA. Offshore Technology Conference. 193
- [6] Brouwer, J., Hagesteijn, G., and Bosman, R. (2013). Propeller-ice impacts measurements with a six-component blade load sensor. In *Third International Symposium on Marine Propulsors (SMP13)*, Tasmania, Australia. 194
- [7] Burella, G. and Moro, L. (2017). Transient torsional analysis of polar class vessel shafting systems using a lumped model and finite element analysis. In *The 27th International Ocean and Polar Engineering Conference*, San Francisco, USA. 195, 209
- [8] Burella, G., Moro, L., and Oldford, D. (2018). Analysis and validation of a procedure for a lumped model of Polar Class ship shafting systems for transient torsional vibrations. *Journal of Marine Science and Technology*, 23(3):633–646. 195, 209
- [9] Carlton, J. S. (2007). *Marine Propellers and Propulsion*. Butterworth-Heinemann, Elsevier, 2nd edition. 210
- [10] de Waal, R. J. O., Bekker, A., and Heyns, P. S. (2017). Bi-Polar Full Scale Measurements of Operational Loading on Polar Vessel Shaft-lines. In *Proceedings of the 24th International Conference on Port and Ocean Engineering under Arctic Conditions (POAC 2017)*, Busan, South Korea. 194
- [11] de Waal, R. J. O., Bekker, A., and Heyns, P. S. (2018). Indirect load case estimation for propeller-ice moments from shaft line torque measurements. *Cold Regions Science and Technology*, 151:237–248. 194, 195
- [12] Dien, R. and Schwanecke, H. (1973). Die propellerbedingte Wechselwirkung zwischen Schiff und Maschine. *Motortechnische Zeitschrift*, 34(12):425–430. 201, 253
- [13] DNV (2021). *Part 6: Additional Class Notations, Section 7: Polar Class, Par. 11: Ice interaction loads – machinery*, chapter 6: Cold climate. Det Norske Veritas, Edition July 2021. xxii, 195, 198, 212, 213, 214, 218, 222, 237, 245, 247, 248, 249, 251

- [14] Ehlers, S., Kujala, P., Veitch, B., Khan, F., and Vanhatalo, J. (2014). Scenario based risk management for arctic shipping and operations. In *ASME 2014 33rd International Conference on Ocean, Offshore and Arctic Engineering*. American Society of Mechanical Engineers (ASME). 193
- [15] Gunnarsson, B. (2021). Recent ship traffic and developing shipping trends on the Northern Sea Route—Policy implications for future arctic shipping. *Marine Policy*, 124:104369. 192
- [16] Hindley, R. J. and Tustin, R. D. (2009). Guidance notes for the classification of stern first Ice Class ships. In *RINA International Conference on Ship and Offshore Technology: Ice Class Vessels*, pages 53–61, Busan, South Korea. Royal Institution of Naval Architects. 193
- [17] Hindley, R. J., Tustin, R. D., and Upcraft, D. S. (2007). Environmental protection regulations and requirements for ships for Arctic sea areas. In *RINA International Conference - Design and Construction of Vessels Operating in Low Temperature Environments*, pages 107–118, United Kingdom. Royal Institution of Naval Architects. 193
- [18] Hoffmann, K. (2001). Applying the Wheatstone Bridge Circuit. Technical report, Hottinger Baldwin Messtechnik (HBM) GmbH. Version W1569en-1.0. 204
- [19] Ikonen, T., Peltokorpi, O., and Karhunen, J. (2015). Inverse ice-induced moment determination on the propeller of an ice-going vessel. *Cold Regions Science and Technology*, 112:1–13. 195
- [20] International Association of Classification Societies (IACS) (2006). Requirements concerning Polar Class - Polar Rules. Rev. 1 Jan 2007, Corr. 1 Oct 2007. xxii, 194, 198, 212, 213, 214, 216, 218, 219, 220, 222, 237, 247, 249, 251
- [21] Irgens, O.-J., Kokkila, K., Hänninen, S., et al. (2018). Propulsion Technology for Polar Expedition Ships. In *OTC Arctic Technology Conference*. Offshore Technology Conference. 193
- [22] Kämäräinen, J. (2013). IMO regulations and Ice Class Rules. In *22nd International Conference on Port and Ocean Engineering under Arctic Conditions (POAC 2013)*. 193
- [23] Kendrick, A. and Santos-Pedro, V. (2010). The future of polar shipping rules. In *International Conference and Exhibition on Performance of Ships and Structures in Ice - ICETECH 2010*, pages 31–35. 193
- [24] Kendrick, A. M. (2014). Polar ship design standards - state of the art, and way forward. In *Transactions - Society of Naval Architects and Marine Engineers (SNAME)*, volume 122, pages 428–433, Houston, TX, USA. 193
- [25] Khan, A. G., Hisette, Q., Streckwall, H., and Liu, P. (2020). Numerical investigation of propeller-ice interaction effects. *Ocean Engineering*, 216:107716. 194, 221, 249
- [26] Kinnunen, A., Turunen, T., Koskinen, P., and Heinonen, J. (2017). Propulsion Shaft Line Ice-Induced Dynamic Torque Response. In *Proceedings of the 24th International Conference on Port and Ocean Engineering under Arctic Conditions (POAC 2017)*, Busan, South Korea. 195

- [27] Kitagawa, H. et al. (2011). Safety and Regulations of Arctic Shipping. In *The Twenty-first International Offshore and Polar Engineering Conference*. International Society of Offshore and Polar Engineers. 193
- [28] Kujala, P., Goerlandt, F., Way, B., Smith, D., Yang, M., Khan, F., and Veitch, B. (2019). Review of risk-based design for ice-class ships. *Marine Structures*, 63:181–195. 193
- [29] Lecourt Jr, E. J. (1998). Using Simulation to Determine the Maneuvering Performance of the WAGB-20. *Naval Engineers journal*, 110(1):171–188. 195
- [30] Lee, S.-K. (2006). Rational approach to integrate the design of propulsion power and propeller strength for ice ships. *ABS Technical Papers*. Originally presented at the 2006 SNAME ICETECH conference; Banff, Canada, July 16-19, 2006. 194
- [31] Lee, S.-K. (2007). Engineering practice on ice propeller strength assessment based on IACS polar ice rule-URI3. In *10th International Symposium on Practical Design of Ships and Other Floating Structures, ABS Technical Papers*. Citeseer. 221
- [32] Liu, P., Bose, N., and Veitch, B. (2015). Evaluation, design and optimization for strength and integrity of polar class propellers. *Cold Regions Science and Technology*, 113:31–39. 193, 250
- [33] MAN (2011). Basic Principles of Ship Propulsion. Frederikshavn, Denmark. MAN Diesel & Turbo. 210
- [34] Mollenhauer, K. and Tschöke, H. (2010). *Handbook of Diesel Engines*. Springer. 201, 253
- [35] Nickerson, B. and Bekker, A. (2021). Recommendations for regularization in the inverse estimation of ice-induced propeller moments for ice-going vessels. *Cold Regions Science and Technology*, page 103378. 195
- [36] Polić, D., Æsøy, V., and Ehlers, S. (2016). Transient simulation of the propulsion machinery system operating in ice—modeling approach. *Ocean Engineering*, 124:437–449. 195
- [37] Polić, D., Æsøy, V., Ehlers, S., and Pedersen, E. (2014). Shaft response as a propulsion machinery design load. In *Proceedings of the ASME 2014 33rd International Conference on Ocean, Offshore and Arctic Engineering (OMAE2014)*, San Francisco, California, USA. 195
- [38] Polić, D., Ehlers, S., and Æsøy, V. (2019). Inverse modeling approach for transformation of propeller shaft angular deformation and velocity to propeller torque load. *Marine Structures*, 67. 195
- [39] Polić, D., Ehlers, S., Æsøy, V., and Pedersen, E. (2013). Propulsion Machinery Operating In Ice-A Modelling And Simulation Approach. In *Proceedings - 27th European Conference on Modelling and Simulation (ECMS 2013)*, pages 191–197. 195, 221
- [40] Rakopoulos, C. D. and Giakoumis, E. G. (2009). *Diesel Engine Transient Operation*. Springer. 208
- [41] Rao, S. S. (2011). *Mechanical Vibrations*. Pearson, 5th edition. 202, 203, 204, 221

- [42] Silber, G. K. and Adams, J. D. (2019). Vessel Operations in the Arctic, 2015-2017. *Frontiers in Marine Science*, 6:573–590. 192
- [43] Silva, C. A. F., Manin, L., Rinaldi, R. G., Besnier, E., and Remond, D. (2019). Dynamics of Torsional Vibration Damper (TVD) pulley, implementation of a rubber elastomeric behavior, simulations and experiments. *Mechanism and Machine Theory*, 142:103583. 204
- [44] Sinha, R. P. and Balaji, R. (2018). A mathematical model of marine diesel engine speed control system. *Journal of the Institution of Engineers (India): Series C*, 99(1):63–70. 208
- [45] Tavares, H. F. and Prodonoff, V. (1986). A new approach for gearbox modelling in finite element analyses of torsional vibration of gear-branched propulsion systems. *The Shock and Vibration Bulletin*, (56):117–125. 201
- [46] Veitch, B. (1995). *Predictions of Ice Contact Forces on a Marine Screw Propeller During the Propeller-Ice Cutting Process*. PhD thesis, Helsinki University of Technology, Finland. Acta Polytechnica Scandinavica, Mechanical Engineering Series. xxii, 194, 215, 249, 250
- [47] Wang, C., Xiong, W. P., Chang, X., Ye, L. Y., and Li, X. (2018). Analysis of variable working conditions for propeller-ice interaction. *Ocean Engineering*, 156:277–293. xxii, 193, 215, 249, 250
- [48] Wang, J., Akinturk, A., and Bose, N. (2006). Numerical prediction of model podded propeller-ice interaction loads. In *25th International Conference on Offshore Mechanics and Arctic Engineering (OMAE2006)*, pages 667–674, Hamburg, Germany. American Society of Mechanical Engineers Digital Collection. 194
- [49] Yang, H. J., Wu, Q. W., and Yang, J. (2020). Torsional Vibration Calculation for Propulsion Shaft of 1A Ice Class Ship. In *The 30th International Ocean and Polar Engineering Conference*. 196
- [50] Yumashev, D., van Hussen, K., Gille, J., and Whiteman, G. (2017). Towards a balanced view of Arctic shipping: estimating economic impacts of emissions from increased traffic on the Northern Sea Route. *Climatic Change*, 143(1-2):143–155. 193
- [51] Zambon, A. and Moro, L. (2022). Torsional vibration analysis of diesel driven propulsion systems: The case of a polar-class vessel. *Ocean Engineering*, 245:110330. xxi, xxii, 196, 198, 199, 200, 202, 204, 205, 206, 207, 208, 210, 211, 221
- [52] Zambon, A., Moro, L., Kennedy, A., and Oldford, D. (2022). Torsional vibrations in icebreaker shaftlines: correlating ice-propeller interaction torque to sea ice thickness. *Ocean Engineering*. Currently under review. 209, 220, 249, 250
- [53] Zhang, Z., Huisingsh, D., and Song, M. (2019). Exploitation of trans-Arctic maritime transportation. *Journal of cleaner production*, 212:960–973. 192

Chapter 6

Summary and final remarks

This Chapter summarizes the thesis' contents and resumes the main accomplishments of the work; finally, the plans to further augment the research project are outlined.

6.1. Summary

The present doctoral thesis regards the subject of Torsional Vibration Analysis (TVA) of marine propulsion systems, in connection with the characterization of the excitation torque induced by ice-propeller impacts. Propulsion shaftlines play a key role among the systems on board Polar-Class vessels, as they are required to ensure the safety of marine operations and the ships' survivability. Hence, the hazard posed by ice-propeller interaction needs adequate modelling approaches in order to obtain reliable predictions of shaftlines' dynamic response. The research activity carried out to produce this thesis has involved both theoretical analysis and full-scale experiments. The two CCG icebreakers *Henry Larsen*

and *Terry Fox* constituted the case studies of the research; numerical models simulating the torsional dynamics of their propulsion systems were developed and validated. The study's results integrated the state of the art of TVA related to ice-propeller interaction and provided elements to update the current regulatory recommendations.

6.2. Conclusions and discussion on the outcomes

The achievements presented in the thesis can be subdivided into four main topics:

1. *Layout of an integrated measurement system to be employed on board icebreakers to monitor shaftline vibrations and sea ice conditions.* Diverse sensors are installed on board CCGS *Henry Larsen* to monitor in parallel: shaft speed, torque, thrust; sea ice conditions; ship's motions. The data is employed to study the ice-induced shaft response and the propulsion performance of the plant. The integration of these diverse full-scale experimental datasets constitutes a unique outcome in the fields of ice engineering and marine propulsion systems for Arctic-going vessels.
2. *Development of a methodology and a modular numerical tool to simulate the torsional dynamics of propulsion systems during transient and steady-state conditions.* The lumped-element concept is used to model the shaftline's structural components; Electric and Diesel-engine prime mover excitation can be applied interchangeably; the Diesel-drive torque is simulated through a novel mathematical model, which was validated against full-scale shaft vibration measurements.

3. *Characterization of the ice-propeller milling torque magnitude as a function of the average sea ice thickness, obtained through full-scale measurements.* Experimental datasets acquired on board CCGS *Henry Larsen* during icebreaking operations are analyzed to correlate those two quantities, hence achieving a unique result in this research sector; an efficient algorithm to process shaft torque signals and obtain the corresponding ice-induced excitation is developed.
4. *Indications to review and possibly update the current Polar-Class guidelines about ice-propeller loads.* The correlation between ice-induced impact peaks on propellers and average ice thickness, as well as the study on the effects of different ice-propeller pulse characteristics, suggest that the mathematical formulations provided by IACS, ABS, DNV [1, 2, 3] may be reviewed to better describe this excitation.

The research has delivered a versatile design methodology to perform TVAs on Polar Class propulsion systems, which can be modelled in diverse configurations. The most relevant result of the numerical modelling phase is represented by the novel mathematical method to simulate the Diesel-drive's dynamic torque and the CPP controller applied to ice-propeller loads (Chapter 3). Also, the lumped-element concept to model propulsion shaftlines has proven efficient and reliable to simulate the shafting segments' response in transient and steady-state operations (Chapters 3, 4, 5).

Concurrently, the combined measurement system devised in the experimental activity of this study gives an important contribution to the current state of the art of the field (Chapters 2 and 4). For the first time, diverse sensor types and datasets aboard Canadian-Arctic-going

vessels are integrated to provide a global overview of shafts' torsional dynamic response and sea ice scenarios, in addition to monitor of the propulsive performance of the vessel. Specifically, the utilization of shaft optical sensors for shafts of icebreakers is an innovation of great importance, whose results will provide valuable indications for the design of future Polar-Class vessels' shaftlines.

Throughout the research activity, the guidelines of the Polar Rules by IACS [3] and their variants by ABS and DNV [1, 2] have been considered for the simulation of ice-induced torque sequences on propellers, and they have been discussed against the research's outcomes. In Chapter 3, it was shown that the CPP reaction to transient perturbations entails significant effects on the actual ice-propeller excitation. In Chapter 4, the correlation between ice-induced torque and ice thickness resulted in exceeding the homologous relation calculated through the Rules in some cases. In Chapter 5, the pattern of the impacting ice torque was examined: the ice pulses and especially the "ramps up-down" features were found to be crucial in determining the transient response of the system. The results concerning the ramps' implementation are currently being discussed between IACS and the American Bureau of Shipping (ABS). Hence, the thesis presents relevant material—also based on full-scale data—that should be considered for the next reviews of the Polar-Class recommendations on this subject.

6.3. Future developments

The study presented in this doctoral thesis gives the start to further developments on the matter of ice-propeller interaction modelling and marine propulsion systems' TVA. The full-scale experimental setup and the numerical methodologies presented in this work can be implemented for diverse types of vessels and hence obtain information on how ice-propeller load characteristics change in relation to different propulsion systems.

Regarding this project, through the support of MUN, NRC, and ABS, additional datasets are going to be acquired through the instrumentation on board CCGS *Henry Larsen*; a broader statistical analysis will provide a better representation of the distributions of actual ice-propeller torque data and sea ice characteristics. The full-scale measurements in ice would also be aimed to characterize different icebreaking manoeuvres to the corresponding response of the shaftline. Moreover, high-frequency vibration measurements regarding the shaftline torsional response are planned to take place on board both CCG icebreakers: the scope of these series of experiments is to obtain short-term signals related to collisions between propeller blades and ice pieces. This dataset will be analyzed to investigate the time-domain pattern of the ice-blade pulse, in order to better characterize the excitation caused by ice-milling processes. In particular, on board the CCGS *Terry Fox* the CPP interaction with ice-induced perturbations will be experimentally monitored. From both icebreakers, the actual ice-propeller excitation series would be then produced. This set of outcomes would be useful to validate the Polar Rules' formulation of the ice-propeller torque, to study how the blade properties of different propeller types affect the ice milling

process, and to integrate the model-scale findings obtained in the work by Veitch [4].

Concerning the numerical modelling and simulations, a more refined mathematical model for the Electric-drive torque should be elaborated and integrated into the tool; a special focus has to be dedicated to the output power control in response to transient load fluctuations. Possibly, FEA and CFD could be employed to investigate more precisely both the ice milling phenomenon on the propeller blades and the local structural response of the shaftline components. Together with the experimental data from the full-scale measurements, these results would further validate the regulatory guidelines on the subject. The outcomes from the ice-torque correlation through full-scale measurements could also be considered to include the thin-ice navigation capability of commercial vessels into the Polar Class framework.

References

- [1] ABS (2019). *Part 6: Specialized Items and Systems, Chapter 1: Strengthening for Navigation in Ice, Section 3: Machinery Requirements for Polar Class Vessels*. Rules for Building and Classing - Marine vessels, American Bureau of Shipping, Edition July 2019. 261, 262
- [2] DNV (2021). *Part 6: Additional Class Notations, Section 7: Polar Class, Par. 11: Ice interaction loads – machinery*, chapter 6: Cold climate. Det Norske Veritas, Edition July 2021. 261, 262
- [3] International Association of Classification Societies (IACS) (2006). Requirements concerning Polar Class - Polar Rules. Rev. 1 Jan 2007, Corr. 1 Oct 2007. 261, 262
- [4] Veitch, B. (1995). *Predictions of Ice Contact Forces on a Marine Screw Propeller During the Propeller-Ice Cutting Process*. PhD thesis, Helsinki University of Technology, Finland. Acta Polytechnica Scandinavica, Mechanical Engineering Series. 264



(a)



(b)

Figure 6.1: View from the CCG pier of CCGS *Henry Larsen* and St. John's downtown at the dawn of August 10, 2019, before the vessel's departure to undergo her open-water sea trials (a); The icebreaker CCGS *Terry Fox* moored at the CCG/Irving pier in the morning of December 22, 2019, getting ready before leaving for a two-day free-running test session (b).